University of Reading

Department of Meteorology

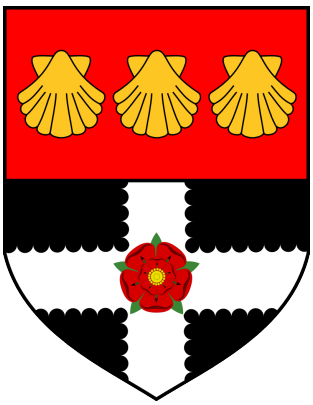

Heat-flux peaks in the atmosphere and their role in the evolution of weather systems

Andrea Marcheggiani

A thesis submitted for the degree of Doctor of Philosophy

October 2021

Abstract

Diabatic processes drive surface heat fluxes and provide energy to weather systems through heating where it is warm and cooling where it is cold, globally increasing the available potential energy and giving a crucial contribution to the maintenance of midlatitude storm track regions. Locally, however, surface heat fluxes can be negatively correlated with lower-tropospheric air temperature so that cold regions are heated and warm regions are cooled.

Peaks of intense air–sea thermal interaction result, on average, in the damping of the temperature variance associated with weather systems, thus depleting the potential energy available for their development, in contrast with the average positive contribution that diabatic processes give globally.

In this thesis we characterise the role played by heat flux peaks in the evolution of storm tracks' life cycle by interpreting the spatial covariance between surface heat flux and lower tropospheric air temperature as a measure of the intensity of thermodynamic activity associated with weather systems. Through the analysis of the temporal evolution of covariance we identify the average response of the atmospheric circulation to surface heat flux peaks, which are found to have the largest impact within cold sectors of weather systems, where the atmospheric boundary layer is deeper and the surface–troposphere thermal coupling is enhanced.

Meridional heat fluxes also feature sporadic bursts of activity that can account for a large fraction of the total meridional heat exchange. Peaks of meridional heat flux result from both strong meridional wind–temperature correlation and variances, which play distinctive roles in the cyclical evolution of heat flux peaks depending on the relative predominance of different storm growth mechanisms.

Heat-flux–temperature correlation can therefore be considered as an independent dynamical variable carrying information about the state of the atmospheric circulation and its thermal interactions.

Declaration

I confirm that this is my own work and the use of all material from other sources has been properly and fully acknowledged.

Andrea Marcheggiani

Acknowledgements

It goes without mention that, like most things in life, I would not have got to the end of this long journey if it were not for the help and support of all the people I have had the honour and delight to meet and get to know better over the past few years.

First and foremost, I want to thank my lead supervisor, Maarten Ambaum, who has provided me with invaluable guidance and advice throughout my PhD experience and beyond, putting up with my ridiculously long paragraphs and more-than-occasionally cryptic wordings. I will surely miss the weekly meetings with countless plots to discuss and make sense of, while sharing the utter disrespect of any bureaucratic hassle and finding ways to (or better, how to safely ignore to) deal with it.

I am also extremely grateful to my second supervisor, Huw Lewis, and his collaborators at the Met Office in Exeter (in particular, Claudio Sanchez), who all invested plenty of their time in helping me tame the Unified Model and provided me with their feedback on my work.

I would like to thank my monitoring committee, John Methven and Keith Morrison, who have been of great help in making sure my research remained on track.

I am at times surprised when I think how many friends surround me in my daily life and how much I owe every single one of them for their friendship. Thanks are due to the many awesome people I met during my time here in Reading, with special mentions to Ana Carolina and all of her surnames, Dan the True Northumbrian lost in the South, Dom (Jom for friends, Empirical Nojinic Modes how I'll always remember him), Kris from Atlanta (Georgia, which they always need to specify for some reason), Jake (pun-master and kingmaker of what you can bring to the pub), The Haonan and Tegwen (sharing a tenancy for two years, during a pandemic, is no mean feat, kudos to both of us for living it through physically unscathed!). I am also grateful to my own network of expat Italian friends (Federica, Katiuscia,

Matteo, Fabio and Dalila) who helped me create my own little Italy here in the UK. Special thanks also go to Laura Ferranti, who has offered great support during my stay in Reading and invaluable advice in taking crucial decisions in my academic career.

I could never be able to appropriately express in words how lucky and grateful I was to find myself with such a great and loving family, whose support I can always rely on and who are the best people I know, which makes finding a new home a hard task and I am yet to find a place in the world that compares to 'home home'.

To all of you, thanks for being there.

Contents

Chapter 1

Introduction and background

The climate system can be described as a heat engine which operates primarily across the temperature difference existing between warm equatorial regions and the colder poles, as lower latitudes receive more solar radiation than higher latitudes due to the angle at which solar radiation reaches the Earth's surface and the mean contrast in albedo. By transporting heat polewards, the climate system aims at neutralising the thermal imbalance that is induced by this differential solar radiative heat input. However, as the meridional temperature gradient is continually restored by the radiative heating, the climate system never reaches thermal equilibrium and remains in ceaseless evolution.

Shifting our focus from the climatological scale onto much shorter time and length scales, tropical and extra-tropical weather systems can be seen as the synoptic-scale response to the global temperature spatial variance, acting as heat engines exchanging heat across temperature gradients.

Tropical cyclones derive their energy primarily from the vertical temperature gradient between the warm ocean surface and the tropopause, which is located at a higher altitude in the tropics relative to higher latitudes, while the horizontal components of the temperature gradient are negligible in comparison and typically do not play a significant role in the growth of the cyclone.

On the other hand, the development and evolution of extra-tropical weather systems rely fundamentally upon the meridional temperature gradient that is characteristic of the temperate zones between the warm subtropics and the cold arctic regions. The temperate, extra-tropical zones extend between 30° and 60° of latitude in either the Northern or the Southern Hemisphere and the extra-tropics are typically referred to as midlatitudes

interchangeably.

Figure 1.1 illustrates the boreal winter (December, January and February, DJF) climatology of the zonal mean potential temperature profile based on the European Centre for Medium-range Weather Forecasts (ECMWF) ERA40 reanalysis dataset. The north–south temperature contrast in the midlatitudes is accentuated in winter, as reduced solar radiation over the poles results in lower temperatures there while the amount of solar radiation received by equatorial regions and the average temperatures remain unaltered. This contributes to the stronger extra-tropical storm activity in the winter season compared with the summer season.

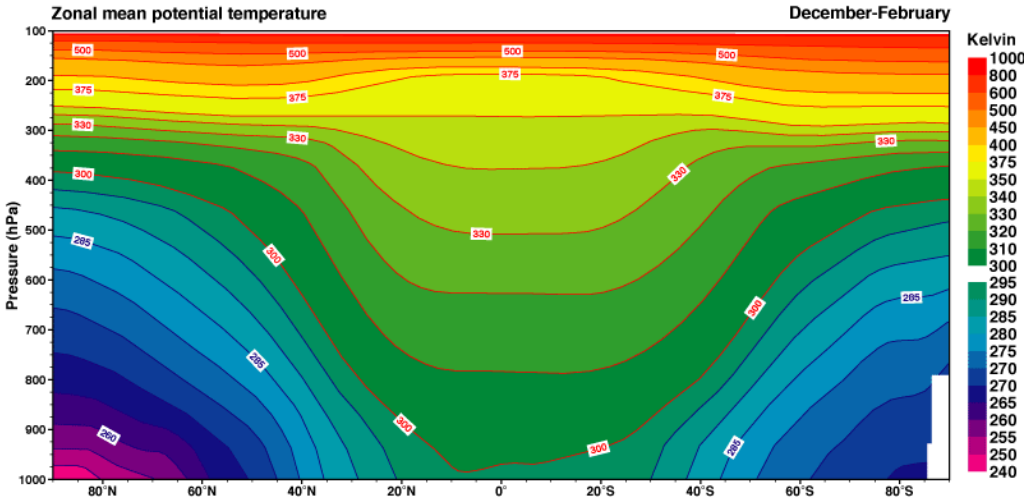

Figure 1.1: Climatology (latitude-pressure projections) of zonal mean potential temperature for the boreal winter season (December-February) from the ECMWF ERA-40 Atlas.

1.1 The atmospheric energy cycle

The concept of Available Potential Energy (typically shortened as APE), first formulated by Margules (1903) and later established by Lorenz (1955), relies essentially on considerations of stability of the atmospheric thermal structure and how much of the potential energy associated with the atmospheric thermal structure is available for conversion to kinetic energy and thus for storm growth. In the atmosphere, we can distinguish two different states of the flow that minimise and maximise the amount of available potential energy and the distinction is made according to the mutual dependency of the pressure and temperature fields.

If the density of air, ρ, is a function of pressure alone (i.e. $\rho = \rho(p)$), the gradients of pressure, ∇p, and density, $\nabla \rho$, become parallel and, therefore, the solenoidal term in the vorticity equation is zero ($\nabla \rho \times \nabla p = 0$). When the atmosphere is found in this state it is said to be *barotropic* (from the ancient Greek *baro*, pressure, and *tropos*, react to a stimulus), as the vertical structure of the flow changes only in response to horizontal pressure variations. In a barotropic atmosphere, despite the large amount of potential energy associated with the vertical distribution of mass, the vertical stability due to the temperature stratification and the uniformity in such a temperature distribution do not allow for any dynamical mechanism to be triggered. In light of this, Peixoto and Oort (1992) describes this configuration as an atmosphere in a *dead state*. A barotropic flow is normally observed where the temperature field is characterised by weak horizontal temperature gradients, which is often the case in the tropics, as it can be seen in Fig. 1.1.

On the other hand, in the midlatitudes the effect of differential radiative heating is most evident and gives rise to substantial horizontal gradients in the temperature field. In this case, air density varies not only in function of pressure but also in response to temperature variations, thus isobaric and isentropic surfaces are significantly misaligned and the flow is said to be *baroclinic* (from the ancient Greek *baro*, pressure, and *clino*, inclined). Peixoto and Oort (1992) denotes a baroclinic atmosphere as in an *alive state*, given that part of the potential energy is in this case available to be converted into kinetic energy in order for the atmosphere to reach a stable state. In simpler terms, midlatitude weather systems develop with the ultimate aim of bringing to alignment the isentropic surfaces with the isobaric surfaces, which corresponds to the state of minimum potential energy.

In light of this, the available potential energy can be defined as the difference in potential energy between the current state of the flow and a reference stable state. The definition of such a stable state might depend on the specific framework that is considered and it has been object of research for a long time. For a detailed account, we refer the reader to the thorough review by Tailleux (2013) and to a subsequent study by Novak and Tailleux (2018) on the formulation of a local expression of available potential energy. In this thesis, we will consider the Eady growth rate, σ_{BI}, as a simple measure of the average potential energy available to weather systems for conversion into kinetic energy. It represents the fastest growth

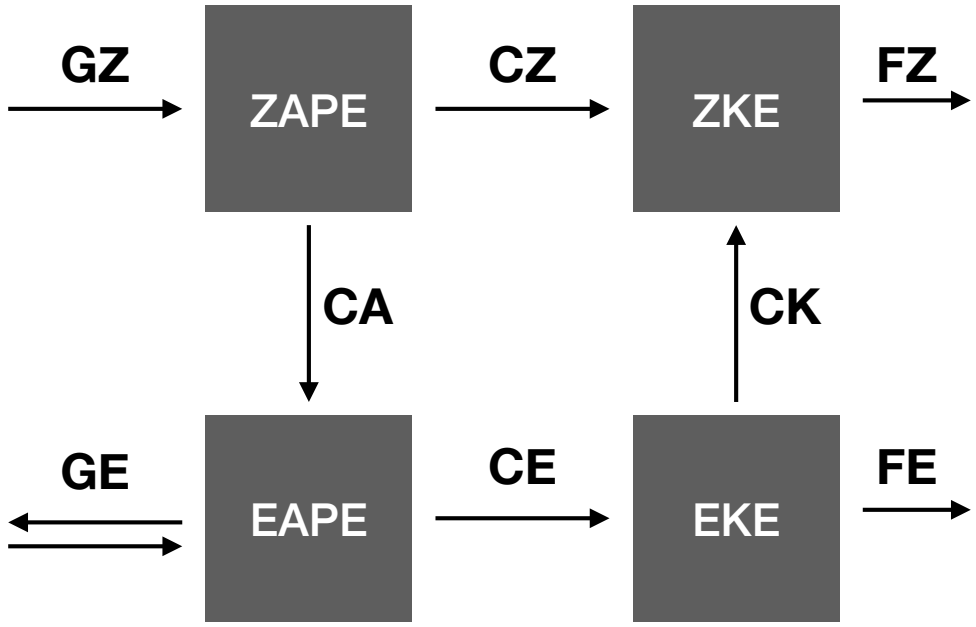

Figure 1.2: Diagram of the Lorenz energy cycle for the atmosphere. G stands for generation terms; C for conversion; F for frictional dissipation; Z and E indicate zonal and eddy components, respectively; finally, A and K correspond to available potential and kinetic energy.

rate of baroclinic instabilities according to the Eady model (Eady, 1949) and is directly proportional to the meridional temperature gradient and, indirectly, to the local static stability of the atmosphere (i.e. to its inverse),

$$\sigma_{BI} = 0.31 \frac{f}{N} \frac{\partial u}{\partial z}, \tag{1.1}$$

where f is the Coriolis parameter, N the static stability, u the wind zonal component and BI stands for Baroclinic Instability.

In order to keep the general circulation *alive*, available potential energy must be generated through heating and cooling of warm and cold regions respectively, and this is globally achieved by the differential solar radiative heating (Peixoto and Oort, 1992). Kinetic and potential energies are traditionally decomposed into their zonal mean-flow and an eddy component, meant as a deviation from the zonal mean-flow. In fact, in the seminal work by Lorenz (1955) the mathematical formulation of the energy cycle for the atmosphere (also know as Lorenz energy cycle) is based on this decomposition.

Starting from the momentum and the thermodynamic equations, it is possible to yield balance equations for the different energy reservoirs that

are considered in the Lorenz energy cycle. Analytical expressions are widely available in the literature and the reader is referred specifically to James (1995) for a thorough derivation of these. As exemplified by a diagram in Fig. 1.2, the energy cycle involves four main energy reservoirs, namely zonal (ZKE) and eddy (EKE) kinetic energy and zonal ($ZAPE$) and eddy ($EAPE$) available potential energy. The interactions between these energy reservoirs are represented by conversion terms, C, and the generation and dissipation of energy respectively by G and F (which stands for friction).

Average values and deviations from these can be defined either in a time domain (time means and anomalies) or in a spatial domain (area mean and deviations from it) or even in a mixed space–time domain (e.g., considering the spatial average of time anomalies). The specific framework adopted can change the representation of the energy cycle and, most importantly, its interpretation.

The balance between the production of potential energy and its depletion by the action of transient eddies is at the base for the existence of localised regions in the midlatitudes of intense storm activity that are typically referred to as storm tracks.

1.2 Northern Hemispheric storm tracks

Storm track regions are identified, from a Eulerian point of view, as those regions in the midlatitudes characterised by strong synoptic-scale variance in mean sea level pressure, which can be associated with the most intense weather activity. Figure 1.3a, taken from Hoskins and Valdes (1990), provides a summary of Northern Hemispheric winter storm track structure based on high-pass time-filtered transients in ECMWF data for DJF in the years 1979-1984: the extent of the storm track region is indicated by the maxima in 2–6-day variance of geopotential height (thin contours) at 250hPa and lower-tropospheric horizontal ($\overline{v'T'}$, thick dashed) and vertical ($\overline{-\omega'T'}$, thick dotted) temperature flux. Also plotted are the horizontal components of the **E**-vectors (Hoskins et al., 1983) in the upper troposphere, whose divergence indicates a tendency to produce cyclonic and anticyclonic circulation on the poleward and equatorward flanks of the storm track core, respectively.

Alternatively, if we follow the evolution of extra-tropical cyclones in time (i.e., taking a Lagrangian perspective), we find that their trajectories cluster

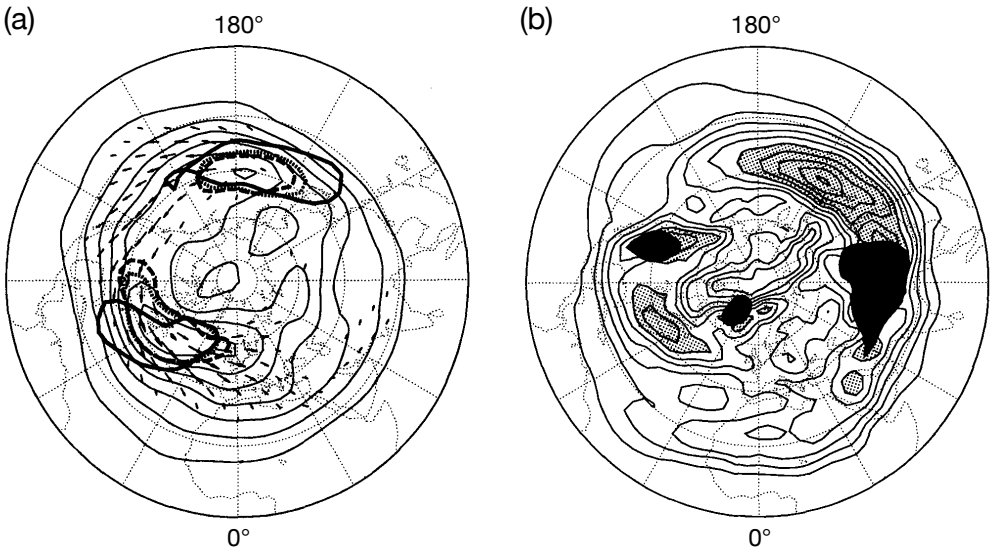

Figure 1.3: Storm tracks Eulerian identification. (a) Geopotential height variance (thin contours, every 15m^2) and **E**-vectors both at 250hPa (arrows); single contours of 700hPa horizontal (thick dashed at 10 K ms^{-1}) and vertical (thick dotted at 0.2 K Pa s^{-1}) temperature flux together with column mean diabatic heating (thick solid at 50 W m^{-2}). (b) Eady growth rate σ_{BI} at 780hPa for the NH winter mean (contours every 0.1 day^{-1}, stippled above 0.6 day^{-1}); regions where the 780hPa level is within 1km of the orography is blacked. Panels (a,b) are taken from Fig. 1 and Fig. 2 in Hoskins and Valdes (1990), respectively.

along the same storm track regions, which can therefore also be identified as those regions where cyclones are statistically more common. The cyclone track density as observed in NCEP-NCAR reanalysis (Kalnay et al., 1996) for the winter half-year (October to March) from 1958 to 2007 is shown in Fig. 1.4a (taken from Ulbrich et al., 2009), where a cyclone is identified by the corresponding quasi-geostrophic relative vorticity maxima (Pinto et al., 2005), while Fig. 1.4b refers to the strongest cyclones only (defined by the 5% largest values of the Laplacian of pressure), which are concentrated on the northern oceanic basins affecting North America and northwestern Europe.

The mean Eulerian picture is implicitly related to the Lagrangian picture of individual storms and this is concisely summarised in Fig. 1.5 which is taken from a review study by Shaw et al. (2016) on the effects of climate change on storm track processes. Figure 1.5a shows the wintertime cyclone track density and vertically averaged eddy kinetic energy (10-day high-pass filtered) from the ERA-Interim reanalysis (Dee et al., 2011) in both the

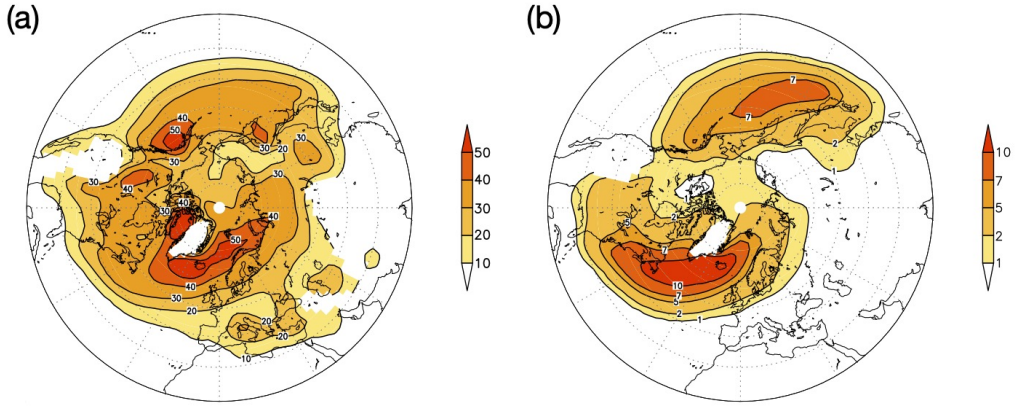

Figure 1.4: Storm tracks Lagrangian identification. (a) NCEP-NCAR reanalysis storm track density for the Northern Hemisphere extended winter (October to March, 1958–2007). (b) As in (a) for the 5% strongest storms. Systems identified at grid points with orography above 1500m are removed. Figure taken from Ulbrich et al. (2009).

Northern (DJF) and Southern (June-July-August, JJA) Hemispheres. Cyclones are tracked and their density computed (Hanley and Caballero, 2012) and shown in black contours, with the location of tracks of the 0.5% most intense cyclones (plotted in blue) consistent with Fig. 1.4b. The correspondence between extrema in meridional energy transport and storm track regions is evident from inspection of Fig. 1.5b, where the vertically and longitudinally averaged northward transport of momentum transport and dry static, latent and eddy kinetic energy transport are shown. A large fraction of the seasonal poleward total energy transport is observed to be associated with intermittent bursts of storm track activity (Swanson and Pierrehumbert, 1997; Messori and Czaja, 2013) linked to the action of individual systems (or cluster of systems, Mailier et al., 2006) and Eulerian measures of storm track activity are essentially shaped by the integral over time of the contribution from each of these systems. The differences in the diagnosed storm track extent resulting from the use of various Eulerian measures (e.g., time variance of geopotential, eddy kinetic energy, meridional heat flux, etc.) derive essentially by the distinct roles that transient eddies play across the storm track as they evolve into mature systems and, depending on the large-scale flow configuration (i.e., the position of the eddy-driven jet), potentially give rise to secondary cyclogenesis (Priestley et al., 2017).

In the Northern Hemisphere, storm tracks are longitudinally localised

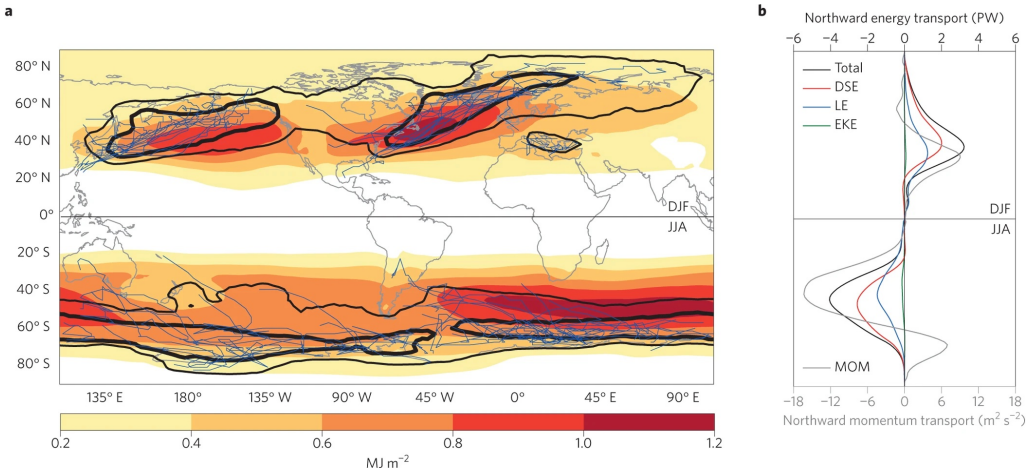

Figure 1.5: Wintertime (DJF, 0–90°N; JJA, 0–90°S) storm tracks in the ERA-Interim reanalysis data set. (a) Vertically averaged, 10-day high-pass filtered eddy kinetic energy (colour shading) and cyclone track density (thin and thick black contour for 10 and 20 tracks, respectively, per 10^6 km^2 per season), with individual cyclone tracks for the top 0.5% most intense cyclones ranked by minimum sea-level pressure (blue lines, shown separately for the Pacific, North Atlantic, Mediterranean and Southern Oceans). (b) Vertically and longitudinally averaged, 10-day high-pass filtered, northward transport of momentum (MOM; grey), dry static energy (DSE; red), latent energy (LE; blue), eddy kinetic energy (green) and total energy (black). Figure and caption adapted from Shaw et al. (2016).

and coincide with regions where the structure of the atmospheric circulation is baroclinic in nature. In a baroclinic flow, isentropic surfaces are not aligned with the geopotential and this occurs primarily over regions where the meridional temperature gradients are most accentuated. A baroclinic region is characterised also by a large value of the maximum Eady growth rate σ_{BI} (Eq. 1.1). While the Eady growth rate is primarily relevant to the early stages of baroclinic development (Eady, 1949), it can be viewed as a measure for local baroclinicity and, more generally, for the potential energy available to weather systems (Hoskins and Valdes, 1990; Ambaum and Novak, 2014).

Hoskins and Valdes (1990) were among the first to investigate the mechanisms that could explain the existence of storm tracks. They made use of a linear, stationary wave model with storm track region forcings taken from ECMWF data for winters from 1979 to 1984 (where net diabatic heating is deduced as a residual from the thermodynamic equation) to examine the response of the mean flow to the different forcings.

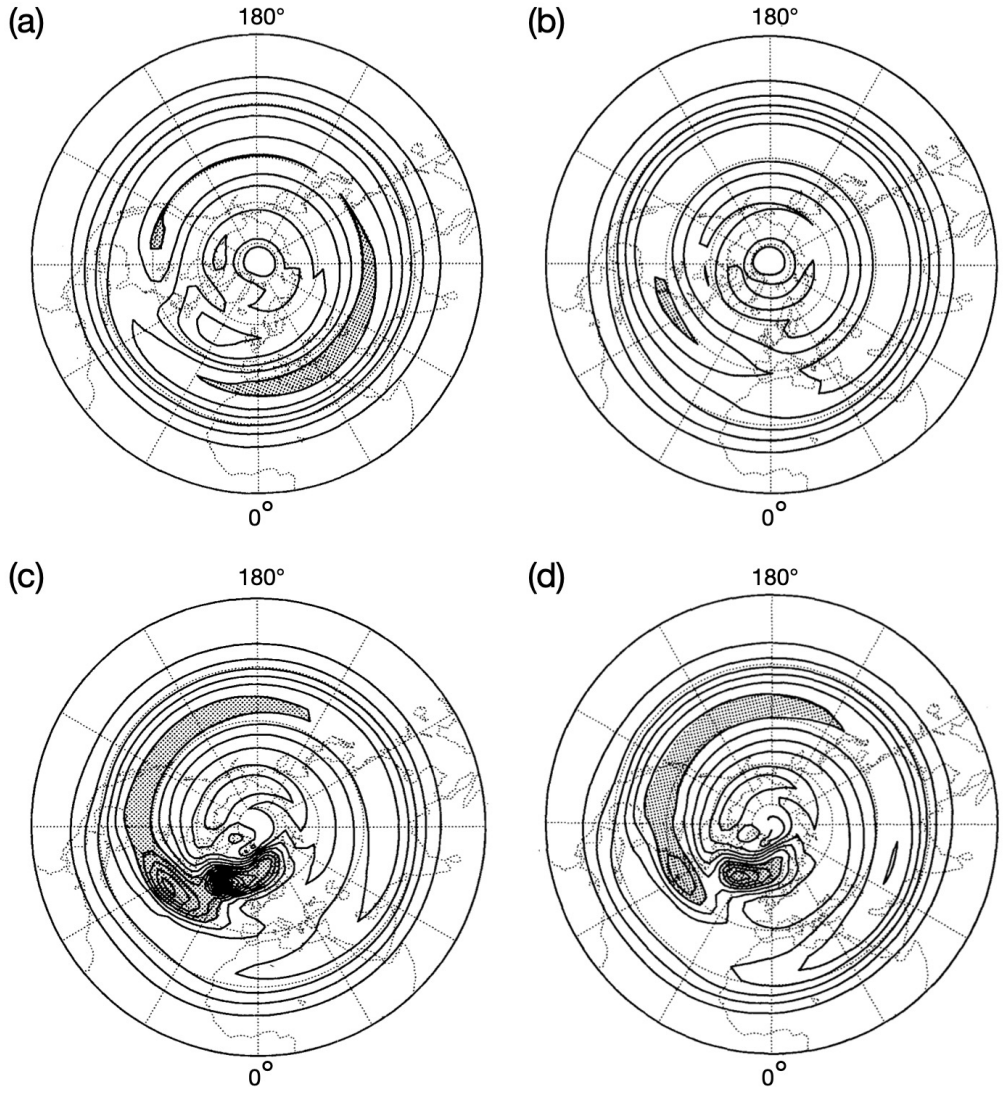

Figure 1.6: The baroclinicity parameter σ_{BI} (Eq. 1.1) associated with the steady state linear response to North Atlantic direct thermal (a) and vorticity forcings (b) by synoptic scale transient eddies, to North Atlantic diabatic heating (c) and to the sum of these forcings (d). Contours as in Fig. 1.4b. Collated from Hoskins and Valdes (1990).

The effects of the direct thermal forcing by midlatitude weather systems, associated with their *sloping convection* nature, whereby heat is exported from lower-level low latitudes to upper-level high latitudes, were found to lead to a minimum of baroclinicity along the storm track (Fig. 1.6a), effectively opposing its existence.

On the other hand, the vorticity forcing acts to enhance the confluence at the upstream end of the storm track as a result of cyclonic and anticyclonic induced circulations on the poleward and equatorward flanks of the storm

track, thus partly compensating the reduction in baroclinicity (Fig. 1.6b).

The largest contribution to the maintenance of high levels of baroclinicity, however, derives from the response of the mean flow to diabatic heating which restores the initial temperature gradients (Fig. 1.6c). The overall response to the different forcings eventually shares a close affinity with the observed climatology for baroclinicity, especially for the North Atlantic storm track (compare Fig. 1.6d and Fig. 1.4b).

Ambaum and Novak (2014) proposed a non-linear model whereby the evolution of baroclinicity, s, and eddy heat flux, f, is described by the following set of equations,

$$\dot{s} = F - f, \tag{1.2a}$$

$$\dot{f} = 2(s - s_0)f, \tag{1.2b}$$

where F and s_0 are constants representing, respectively, the diabatic forcing that restores baroclinicity and the eddy dissipation rate. Figure 1.7a shows a numerical solution of Eqs. 1.2 for a large value of the conserved energy (Ambaum and Novak, 2014) and it evidences the ability of the Ambaum–Novak model in reproducing the sporadic nature of eddy meridional heat flux that is observed in the real atmosphere (Swanson and Pierrehumbert, 1997) and shown to be important in setting the climatological picture as the intermittent bursts of heat flux in the storm track regions can account for a large fraction of the total heat transport (Messori and Czaja, 2013). Furthermore, predictions of the model (Eq. 1.2) also capture the observed link between the erosion of baroclinicity by transient eddies and its ensuing restoration, which is seen from lagged composites of excess baroclinicity and eddy heat flux centred on a peak of the latter (Fig. 1.7b).

In a later study by Novak et al. (2017), the evolution of the North Atlantic storm track is then placed in the context of a predator–prey relationship between eddy heat flux and baroclinicity. According to the model by Ambaum and Novak (2014), diabatic forcing from land-sea contrast and from SST gradients associated with western boundary currents generate a background baroclinic state which is conducive for eddy growth and, consequently, higher storm track activity. In fact, land-sea contrast and SST fronts are weaker in summer than in winter and storm-track activity declines significantly. As active eddy mixing gradually depletes baroclinicity along the storm track, further eddy production is inhibited and baroclinicity is

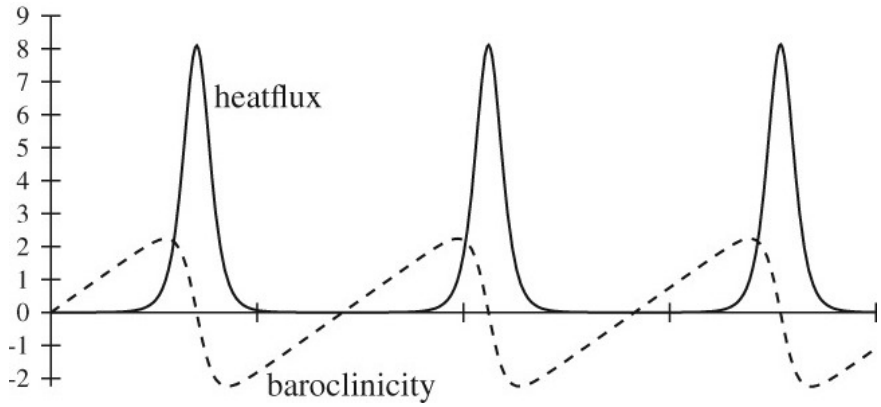

(a) Numerical solution of the Ambaum-Novak model (Eqs. 1.2) for excess baroclinicity $s - s_0$ (dashed line) and eddy heat flux f (solid lines), rescaled with F and $\sqrt{F}$ respectively. The time is rescaled with the natural frequency $\sqrt{2F}$ of the system and each tick mark corresponds to one period of this natural frequency.

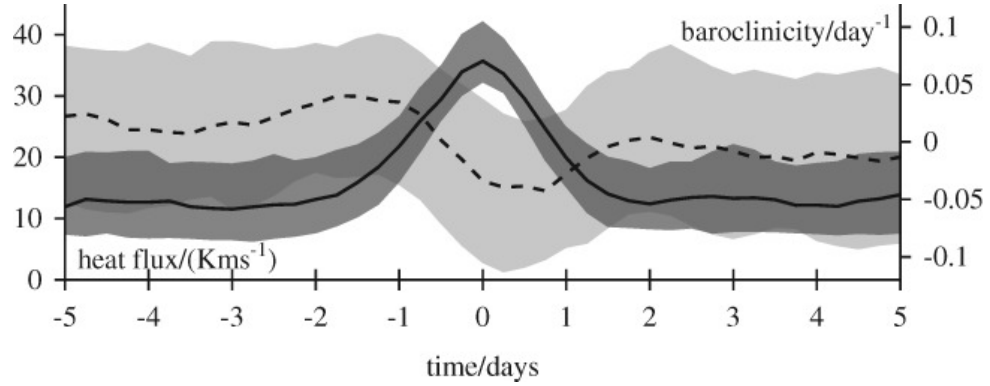

(b) Composite of heat flux and baroclinicity for the winters of 1957–2001, centred around the maxima of the heat flux. The solid line is the median value of the heat flux and the dashed line is the median value of the baroclinicity. The shading corresponds to the interquartile range of each quantity. The anomalous (excess) baroclinicity has been plotted; the mean offset in the baroclinicity is 0.46day^{-1}.

Figure 1.7: Figures and captions for panels (a) and (b) adapted, respectively, from Figures 2 and 5 in Ambaum and Novak (2014).

restored to the initial background due to diabatic forcing. The cycle then repeats itself as long as the diabatic forcing is able to maintain its role as source of baroclinicity.

Novak et al. (2015) further explored the importance of this predator–prey relationship in driving the life cycle of the North Atlantic storm track. They linked the observed transitions of the North Atlantic eddy-driven jet (Woollings et al., 2010; Franzke et al., 2011) to its northward deflection at the downstream end of the storm track during bursts of high meridional heat flux, which is associated with strongly stretched eddies that enhance anticyclonic breaking ultimately pushing the jet northwards, as we can see

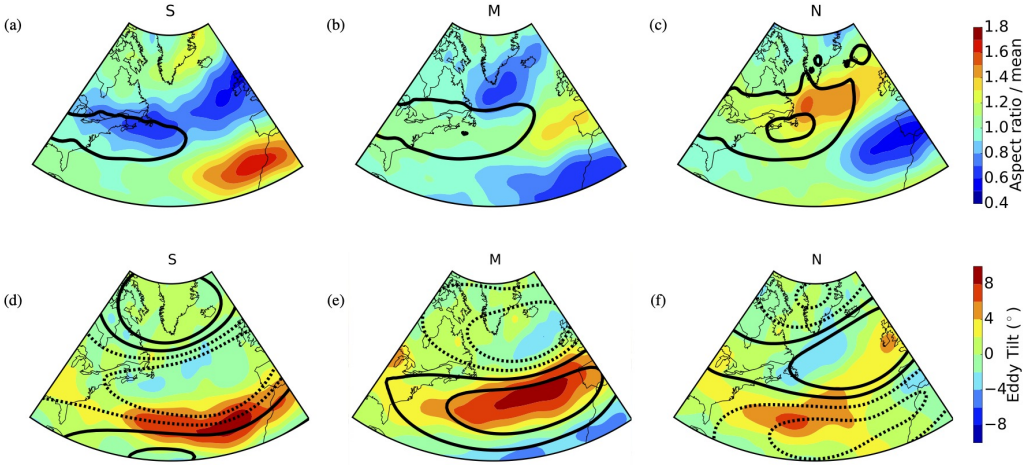

Figure 1.8: Upper panels: regime composites of aspect ratio (color) with heat flux (10 and 20 K ms^{-1}) in thick black contours; lower panels: regime composites of eddy tilt (color), with 250hPa stream function anomaly (-6×10^6, -2×10^6, 2×10^6 and 6×10^6 m^2s^{-1}) in thick black contours (lower panels). *S*, *M* and *N* stand for southern, middle/central and northern jet regimes. Figure and caption adapted from Figure S2 in Novak et al. (2015).

most clearly in Fig. 1.8c,f and specifically in the region to the northwest of the British Isles. Conversely, low meridional heat flux corresponds with less stretched and more extensive eddies that are more conducive to cyclonic breaking and a more zonal jet (Fig. 1.8a,d and also Fig. 1.8b,e).

1.2.1 The maintenance of storm tracks

Hoskins and Valdes (1990) concluded that storm tracks could be said to be self-maintaining as they ascribed the existence of diabatic heating maxima to the horizontal and vertical displacements associated with individual systems that form the storm track itself. Furthermore, they pointed out that the low-level mean flows induced by all the eddy effects have wind-stress curls that are in the sense of driving the warm western boundary currents in the northern Atlantic and Pacific Oceans (respectively the Gulf Stream and the Kuroshio currents) which in turn are crucial to the existence of the storm tracks.

Hoskins and Valdes (1990) focussed their attention upon the effects of the different forcings on baroclinicity at the steering level (i.e. at a height, above the surface, of one Rossby radius rescaled by f/N) and, specifically, did not distinguish between the different components of the diabatic heating forcing. Hotta and Nakamura (2011) subsequently extended the framework

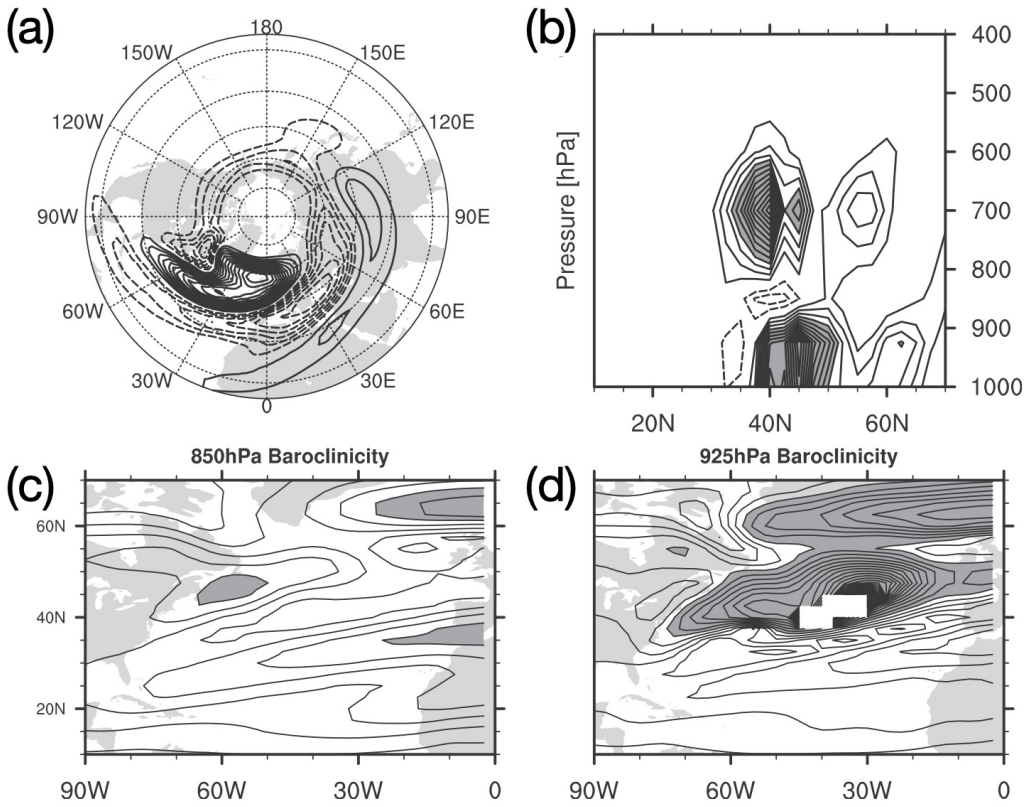

Figure 1.9: Steady linear response to the North Atlantic subgrid scale sensible heat forcing, in (a) zonally asymmetric temperature field (every 2 K) at the 925hPa level, (b) anomalous model baroclinicity response (every 0.05 day^{-1}, shaded above 0.2 day^{-1}) averaged between 80° and 20°W, and in the background baroclinicity (every 0.1 day^{-1}, shaded above 0.6 day^{-1}) at the (c) 850hPa and (d) 925hPa levels. Negative contours are dashed. Zero contours are omitted. Figure and caption adapted from Hotta and Nakamura (2011).

of Hoskins and Valdes (1990) to the whole troposphere and considered the effects of sensible heating, large-scale condensation and convective latent heating forcings individually. In this way they were able to emphasise the strong local effect of sensible heat fluxes in relaxing the lower troposphere towards the underlying sea surface, shown in Fig. 1.9 for lower tropospheric temperature and baroclinicity in the North Atlantic, which is found to be the dominant factor compared with latent heating in shaping the response to the total diabatic forcing considered by Hoskins and Valdes (1990). The action of sensible heating at the surface arguably anchors the storm track to the stark SST gradients associated with western boundary currents (Gulf Stream and Kuroshio) where cross-frontal contrast in heat supply enhances surface westerlies and leads to high baroclinicity at the surface. Nakamura

et al. (2008) had previously suggested that the collocation of SST fronts, surface westerly jets and storm tracks was not coincidental, as idealised experiments in an *aquaplanet* configuration (i.e. simulation of the global atmospheric circulation in the absence of orography) where the SST fronts are substantially smoothed showed a considerable reduction in storm track activity both in the upper and lower levels, while location of the storm track was found to be much more latitudinally variable. An *oceanic baroclinic adjustment* mechanism was proposed whereby the differential heating from the ocean crucially replenishes the surface baroclinicity in the storm track regions, essentially fuelling storm track activity. The findings of Hotta and Nakamura (2011), therefore, question the self-maintaining nature of storm tracks, advocating for the importance of external heating from the ocean in counteracting the relaxing effect by eddy heat transport. Their conclusions are in contrast with Hoskins and Valdes (1990) who argued that internal heating from storms was key to the storm track's maintenance.

The traditional perspective used in both Hoskins and Valdes (1990) and Hotta and Nakamura (2011) to study the evolution of baroclinicity, and potential energy more in general, involves essentially the inspection of horizontal temperature gradients on pressure levels: the starker the temperature gradients, the higher potential for baroclinic instabilities to occur. However, since strong static stability is inhibitive to baroclinic development (as follows from Eq. 1.1) even in regions with large horizontal temperature gradients, the magnitude of the temperature gradients does not necessarily reflect the actual potential for baroclinic development. In view of this, to examine the maintenance of baroclinicity along the North Atlantic storm track, Papritz and Spengler (2015) offers a new perspective whereby baroclinicity is linked to the slope of isentropic surfaces: steeper slopes correspond to baroclinic conditions more favourable for conversion of potential to kinetic energy, while weaker slopes correspond to flat isentropic surfaces symptomatic of a barotropic structure.

The material tendency of the slope of an isentropic surface is broken down in three separate contributions:

- differential isentropic displacement, i.e. the tilting of isentropic surfaces by isentropic displacement vertical wind, defined as in Hoskins et al. (2003) and illustrated in Fig. 1.10a where the mean motion in a baroclinically growing disturbance is shown by the red and blue arrows, denoting ascending warm and descending cold air, respectively,

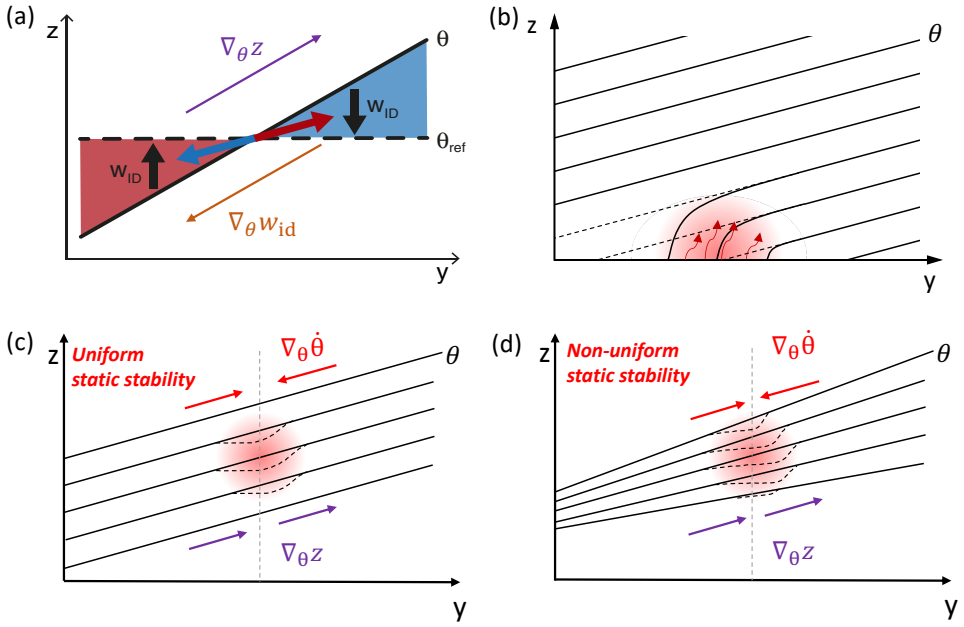

Figure 1.10: (a) Sloping isentropic surface (solid black) depicting a baroclinic zone with warm air to the south (red shading) and cold air to the north (blue shading); the dashed line θ_{ref} denotes the reference state with flat isentropic surface while purple and orange arrows denote the along-slope gradient of the geopotential and w_{id}. Schematic illustrating how (b) upward surface sensible heat fluxes and a confined region of latent heat release in a statically uniform (c) and non-uniform (d) atmosphere deform an isentropic surface and change its slope. Red and purple arrows denote the along-slope gradient of the heating and geopotential, respectively. Solid and dashed lines in panels (b) correspond to isentropic surfaces before and after heating (the opposite in panels c,d). Adapted from Papritz and Spengler (2015).

with the associated isentropic displacement, w_{id}, indicated by black arrows;

- differential diabatic heating, i.e. the deformation of an isentropic surface due to heating pulling isentropes down towards the surface, increasing and decreasing the slope upslope and downslope respectively (Fig 1.10b,c,d);

- isentropic advection following the flow, reflecting the fact that isentropic slope is generally not a property inherent to air parcels but a characteristic of the surrounding environment.

It is argued that diabatic heating ensuing from latent heat release provides for the maintenance of the slope in the lower troposphere (while mi-

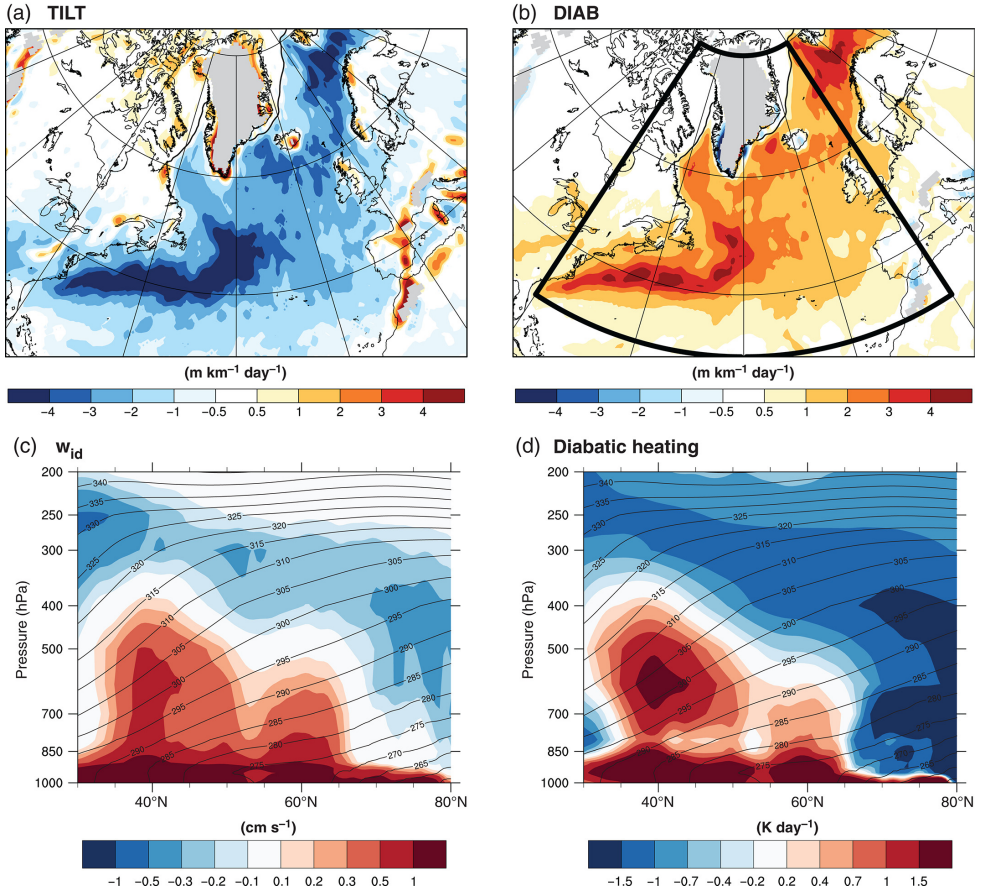

Figure 1.11: Tendencies of the slope of isentropic surfaces in DJF due to (a) isentropic displacements and (b) diabatic processes vertically averaged between 900 and 200hPa. Lower panels show meridional cross-sections of (c) isentropic displacement vertical winds w_{id} and (d) total diabatic heating $\dot{\theta}$, zonally averaged over the North Atlantic between 80°W and 0°E (cf. box in (b), excluding land grid points). Grey contours denote potential temperature at intervals of 5 K. Figure and caption adapted from Papritz and Spengler (2015).

crophysical processes in the free troposphere restore the upper-level slope), as it leaves behind a confined region of increased slope, thus restoring the baroclinic structure of the flow which favours the development of subsequent cyclones. Figure 1.11 presents a time average (DJF, 2008 to 2010) for the isentropic tilting (a) and diabatic deformation (b) contributions to the isentropic slope tendency and are seen to almost cancel each other along the North Atlantic storm track region, as isentropic displacements must compensate for the effect of diabatic heating. This is also confirmed by inspecting the zonally-averaged cross section of the isentropic displacement wind and diabatic heating (panels c and d of Fig. 1.11, respectively), as the

associated lowering of the isentropic surfaces by the mean diabatic heating is compensated by isentropic lifting. The co-location of the largest contributions from isentropic tilting and diabatic heating to the slope tendency is arguably indicative of their equal importance in the maintenance of the storm track. Furthermore, a large fraction of the total diabatic tendency is ascribed to cold-air outbreaks events, when turbulent air–sea heat fluxes are found to peak, which is consistent with the location of the largest values of diabatic heating near the surface in Fig. 1.11d.

1.2.2 The role of local sensible heating

Diabatic processes at the surface, such as sensible and latent heat fluxes, can amplify horizontal temperature gradients by heating where it is warm and cooling where it is cold, resulting in the generation of available potential energy. From a global perspective this is achieved by the global differential in radiative heat input. However, the local thermodynamic effects of latent and sensible heat fluxes are much less clear, as upward air–sea heat fluxes typically may be expected to coincide with a cooler local atmosphere, which would point towards a negative contribution to the local potential energy budget.

In the Lorenz energy cycle, diabatic processes are considered as generation terms for both the zonal and eddy components of the available potential energy reservoir. In particular, these terms (GZ and GE in Fig. 1.2) are proportional to the covariation of heat flux and temperature anomalies (see section 5.3 of James, 1995). The global estimates of available potential energy generation (e.g., Oort, 1964; Oort and Peixóto, 1974; Ulbrich and Speth, 1991; Li et al., 2007; Marques et al., 2009) are found to vary not only in time from seasonal to inter-annual scales, but also depending on the type of domain selected, be it purely temporal, spatial or a combinations of these. In particular, Oort (1964) initially found that generation of eddy available potential energy was negative in a space domain, whereas in a mixed space-time domain it flipped sign. In a later study, Ulbrich and Speth (1991) further decomposed eddy energy into stationary and transient components and estimated the former to be positive and the latter to be negative, though with different magnitudes.

It must be noticed that early estimates of these generation terms were based on residuals from the main balance equations, as their direct computation was not viable due to lack of archived data (e.g., Ulbrich and

Speth, 1991, based their results on a dataset consisting of January and July from 1980 to 1986). More recent studies have further shown that the total diabatic generation of transient eddy potential energy is largely negative across the majority of the Northern Hemisphere's mid-latitudes (Chang et al., 2002), with diabatic heating damping transient eddy evolution, particularly during the winter season (Chang and Zurita-Gotor, 2007).

In their work, Papritz and Spengler (2015) put in clear evidence the positive role of latent heat release through generation of isentropic slope in the restoration of baroclinicity, following its depletion by the large-scale flow associated with extra-tropical cyclones. While sensible heat fluxes clearly contribute to the generation of slope at the surface (see Fig. 1.10b), their input into the total diabatic generation of slope was found to be of secondary importance compared to that of latent heat release. This appears to be in contrast with findings by Hotta and Nakamura (2011) who showed that sensible heating at the air–sea interface (despite hampering storm development by damping individual storms) helps maintain surface baroclinicity, fundamental in the development of transient eddies. However, the contradiction might lie in the different timescales that the two studies implicitly focus on. In fact, the effects of persistent sensible heating at the surface, especially across SST fronts, may become more evident on longer time scales, while on shorter timescales latent heating dominates the generation of isentropic slope linked with higher baroclinicity.

The local effects of sensible heating at the surface on the available potential energy in the storm track region, therefore, are not unequivocal, prompting the need for a more thorough assessment of their role in the evolution of storms and of storm tracks more in general.

1.3 The importance of air–sea interactions to the atmosphere

The interactions between the atmosphere and the oceans undoubtedly have a conspicuous influence on the evolution of the atmospheric circulation on a wide range of spatial and temporal scales.

The coupled atmosphere–ocean variability is a fundamental driver and component of large-scale dynamics like the development of monsoonal circulations or the evolution of El Niño-Southern Oscillation. The development of individual tropical and extra-tropical weather systems is also crucially

dependent on the influence exerted by the ocean on the atmospheric circulation and, in the long term, the limited longitudinal extent of storm tracks in the Northern Hemisphere can be taken as the most notable example, as their location coincide with regions of strong SST gradients. Indeed, this is shown to be a major contributing factor to the anchoring of the North Atlantic storm track to the Gulf Stream's trajectory (Nakamura et al., 2008; Brayshaw et al., 2011), together with the particular disposition of orography and land–sea contrast (Brayshaw et al., 2009).

1.3.1 Identifying the oceanic forcing on the atmosphere

The interplay between atmospheric and oceanic dynamics unfolds on a wide range of time and length scales and the mutuality is not always evident, as the ocean forcing on the atmospheric circulation is not straight-forward to disentangle from its intrinsic variability. Indeed, the prime direction of forcing is from the atmosphere to the ocean, as the success of ocean models in reproducing the temporal evolution of SST anomalies when forced with observed surface atmospheric data seems to suggest (Kushnir et al., 2002).

In an early study by Davis (1976), it was found that the only significant connection between SST and sea level pressure, regularly occurring throughout the year, is one where pressure anomalies (atmospheric component) leads in time on the SST anomalies (oceanic component), thus suggesting the existence of an atmospheric forcing on the ocean. Frankignoul and Hasselmann (1977), with the help of a simple stochastic climate model later extended by Deser et al. (2003) to include seasonal variations in the upper-ocean mixed layer, showed that SST variability in the midlatitudes largely ensued from this atmospheric forcing, highlighting the red-noise response spectrum of the low-frequency ocean variability to the high-frequency atmospheric input, which behaves as a white-noise forcing. Wallace et al. (1990) subsequently provided evidence for an oceanic response to atmospheric forcing through wind modulation.

The assessment of the atmospheric response to SST anomalies, on the other hand, has proven to be less straight-forward, one of the reasons being that observed responses change depending on the geographical location of the oceanic forcing, as SST anomalies in the tropics exercise a larger influence on the global atmospheric circulation than those in the midlatitudes (Ferranti et al., 1994).

While results from Wallace et al. (1990) did not exclude the possibility

that the oceans could drive the atmosphere also in the extra-tropics, Deser and Timlin (1997) pointed out that a finer temporal resolution would be required in order to assess the magnitude of such a response, arguing that the atmosphere would respond within a week if it were indeed sensitive to SST anomalies. Despite narrowing down to 2–3 weeks the time window for an oceanic response to atmospheric forcing to occur, their attention did not focus on any specific SST pattern that could be driving atmospheric variability.

In a review of the atmospheric response in General Circulation Models (GCMs) to extra-tropical SST anomalies, Kushnir et al. (2002) identified one of the main difficulties in isolating the atmospheric response to oceanic forcing with the centrality of the role played by transient eddies in shaping the response itself. It was argued that a direct linear response to any forcing would rarely be relevant in the extra-tropics and therefore responses should be sought in potentially subtle changes in the probability distributions of internal modes of variability.

Peng and Robinson (2001), by examining the response of GCMs to extra-tropical SST anomalies, revealed that there exist specific SST patterns that are most effective in perturbing storm tracks and are statistically associated with the dominant modes of atmospheric variability. The primary mode of atmospheric variability in the boreal hemisphere in winter corresponds with a geopotential dipole across the North Atlantic sector, typically referred to as the North Atlantic Oscillation (NAO, Marshall et al., 2001b), and a ridge over the North Pacific. The SST anomalies that are found to be dynamically coupled to these leading modes in the atmosphere through turbulent energy flux anomalies (Marshall et al., 2001a) form a *tripole* in the North Atlantic (Fig. 1.12) and a positive centre in the North Pacific. While the SST tripole configuration is driven by the atmospheric anomalous circulation associated with the NAO in the first place, Czaja and Frankignoul (2002) showed that the SST tripole also acts as an effective forcing on the NAO, which is indicative of the existence of a positive feedback mechanisms between the NAO and the SST tripole pattern.

Peng et al. (2003) further examined the atmospheric response to the SST anomaly tripole in the North Atlantic and identified a symmetric component about the sign of the tripole (a NAO-like dipole with an equivalent barotropic structure over the Atlantic) and an asymmetric component specific to the sign of the tripole (weaker and smaller-scale dipole response over

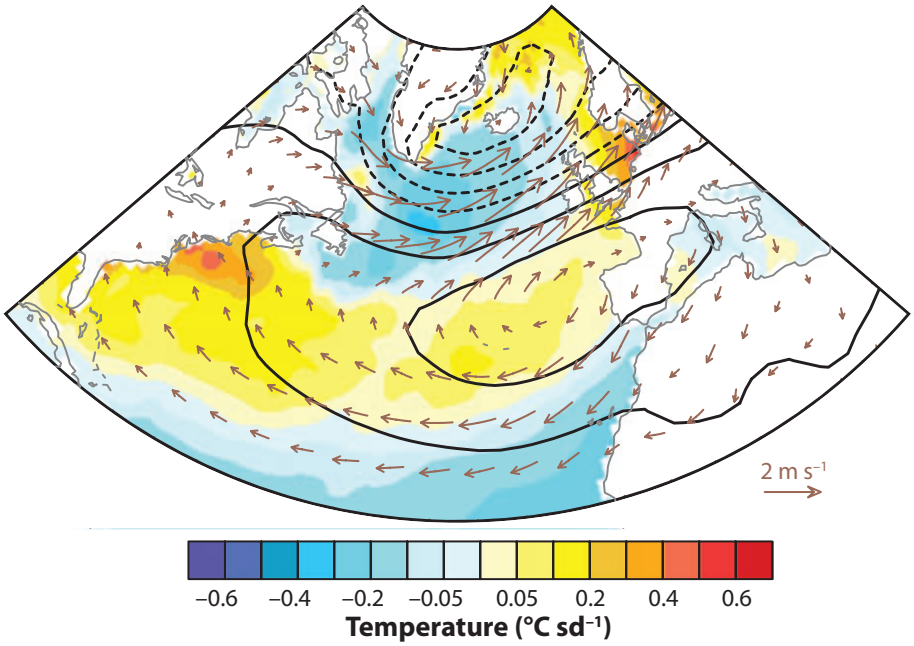

Figure 1.12: Anomaly patterns associated with a +1 standard deviation departure of the NAO Index during winter (December–March) of SST (shading), sea-level pressure (contours) and surface wind (arrows). Figure and caption adapted from Deser et al. (2010).

the eastern Atlantic with a downstream wave train to the positive tripole, in contrast to a stronger and more zonally elongated dipole response across the entire Atlantic to the negative tripole). In their study, extra-tropical SST anomalies were observed to effectively influence the atmosphere by perturbing the storm tracks rather than through direct thermal forcing.

On intraseasonal timescales, Czaja and Frankignoul (1999) showed that significant anomalies of the extra-tropical atmospheric circulation were related to previous SST anomalies in the North Atlantic on seasonal time scales, with the ocean leading on the atmosphere by 3 to 5 months. In a following study, Czaja and Frankignoul (2002) found that extratropical SST anomalies in the North Atlantic influence the NAO more efficiently than tropical SST anomalies, specifically when the SST pattern leads the NAO by up to 6 months. Ciasto and Thompson (2004) detected an anomalous SST pattern preceding the Northern Hemisphere annular mode (NAM, i.e. the dominant pattern of variability in the Northern Hemisphere) by two weeks in winter. However, the magnitude of the anomalies accounted only for a small fraction of the total SST variance and the lack of consistency, at the time, in GCMs response to midlatitude SST anomalies did not allow

for a more robust interpretation of their findings.

The recent increase in resolution of both satellite observations and numerical models had a beneficial effect on our understanding of the role of mid-latitude SSTs in climate variability. Wills et al. (2016) performed further analyses on SST variability in the Gulf Stream extension region to gather evidence of a reciprocal relationship between SST anomalies and the atmospheric circulation on transient time scales. They found two patterns of particular interest, peaking several weeks before (atmospheric forcing) and after (atmospheric response) SST anomalies over the Gulf Stream extension reached a local maximum in time, with the two patterns being linearly independent from each other. In fact, the geopotential pattern associated with the atmospheric response to an oceanic forcing only emerges from regression analyses that include direct information from the SST field. Specifically, the atmospheric response is associated with the perturbation of the free-tropospheric circulation through the advection along the climatological northeastward flow of temperature anomalies generated by the anomalous heating from the ocean over the Gulf Stream extension region. This pattern had not been observed before and Wills et al. (2016) argued that the examination of daily mean data was key to its identification and to any further analyses of extra-tropical air–sea interactions.

1.3.2 The role of horizontal resolution

Held and Phillipps (1993) had initially suggested that resolution had little impact on eddy heat transport, arguing that a self-correcting feedback comes into play as the temperature gradient steepens in response to underestimated heat transport. However, Willison et al. (2013) later assessed the diabatic contribution to storm-track dynamics and cyclogenesis and demonstrated the importance of resolving mesoscale features associated with precipitation and latent heat release. As resolution is increased from 120-km to 20-km grid spacing, it was found that the intensities of individual storms and of storm tracks are strongly sensitive to horizontal resolution due to the enhancement of the positive cyclone-intensification–latent-heat-release feedback associated with increased eddy intensity, although the limited area models (LAMs) used by Willison et al. (2013) do not have a global energy constraint and thus might miss feedbacks rectifying the mean state on which eddies develop. Willison et al. (2013) concluded that the enhanced mesoscale heating that is observed at higher resolutions is broadly captured

by lower resolution but underestimated, as the heat-flux–temperature covariance associated with eddy available potential energy generation is seen to increase by about 60% over the maritime North Atlantic storm track between low and high resolution.

Czaja et al. (2019), in a recent review on the oceanic forcing of the atmospheric circulation in high-resolution models of the atmosphere, highlighted how the correct representation of mesoscale dynamics ($\approx$ 10–100km) leads to improved estimates of the atmospheric response to extra-tropical SST anomalies.

The effective resolution of a numerical model can be defined as the smallest scale that is effectively reproduced by the model. Klaver et al. (2020) recently demonstrated that the effective resolution of atmospheric GCMs corresponds to 3–5 times the underlying grid resolution. It follows that climate models where the grid spacing is larger than 25km are barely able resolve the large scale end of the mesoscale energy spectrum ($\approx$ 100km), as shown in Fig. 1.13. Given the considerable growth of computational costs in further increasing the resolution, attention has shifted towards the study of models with a limited area extent where very high resolutions can be achieved and boundary conditions are provided by lower resolution global driving models.

While increasing the horizontal resolution of the atmospheric component is a primary contributor to the improvement of GCMs, a finer representation of the oceanic component is also beneficial. In fact, oceanic mesoscale eddies are characterised by short length-scales (10–100km) and their correct representation in atmospheric models is crucial in capturing the full response of the atmosphere to ocean forcing (Frenger et al., 2013; Ma et al., 2017; Zhang et al., 2019; Foussard et al., 2019). The largest impact of higher horizontal resolution of the SST field on the overlying atmospheric circulation is seen in coupled climate models. In fact, resolving smaller oceanic eddies in western boundary currents like the Gulf Stream can account for an improved representation of the thermal interaction between the ocean and the atmosphere, granted that the horizontal resolution of the atmospheric counterpart of the model is appropriately matched to that of the ocean (Moreton et al., 2020, 2021).

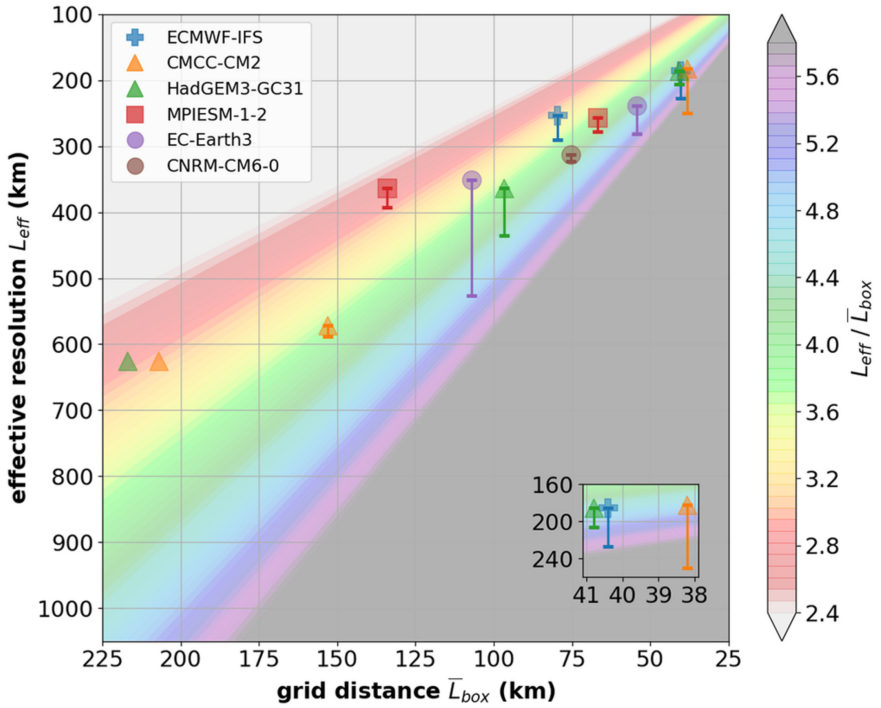

Figure 1.13: Scatter plot of the effective resolution L_{eff} versus the representative grid box distance $\overline{L}_{\text{box}}$ for a number of GMCs. Colour shading depicts the scaling between effective resolution and representative grid box distance (i.e., y/x). Figure and caption adapted from Klaver et al. (2020).

1.3.3 Air–sea interaction in the North Atlantic

Restricting our attention to the North Atlantic region, Minobe et al. (2008) explored the influence of the SST pattern associated with the Gulf Stream on the overlying atmosphere and revealed its deep vertical extent as the SST fronts anchor a narrow band of precipitation, whose associated upward motions reach into the upper troposphere. While Minobe et al. (2008) focussed on the mean state response and provided a climatological perspective, later studies aimed at narrowing down the gap between climate and individual case studies on the effect of SST gradients on the atmospheric circulation.

Vannière et al. (2017a) compared the evolution of a single extra-tropical storm when the SST field is spatially smoothed (which translates to weaker SST gradients) to the same evolution in the case of real SSTs. In this way they evinced a pathway for the SST gradients to affect the atmospheric circulation and proposed a simple model for the boundary layer whereby, as the cold front progresses along the SST front, cold air masses accumulate moisture preferentially on the warm side of the front, thus leading to a stronger differential convection across the SST gradient. The stronger con-

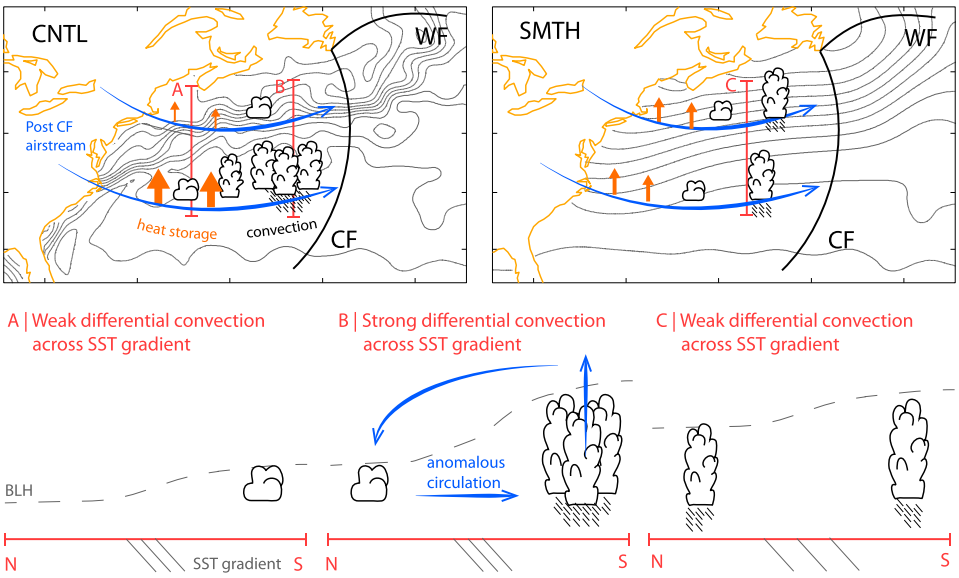

Figure 1.14: (top) Schematic of the cold-sector air–sea interactions in a control run (left, CNTL) with real SSTs and in the case of smoothed SSTs (right, SMTH). Black lines denote the warm front (WF) and cold front (CF). SST contours in grey are shown with interval of 2 K. The blue arrows give the direction of the airflow. The size of orange arrows symbolises the intensity of the surface heat fluxes. (bottom) North–south cross sections in the cold sector of CNTL (labeled A and B) and SMTH (labeled C) as depicted in (top). Figure and caption from Vannière et al. (2017a).

vection over the warm flank of the Gulf Stream then leads to negative pressure anomalies at the surface, which drive the convection cell further across the SST front, while the latent heat release in its wake potentially restores the slope of isentropic surfaces to a more baroclinic structure conducive to further synoptic eddy development (Papritz and Spengler, 2015). The presence of the SST front is crucial, as the differential convection would not be as strong in the case of weaker SST gradients, as illustrated in Fig. 1.14. The model by Vannière et al. (2017a) explains how the SST front anchors a band of precipitation even during a single synoptic event, which eventually results in the mean picture described by Minobe et al. (2008).

Using a similar experimental setup, De Vries et al. (2018) examined a number of storms travelling over the Gulf Stream region in order to identify the typical response of a weather system to the presence of the Gulf Stream strong SST gradient, spatially smoothing the underlying SST fields while keeping large-scale conditions fixed. It was shown that a good representation of SST fields is necessary for a correct modelling of storms, as the sharp SST

gradient in the North Atlantic affects both boundary layer heat fluxes and low-level baroclinicity that allow for the storms to strengthen.

1.3.4 Current challenges in representing air–sea interactions

Despite the improvements over the recent decades of our understanding of air–sea coupling mechanisms on a wide range of time and length scales, current climate models are not yet able to capture the full spectrum of complexity associated with the atmosphere–ocean coupled system. A recent example of our lack of understanding is the so-called signal-to-noise paradox.

The signal-to-noise paradox refers to the inconsistency between the low strength of predictable signals in climate models and the relatively high level of agreement they exhibit with observed variability of the atmospheric circulation (Scaife and Smith, 2018). In simpler terms, climate models are counterintuitively better able to predict observed climate variability than predicting itself (i.e., taking observations as one of the ensemble members and using one of the members as the observation to test the skill against, see Fig. 1.15). Scaife and Smith (2018) showed that this occurs across a wide range of external forcings (e.g., volcanic eruptions, solar variability, ozone depletion) and time scales (from seasonal to multidecadal and multi-century time scales in the North Atlantic).

Scaife and Smith (2018) argue that the apparent paradox might arise from the incorrect representation or underestimation of ocean-atmosphere coupling, eddy feedback mechanisms, remote teleconnections or parametrised processes (e.g., atmospheric convection). In fact, Barsugli and Battisti (1998) showed that the use of prescribed SST variability in atmosphere-only (i.e. uncoupled) models could result in spurious low-frequency air–sea heat fluxes which would constrain the amplitude of atmospheric temperature anomalies on seasonal and longer timescales, while the effect of imposing observed fluxes on ocean models can lead to potentially large errors in low-frequency oceanic temperature variance. Therefore, the signal-to-noise paradox can be interpreted as a symptom of the misrepresentation of the dynamical and thermodynamical interactions between the atmosphere and the ocean. Improving our understanding of the extent of their impact on long-term predictability of the atmospheric flow is object of ongoing research (Smith et al., 2020).

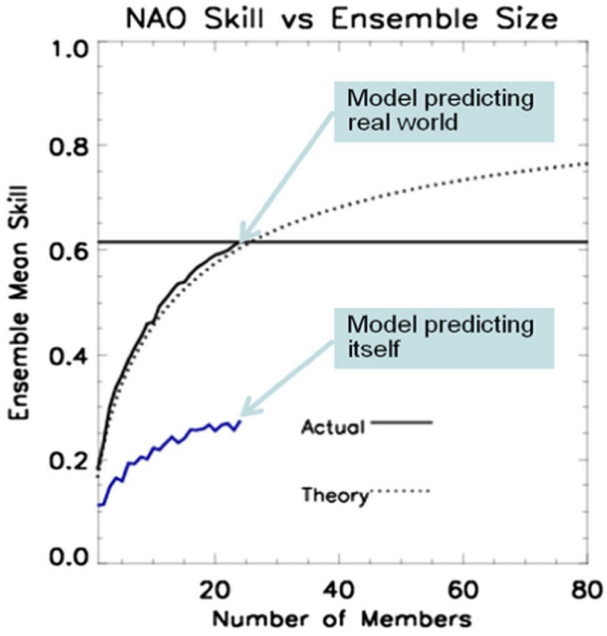

Figure 1.15: Predictability of the North Atlantic Oscillation in the real world (black) is higher than the predictability in the model (blue). The effects of ensemble size on seasonal hindcasts of the winter North Atlantic Oscillation are plotted. The black line shows the average correlation score when different size ensemble averages are correlated with the observed NAO. The blue line shows the same quantity when ensemble means are correlated with a single forecast member. The black dotted line is a theoretical fit to the solid black line. The skill grows with ensemble size due to the suppression of unpredictable noise, but in principle the curves should be the same. In practice the model is better able to predict the real world than itself. Figure and caption from Scaife and Smith (2018).

1.4 Outline of the thesis

Heat fluxes in the atmosphere are essentially sporadic in nature and the influence they exert on weather and climate systems is manifold. Heating can damp the temperature perturbations associated with growing weather systems and therefore locally reduce the potential energy available for conversion to kinetic energy. At the same time, heat fluxes can also effect the relaxation of the atmosphere back to a baroclinic background state, thus driving the restoration of baroclinicity crucial for the development of weather systems in the first place.

Diabatic processes undoubtedly play a major role in the dynamics and thermodynamics of the atmosphere and, in the extra-tropics, are typically linked to generation of available potential energy, thus favouring the de-

velopment of weather systems and, on longer timescales, contributing to the maintenance of midlatitude storm tracks. However, the contribution of local heat exchange in the atmosphere to the evolution of the atmospheric flow on synoptic timescales is not univocal, as diabatic heating is observed to act both as a sink and a source of available potential energy, depending on the timescale at which it unfolds (Chang et al., 2002).

The relative importance of sensible and latent heating in the maintenance of storm tracks, specifically the mean baroclinicity corresponding to the meridional tilt of isentropic surfaces, is still object of current debate. While Hoskins and Valdes (1990) advocate for the self-maintenance of storm tracks through the restoration of baroclinicity by latent heating associated with transient eddies, later research by Hotta and Nakamura (2011) highlights the crucial role played by sensible heating at the surface in relaxing the lower troposphere to the meridional gradient in sea surface temperature, which leads to steeper isentropic surfaces and replenishes the local baroclinicity. On the other hand, Papritz and Spengler (2015) show that latent heating is the dominant process in the restoration of baroclinicity in the free troposphere as it contributes to reinstate the slope of isentropic surfaces previously flattened by transient eddies.

The timescales associated with ocean dynamics are much longer than those associated with synoptic scale variability in the atmosphere, which makes it easier to identify the oceanic response to atmospheric variability but hinders the detection of any atmospheric response to oceanic forcings. In fact, the response of the atmosphere is hidden in potentially subtle changes in the probability distributions of internal modes of atmospheric variability (Kushnir et al., 2002). Nonetheless, the spatial configuration of the ocean's surface temperature field can exert a tangible impact on the evolution of the atmospheric circulation on a wide range of timescales (synoptic to intraseasonal and longer). It has been shown how oceanic features like the Gulf Stream in the North Atlantic or the Kuroshio Stream in the North Pacific affect synoptic development and anchor the location of midlatitude storm tracks (Nakamura et al., 2008; Brayshaw et al., 2011).

The resulting picture suggests that our understanding of the impact of local heat exchange between the atmosphere and the ocean on the evolution of weather systems, despite the outstanding progress over the recent decades, is still incomplete. The misrepresentation of some aspects of air–sea coupling can have repercussions on the reliability of long-term predic-

tions of the Earth's climate and, as the climate adjusts to the global warming associated with increased concentrations of carbon dioxide and other greenhouse gases, this can have a broader societal impact as we design policies to build resilience to climate change.

The thesis is structured in four main chapters each focussed on answering one of the questions outlined below. A summary is then provided in Chapter 6 where we briefly discuss the main conclusions of this thesis and possible directions of future research, while in the following appendices we describe the technical details of the analytical tools that are utilised in the thesis.

Does the local heat exchange in the atmosphere always benefit storms' evolution? The primary aim of this thesis is to shed some light onto the local effects that sensible heating at the surface exerts on the evolution of synoptic dynamics. To that extent, we construct a special framework which accounts for both time and space variability. This hybrid framework is used to quantify the intensity of local heat exchange at the air–sea interface and explore its links to the dynamics of the North Atlantic storm track. Chapter 2 explores the physical meaning of the covariation of surface heat flux with air temperature over the Gulf Stream Extension region. It first provides a brief description of atmospheric energetics that forms the base for the subsequent investigation into the role of surface-heat-flux–temperature covariance in the evolution of extra-tropical weather systems and the associated storm tracks regions. In particular, we highlight the link between bursts of heat-flux–temperature covariance and the depletion of the mean baroclinicity of the spatial domain considered. This is seen to occur primarily within cold sectors of weather systems and it is arguably indicative of the detrimental effect that the synoptic-scale surface–troposphere thermal coupling has upon the evolution of storms over the Gulf Stream, where the higher level of the ocean's surface temperature spatial variability exerts a direct influence on surface heat flux spatial variance. A distinct evolution of covariance is observed over ocean basins with lower surface temperature spatial variability, although preliminary results suggest that the contribution of surface–troposphere thermal coupling is still negative on synoptic timescales.

What are the physical mechanisms that lead to peaks of air–sea heat flux in the atmosphere? In our analysis of the heat-flux–

temperature spatial covariance life cycle, we observe a joint increase of correlation and variances of surface heat flux and lower tropospheric air temperature. We would not expect the correlation to change significantly depending on the amplitude of variances on purely statistical grounds and the observed covariation must be due to the effect of physical processes associated with a stronger thermal coupling between the two levels. This appears to indicate that the correlation between the surface and the lower troposphere can be interpreted as an independent dynamical variable carrying information about the evolution of weather in the midlatitudes. In Chapter 3, we explore in more detail the link between correlation and variances in the build up to peaks of flux–temperature covariance with the aim to identify the driving mechanisms behind the joint increase in correlation and variance. In particular, we present a qualitative model for the atmospheric boundary layer whereby the presence of a deeper mixed layer with an almost adiabatic vertical thermodynamic structure (i.e. vertically aligned isentropic surfaces) leads to a stronger thermal coupling between surface temperatures and the lower troposphere, which eventually results in enhanced relaxation of large scale temperature gradients to the underlying ocean temperature field.

How are these physical mechanisms represented in high-resolution numerical models of the atmosphere? In Chapter 2 we first noticed the non-trivial relationship between heat-flux–temperature correlation and variances and surmised that the spatial variability in SSTs associated with the Gulf Stream front and mesoscale variability in its proximity could explain why spatial variance in surface heat flux leads in time on the spatial variance in temperature. Next, in Chapter 3 we proposed a qualitative model of the role played by air–sea thermal coupling within the atmospheric boundary layer in driving the simultaneous evolution of correlation and variance.

In Chapter 4, we further test the validity of our hypotheses on the driving mechanisms behind the evolution of heat-flux–temperature correlation and variances through numerical simulations of a selection of case studies characterised by intense thermodynamic activity and air–sea heat exchange, which is reflected in the peak values of the corresponding flux–temperature spatial covariance.

The simulations are run using a high resolution, regional configuration of

the Unified Model developed by the UK Met Office and provide a detailed insight into the evolution of surface heat exchange and its effects on the vertical structure of the lower layers of the troposphere, evidencing the validity of the qualitative model for the atmospheric boundary layer that was introduced in the previous chapter.

What is the role of correlation in the life cycle of meridional heat flux peaks? In Chapter 5, we finally extend our analysis of the origin of heat flux peaks to examine the life cycle of local meridional heat transport within the North Atlantic storm track region, which play a decisive role in the life cycle of the storm track itself (Ambaum and Novak, 2014; Novak et al., 2015). In fact, the meridional transport of heat (or dry static energy) is also characterised by bursts of activity that can account for a significant fraction of the climatology. While surface heat fluxes are observed to primarily exert their influence upon the evolution of a system locally through direct damping of temperature variance, the different degree of correlation between meridional wind and air temperature in the lower troposphere is observed to be linked to the large scale structure of the flow and different system growth mechanisms might be expected to contribute to or to derive from changes in correlation.

Chapter 2

The role of heat-flux–temperature covariance in the evolution of weather systems

Apart from supplementary material provided in Section 2.6, the work presented in this chapter is published in Marcheggiani and Ambaum (2020). Any differences (rewording, additional material) are marked individually with footnotes.

Abstract

Local diabatic heating and temperature anomaly fields need to be positively correlated for the diabatic heating to maintain a circulation against dissipation. Here we quantify the thermodynamic contribution of local air–sea heat exchange on the evolution of weather systems using an index of the spatial covariance between heat flux at the air–sea interface and air temperature at 850 hPa upstream of the North Atlantic storm track, corresponding with the Gulf Stream extension region. The index is found to be almost exclusively negative, indicating that the air–sea heat fluxes act locally as a sink on potential energy. It features bursts of high activity alternating with longer periods of lower activity. The characteristics of these high-index bursts are elucidated through composite analysis and the mechanisms are investigated in a phase space spanned by two different index components. It is found that the negative peaks in the index correspond with thermody-

namic activity triggered by the passage of a weather system over a spatially variable sea-surface temperature field; our results indicate that most of this thermodynamically active heat exchange is realised within the cold sector of the weather systems.

2.1 Introduction

In the Northern Hemisphere, storm tracks have a limited longitudinal extent and are located mainly off the eastern coasts of mid-latitude Asia and North America. This is the case from an Eulerian (Blackmon et al., 1977) as well as a Lagrangian (Hoskins and Hodges, 2002) perspective.

Hoskins and Valdes (1990) emphasise the local Eady growth rate, the *baroclinicity*, as the dynamically relevant variable to determine the geographical structure of storm tracks. Ambaum and Novak (2014) point out the relevance of baroclinicity in describing the temporal structure of storm tracks. They define a two-variable model which combines local baroclinicity and meridional eddy heat fluxes in a nonlinear oscillator and subsequently Novak et al. (2015) make use of it to explain regime transitions of the mid-latitude eddy-driven jet stream, which had been previously observed by Franzke et al. (2011). In particular, Novak et al. (2015) found that oscillations in baroclinicity and heat flux lead to variability in eddy anisotropy, which could then be associated with a major change in the dominant type of wave breaking (Hoskins et al., 1983), consequently affecting the jet stream latitudinal position, as is also observed in idealised experiments (Rivière, 2009; Orlanski, 2003).

Meridional heat fluxes can be interpreted as an indicator for the conversion of mean-flow to eddy available potential energy in the Lorenz energy cycle (Lorenz, 1955). Meridional and vertical heat fluxes act as conversion terms across different types of energy reservoirs, whereas surface heat fluxes are associated with generation and dissipation of available potential energy.

Global estimates of these terms have been computed (Peixoto and Oort, 1992) and were used to identify the direction of energy flow within the Lorenz energy cycle. Novak et al. (2017) demonstrate that the dynamical relationship between storm track intensity and available potential energy as measured by baroclinicity can be described by a predator–prey relationship, whereby storm tracks can be thought of as *feeding* on baroclinicity.

The generation of eddy available potential energy in the Lorenz energy

cycle is described analytically by a term which is proportional to the covariance between local heating and temperature (Lorenz, 1955; Peixoto and Oort, 1992; James, 1995). This term has been estimated to be positive globally (Oort, 1964; Oort and Peixóto, 1974; Ulbrich and Speth, 1991; Li et al., 2007; Marques et al., 2009), suggesting that diabatic processes are acting as a source of energy in storm development. However, this picture changes when we focus on the contribution of transient eddies, which correspond to synoptic-scale weather systems, to eddy available potential energy. Ulbrich and Speth (1991) provided a first estimate of the negative contribution of diabatic processes upon transient eddy energy, and more recent studies have further shown that the total diabatic generation of transient eddy potential energy is largely negative across the majority of the Northern Hemisphere's mid-latitudes (Chang et al., 2002), with diabatic heating damping transient eddy evolution, particularly during the winter season (Chang and Zurita-Gotor, 2007).

Diabatic processes at the surface, such as sensible and latent heat fluxes, can amplify horizontal temperature gradients by heating where it is warm and cooling where it is cold, which is linked to the generation of available potential energy. From a global perspective this is achieved by the global differential in radiative heat input. However, the local thermodynamic effects of latent and sensible heat fluxes are much less clear: upward air–sea heat fluxes typically may be expected to coincide with a cooler local atmosphere, suggesting a negative contribution to the local potential energy budget.

The importance played by sea surface temperature (SST) fronts in forcing surface air temperature gradients through differential sensible heating across the SST front has been highlighted in a series of studies (Nakamura et al., 2008; Hotta and Nakamura, 2011). This mechanism, called *oceanic baroclinic adjustment*, was shown to be essential for the maintenance of strong near-surface baroclinicity, which anchors the climatological storm track [1].

Chang et al. (2002), using a dataset composed by Januaries from 1980 to 1993, described the contributions of the different components of diabatic heating to eddy available potential energy and showed that latent and sensible heating can have different effects on the potential energy budget. In

[1] The reader is referred to 1.2.1 for a more detailed discussion on the self-maintenance nature of the North Atlantic storm track.

particular, sensible heat flux was shown to have a strong local effect of relaxing the lower troposphere towards the underlying sea surface (Chang et al., 2002; Swanson and Pierrehumbert, 1997; Hotta and Nakamura, 2011), while latent heating was not necessarily linked to local provision of heat input, because condensation may happen at a different location.

The intensity and sign of surface heat fluxes are typically computed from the near-surface atmospheric conditions; hence, their covariation with higher layers of the atmosphere is non-trivial and it can have an effect on the evolution of weather systems. The aim of this chapter[2] is to identify and describe this local thermodynamic effect of air–sea heat fluxes.

In particular, we examine how synoptic heat fluxes contribute to enhancing or depleting the local synoptic temperature variance in the lower troposphere. This local temperature variance is part of the global available potential energy integral in the standard Lorenz energy cycle. Therefore, we construct a hybrid framework where we can consider the spatial covariance between anomalous heat flux and temperature fields as a measure of the local contribution to diabatic generation or destruction of available potential energy. We focus on the link with synoptic storm evolution by using time anomalies for all atmospheric fields as deviations from a synoptic-timescale mean.

This chapter[3] is structured as follows: Section 2.2 briefly summarises the Lorenz energy cycle and the approach we take in our study. Section 2.3 introduces heat-flux–temperature spatial covariance and examines its main features through the definition of an index. Section 2.4 investigates the driving mechanisms of the index previously introduced. Finally, in the final section results are summarised and discussed.

2.2 Lorenz energy cycle and flux–temperature covariance

Available potential energy can be generated globally through differential heating which amplifies the global meridional temperature gradient and gives the troposphere in the mid-latitudes a baroclinic structure favourable to the growth of extra-tropical weather systems (Peixoto and Oort, 1992). In the Lorenz energy cycle (Lorenz, 1955) the interaction between different

[2] 'study' in published article
[3] 'article' in published article

types of energy reservoirs is represented by conversion terms while surface heat exchange appears in energy generation and dissipation terms. Global estimates of these terms have been computed (Oort, 1964; Oort and Peixóto, 1974; Ulbrich and Speth, 1991; Li et al., 2007; Marques et al., 2009), and they are found to differ not only in time from seasonal to inter-annual scales, but also depending on the type of data variability considered, be it purely temporal, spatial or a combination of these. For example, Oort (1964) found that generation of eddy available potential energy was negative in a spatial domain, whereas in a mixed space–time domain this was found to be positive. Ulbrich and Speth (1991) further decomposed eddy energy into stationary and transient components and estimated their generation to be positive for the stationary and negative for the transient component. Their estimates were based on January and July from 1980 to 1986 and shared the same signs, although with a difference in magnitude.

The generation and dissipation terms have normally been estimated as residuals in the main balance equations, as data for their direct computation typically were not archived. Global estimates normally suggest a positive generation of eddy available potential energy, which would involve heating of warm and cooling of cold air masses. Locally, however, model experiments with simplified climate models, where diabatic heating is determined as a relaxation of the temperature field, show a negative generation of eddy potential energy, with diabatic effects damping eddy available potential energy. This is also supported in studies by Swanson and Pierrehumbert (1997) and Chang et al. (2002), where they highlighted the importance of lower tropospheric thermal adjustment on short timescales to the underlying sea surface.

Given that storm tracks are by definition the main reservoirs of eddy potential energy, this begs the question of whether diabatic effects in storm tracks actually help or hinder their development, as investigated by Hoskins and Valdes (1990) who envisaged that sensible heating of cold air masses actually decreases the energy of weather systems while latent heating helps in their intensification in the warm sectors.

Given that there are different formulations of available potential energy budgets with each giving different interpretations from the same data, we will not favour any particular formulation here. Instead, we take a hybrid approach: we use direct estimates of surface heat fluxes over the upstream sector of the North Atlantic storm track region and use it to estimate

whether it can serve as a source or as a sink of spatial variance in temperature. Available potential energy is a global measure of such temperature variance. By defining a spatial covariance index between air–sea heat fluxes and lower[4] atmospheric temperature we can quantify the extent to which the local heat fluxes help build available potential energy, or deplete it.

In particular, we consider the spatial covariance between time anomalies in instantaneous air–sea heat fluxes F' and air temperature T' at 850 hPa to define an area-specific FT index,

$$\mathrm{FT} = \langle F'^{*} T'^{*} \rangle = \langle (F' - \langle F' \rangle)(T' - \langle T' \rangle) \rangle = \langle F'T' \rangle - \langle F' \rangle \langle T' \rangle, \qquad (2.1)$$

where primes denote time anomalies, angle brackets spatial averages over the area selected and stars' deviations from this spatial average. The reasons behind the choice for the 850 hPa level as reference temperature are presented later in Section 2.3.

In order to concentrate on synoptic-scale variability, time anomalies are defined as deviations from a running mean with a time window of 10 days (Athanasiadis and Ambaum, 2009). By removing a 10-day running mean in the construction of anomalies, we are filtering out lower-frequency variability, such as seasonal variations, which may otherwise dominate the spatial variance, and which describes different physical processes.

Data come from the ECMWF Re-Analysis Interim dataset (ERA-Interim, see Dee et al., 2011), restricting our attention to wintertime only (DJF)[5], 6-hourly data from December 1979 to February 2019, for a total of 40 winters, interpolated onto a spatial grid with a resolution of 1.5° in both latitude and longitude. Instantaneous surface sensible heat fluxes[6] have been utilised as a measure for heat exchange, F, which we define as positive if heat flows upwards from the ocean to the atmosphere.

Repeating our analysis with latent heat fluxes or the sum of latent and sensible heat fluxes did not substantially change the outcomes we report on here, although values depending on heat flux magnitude of course change. The fact that the analysis seems mostly independent of which flux is used, indicates that the space- and time-filtered fluxes have a broadly fixed Bowen

[4] around 850 hPa

[5] A brief look at other seasons is presented in the supplementary, unpublished section at the end of this chapter.

[6] Given that latent heat fluxes are not necessarily associated with local heat exchanges, we chose to consider only sensible heat fluxes in the definition of F.

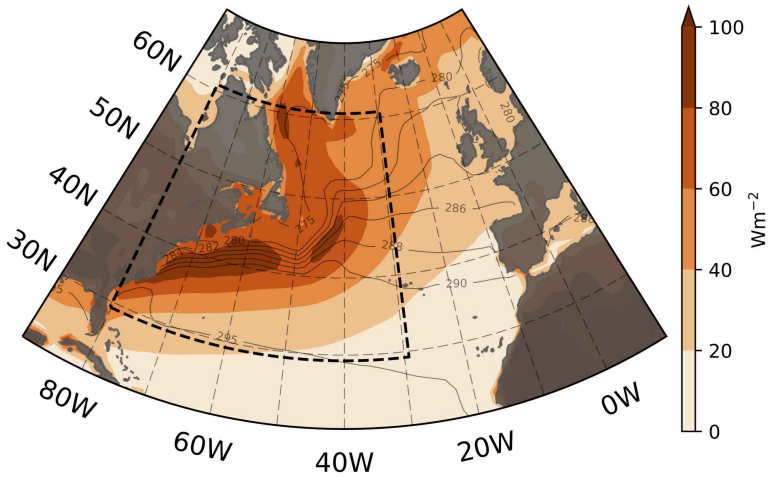

Figure 2.1: Temporal standard deviation of F (shading) and SST winter climatology (contours, every 2 K from 280 K to 290 K, every 5 K otherwise). The area within the dashed box (30–60°N, 30–79.5°W) corresponds to the region of the North Atlantic considered in the next sections for the computation of spatial averages.

ratio[7] on synoptic timescales.

The FT index was calculated over the western North Atlantic, extending from 30°N to 60°N and 30°W to 79.5°W, masking out land grid points in order to concentrate on air–sea interaction only. The domain selected is shown in Fig. 2.1 and coincides with both the upstream region of the storm track and the Gulf Stream extension, where the largest SST variability is observed across different scales (e.g. large-scale meridional gradients and small-scale oceanic eddies). Neither the spatial resolution chosen nor the finest resolution available in ERA-Interim would allow for oceanic eddies to be fully resolved. However, given that the computation of F relies on T at the surface and air temperature is assimilated from observations, their effect on F at the resolved scales would be captured by the reanalysis system and

[7]The relative importance of the sensible and latent components of the total surface heat flux is measured by the Bowen ratio,

$$B = \frac{\text{sensible heat flux}}{\text{latent heat flux}},$$

first introduced by (Bowen, 1926) and used extensively in boundary layer meteorology (Stull, 1988).

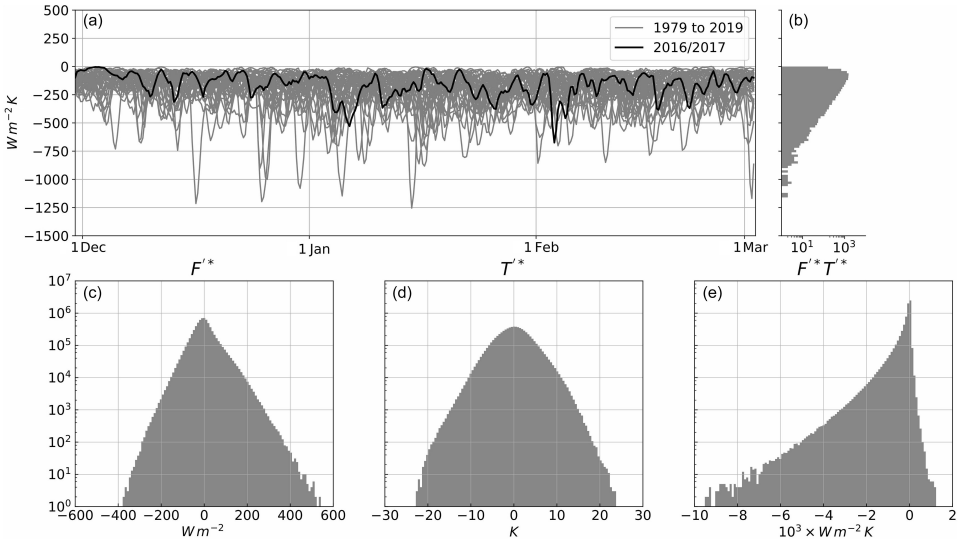

Figure 2.2: (a) Index time series computed over the upstream region of the North Atlantic storm track (30–60°N, 30–79.5°W), spanning the full ERA-Interim time series (grey solid lines), highlighting a sample season (2016–2017 winter, solid black line); (b) empirical distribution of index values (semi-log scale). (c–e) Empirical distribution of instantaneous space–time anomalies in surface heat flux and temperature over the upstream region (semi-log scale).

they would still contribute some residual variance which is included in our analysis.

2.3 Temporal properties of the FT index

Figure 2.2a shows the temporal behaviour of the FT index, Eq. 2.1, as defined for the upstream region of the North Atlantic storm track.

The index is found to be always negative and it features moderately frequent (strongest 5th percentile occurring once every 2–3 weeks) bursts of intense activity peaking at values down to almost -1500 Wm^{-2}K among periods of weaker activity during which the index fluctuates around values closer to zero, although still keeping its negative sign. This is reflected in the empirical distribution of the index values, plotted to the right of the index time series in Fig. 2.2, featuring large skewness and an extended tail towards negative values, as well as a cut-off for positive values.

The empirical distributions for the local values of F'^*, T'^* and $F'^*T'^*$ are shown in Fig. 2.2c, d, and e, respectively. More than 9.5×10^6 data points across both the spatial and time domains were used, which allowed for the

distributions in Fig. 2.2 to be examined without any sort of data filtering. These anomalies correspond to the anomalous fields constructed in order to calculate the index, which is the spatial average of $F'^*T'^*$.

The distribution for heat flux space–time anomalies is distinctively skewed towards positive values, whereas temperature anomalies follow more a Gaussian distribution. This is consistent with the different heat capacities of the atmosphere and the ocean, as the atmosphere is more easily heated by the ocean, while it takes both a longer time and a stronger vertical gradient in temperature for the atmosphere to flux heat into the ocean.

The product of the local heat flux and temperature anomalies, on the other hand, shows an asymmetric distribution markedly skewed towards negative values with a long negative tail, indicating strong local negative correlation between the two variables. There are, however, a substantial number of positive values of the local product. These positive values correspond to heat flowing from an anomalously cold sea-surface to an anomalously warm air mass (and vice versa). The FT index is the spatial average of this signal and it is found to be always negative.

The local product is most often negative given that the air–sea heat fluxes are parameterised in terms of the temperature difference between the sea surface and the lower atmosphere. However, high instability in the lowest layers of the troposphere could cause the local product to become positive, as air temperature at 850 hPa is not directly used in the computation of surface heat fluxes. Furthermore, the transfer coefficient is a non-trivial function of boundary layer properties, not directly linked to the temperature at 850 hPa. It is therefore a non-trivial result that the FT index is observed to be negative at all times.

The sporadic nature of the strong negative index values suggest a link with weather system activity, as observed in Messori and Czaja (2013) and Ambaum and Novak (2014), for example. Evidence for this link is shown in Fig. 2.4[8], where composites on the strongest and weakest FT index values are shown for mean sea level pressure, air temperature at 850 hPa and surface sensible heat flux. Strong FT index values (in the most negative 5th percentile) correspond to patterns associated with a low pressure system, with stronger than usual surface heat flux coinciding with cold air being advected from the American continent. A weak FT index (values in the top 5th percentile) corresponds instead to inhibited storm activity, with weaker

[8]This figure is a rotated version, with larger font, of the figure in published article.

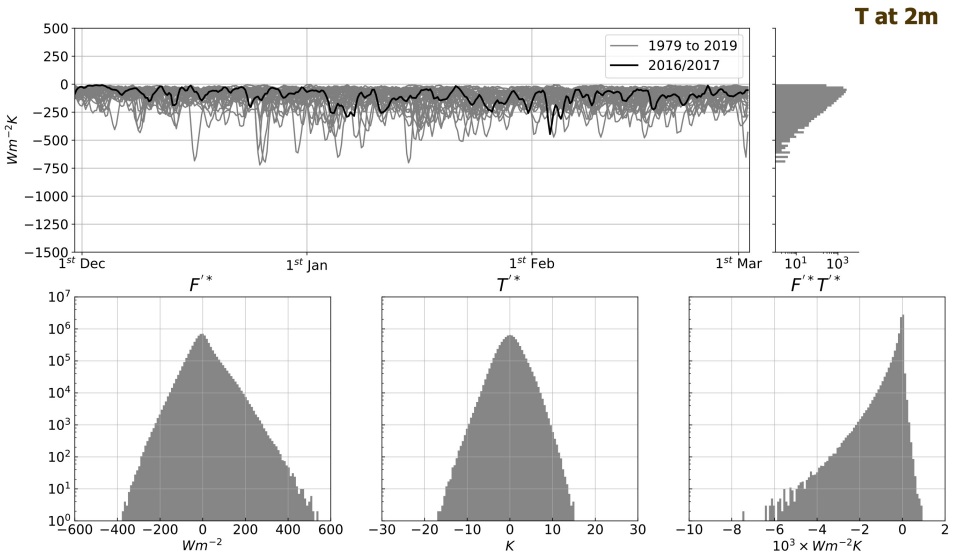

Figure 2.3: Same as in Fig. 2.2 using surface (2-metre height) air temperature for T.

surface heat flux consistent with a pressure pattern which leads to weakened low-level westerlies.

We chose T at 850 hPa as it is not directly involved in the computation of F and, therefore, its covariation with F is non-trivial and entails more information about development of the synoptic systems. Use of surface air temperature (T at 2-metre height) would serve to emphasise the strong interlink between temperature and surface heat fluxes, the computation of which directly involves T at the surface. In fact, covariances appear to be *weaker* when considering T at the surface, as temperature variance is higher at the 850 hPa level and, indeed, the distribution for correlation between F and T at the surface (Fig. 2.3[9]) is slightly shifted towards stronger values, while correlation between F and T at 850 hPa (Fig. 2.2) features a longer tail towards weak values. Composites for 2 m temperature for weak and strong FT indices (defined, as before, using T at 850hPa) are found to be similar to composites for T at 850 hPa (Fig. 2.4b,e) with slightly weaker anomaly values. This is likely caused by contribution from uncorrelated boundary layer dynamics to surface temperature and the suppression of correlated variance by relaxation to the underlying SSTs.

Lagged composites centred on extreme events were also computed for mean sea level pressure, air temperature and precipitation rates, both con-

[9]This figure is not shown in the published article.

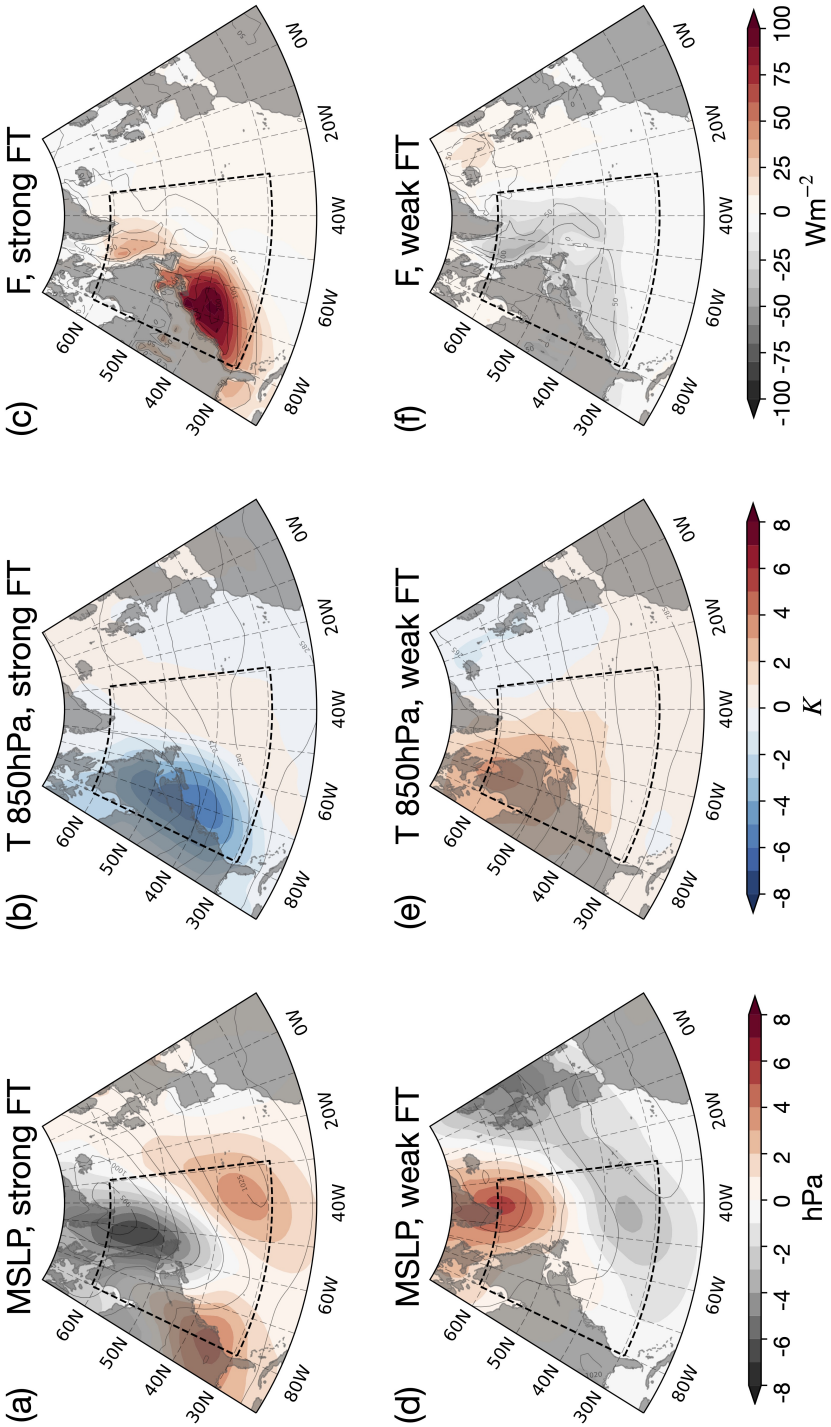

Figure 2.4: Composites of strongest (a–c) and weakest (d–f) FT index values (top and bottom 5th percentiles) for mean sea level pressure (a,d), air temperature at 850 hPa (b,e) and surface sensible heat flux (c,f). Contours and colour shadings represent composites and their difference from winter climatology, respectively; dashed boxes indicate the spatial domain where the FT index is defined.

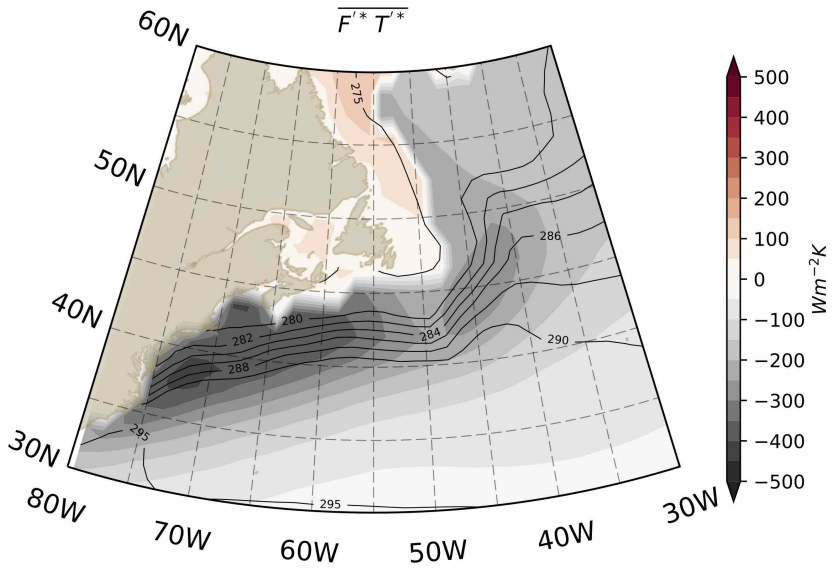

Figure 2.5: Wintertime (DJF, 1979-2019) mean of the product between time–space anomalies in F and T over the spatial domain selected for our study (shading) and wintertime SST climatology (contours, every 2K from 280K to 290K, every 5K otherwise).

vective and large-scale (as available from ERA-Interim; Dee et al., 2011), though this is not shown for the sake of conciseness. Between 4 and 3 d before the peak intensity in the FT index is reached, a low pressure system was observed entering the spatial domain, then intensifying at the FT index peak and finally decaying within synoptic timescales (3–4 d).

The intensification and decay phases observed in the lagged composites partially derive from a gain or loss of signal due to averaging of several different kinds of events, especially at longer lags. However, the decay phase was observed to be relatively rapid compared to the intensification phase, as weather patterns leading to the peak were observed to last longer than those following the peak. This asymmetry between the initial and final stages of the FT index intensification is consistent with the idea that a strong negative FT index indicates a thermodynamic sink on the system.

The time average of $F'^* T'^*$, shown in Fig. 2.5, provides us with a picture of where the spatial covariance between F' and T' is realised within the spatial domain under consideration. This is found to peak along the Gulf Stream, where the largest F time variance is also observed (compare with Fig. 2.1), thus advocating for the importance of SST variability in shaping

the $F' - T'$ spatial covariance.

Note in addition that the FT index is a measure of spatial variability, and concurrent positive or negative anomalies in F and T do not necessarily correspond to stronger or weaker values compared to climatology; rather it would indicate a stronger or weaker intensity compared to both the surrounding area and the previous and following 5 days. We also found weaker negative FT index values to be indicative primarily of diminished storm activity, as Fig. 2.4 shows. Hence, it is reasonable to interpret any positive instances or moderately negative values as indicative of a relatively weak heat exchange, in the quiescent period between storm systems.

2.4 Phase-space properties of the FT index

We expect the FT index to be associated with variations in storm track properties. In order to get a clear picture of these associations we will employ a phase space kernel averaging technique.

The phase space is spanned by two variables. Any quantity can be kernel-averaged at any point in the phase space. We thus obtain a picture of how the quantity will depend on the two variables spanning the phase space.

A particularly interesting quantity to represent in such a phase space is the tendency of the variables that span the phase space. In this way we can construct a flow in the phase space, representing the kernel-averaged tendencies in the data.

The technical details of constructing the phase space averages and tendencies are described in Novak et al. (2017). They constructed a two-dimensional phase space where they were able to identify a predator–prey relationship between meridional heat fluxes and mean baroclinicity respectively, as these were used as coordinates in the phase space. Results may vary somewhat according to the kernel size chosen[10], though in our study the results were observed to be broadly independent of the size of the kernel used for all reasonable size choices (not shown).

We start our analysis by constructing a phase space spanned by the FT index and baroclinicity spatially averaged across our chosen North Atlantic storm track domain. Following Hoskins and Valdes (1990) and Ambaum and Novak (2014), we calculated baroclinicity as the Eady growth

[10]See Fig. A.2 in Appendix A.

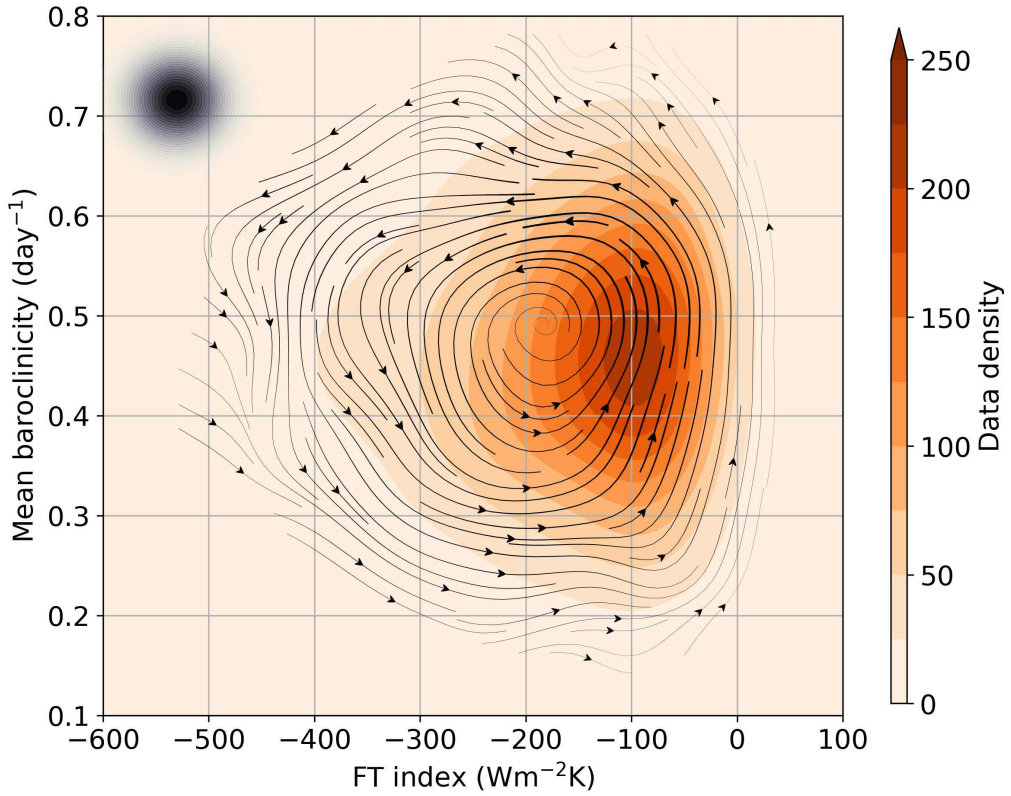

Figure 2.6: Kernel-averaged circulation in the FT index-mean baroclinicity phase space. Streamlines correspond to kernel-averaged rates of change in FT and baroclinicity (line thickness proportional to phase speed, plotted where data density is larger than 10). Colour shading represents kernel-smoothed data density. The size of the averaging Gaussian filter is indicated by the black-shaded dot in the upper-left corner.

rate maximum at 750hPa (Ambaum and Novak, 2014, see Eq. 10), taking a linear approximation for the vertical gradient in zonal wind between the 650hPa and 850hPa levels. The kernel-averaged phase tendencies for the FT index and mean baroclinicity are shown in Fig. 2.6.

We find that the circulation in the FT–baroclinicity phase space lies entirely on the negative side of the FT index axis and it is in the anti-clockwise direction. (The few trajectories crossing into the positive FT index region are due to kernel smoothing.) The phase portrait indicates that mean baroclinicity starts becoming depleted once the FT index has strengthened enough, and it recovers only at lower FT index values, which is consistent with results of composite analysis, whereby baroclinicity was found to decrease during extreme events in the FT index (not shown). The observed baroclinicity depletion could be linked to the growth of baroclinic

waves happening at the same time as the FT index increases; therefore care should be taken in inferring causality. Nonetheless, while air–sea fluxes at low frequencies maintain and anchor the high-baroclinicity regions (Hotta and Nakamura, 2011), our analysis is consistent with the picture that, at higher frequencies locally in time and space, these heat fluxes damp the synoptic-scale temperature variance, as the negative FT index acts as a measure both of eddy amplitude and of how air–sea heat fluxes might erode local temperature gradients (i.e. baroclinicity).

These results do not contradict the findings by Hotta and Nakamura (2011) on the role of sensible heating at the surface in restoring baroclinicity and are actually complementary to them. In fact, the spatial variance of the fluxes also includes contributions from the north-south gradient of SSTs over the oceanic front. This is consistent with the mechanism discussed in Ambaum and Novak (2014) and Novak et al. (2017), who highlight the role that eddies play in temporarily depleting the baroclinicity in a predator–prey-like relationship. This relationship is really an instance of the nonlinear life cycle of mid-latitude eddies, where eddy activity locally depletes the meridional temperature gradient in the atmosphere. (In the older literature this quasi-periodic predator–prey relationship would have been described as an index cycle.) However, this does not contradict the fact that high eddy activity on average must be geographically associated with high baroclinicity, as argued by Hotta and Nakamura (2011) and Ambaum and Novak (2014) and also elucidated in earlier studies by Swanson and Pierrehumbert (1997) and Hoskins and Valdes (1990).

Our analysis suggests that the flux-temperature spatial covariance plays an important role in the budget for mean baroclinicity and, more generally, for available potential energy (Ambaum and Novak, 2014), alluding to the existence of a link between any driving mechanism behind the FT index and storm evolution. In fact, our result shows that the FT index is a good measure of processes that deplete baroclinicity.

The FT index can be decomposed into the product of flux-temperature spatial correlation and spatial standard deviations in flux and temperature,

$$\text{FT index} = \operatorname{cov}(F', T') \equiv \operatorname{corr}(F', T')\, \sigma(F')\, \sigma(T'). \tag{2.2}$$

This suggests we can also use spatial standard deviations in F' and T' as coordinates of the phase space where trajectories traced by the index components would represent its evolution across the various components of

the index.

The occurrence of strong index values can be explained by increasing variance in either heat flux or temperature, or anomalously strong correlations between the two variables. Another possibility is of course that a combination of any of these three factors produces strong index events. This question of magnitude-driven or phase-driven index extremes is analogous to that presented in Messori and Czaja (2013) for meridional heat transport and our phase space analysis provides a novel viewpoint of the phenomenon.

Figure 2.7a shows the result from kernel averaging in a phase space spanned by the variances in heat flux and air temperature. Here streamlines indicate the phase space mean trajectories and their thickness is proportional to the phase speed, while the shading represents the typical value of the FT index at each point in the phase space as a result of kernel averaging.

Regions in the phase space where data are scarce (less than 10 and 1 data points respectively for streamlines and FT index value) are hidden, as kernel averages there are not representative of the local value of the variable.

The trajectories traced by the FT index components are found, on average, to be oscillating between low and high values of the index, which is consistent with the behaviour observed in the time series and shows that stronger index values are associated with larger variances in F' and T'. The trajectories are also observed to be oscillating between weak and strong F'-T' spatial correlation, as shown by spatial correlation phase tendencies illustrated in Fig. 2.7b.

Taking a closer look at the relationship between spatial correlation and standard deviations in F' and T', these appear to be growing concurrently. This can be deduced by inspecting Fig. 2.7b, as spatial correlation is observed to increase together with the product of spatial standard deviations in F' and T', which is represented by grey contours.

In Fig. 2.8, spatial correlation is plotted against the product of standard deviations in F' and T' using values from Fig. 2.7b (dark-grey dots) and then compared with raw data (light-grey dots) in order to exclude it being an artefact of kernel averaging. Spatial correlation and variances are found to be in an almost log-linear relationship, with both phase space data and raw data indicating an increase in correlation strongly linked to an increase in variances.

These results suggest that the observed bursts in flux-temperature spa-

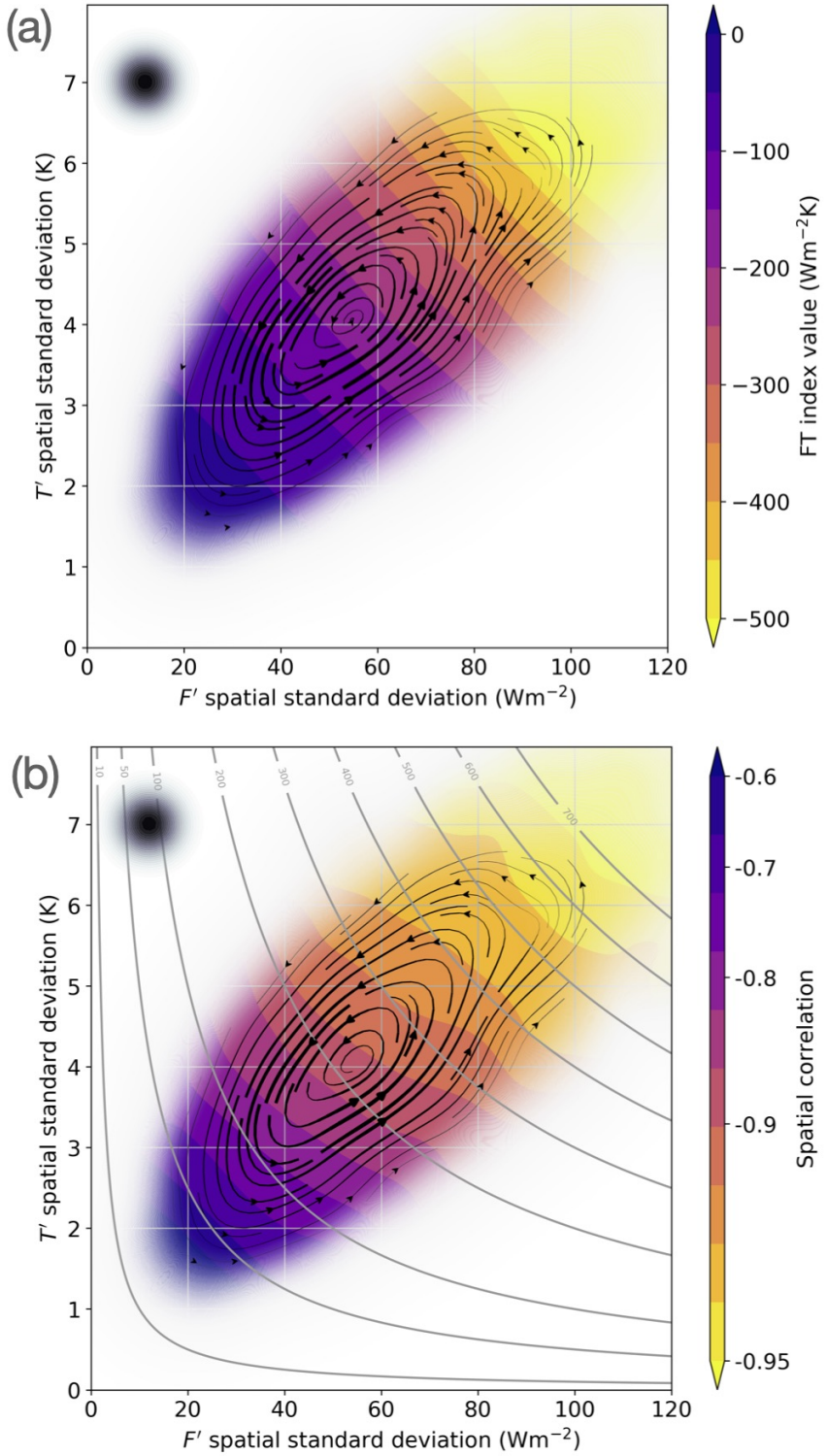

Figure 2.7: Kernel-averaged circulation in the F'-T' spatial standard deviations' phase space. Streamlines correspond with kernel-averaged trajectories traced by the product of spatial standard deviations (line thickness proportional to phase speed, plotted where data density is larger than 10). Shading represents values of the FT index value (panel a) and FT spatial correlation (panel b). Grey contours in panel (b), drawn at 10 $\mathrm{Wm^{-2}K}$, 50 $\mathrm{Wm^{-2}K}$, 100 $\mathrm{Wm^{-2}K}$ and then every 100 $\mathrm{Wm^{-2}K}$, indicate the product of spatial standard deviations. The size of the averaging Gaussian filter is indicated by the black-shaded dot in the upper-left corner.

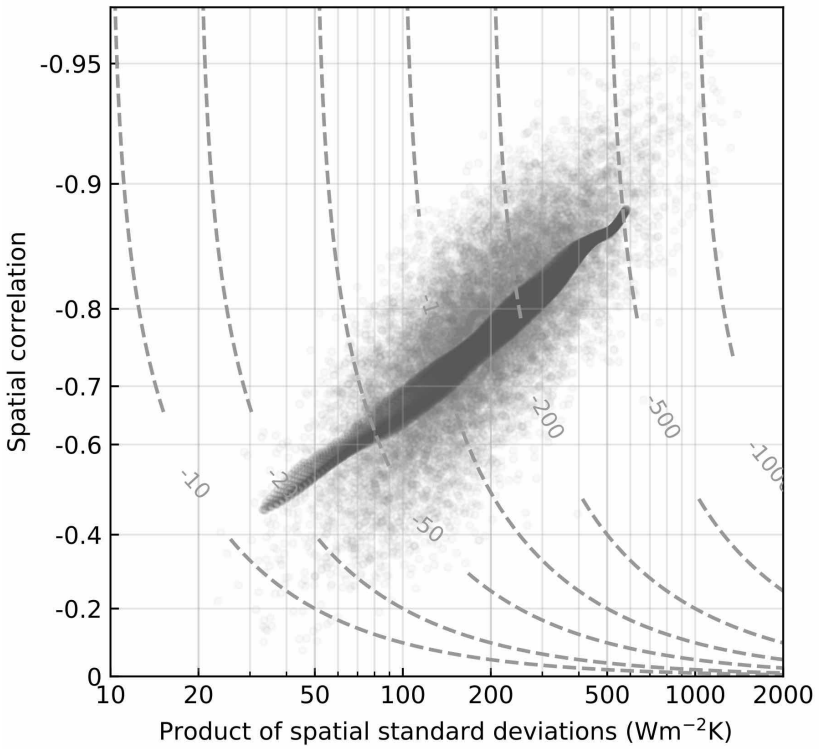

Figure 2.8: Scatter plot of F'-T' spatial correlation against the product of F' and T' standard deviations using kernel-averaged data points from phase portrait (dark shading) and raw data (grey dots); grey contours (Wm^{-2}K) indicate FT index value.

tial covariance are neither exclusively phase-driven nor exclusively magnitude-driven. Both high flux and air temperature spatial variability and correlation are characteristic features of the bursts. We conclude that both strength and correlation in spatial variability are equally fundamental to the build-up of flux–temperature spatial covariance.

It is not clear why the correlation between the two variables increases so markedly with their variability. The simple model of flux being essentially proportional to the temperature at 850 hPa (minus the SST) would not exhibit such a behaviour.

The simultaneous growth of correlation and variance is a non-trivial result, and it suggests further research into assessing whether this is a general feature of the relationship between flux and lower atmospheric temperature or if it is limited to spatial variability dynamics or to the specific timescales considered. This will be treated more in depth in the following chapter but

we can anticipate[11] that the increase in correlation with variance may be a more generic property of the relationship between air–sea flux and lower atmosphere temperature.

The kernel-averaged trajectories in the phase space are organised in concentric ellipses, which suggests that the evolution of the FT index is cyclical in nature. By computing the average phase speed at which the trajectories are traced, it is estimated that it takes between 4 and 6 days for the FT index to go round a full cycle (see Fig. 2.11a for a sample trajectory). This time frame (4-6 days) falls within the range of synoptic timescales, consistent with the idea that the index is closely linked to the evolution of a storm system.

We then notice that the observed circulation spins in an anticlockwise direction. This indicates that the spatial variability in F' leads in time on the spatial variability in T', as can be seen by following any of the trajectories starting from weak index values.

This is somewhat counter-intuitive. A possible explanation is that this effect could be caused by the advection of cold air with a more spatially uniform temperature pattern over the Gulf Stream extension region, which features a much more spatially variable temperature field. SST spatial variability would then trigger heat flux spatial variance and subsequently lead to temperature variance generation. In the case of a weather system, the effect of surface heat fluxes would be that of eroding the spatial temperature variance by damping the cold-sector temperature anomaly, while the warm sector is less affected by this coupling with the surface. Kernel averages for strong and weak spatial standard deviations in F' and T' (not shown) were found to be able to reproduce the same spatial structures that are found by compositing on extreme values (Fig. 2.4), which further supports the idea of the cold sector playing a primary role in the evolution of the FT index.

Further evidence of the importance of the cold sector is gathered by inspecting phase tendencies of F and T.

Figure 2.9 shows phase tendencies for spatial-mean heat flux F and air temperature T. We find that the growing phase of the FT index coincides with a decrease in mean T and a concomitant increase in mean F. A decay phase then follows, characterised by the opposite trends.

Heat flux anomalies range from -20 Wm^{-2} in the decay phase up to

[11]'This would go beyond the scope of the present paper, but preliminary analysis indicates that' in published article.

40 Wm^{-2} in the growing phase, while air temperature anomalies stretch between -2 K and 2 K respectively. The standard deviations in time of spatial-mean F and T are 23.3 Wm^{-2} and 2.2 K, respectively, suggesting that these signals do not arise exclusively from random fluctuations and thus providing our results with robustness.

Phase tendencies in Fig. 2.9 may be explained by relating the growing and decaying phases to an increased dominance of the cold sector of weather systems in the former, while the warm sector influences the latter. This would be in agreement with composite analyses for convective precipitation (not shown), which showed a precipitation band coinciding with the cold front as identifiable from the air temperature composite.

Further evidence of the importance of the cold and warm sectors in the evolution of the FT index can be found in a more detailed analysis of the index dynamics in the phase space. A closed trajectory in the phase space is chosen by selecting a line of constant value of the stream function which was computed to draw the streamlines shown in the phase portraits. The selected closed trajectory is illustrated in Fig. 2.10, and a complete revolution takes about 5 days. It crosses regions of high data density so that it corresponds to a large number of unfiltered trajectories (i.e. not kernel-averaged) and thus presents a statistically robust picture.

The evolution in time of the potential temperature vertical profiles along the closed trajectory is portrayed in Fig. 2.11a, which shows the difference between the kernel-average and climatology along the closed trajectory shown in Fig. 2.10. The kernel-averaged mean boundary layer height is also plotted, together with the climatological mean.

The cold and warm phases are characterised by deeper and shallower atmospheric boundary layer, respectively. This is compatible with the idea that the growing phase corresponds to the advection of the cold sector into the spatial domain over a warmer SST, leading to instability and convective heat fluxes. Furthermore, we inspected the time evolution of the anomalous wind direction closer to the surface, at the 950hPa level, as shown in Fig. 2.11b, and we found it to be consistent with cold air advection in the first half of the cycle, with a north-westerly anomaly backing to a south-easterly wind anomaly and warm air advection in the second half of the cycle. The anomalous wind was computed by removing the climatological mean wind, which is broadly westerly as expected along the storm track.

The strongest temperature anomalies are observed in the lower layers

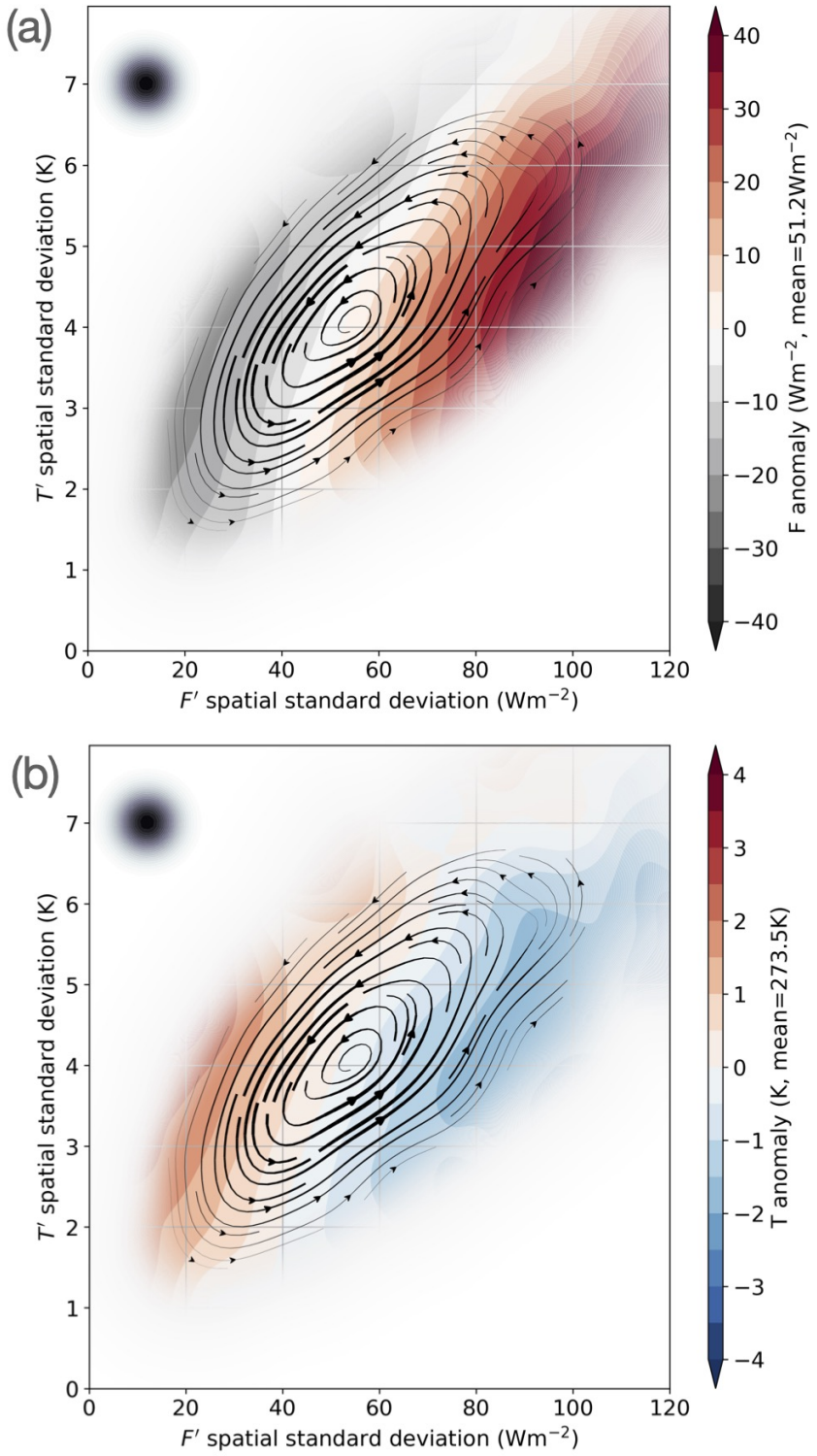

Figure 2.9: Phase tendencies for spatial-mean F (a) and T (b). Shading represents the difference between phase tendency and the mean value of F and T, as reported next to each colour bar. Streamlines as in Fig. 2.7. The size of the averaging Gaussian filter is indicated by the black-shaded dot in the upper-left corner.

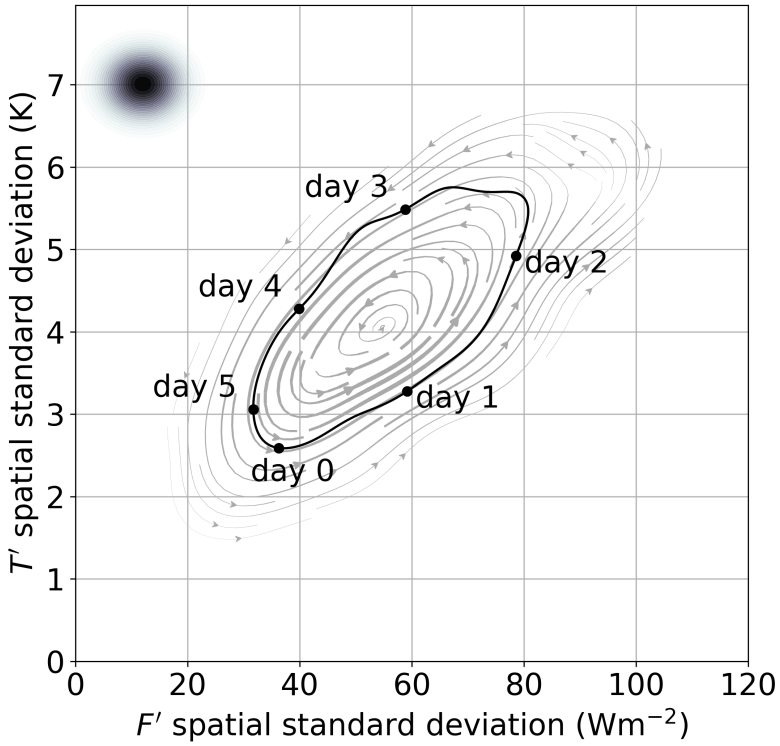

Figure 2.10: Closed trajectory in the phase space of F' and T' spatial standard deviations chosen for the computation of phase tendency evolution. Black dots along trajectory indicate time duration in days of each section. The size of the averaging Gaussian filter is indicated by the black-shaded dot in the upper-left corner.

of the troposphere, which is symptomatic of the close relationship between the FT index and surface heat exchange, as per definition of the index itself. A tilt in the anomalous temperature profile is observed, especially in the cooling phase where the temperature anomalies are largest, as the cold sector moves across the spatial domain. It is not clear whether this tilt can be related to the baroclinic life cycle. Lim and Wallace (1991) also diagnosed a weak forward tilt of temperature at lower levels, as it must be for growing waves (Hoskins and Heckley, 1981), though substantially less than the westward tilt of geopotential. The magnitude of the tilt is hard to compare to our results as the abscissa in Fig. 2.11 maps onto time in a non-trivial way. The stronger tilt or lag of temperature at upper levels that we find is not consistent with observations or expected from theory of idealised life cycles, where in the lower stratosphere at least, the tilt or lag

is expected to reverse, as suggested in Lim and Wallace (1991) and Hoskins and Heckley (1981).

The warm phase coincides with a shallower boundary layer, as warm air is advected over the cold side of the SST front, which results in a more stable atmospheric boundary layer and weaker heat exchange. Indeed, the sea surface does not reach temperatures as low as in the preceding cold sector; hence, it does not interact as strongly as in the cold phase, and this could explain the rapid decay of the heat-flux–temperature spatial covariance.

We find that these results are not sensitive to the choice of the specific closed phase space trajectory (not shown).

The heat exchange within a cold sector arguably plays a primary role in driving the FT index. The phase tendency of the area fraction of the spatial domain occupied by the cold sector, shown in Fig. 2.12, illustrates this further. To estimate the area fraction, we utilise a diagnostic based upon potential vorticity at the 950hPa level as proposed in a study by Vannière et al. (2016), where it is shown that the cold sector is characterised by a negative potential vorticity signature which proved to be effective as a diagnostic through the comparison with more traditional indicators of the cold sector of extra-tropical weather systems.

In the strengthening phase of the FT index life cycle, the extent of the cold sector almost doubles from about 20% to almost 40% of the domain. This suggests that air–sea heat exchange in the cold sector may have significant effects on storm evolution, in particular by driving the depletion of the baroclinicity over the domain, in accordance with Fig. 2.6. This appears to be in contradiction with earlier findings in Vannière et al. (2017b), where it was suggested that baroclinicity is mainly restored in the cold sector[12].

Looking at specific events in the FT index, we find that surface heat flux and SST fields are well correlated, especially over warmer sea surfaces. SSTs over the Gulf Stream extension region are indeed characterised by higher spatial variability than air temperatures due to the presence of both a strong SST front linked to the Gulf Stream and mesoscale oceanic eddies.

Oceanic mesoscale eddies have been shown to play a decisive role in shaping the North Atlantic storm track as they support stronger storm growth rates, making their representation essential for a better description of the storm track (Ma et al., 2017; Zhang et al., 2019). In particular,

[12]The contradiction lies in the different time and space scales involved, as surface heat fluxes in the cold sector act to restore the environmental baroclinicity in the long term, while appearing, locally in space and time, to damp the temperature variance.

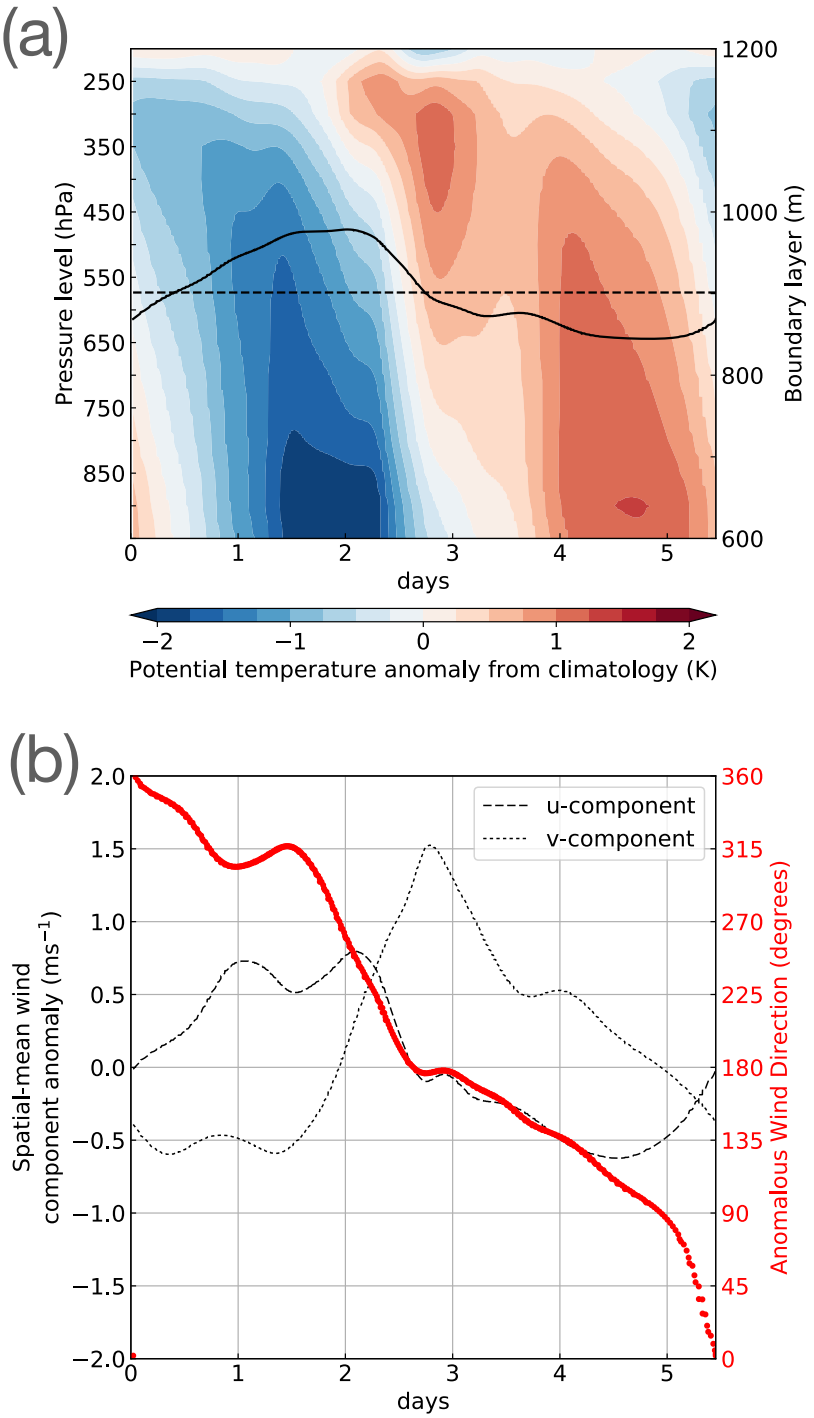

Figure 2.11: Phase tendency analysis along the closed trajectory shown in Fig. 2.10 for (a) area-averaged potential temperature profile (colour shading, difference from winter climatology) and boundary layer height (dashed line, with winter climatological mean indicated by solid line); (b) meridional (dotted), zonal (dashed) anomalous wind components and corresponding anomalous wind direction (red dots) at the 950hPa level. The horizontal coordinate axis indicates the time progression in days along the closed trajectory.

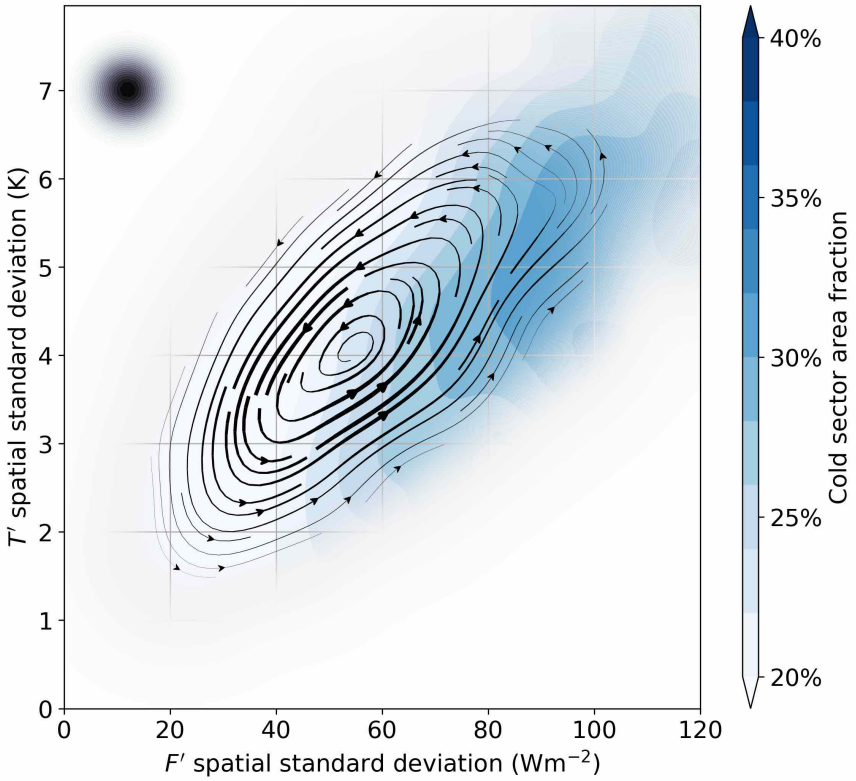

Figure 2.12: As in Fig. 2.9, for the phase tendency of cold-sector area fraction (percentage of spatial domain occupied by cold sector). The size of the averaging Gaussian filter is indicated by the black-shaded dot in the upper-left corner.

Foussard et al. (2019) examined the effect of oceanic eddies on storm tracks through an idealised experiment focused on the mid-latitudes, observing a poleward shift of storm trajectories compared to simulations in which mesoscale eddies are removed, as found by Ma et al. (2017) in more realistic simulations for the North Pacific. Foussard et al. (2019) also noticed a larger sensitivity of the atmosphere to positive than to negative anomalies in SST, as the former correspond to a stronger temperature gradient at the air–sea interface.

Vertical motions associated with along-frontal flow could be expected to play a significant role in driving the FT index[13]. However, our data would suggest that their role is not dominant.

In fact, if the FT index reached its highest point when frontal circulation is strongest we would expect the mean temperature to be around average,

[13]via adiabatic and diabatic modification of air temperature affecting T' at 850 hPa, and consequently the FT index

as a front is associated with both anomalously warm and cold air masses. Instead, we find that the FT index peaks when the area mean temperature is coldest, and when the cold-sector area is largest. Furthermore, we find that temperature variance peaks when the FT index (i.e. FT co-variance) also peaks, which implies that any frontally induced temperature variance does not seem to dominate the signal, as the temperature variance generated by frontal circulations may not co-vary with surface flux variance.

In light of this, we conclude that in the FT index growing phase the trigger for heat flux variability corresponds to the advection of (relatively) uniformly cold[14] air masses over the spatially varying SSTs of the Gulf Stream extension region. The strong vertical contrast in temperatures causes enhanced surface heat fluxes which are then followed by a reaction in the lower atmosphere which experiences a subsequent increase in temperature spatial variability. Despite the SST field changing on much longer timescales, a fixed SST front would therefore still induce heat flux spatial variance on synoptic timescales.

2.5 Summary and conclusion

Lorenz (1955) showed that diabatic generation of available potential energy is proportional to the covariance between heating and air temperature. Globally, the stationary component of this term has been estimated to be positive as the residual of momentum and thermodynamic equations (Oort, 1964; Oort and Peixóto, 1974; Ulbrich and Speth, 1991; Li et al., 2007; Marques et al., 2009), which suggests it acts as a source of energy for weather systems to feed on. A different picture is obtained for the transient component whose sign and magnitude has been observed to vary seasonally, with the strongest negative values occurring in the winter months (Ulbrich and Speth, 1991; Chang et al., 2002; Chang and Zurita-Gotor, 2007). This provides hints that, locally, surface heat fluxes behave overall as a sink of energy in the evolution of weather systems. Using data for surface heat fluxes and air temperatures from ERA-Interim, we find that they are locally negatively correlated in time and space, in particular upstream of the North Atlantic storm track, consistent with more recent literature.

In particular, we investigate the heat-flux–temperature covariance through

[14]and, specifically, continental, as the land-sea contrast between the North American continent and the North Atlantic ocean also contributes to the magnitude of the air–sea thermal interactions

the definition of an index (FT index) that measures the local spatial covariance between sensible heat flux and air temperature at 850 hPa. To that effect, a hybrid approach was taken where anomalies are defined as deviations from a spatial mean relative to a limited spatial domain, in our case, the Gulf Stream extension region.

The FT index is found to be always negative and characterised by bursts of activity coinciding with strong synoptic storm activity within the spatial domain considered. Composite analysis of strong index values suggest that heat-flux–temperature spatial covariance behaves as an energy sink in the evolution of a storm. The peak of the FT index coincides with the onset of the decaying phase of the storm.

Heat-flux–temperature spatial covariance, as measured by the FT index, and local baroclinic growth rate, as identified by baroclinicity, are seen to be interacting in a cyclical evolution. Strong FT index values coincide with baroclinicity depletion, while a weaker FT index allows the baroclinicity to recover. [15]

Spatial correlation and standard deviations in heat fluxes and air temperatures are observed to be equally important in the build-up of strong spatial covariance, with an increase in spatial variability in surface heat fluxes typically preceding an increase for air temperature spatial variability. In fact we find, rather counter-intuitively, that the correlation between flux and temperature increases strongly with their variances.

We show that the intensification phase of the FT index coincides with the passage of a storm's cold sector across the region considered, which is compatible with the flux variance field shown in Fig. 2.1. The advection of cold air masses across the meridional SST gradient and mesoscale oceanic eddies then leads to an increased spatial variability in the surface heat flux field, which leads to the FT index peak values, as heat flux and temperature fields correlate spatially.

Because the FT index is shown to be a good measure of baroclinicity depletion, and peak FT index values are dominated by cold-sector interaction with the spatial SST variance, our results show that the cold-sector air-sea fluxes are a thermodynamic sink on the growth potential of storms[16].

[15]We should point out that surface heat fluxes appear to have a damping effect on the transient component of the available potential energy specific to an individual eddy, while their long term action contributes to the restoration of environmental baroclinicity within the storm track region.

[16]We suggest that cold-sector air-sea thermal interactions exert a damping effect on the individual storm rather than the storm track more in general; the distinct effects

of surface heat fluxes on the baroclinicity can be linked to the different components of baroclinicity, namely an environmental component which is associated with the storm track and a transient, eddy component associated with the individual storm.

2.6 Supplementary material

In this section we present additional material that was not discussed in the paper.

2.6.1 Synoptic scale variability

In the definition of the FT index we compute time anomalies in F and T as departures from a 10-day running mean. In Fig. 2.13 we show an example from January 2019 of the kind of structures that are highlighted by concentrating on synoptic-scale time variability. While the actual heat flux and temperature fields are not visibly correlated in space (compare Fig. 2.13a and c), removing a 10-day running mean (Fig. 2.13b,d) brings to the fore the synoptic-scale components of the atmospheric flow, in particular enhancing the temperature contrast between cold and warm sectors of the extra-tropical weather system centred over Newfoundland (compare

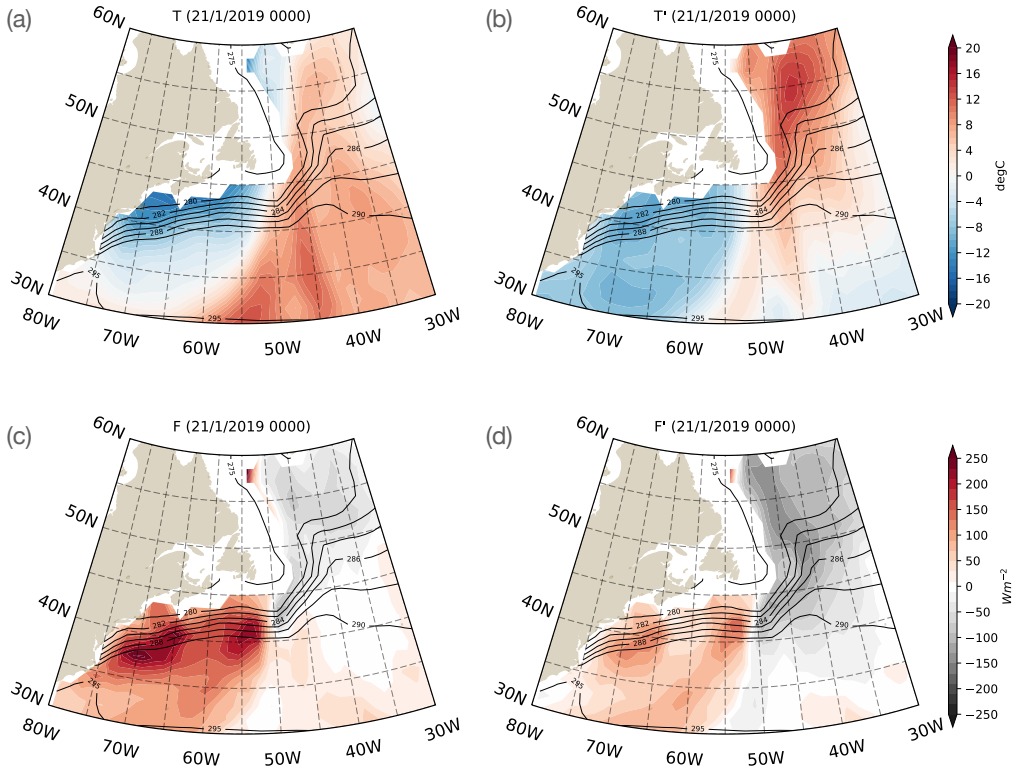

Figure 2.13: Air temperature at 850hPa T (a-b, shading) and surface sensible heat flux F (c-d, shading) on 21st January 2019 at 0000UTC. Panels on the left (b,d) correspond to removing from T and F their 10-day running mean. Contours represent SSTs.

Fig. 2.13a and b). Similarly, the signature of damped surface heat exchange becomes more evident (Fig. 2.13c,d). The resulting spatial covariance between F and T time anomalies is $\approx -400\mathrm{Wm}^{-2}$, which is a relatively strong value (within the strongest 5th percentile in the FT index value distribution).

2.6.2 FT index in other seasons

In the study of the spatial covariance between F and T, we chose to restrict our attention to the winter season given that synoptic activity in the North Atlantic ocean is most intense between November and March. In fact, during other seasons we observe lower heat flux and temperature variances linked to reduced cold air advection over less sharp SST gradients, which lead eventually to a weaker FT index. As an example, we can take the evolution of the FT index between March 2017 and March 2019, shown in Fig. 2.14, where we can see that the index becomes visibly weaker, especially during the summer months when the index activity is at its minimum.

Although the dynamical relationship between variances and correlation in the build up of covariance does not appear to change significantly throughout the year (similar structure of the respective standard deviations' phase portraits), in the summer months, as the oceanic mixed layer in the

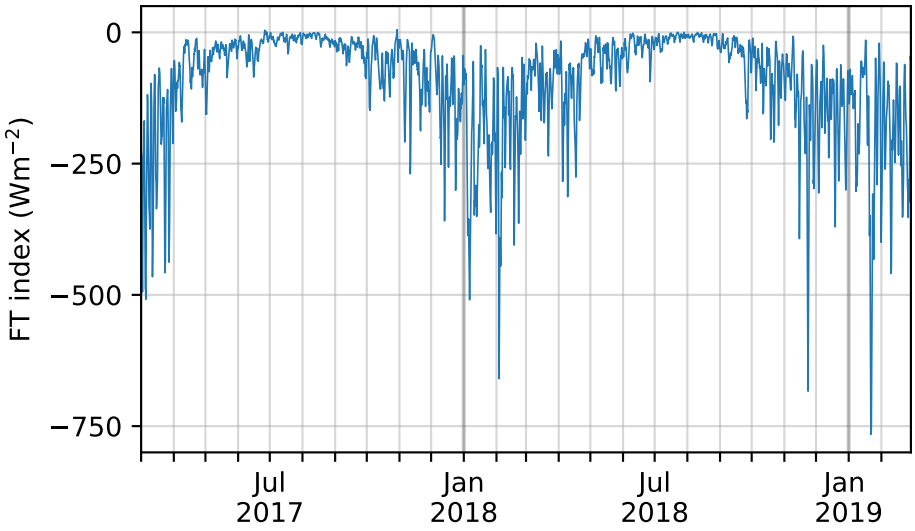

Figure 2.14: Time series of the FT index between 1st March 2017 and 1st March 2019.

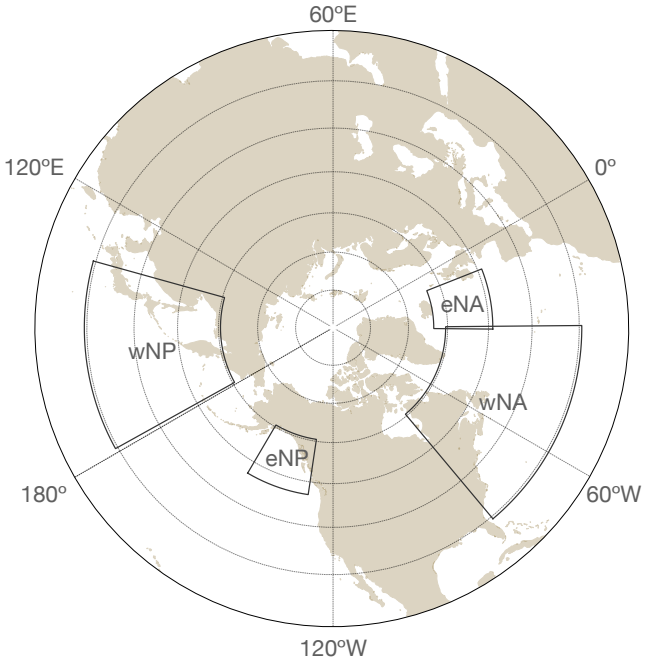

Figure 2.15: Regions of the Northern Hemisphere over which we calculate the spatial variances and covariance between F and T time anomalies. Results from this chapter are based upon the western North Atlantic (wNA) region while in this section we look at the eastern North Atlantic (eNA), western North Pacific (wNP) and eastern North Pacific (eNP) regions.

Gulf Stream region reaches its shallowest point, the atmospheric forcing of the ocean might be expected to become prominent (Frolov et al., 2021) and that could lead to different driving mechanisms for the evolution of FT covariance and its influence on storm evolution. However, this is beyond the scope of this thesis.

2.6.3 FT index in different regions

The spatial covariance between surface heat flux and temperature was shown to capture events of enhanced thermodynamic activity during which, on average, baroclinicity is depleted as surface heat fluxes partly damp the temperature spatial variance associated with an extra-tropical weather system (specifically in its cold sector), which can be taken as a measure of the area-mean baroclinicity in the region.

The current chapter focused on the western sector of the North Atlantic ocean basin, broadly corresponding with the Gulf Stream extension region, although we expect to obtain similar results also when we consider

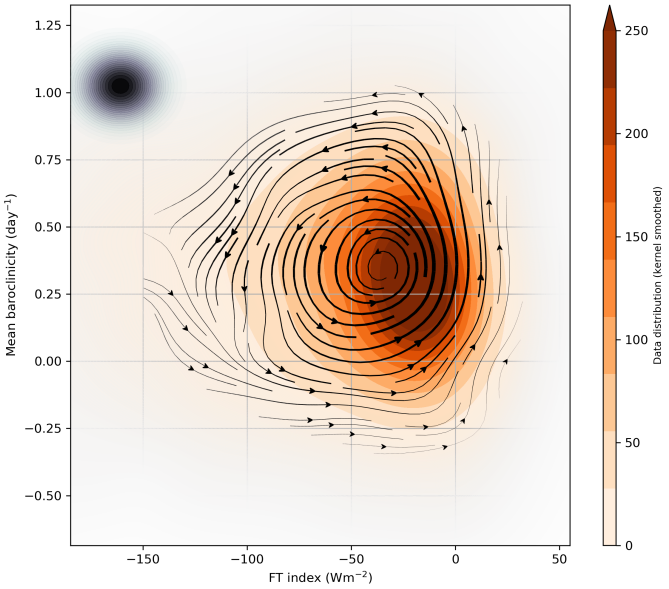

Figure 2.16: As in Fig. 2.6, for the eastern North Atlantic sector. The size of the averaging Gaussian filter is indicated by the black-shaded dot in the upper-left corner.

oceanic regions with similar characteristics and location with respect to the overlying atmospheric circulation (i.e. upstream of a storm track), as indicated in Fig. 2.15. On the other hand, we observe some differences in the characteristics of the temporal evolution of spatial variances over the northeastern sectors of the North Atlantic and Pacific oceans. Specifically, while the relationship between $F' - T'$ covariance and mean baroclinicity remains qualitatively unaltered (as the covariance–baroclinicity phase portrait shown in Fig. 2.16 indicates), we notice that the increase of heat-flux spatial variance follows in time from air temperature variance (Fig. 2.17a) and the signature of the cold sector is stronger in the decaying stage of the covariance life cycle, as the phase portrait for mean anomalous temperature suggests (Fig. 2.17b). We speculate that the lack of western boundary currents propelling large-scale temperature variance (i.e. SST fronts) and enhancing mesoscale variability (i.e. more active eddies compared to other regions) may be expected to result in this opposite circulation in the variances phase space, though further analysis would be needed to demonstrate this hypothesis.

We find a similar duality between regions upstream and downstream

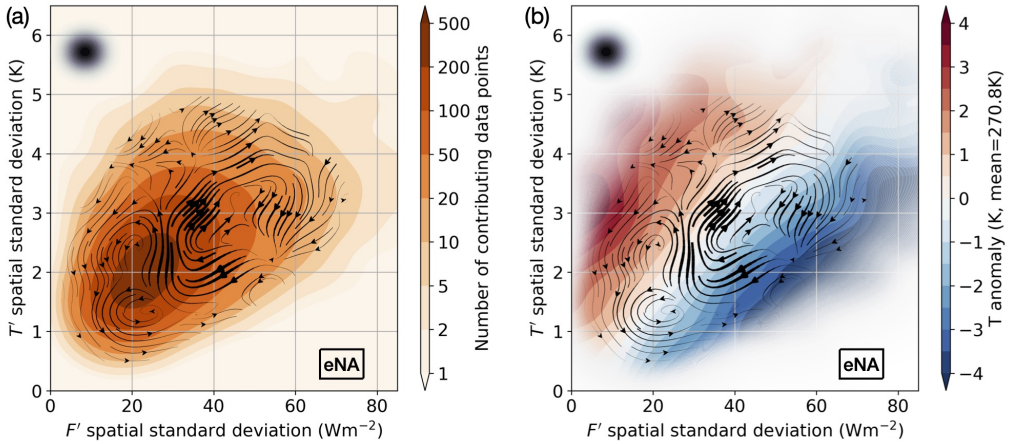

Figure 2.17: Kernel averaged circulation in the $F' - T'$ spatial standard deviations' phase space for the eastern North Atlantic region, with colour shading representing data density (a) and mean air temperature at 850hPa (b). Streamlines and black-shaded dot in the upper-left corner as in Fig. 2.9.

of storm tracks also across the North Pacific ocean. In particular, over the Kuroshio-Oyashio extension region in the western North Pacific (region 'wNP' in Fig. 2.15), the typical evolution of the spatial covariance between surface heat-flux and temperature at 850hPa qualitatively resembles what we observed for the western North Atlantic (compare Fig. 2.9b with Fig. 2.18a), with heat flux variance leading in time on temperature variance as the atmosphere reacts to the SST variability associated with the Kuroshio oceanic current.

The co-evolution of variances in the eastern North Pacific (region 'eNP' in Fig. 2.15) is analogous to that seen in the eastern North Atlantic, as the direction of the circulation in the variances phase space is reversed (temperature variance leading in time on heat flux variance) and the intensification phase is characterised by warm temperature anomalies, as we can see from the phase portrait for mean anomalous temperature shown in Fig. 2.18b.

It must be noticed that the eastern downstream regions we considered have a much more limited spatial extent and the observed dynamics could be circumstantial to local variability. In fact, the signal from these regions might be lost if we consider a larger encompassing spatial domain, as some preliminary analyses seem to suggest (not shown). However, the analogies between the North Atlantic and North Pacific are indicative of the significance of the observed differences.

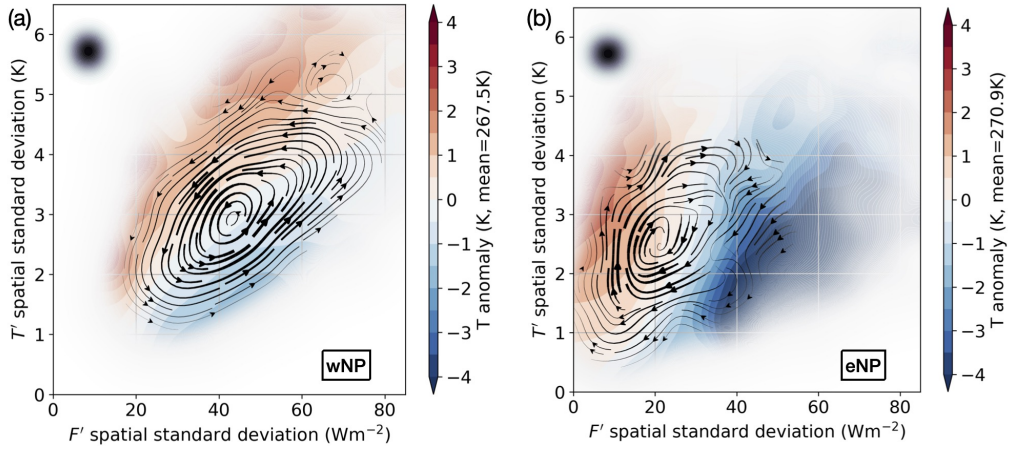

Figure 2.18: As in Fig. 2.9 for the mean temperature in the western (a) and eastern (b) North Pacific region, using time series of variances in the same region (eNA).

Chapter 3

Correlation and variance as independent dynamical variables and their relationship in the North Atlantic

3.1 Introduction

In Chapter 2, the cyclical evolution of spatial covariance between surface heat flux and air temperature in the western North Atlantic was shown to be driven by the advection of cold sectors of extra-tropical weather systems across the spatial domain considered, which is characterised by a high degree of spatial variability in ocean surface temperatures. It was observed that, over the Gulf Stream extension region, increasing spatial variability in surface heat flux leads in time on a similar increase in temperature variability, which eventually culminates in strong spatial covariance between heat flux and temperature.

Furthermore, we explored the evolution of FT spatial covariance through its dissection into the individual components, i.e. correlation and standard deviations and we acknowledged that, on average, higher spatial correlation between surface heat flux and temperature coincide with stronger variances, as both partake equally in the build-up to a peak in covariance.

In statistics, the correlation coefficient between two variables is a measure of their statistical association (not necessarily causal) and is defined as the ratio of their covariance to the product of the standard deviations (Wilks, 2011). Hence, the correlation coefficient (also simply referred to as

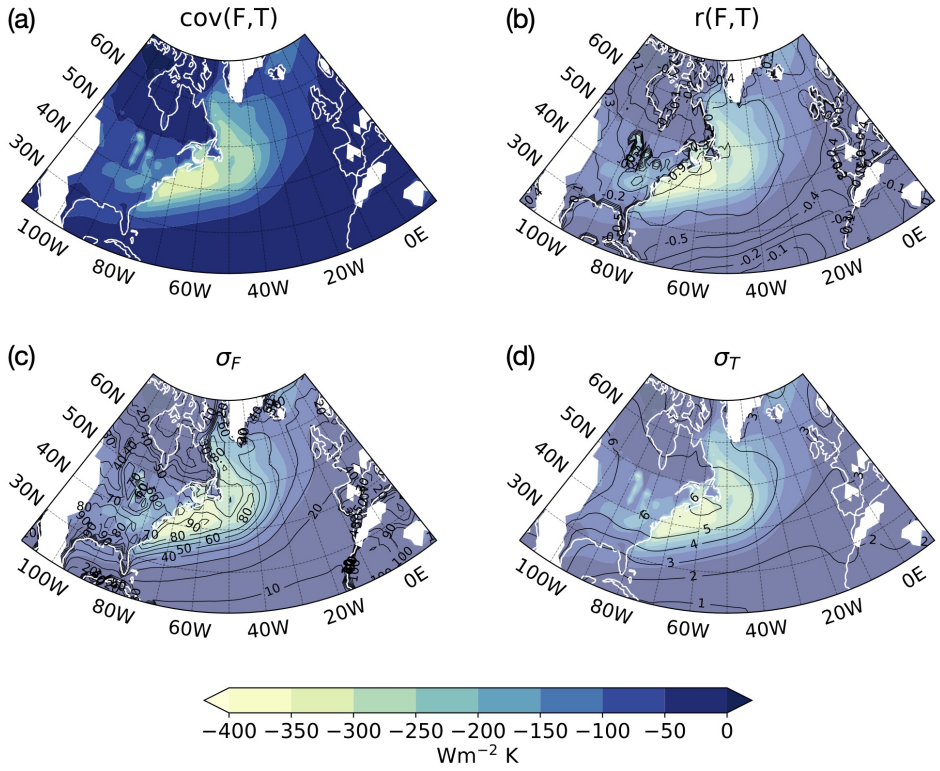

Figure 3.1: Decomposition of FT time covariance into its components. Time covariance (colour shading), correlation and standard deviations of F at the surface and T at 850hPa (black contours) are represented in panels (a-d) respectively. Colour shading in (b-d) is the same as in panel (a) and indicates $F' - T'$ covariance. The area within the light grey contour in panel (a) corresponds with the spatial domain where $F' - T'$ spatial covariance is calculated.

correlation) can be seen as a normalised version of covariance, independent of the size of the variances.

The effects of a change in variance on the correlation coefficient depend, from purely statistical grounds, on the degree of correlation with the other variable associated with the difference in variance. Given two variables x_1 and x_2, if variance in x_1 increases and the additional variance is perfectly correlated with x_2, then the correlation coefficient is unaltered, as covariance and variance increase at the same rate. On the other hand, if the additional variance is uncorrelated (e.g., if we add noise to x_1), the correlation coefficient would be reduced, as the denominator in the covariance–variances ratio increases while covariance does not increase as much as in the case of perfectly correlated extra variance.

As a consequence, we do not expect a larger variance in one or both of the variables considered to correspond, in general, to higher levels of correlation.

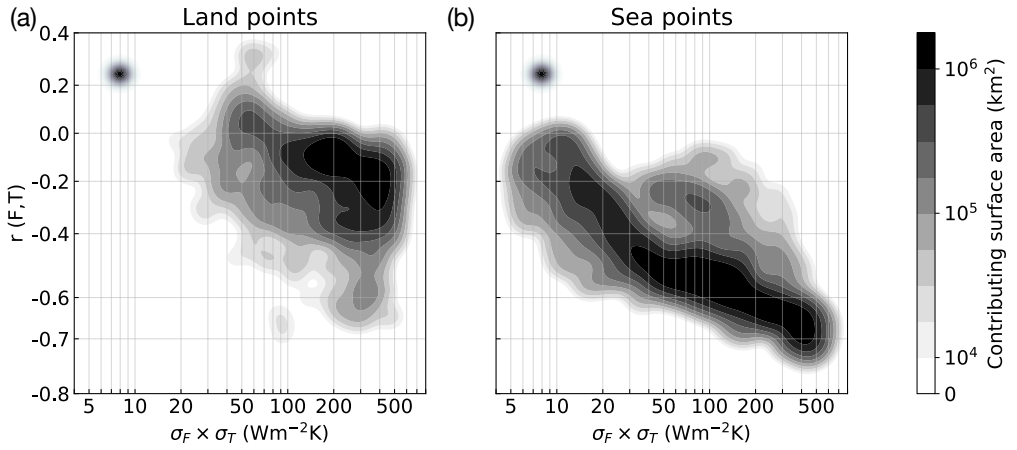

Figure 3.2: Kernel density estimation for the distribution of FT correlation versus the product of σ_V and σ_T over land-covered (a) and sea-covered grid points (b). Shading represents surface area extent contributing to each point. The black-shaded dot in the left side of the plots indicates the size of the Gaussian kernel.

This leads to the conclusion that the behaviour between correlation and variances cannot derive exclusively from trivial statistics. Instead, it stems from the physical characteristics of the system under scrutiny. Thus we postulate that there exist physical processes that can modulate the strength of the statistical coupling when the signal amplitude increases.

In Fig. 2.8 we could clearly discern the link between heat-flux–temperature correlation and variances in the hybrid spatial framework we used in Chapter 2. We can recognise a similar behaviour also from a more canonical time variability perspective, as we can see in Fig. 3.1, where we show the different components of FT time covariance over the North Atlantic sector. At a first visual inspection, the spatial patterns for FT correlation and standard deviations are seen to share a geographical correspondence, with peaks co-located along the North Atlantic storm track, which is associated with the most intense weather activity.

In order to evince the spatial connection between correlation and variances, we can inspect the kernel density estimation of the correlation–variances distribution over a given spatial domain. Figure 3.2 illustrates the results of the kernel density estimation using a Gaussian kernel with a bandwidth of 15% of the standard deviations associated to the distribution of correlation and variances values (the size of the kernel is indicated by the black dot in the top-left corner of each panel of Fig. 3.2). In particular, we estimate the spatial extent represented by each point in Fig. 3.2, that is, the

contribution from each grid point is multiplied by the area over which it extends. Furthermore, we also distinguish between grid points covered by land and by ocean and produce two separate density estimations accordingly.

The joint increase of correlation and variances is evident when we consider oceanic regions, where both reach peak values at the same location, especially along the Gulf Stream. When we look at grid points covered by land, the connection between correlation and variances is substantially weaker than what we observed over sea surfaces and this might hide the link between higher correlation and stronger variances given the limited extent of their range of variability. This points to the idea that the physical mechanisms driving the changes in surface heat-flux–temperature correlation derive primarily from the thermal interaction between the ocean and the lower layers of atmosphere, while land surface processes arguably play a minor role.

In this chapter, we will explore the mechanisms that drive the change in correlation at increasing variance, with a special focus on the role of the atmospheric boundary layer dynamics. This chapter is structured as follows: Section 3.2 introduces statistical models for sensible heat flux and describes their implications; Section 3.3 explores the effects of the different statistical model on the representation of FT spatial covariance (i.e. FT index); Section 3.4 then presents a qualitative model of how boundary layer dynamics drive the joint increase of correlation and variances; finally, Section 3.5 provides a summary of the findings and the deriving conclusions.

3.2 Statistical estimation of surface heat flux

Sensible heat fluxes are dependent on wind speed and surface air temperature compared to the sea surface (Gill, 1982) and their computation in numerical models involves surface variables exclusively (e.g., see IFS documentation, ECMWF, 2010). However, given the turbulent nature of the atmospheric boundary layer, sensible heating can reach deep into the lower layers of the free troposphere, thus having the potential to exert a direct influence on large-scale dynamics such as extra-tropical cyclones. In fact, sensible heat fluxes can have a direct impact on the evolution of weather systems (Hoskins and Valdes, 1990; Swanson and Pierrehumbert, 1997; Chang et al., 2002; Marcheggiani and Ambaum, 2020).

In order to investigate the strength of the thermal coupling between

the surface and higher levels, we construct and examine a simple statistical model for sensible heat flux. To a first approximation, the sign and magnitude of surface sensible heat fluxes depend essentially on the temperature difference between the sea surface and the lower troposphere. We can express this linear dependence mathematically,

$$F = k_1(x, y)\ (T_{sea} - T_{air}), \tag{3.1}$$

where F stands for upward sensible heat flux, k_1 is a heat transfer coefficient ($Wm^{-2}K^{-1}$) that is a function of longitude (x) and latitude (y), T_{sea} is the temperature of the sea surface and T_{air} is the temperature of the air.

Using temperature at 850hPa for T_{air} in Eq. 3.1, the transfer coefficient $k(x, y)$ can be estimated by regressing surface sensible heat flux (Dee et al., 2011, as archived in ERA-Interim) onto the temperature difference at the ocean–atmosphere interface. The estimates of the heat transfer coefficient k_1 in Eq.(3.1) are shown in Figure 3.3a for the North Atlantic region and are based on boreal winter months (DJF, 1979-2019).

The first thing to notice is that k_1 is found to be positive everywhere, which indicates that a larger amount of sensible heat flows from the ocean into the atmosphere when the former is warmer than the latter, while the heat flux weakens or even changes sign when the atmosphere is colder than the underlying ocean waters. This is entirely consistent with the natural flow of heat across a temperature gradient from warm to cold.

Secondly, the values for k_1 are not spatially uniform and vary considerably across the North Atlantic ocean, ranging from $1 - 2\mathrm{Wm}^{-2}\mathrm{K}^{-1}$ over the eastern side of the North Atlantic to $15\mathrm{Wm}^{-2}\mathrm{K}^{-1}$ over the Gulf Stream track. This suggests that heat transfer is most efficient along the SST fronts that are associated with western boundary currents, as thermal contrasts of equal magnitude correspond to a more vigorous exchange of heat over the Gulf Stream compared to the rest of the North Atlantic ocean. The stark land-sea contrast between the North American continent and the western North Atlantic (Brayshaw et al., 2009, which, together with orographic forcing, explains the southwest-northeast tilt in the storm track) may also contribute to shaping the heat transfer coefficient, as surface heat exchanges would be expected to be stronger over the western compared to the eastern sector of the North Atlantic ocean.

We also take note of the striking similarity between the spatial pattern for k_1 and the spatial distribution of cold sector's occurrence, as presented

by Vannière et al. (2017b) in their Figure 11 (here reproduced in Fig. 3.4). This would suggest that the structure of cold sectors of weather systems and the associated dynamics (e.g., enhanced convection, stronger vertical heat fluxes, lower static stability) have a positive effect on the thermal coupling of the surface to the lower troposphere, which allows the surface–troposphere temperature difference to exert a more substantial influence on surface sensible heat fluxes. Consistent with this view is the spatial configuration of sources of spatial covariance between surface heat fluxes and air temperature, as illustrated in Fig. 2.5, which also shares a clear similarity to the spatial pattern for k_1.

In order to quantify the relative importance of the temperature difference in setting sensible heat flux, we need to validate the statistical model of Eq. 3.1 against reanalysis data.

To test the goodness of Eq. 3.1 in predicting surface heat exchange, we evaluate the ratio between the variance of the residuals from predicted surface heat flux F_p and the variance of the actual surface heat flux F as archived in the reanalysis,

$$\frac{\overline{(F - F_p)^2}}{\overline{(F - \overline{F})^2}}, \tag{3.2}$$

where F is the observed surface heat flux, F_p the heat flux as predicted by Eq. 3.1, and the bar indicates a time average.

A goodness-of-fit ratio below unity is indicative of the statistical model's ability in reliably predicting the behaviour of the system, as the deviations of the model's predictions from reality would be smaller than the average variability associated with the system.

The goodness-of-fit of the model described by Eq. 3.1 is shown in Fig. 3.3a in grey contours. The goodness-of-fit is close to unity near the North American continent and can be seen to deteriorate considerably in the eastward direction across the North Atlantic ocean, with values reaching up to 4 to the southeast of the Gulf Stream extension region. This implies that the residuals from Eq. 3.1 can become four times larger than the variance in time. In light of this, we must conclude that the difference in temperature between the sea surface and the 850hPa level alone cannot be regarded as a good predictor for F, despite the strong signal emerging along the Gulf Stream.

We obtain refined estimates for F when we take for predictor of our

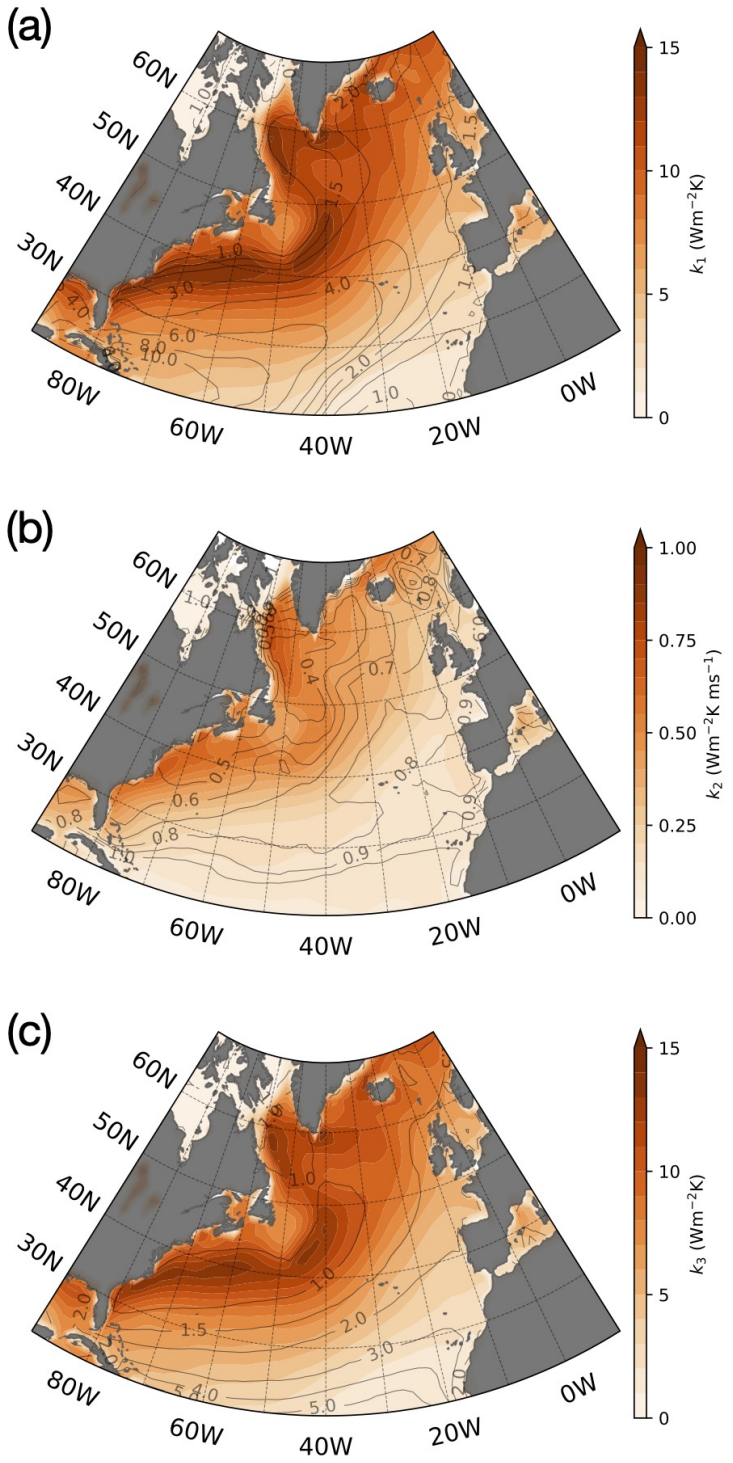

Figure 3.3: Heat transfer coefficients (colour shading) and goodness-of-fit (grey contours, from Eq. 3.2) k_1 (a) from Eq. 3.1 ($Wm^{-2}K^{-1}$), k_2 (b) from Eq. 3.3 ($Wm^{-2}K^{-1}m^{-1}s$) and k_3 (c) from Eq. 3.4.

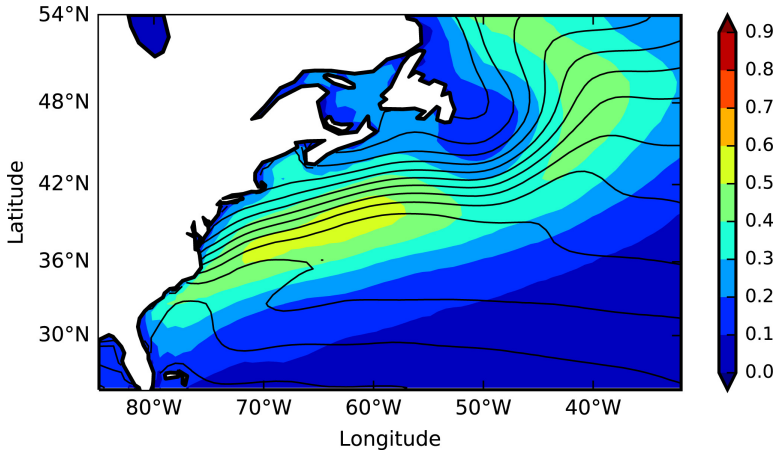

Figure 3.4: Frequency (shading) of detection of the cold sector with the mask combining PV and sensible heat flux (section 2.2 gives a description of the mask) and SST (black contours every 2K). Figure and caption taken from Figure 11 in Vannière et al. (2017b).

statistical model the product of wind speed and air–sea temperature difference,

$$F = k_2(x, y)\ U_{850}\,(T_{sea} - T_{air}). \tag{3.3}$$

Here k_2 is the new heat transfer coefficient with units of $\mathrm{Wm^{-2}K^{-1}m^{-1}s}$, U_{850} is the wind speed at 850hPa and T_{sea}, T_{air} are the same as in Eq. 3.1. Results of the linear regression analysis to estimate k_2 are shown in Figure 3.3b, where grey contours indicate the goodness-of-fit.

The new heat transfer coefficient k_2 resulting from Eq. 3.3 is found to be positive, consistent with the idea that strong winds enhance the exchange of heat through wind stress and turbulent mixing. The goodness-of-fit is visibly improved, with average values below 1. However, in this case we obtain a different spatial pattern for k_2 compared to that found for k_1 from Eq. 3.1. The strongest values are now located off the east coast of the North American continent, which suggests that the advection of cold continental air over warm coastal waters plays a larger influence in setting the transfer coefficient. Furthermore, by including wind speed, the statistical model involves a higher level of complexity which hides the relative importance of the two components of the predictor in setting the surface heat flux response. It should be pointed out that this is not a case of multi-linear regression, as we only use one predictor rather than individual predictors for wind speed and temperature difference.

In formulating a more reliable and simpler statistical model, we can explore the impact that the structure and dynamics of the atmospheric

boundary layer (ABL) has on air temperature co-variability with surface heat exchange.

During daytime, a large fraction of the boundary layer is composed of the mixed layer, which is notably characterised by turbulent mixing leading to temperature vertical profiles following almost adiabatic lapse rates. The boundary layer is strongly affected by solar radiation and it undergoes a diurnal cycle during which its composition changes according to the time of day. At night, in particular, a small fraction at the bottom of the mixed layer is replaced by a nocturnal stable layer of highly stratified air, while above it a residual layer establishes itself, taking up a larger fraction of the boundary layer composition. The residual layer retains the structure of the mixed layer to some degree, as the cooling rate is broadly uniform throughout, which allows for the potential temperature to remain nearly adiabatic. For an exhaustive and thorough description of the life cycle of the atmospheric boundary layer we refer to Stull (1988).

Air from the free troposphere is entrained into the boundary layer and brought adiabatically to the surface through turbulent convection. In light of this, we surmise that the vertical heat exchange between the surface and the lower troposphere is proportional to the difference between the SST and the potential temperature of air θ, which translates into the following statistical model for F,

$$F = k_3(x, y)\ (T_{sea} - \theta_{air}), \tag{3.4}$$

where θ_{air} is taken to be at the 850hPa level. The estimates for the heat transfer coefficient k_3 are shown in Fig. 3.3c together with the corresponding goodness-of-fit ratio. The resulting spatial pattern for k_3 shares an evident similarity with that found for k_1 from Eq. 3.1, with the additional benefit of increased robustness as the goodness-of-fit is considerably improved.

We choose the 850hPa level as it is not directly involved in the parametrisation of sensible heat fluxes at the surface and carries more information about the synoptic circulation (as it was argued in Section 2.3). Furthermore, the thermal coupling of this level to the surface will also depend on the mass of cold air that is advected over the ocean. Iwasaki and Mochizuki (2012) observed that, in the zonal mean, cold air mass streams in the Northern Hemisphere undergo a transition from downward to equatorward in the midlatitudes around 850hPa. In particular, in the exit regions of the major cold airmass pathways (e.g., the North American stream), wave-mean

flow interactions are considered to transfer the angular momentum from the cold airstreams to the upward Eliassen-Palm flux and convert the available potential energy to wave energy (Iwasaki et al., 2014), highlighting the link between the 850hPa level and the amount of extractable energy.

The statistical model in Eq. 3.4 hints at the idea that a large contribution to surface heat exchanges derives from the defining characteristics of the boundary layer, as the turbulent mixing within the mixed layer leads to almost adiabatic vertical temperature profiles which reinforces the thermal coupling between the surface and the lower troposphere. In view of the relative importance of the boundary layer in setting the magnitude of the thermal coupling, we suspect that the dynamics associated with the boundary layer have a key role in the evolution of FT spatial covariance examined in Chapter 2 and, in particular, it can help explain the observed increase in correlation with variances.

3.3 Effects of different statistical models on the FT index

In this section we examine how the FT index changes when we use predictions for F from the different statistical models introduced in Eqs. 3.1,3.3,3.4. In this way, we can ascertain which model leads to a representation of the flux–temperature covariance closest to reality and infer what are the physical mechanisms crucial to the co-evolution of flux–temperature correlation and variances.

We can rewrite Eq. 3.4 in terms of the actual (as opposed to potential) temperature of air at 850hPa,

$$F = k(T_s - T_a) + kT_a(1 - s), \tag{3.5}$$

with $k = k(x, y)$ a spatially-varying heat transfer coefficient (see previous section) and $s = (p_0/p)^{R/c_p} \approx 1.05$ for $p = 850hPa$.

If we substitute the expression for F of Eq. 3.5 into the definition of the FT index (Eq. 2.1) we obtain

$$\langle F'^* T'^* \rangle \approx \langle kT'_s T'_a \rangle - \langle kT'_s \rangle \langle T'_a \rangle + s\langle kT'_a \rangle \langle T'_a \rangle - s\langle kT'^2_a \rangle. \tag{3.6}$$

We point out that terms including temporal anomalies in SST are negligible compared to those containing air temperature variability only (not shown) due to the longer timescale characterising the SST time variance. Therefore, we can further simplify Eq. 3.6 to

$$\langle F'^* T'^* \rangle \approx s\langle kT'_a \rangle \langle T'_a \rangle - s\langle kT'^2_a \rangle, \tag{3.7}$$

which is equivalent to assuming that time anomalies in F are directly proportional to those for T,

$$F' = -skT'_a. \tag{3.8}$$

Equation 3.8 signifies that the heat transfer coefficient k, which is a function of position and encodes the influence of spatial variability in SSTs, is essentially acting as a weight function in the spatial averaging involved in the computation of the spatial covariance. Therefore, the spatial structure that characterises k is key to a good representation of the surface heat exchange based on temperature difference. In fact, if we assume k to be uniform in space and equal to its spatial average $\langle k \rangle$, we would be able to

factorise k on the right-hand-side of Eq. 3.7 and the resulting FT index would represent the covariance of air temperature with itself (i.e. its auto-covariance) and consequently fail to capture the thermal interaction of the lower troposphere with the surface.

This is evident from inspection of Fig. 3.5, where we put into comparison the different FT indices that are obtained using the alternative versions for F, focussing on four recent winter seasons. The time series in blue correspond to the original definition of the FT index, with F coming from archived reanalysis data, while the time series in black derive from the different predictions for F based on Eqs. 3.1, 3.3, 3.4 using the spatially-varying estimates for k. Temperature fields are always taken from reanalysis. We notice immediately that there is no appreciable difference between the time series resulting from Eq. 3.1 and Eq. 3.4, despite the improved goodness-of-fit that comes with the latter. This can be explained in light of the fact that when we compute the variance in F, the contribution from SST synoptic-scale time variability is negligible compared to the time variance associated with air temperature, as we implied in Eq. 3.8. The differences between the two statistical models of Eq. 3.1 and Eq. 3.4 thus reduce to a fixed rescaling factor associated with the computation of the potential temperature at 850hPa, which is filtered out in the computation of the spatial anomalies.

If we focus on the time series resulting from the different statistical models of Eq. 3.3 and Eq. 3.4, we can see that the predictions of Eq. 3.3 (dotted lines in Fig. 3.5) lead to an overall weaker covariance between surface heat flux and temperature compared to that resulting from predictions of Eq. 3.4. The use of Eq. 3.3 is associated with a weaker covariance and, due to the reduction in peak intensities, it conduces to an FT index that is unable to capture the full range of events associated with the thermodynamic activity within the region of interest. Furthermore, the weaker covariance coincides also with a markedly lower correlation between air temperature and the predicted F, as it can be seen from Fig. 3.6a, where we compare the distributions of correlation and standard deviations resulting from the use of Eq. 3.3 to that corresponding to the original FT index. The distribution associated with the use of predictions from Eq. 3.4 is shown in Fig. 3.6b and we notice that correlation values are visibly higher, which is representative of a stronger thermal coupling between the surface and the free troposphere whereby surface heat fluxes are linked more tightly to the thermal structure of the lowest layers of the atmosphere.

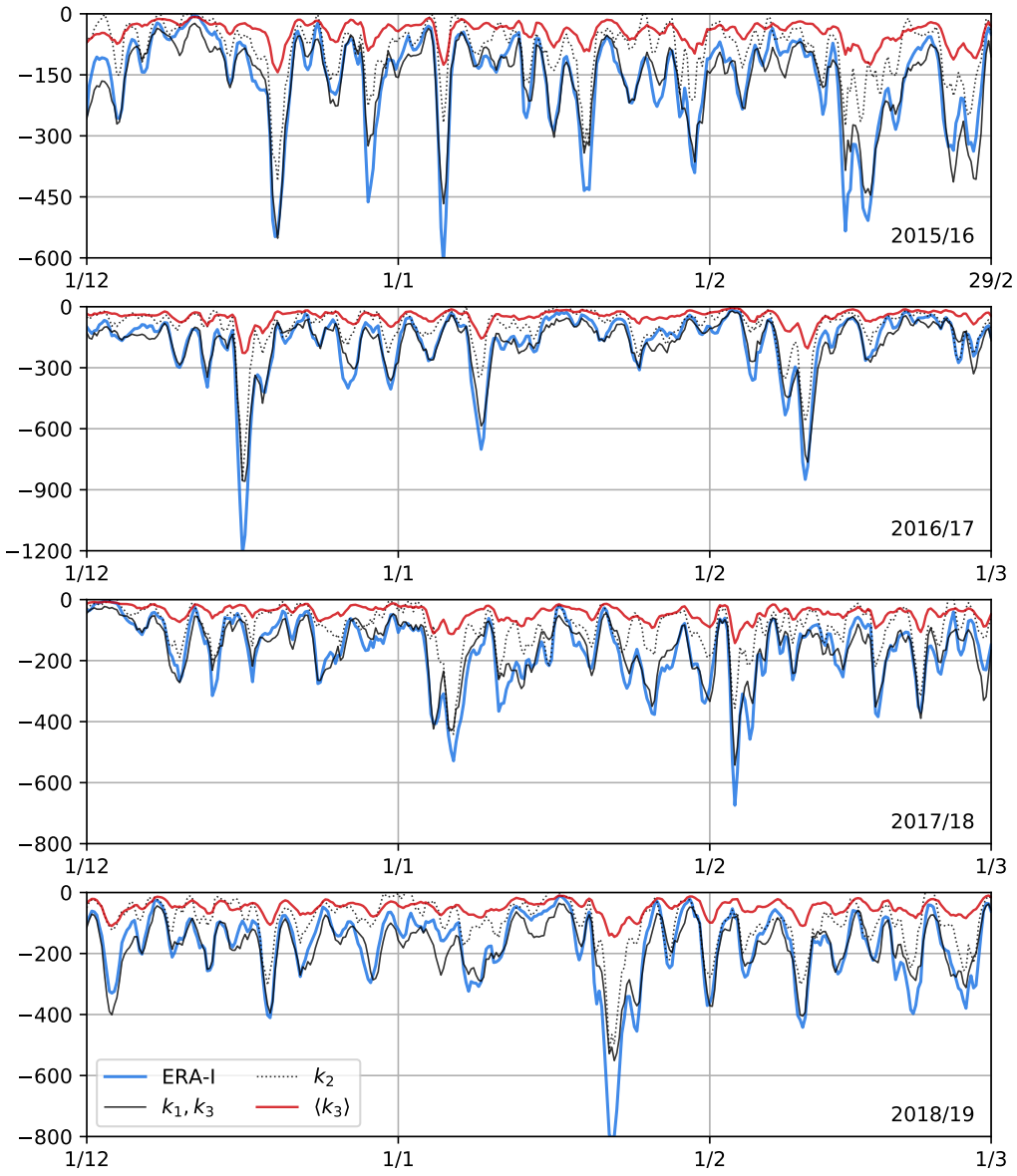

Figure 3.5: Time series of the FT index for the DJF winter, for years 2015–2018, computed as in Eq. 2.1 using different values for F: from reanalysis (ERA-I, blue solid lines); from Eq. 3.1 and Eq. 3.4 (k_1, k_3, black solid lines); from Eq. 3.3 (k_2, black dotted lines); and from 3.4 imposing $k_3 = \langle k_3 \rangle$ ($\langle k_3 \rangle$, red solid lines). Time series using F from Eq. 3.1 and Eq. 3.4 consistently overlap throughout the time period considered and are represented by the same lines (see text for further details).

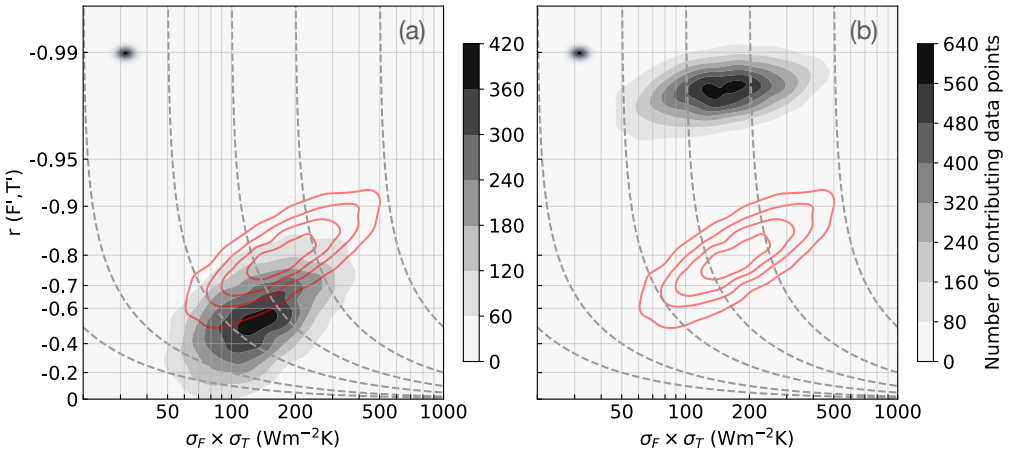

Figure 3.6: Distribution of correlation against the product of standard deviations between T' and F', with F taken from reanalysis (red contours, every 100 points) and from predictions of (a) Eq. 3.3 and (b) Eq. 3.4 (grey shading). Distributions reflect the number of data points contributing to each point in the correlation–standard deviations space, each weighted according to their distance using a Gaussian kernel (black dot in the upper left corner).

Finally, it can be seen that the variability associated with the FT index that results from imposing a uniform heat transfer coefficient (time series in red in Fig. 3.5) has a lower amplitude, despite featuring some level of correlation with the actual FT index. Furthermore, the use of a uniform k does not appear to help reproduce the peaks that characterise the FT index, which we have shown in Chapter 2 to be associated with events of intense thermodynamic activity. This constitutes further evidence of the importance of the thermal interaction of air masses in the cold sectors of weather systems with the underlying sea surface in driving the depletion of temperature variance and the local mean baroclinicity. This is not in contrast with the analysis by Papritz and Spengler (2015), where sensible heating at the surface was shown to be a source of environmental baroclinicity, while we highlight its negative effect on the transient baroclinicity associated with a midlatitude eddy.

3.4 A model for the influence of boundary layer dynamics on FT correlation

Results from the statistical model examined in the previous section (Eq. 3.4) seem to indicate that the thermal coupling between the surface and the lower

troposphere is best captured by the difference between SST and potential temperature in the boundary layer. This thermal coupling was shown in Chapter 2 to be associated with a reduction of temperature variance in the lower troposphere and thus having a damping effect on the mean baroclinicity, especially within the cold sector of weather systems. In addition, we highlighted the link between the strength of the surface–troposphere thermal coupling and the structure of the atmospheric boundary layer, specifically with the thermodynamic profile of the mixed layer which constitutes a large fraction of the entire atmospheric boundary layer.

In this section, we present and describe a qualitative model for the increase of FT correlation based on the influence of the dynamical evolution of the boundary layer on the thermal structure of the lower layers of the troposphere.

Time scales associated with SST variability are much longer than the diurnal cycle, given the larger heat capacity of the ocean in comparison with the atmosphere. Hence, SSTs act as a slowly varying forcing into the bottom of the boundary layer and we expect the depth of the boundary layer to vary relatively slowly in space and time in the absence of SST gradients and significant weather activity, apart from diurnal variations (Stull, 1988).

In fact, most changes in the boundary layer depth are caused by synoptic and mesoscale processes of vertical motion and advection over the sea surface of air masses with a different temperature from that of the ocean's surface. These air masses undergo a modification as their temperature equilibrates with that of the sea surface and, once equilibrium is reached, the resulting boundary layer depth might vary by only 10% over a horizontal distance of 1000 km in the case of a spatially uniform SST (Stull, 1988). However, exceptions to this gentle variation can occur near the borders between two ocean currents of different temperatures, as is the case in the Gulf Stream extension region: in these regions, wind speed changes associated with the SST fronts lead to larger surface wind stress especially over warmer waters (Wai and Stage, 1989), resulting in pronounced deepening of the boundary layer, which is also confirmed by satellite observations (Chelton et al., 2004).

Recent studies have examined in much more detail the difference in the response of the boundary layer to the SST front depending on the orientation of the atmospheric flow with respect to the SST front, i.e. cross-frontal (e.g., Frenger et al., 2013) or along-frontal (e.g., Kilpatrick et al., 2016),

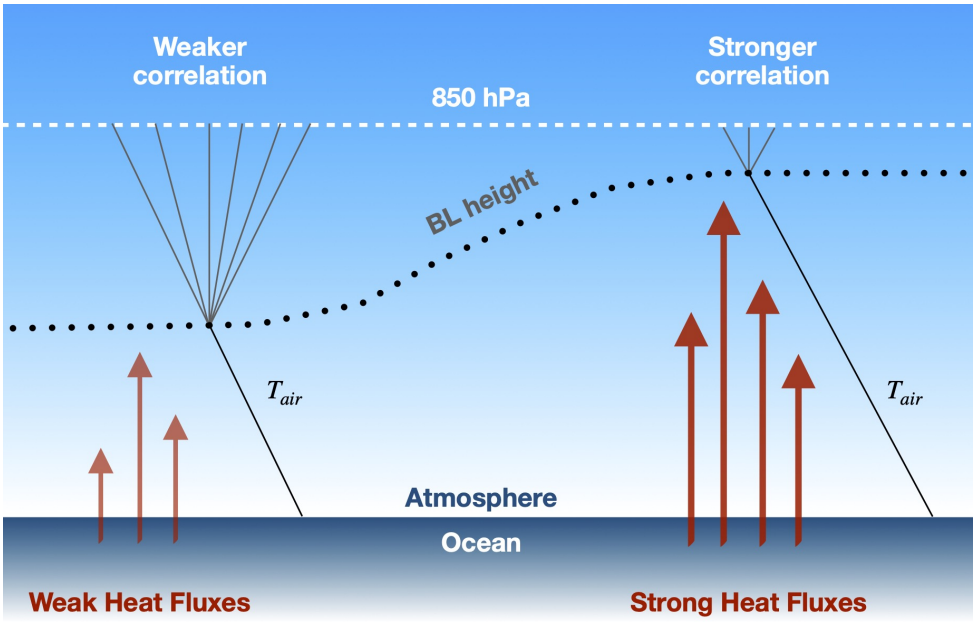

Figure 3.7: Visual scheme of the effect of a different boundary layer (BL) depth on the correlation between surface heat flux and temperature at 850hPa. Horizontal axis not to scale; temperature profiles are traced qualitatively, linearly decreasing with height within the boundary layer. See text for a more detailed explanation.

however, they all seem to suggest that warmer SST anomalies coincide on average with a deeper boundary layer, which is indicative of a stronger thermal coupling between the surface and the free troposphere.

The model we propose for the increase in correlation with variance in the build-up to peaks of heat-flux–temperature spatial covariance is based on the idea that a deeper boundary layer, associated with enhanced sensible heating within the cold sector of a weather systems, strengthens the coupling between the surface and the lower troposphere, thus inducing the observed increase in correlation. Following from this idea, we can distinguish two alternative situations, complementary to each other, for the intensification and decay stages of the FT spatial covariance life cycle.

The phase portrait in Fig. 2.9a indicated that, on average, the increase of surface heat flux variance is associated with intensifying upward heat fluxes. The boundary layer is convectively unstable and turbulent surface heat fluxes are associated with convective eddies. Strong surface heat fluxes are indicative of vigorous eddies, which then lead to a faster deepening of the boundary layer. As the height of the boundary layer reaches higher into the lower layers of the free troposphere, the layer of air between the surface and the 850hPa level get closer to the almost adiabatic temperature

profile associated with the mixed layer. This implies that temperatures at the 850hPa level become more strictly tied to surface temperatures and are less likely to deviate significantly from the adiabatic profile, thus leading to the observed increase in correlation between surface heat flux and air temperature at 850hPa. The left section of the diagram in Fig. 3.7 provides a visual representation of the correlation enhancement stage.

On the other hand, when the spatial variance of surface heat fluxes decreases together with their average intensity, the boundary layer becomes shallower and exerts a lower influence on the 850hPa level. Air temperatures are not constrained anymore to follow the adiabatic profile tied to surface temperatures, so that they are now driven by the large-scale flow instead, which is not necessarily well correlated with the surface and thus would result in a reduction of correlation. The right section of Fig. 3.7 corresponds to this second stage.

The average vertical potential temperature profile following the evolution of the FT index, together with the average boundary layer depth, both shown in Fig. 2.11, further corroborate the validity of the model we describe above, as the intensification phase of the index life cycle is seen to be characterised by a deeper boundary layer within which the vertical temperature profile is closest to being adiabatic, while in the decay phase potential temperature starts tilting slightly as the boundary layer becomes more shallow.

Despite the apparent weakness of the signal emerging from Fig. 2.11, the range of variability of the anomalies is of the same order of magnitude of the standard deviations of the averaged quantities, which advocates for their robustness.

Further evidence in support of our model can be gathered if we consider the climatological mean of the depth of the boundary layer and compare it with that for the 850hPa geopotential height (Z850). Figure 3.8 shows the winter climatology of the ratio between the boundary layer height to the 850hPa geopotential height (a) and the relative occurrence of the ratio being above one across winters 1979 to 2019 (b). Peaks in the average value and relative occurrences of a boundary layer reaching into and above Z850 geopotential (ABL height–Z850 ratio > 1) are collocated with maxima of the heat transfer coefficient from Eq. 3.4, shown in Fig. 3.3c. The similarity is not coincidental, as a deeper boundary layer in those locations would be consistent with the observed higher time correlation between surface heat flux and air temperature (compare with Fig. 3.1).

In addition, we also take notice of the spatial correspondence between peaks of observed boundary layer depths and the largest SST spatial variability that is found around the strongest SST gradients. These are essentially driven by western boundary currents and the presence of mesoscale oceanic eddies that detach from the main SST front. These mesoscale eddies have a significant influence on the air–sea thermal interaction and its effects on storm evolution, as we concluded at the end of Chapter 2. This spatial correspondence is consistent with the study by Hausmann et al. (2017), who observed a fast atmospheric export of temperature and moisture anomalies away from the marine boundary layer occurring over the Gulf Stream extension (whereas over colder SST this export is slower). This fast atmospheric export was ascribed to the compensation between the thermodynamic adjustment of the marine boundary layer and the enhancement of surface winds over warm SST anomalies. The magnitude of the air–sea heat flux feedback (i.e. the change in the net air-sea heat flux in response to a change in SST) can act, therefore, as a major contributor in setting the damping timescale of SST anomalies.

3.5 Summary and conclusion

A joint increase of correlation and variances is observed in the build-up to peaks in heat-flux–temperature spatial covariance. The explanation for this behaviour is non-trivial as it is not possible to rely exclusively on simple statistical grounds, which implies that the increase in correlation is driven by physical processes.

In this chapter, we explored the plausibility of a qualitative model that describes the role played by the atmospheric boundary layer in driving the observed increase in correlation between surface hat flux and lower-tropospheric temperature. In particular, the largest fraction of the boundary layer's thermo–dynamical structure coincides with the mixed layer, where the almost adiabatic temperature profiles induced by turbulent mixing are conducive to the strengthening of the correlation between the surface and the free troposphere, as a deeper boundary layer occurring during events of strong flux–temperature covariance enhances the thermal coupling between the two levels.

In order to get a clearer and more detailed picture of how the surface interacts with the free troposphere leading to increased correlation, in the

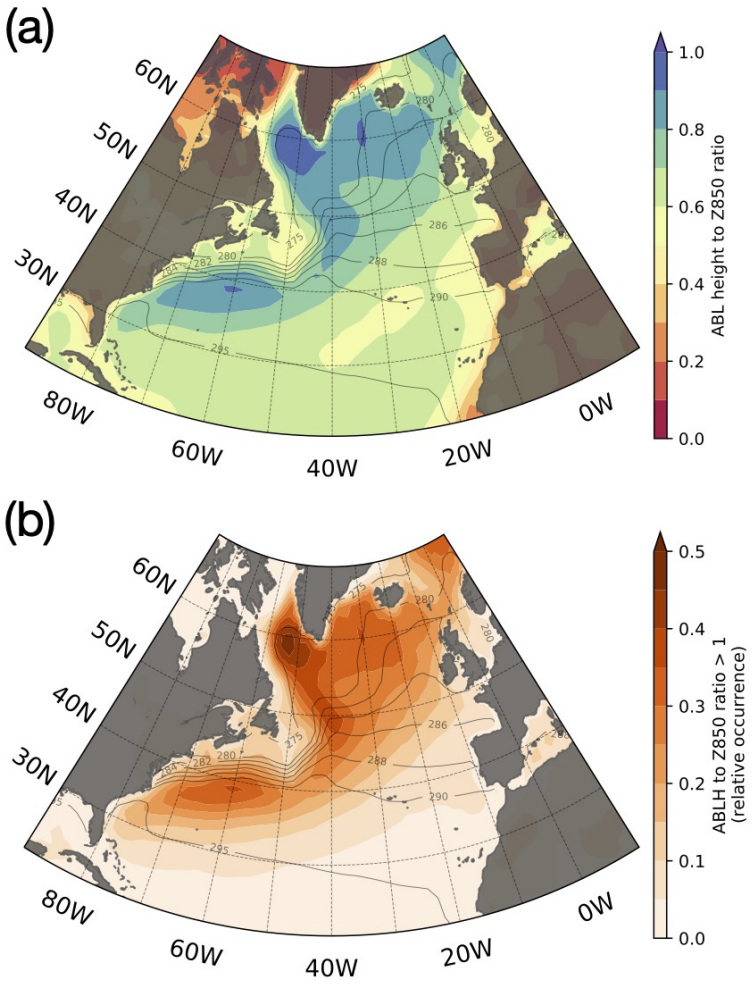

Figure 3.8: (a) Winter climatology of the ratio of the atmospheric boundary layer height (ABLH) to Z850 (colour shading) and SST (black contours). (b) Relative occurrence of a boundary layer deeper than Z850 in winter (colour shading) and SST winter climatology (black contours) as in (a).

next chapter we will select a few events of intense air–sea thermal interaction over the Gulf Stream Extension region and examine the evolution of the system and the mechanisms leading to the increase in correlation with variances, gathering evidence for the relative importance of boundary layer dynamics in driving the observed behaviour of correlation.

Chapter 4

Detailed analysis of the physical processes driving correlation in selected case studies

4.1 Introduction

Spatial covariance between synoptic-timescale anomalies in surface heat flux F and temperature T occurs in intermittent peaks which are driven both by their spatial correlation and their variances. In Chapter 2 we described how these intermittent events unfold, with the covariance peaks corresponding to enhanced damping of synoptic-scale variability.

We noticed that, over the Gulf Stream Extension region, surface heat flux variability leads in time on air temperature variability. This can be explained if we consider the effect of oceanic mesoscale eddies on the atmospheric circulation above, as the mesoscale variability of SSTs is imprinted onto the surface heat flux spatial field (Frenger et al., 2013), eventually triggering a response in air temperatures. At the same time, spatial correlation between surface heat flux and air temperature in the lower troposphere is seen to increase concomitantly with spatial variances in the build-up of covariance.

In Chapter 3 we proposed a qualitative model that linked boundary layer dynamics and its thermodynamic structure to the enhancement of the thermal coupling between the surface and the lower layers of the free troposphere. We surmised that the almost adiabatic temperature profile

that characterises the mixed layer within the boundary layer tied the lower-tropospheric temperature variability to that of the surface. This was shown to be consistent both with the average evolution of air temperature, sensible heat flux and boundary layer height (Fig. 2.11) observed in the heat-flux–temperature variances' phase space and with the climatology of the ratio between boundary layer height and 850hPa geopotential height and the relative occurrence in time of a ratio above unity (Fig. 3.8). However, we only considered the average picture and did not concentrate on any specific event in which the proposed mechanism can be envisaged.

The atmosphere and the ocean interact over a wide range of time and length scales and the effects of this interaction can have a significant impact on both the atmospheric and oceanic circulations (e.g. El Niño events in the tropics or the role of western boundary currents on the climate of the mid-latitudes). Therefore, the skill of numerical weather and climate prediction models relies essentially on their level of horizontal resolution, as the correct representation of finer details allows the models to capture a larger fraction of the full variability associated with air–sea interaction and their role in shaping weather and climate dynamics.

High-resolution numerical models of the ocean and the atmosphere can currently resolve phenomena across a wide range of length scales, from planetary waves to mesoscale variability, down to turbulence in the boundary layer in urban meteorology models.

The aim of this chapter is to test the validity of the hypotheses that were put forward in the previous chapter on the driving mechanisms behind the relationship between heat-flux–temperature correlation and variances in the cyclical evolution of covariance (which was introduced in Chapter 2). To that extent, we make use of very high-resolution numerical simulations of the atmosphere run with the UK Met Office Unified Model and take a closer and more detailed look at boundary layer dynamics and thermodynamics in the run-up to a peak in heat-flux–temperature spatial covariance (which we also refer to as the FT index, see Chapter 2). In particular, we select four events characterised by a peak in covariance and draw a parallel between the high-resolution model representation of the surface–troposphere thermal interaction and our expectations from the model of Chapter 3.

In Section 4.2 we describe the selection of the four case studies, consisting of either an extra-tropical cyclone's cold sector being advected over the Gulf Stream region or cold air outbreaks over the same region, all charac-

terised by intense air–sea thermal interaction. The data output from each of the numerical simulations is subsequently analysed further into detail in Section 4.3. We then provide a preliminary analysis of the effects of increasing model resolution on the representation of the FT index in Section 4.4, while Section 4.5 explores the effects of atmosphere–ocean coupling in a high-resolution limited area model. Finally, in Section 4.6 we provide a summary and conclusions.

4.2 Case study selection and model configurations

In order to test the validity of the boundary layer model that was introduced in Chapter 3, we select a set of individual events associated with a peak in $F' - T'$ spatial covariance over the Gulf Stream Extension region, coinciding with the same region studied in Chapter 2. Covariance, correlation and variances time series used for the selection are computed using hourly data from the ERA5 reanalysis dataset (Hersbach et al., 2020), interpolated on a spatial grid with a resolution of 1.5° in both longitude and latitude.

The type of events that are considered are characterised by strong thermal interaction between the ocean and the atmosphere. Specifically, we

Table 4.1

Case	Date and time of FT peak	FT peak value ($\mathrm{Wm^{-2}\ K}$)	Event description
1	15-11-2018 4:00 UTC	–375	Cyclone over Nova Scotia later advancing towards Europe along the 50°N parallel
2	13-12-2017 17:00 UTC	–350	Low-pressure system developing over North America and later advancing towards Greenland
3	29-12-2015 2:00 UTC	–470	Meandering of the eddy-driven jet that leads to a cold air outbreak over the Gulf Stream region
4	24-11-2015 9:00 UTC	–320	Meandering of the eddy-driven jet that leads to a cold air outbreak over the Gulf Stream region

study four different events associated with peaks in the FT index values of up to almost -500 Wm^{-2} K, as reported in Table 4.1. Two of the case studies coincide with mid-latitude weather systems that travel across the Gulf Stream extension region and proceed downstream along the North Atlantic storm track (Cases 1,2 in Tab. 4.1), pulling cold continental air masses over the Gulf Stream. The remaining two case studies (Cases 3,4 in Tab. 4.1) are denoted by cold air outbreaks over the western North Atlantic oceanic basin, as cold air is advected off the North American continent onto the ocean due to the action of an intense eddy-driven jet stream over the region. For our case studies, we chose to exclude the most extreme events which might lead to circumstantial results that would not be easy to link to the average picture we get from phase portraits. Instead, we focus on relatively moderate cases of strong covariance in order to keep our analysis as general as possible.

The heat-flux–temperature spatial covariance is computed using time anomalies defined as departures from the time mean over the entire duration of the numerical simulation (i.e. 10 days) instead of removing a 10-day running mean. This choice was taken in consideration of the fact that for a comparison with the numerical simulations we would require longer and time consuming simulations in order to compute the FT index over the five days before and after the peaks. The difference in the definition of the index, however, does not change its meaning in a significant way as it is still linked to synoptic scale variability. In particular, the value of the index at the peak is not affected at all, as the two definitions coincide there.

In Fig. 4.1 we plot the time series for the FT index, the product of F', T' spatial standard deviations and their spatial correlation for each of the case studies. In all of the four case studies we can observe a distinctive growth of the standard deviations in the run up to the FT index peak while the picture is less clear for correlation, although in close proximity to the peaks of the index it is seen to be higher relatively to days before and after the peak.

In Fig. 4.2 we present synoptic maps of Mean Sea Level Pressure (MSLP) and 1000-500hPa geopotential thickness at the time of peak FT index intensity, as indicated in Tab. 4.1. Complementary to the maps shown in Fig. 4.2, Figure 4.3 shows the meridional cross section of the lower troposphere (up to 700hPa) across the North Atlantic (averaged over the latitudinal band 40°–45°N, which coincides with the location of both the strongest SST gra-

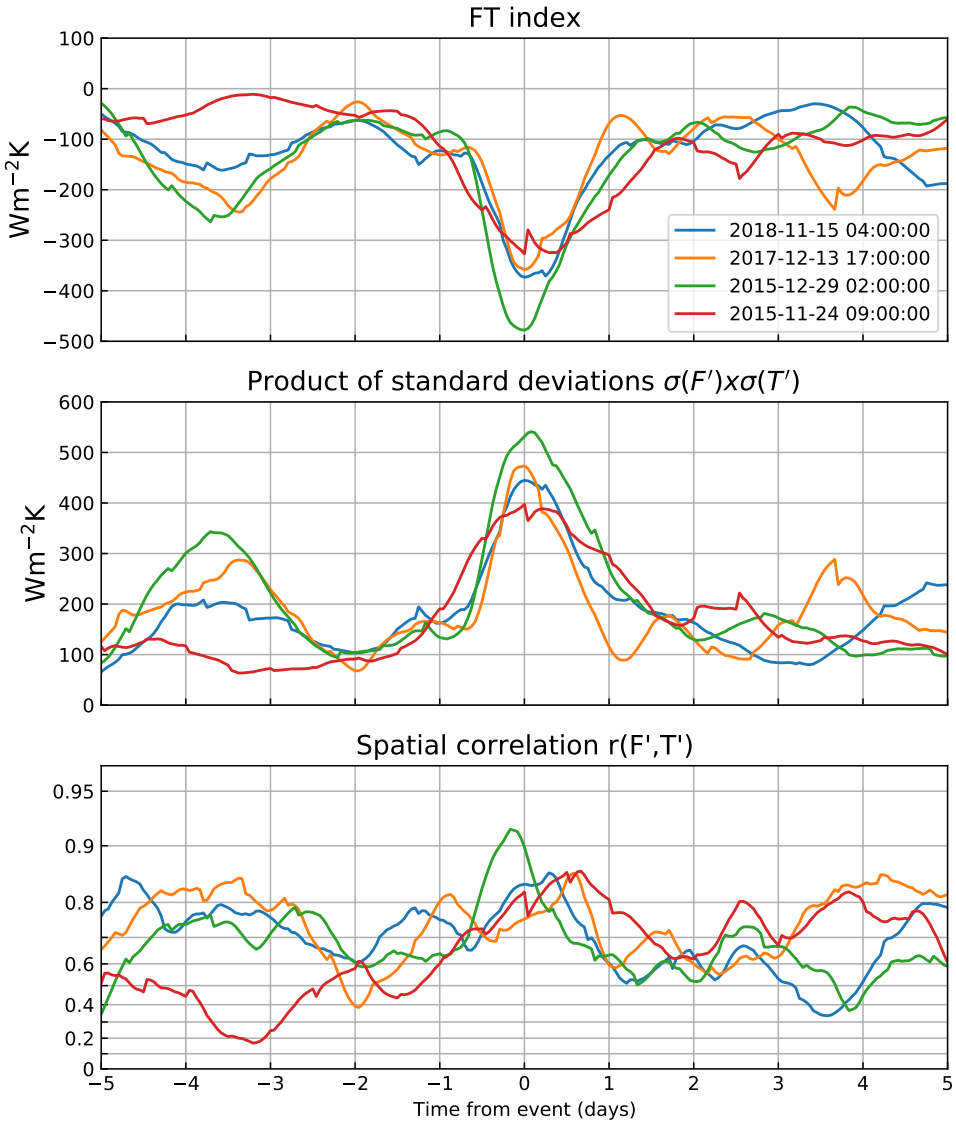

Figure 4.1: Time series of FT index (top), product of spatial standard deviations (middle) and correlation (bottom) between F' and T' for the four selected case studies.

dients and the most intense air–sea thermal interaction). The cross sections include potential temperature, geopotential, pressure at the top of the boundary layer (which indicates its depth), surface sensible heat flux and SST (to compare with potential temperature). We notice that the strongest upward surface heat fluxes coincide with the advection of cold air masses over the starkest SST gradients, which suggests these regions give a primary contribution to the total spatial covariance of the entire domain (compare with Fig. 4.4, where we show sources of covariance for each case study).

In particular, Fig. 4.3 shows the extent of the almost adiabatic temper-

ature vertical profiles (i.e. constant potential temperature in the vertical direction) associated with the mixed layer, which can be seen to reach the 850hPa level and beyond, thus strengthening the coupling of this level to the surface, which is consistent with the boundary layer model we proposed for the increase in correlation between the two levels. If we focus on the profiles of the estimated height of the boundary layer (as diagnosed in ERA5) in Fig. 4.3, we find that the top of the boundary layer can be considered as a demarcation line between a stably stratified free troposphere and a well-mixed boundary layer below it. Although warm boundary layers are seen to be quite stably stratified as well (e.g., Fig. 4.3a), in the case studies considered these appear to coincide with weaker sensible heat fluxes as the thermal contrast between the sea surface and the lower troposphere is minimal.

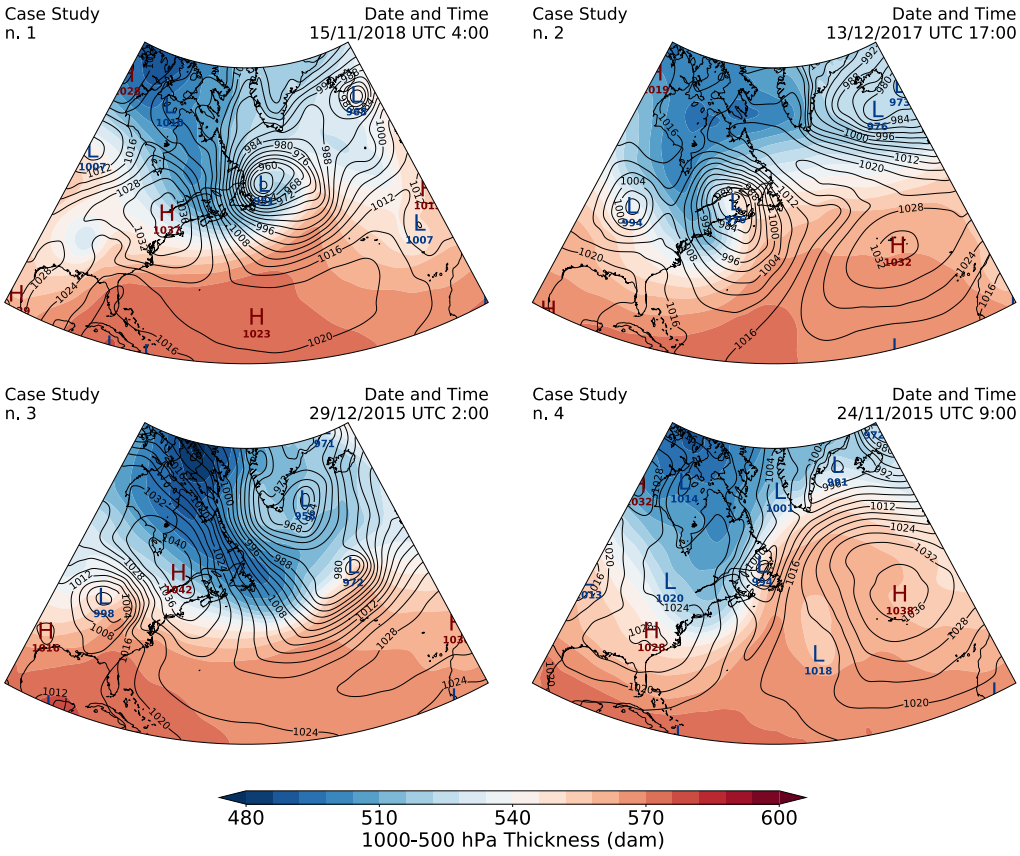

Figure 4.2: Mean Sea Level Pressure (contours every 4hPa, minima and maxima denoted by L and H, respectively) and 1000–500 hPa Thickness (shading) at the time of the peak for the four case studies. Data from ERA5.

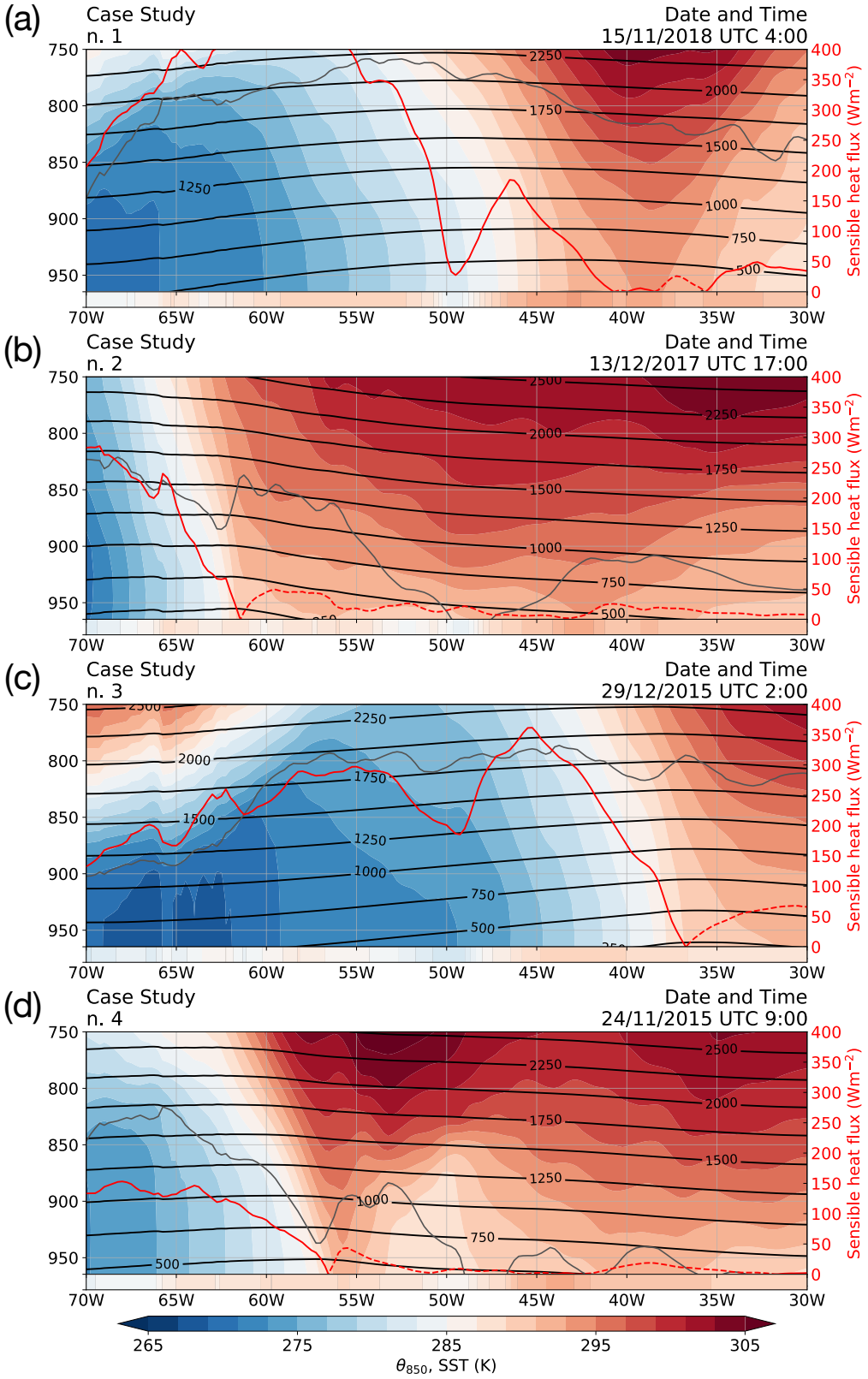

Figure 4.3: Meridional average (40°–45°N) of vertical profiles of potential temperature (shading) and geopotential height (black contours) at the time of the peak for the four case studies (a–d). Superimposed are the meridional averages of surface sensible heat flux (red line, scale on the right of each panel, negative values dashed), pressure at the top of the boundary layer (grey line) and SST (bar at the bottom of each panel, same colour shading as for potential temperature). Data from ERA5.

4.2.1 Model setup

A high-resolution simulation of the selected events would allow us to unpack some of the coupling mechanisms that underpin our conceptual model. To that extent, we examine the output of high-resolution simulations that are run with the Met Office Unified Model (MetUM).

Each case study consists of a numerical simulation lasting between five days before and after the peak in flux–temperature covariance, for a total of 10 days. The simulations are based on convection permitting limited area models (LAMs) of increasing horizontal resolution (average grid spacing of $\approx$ 10km and $\approx$ 4.4km). The higher-resolution LAM (4.4km) is run with the second Regional Atmosphere and Land science configuration (RAL2, built on RAL1, Bush et al., 2020) of the MetUM optimised for the mid-latitudes and is defined over a spatial domain that extends between 30°N–60°N, 80°W–30°W. The high-resolution LAM is nested onto an intermediate LAM (10km) run with the Global Atmosphere 6.0 (GA6, Walters et al., 2017) configuration of the MetUM and extending over a larger domain (20°N–70°N, 90°W–20°W) which contains that of the higher-resolution LAM. The intermediate LAM is driven by ERA5, which acts as the driving model in the first-level nesting.

In both high and low resolution LAMs, sea surface boundary conditions are passed daily from Operational Sea-surface Temperature and Sea Ice Analysis (OSTIA, Donlon et al., 2012), after a reconfiguration from the native 0.05° degree resolution ($\approx$ 5.5km) to match that of the atmosphere (i.e. 4.4km and 10km, respectively, for high and low resolution LAMs).

In simpler terms, in our experiments we essentially simulate what is observed in the reanalysis with a finer horizontal resolution and this allows us to have a closer look at how the surface and the free troposphere thermally interact. Additional diagnostics can be included in the model output and, specifically, we obtained temperature and geopotential fields of the lower troposphere with a vertical resolution of 25hPa between 1000hPa–700hPa and 50hPa above 700hPa. For technical details on the specific configuration of the MetUM and the particular nesting approach that is adopted, we refer to Appendix B.

4.3 Analysis of model output

In this section we present and analyse some of the results from the high-resolution simulations of the four case studies which were designated in the previous section.

For each case study we have hourly output across the 10 days of each simulation, which we used to compute the spatial covariance, standard deviations and correlation between F and T time anomalies, defined as departures from the time mean across the entire duration of the simulations.

On average, covariance computed from finer-resolution simulations feature higher spatial covariance which can be ascribed to the larger variance deriving from smaller-scale variability that is resolved in higher-resolution runs. In fact, standard deviations are seen to increase with the level of spatial resolution, as it goes from 25 km for ERA5 to about 10 km for the first nested LAM, to about 4.4 km for the second higher-resolution nested LAM.

When we compare the time series for covariance, correlation and variances resulting from the use of reanalysis data and those from model output (see Figs. 4.5, 4.8, 4.11, 4.14), we observe that the increase in resolution does not lead to tangible differences at times of low covariance, indicative of weaker weather activity, while the starkest deviations are observed in correspondence with covariance peaks.

Figure 4.4 shows the SST field at the time of the peaks in each of the case studies together with the sources of heat-flux–temperature spatial covariance, similarly to how it was done for Fig. 2.5 (i.e. by looking at peaks in the time mean of the product of F and T space-time anomalies, which, in the computation of the spatial covariance, are then spatially averaged across the domain considered). In all of the four case studies, regions of largest SST spatial variability coincide with peaks of flux–temperature anomalies, which highlights the link between oceanic surface temperature variability (both on the mesoscale and the synoptic scale) and the sources of heat-flux–temperature spatial covariance, in agreement with what was pointed out at the end of Section 2.3.

For each case study, we look at the difference between the air potential temperature at the 850hPa level (θ_{850}) and the SST and then compare it with the actual surface sensible heat flux field. We expect the magnitude of this difference to be proportional to the intensity of surface heat fluxes along the Gulf Stream, especially during times of strong spatial covariance (as we

observed in Chapter 3). In order to probe the validity of our boundary layer model, we then compute the ratio between the atmospheric boundary layer height (ABLH) and the 850hPa geopotential height (Z850) and juxtapose maps of this ratio to those for the temperature difference and surface heat flux. We focus specifically on times of peaks in covariance and the closest points of local minimum of the FT index in order to highlight the different dynamical and thermodynamical structures that are observed as the index evolves.

In addition to maps of the temperature difference, surface sensible heat flux and boundary layer height to Z850 ratio, we also examine the vertical cross sections of the lower troposphere (up to 700hPa) along the path A–B indicated in Fig. 4.4, which runs across the large-scale SST front associated with the Gulf Stream.

Model data presented in this Chapter (maps and cross sections) derive exclusively from the convection-permitting simulations (i.e. 4.4km).

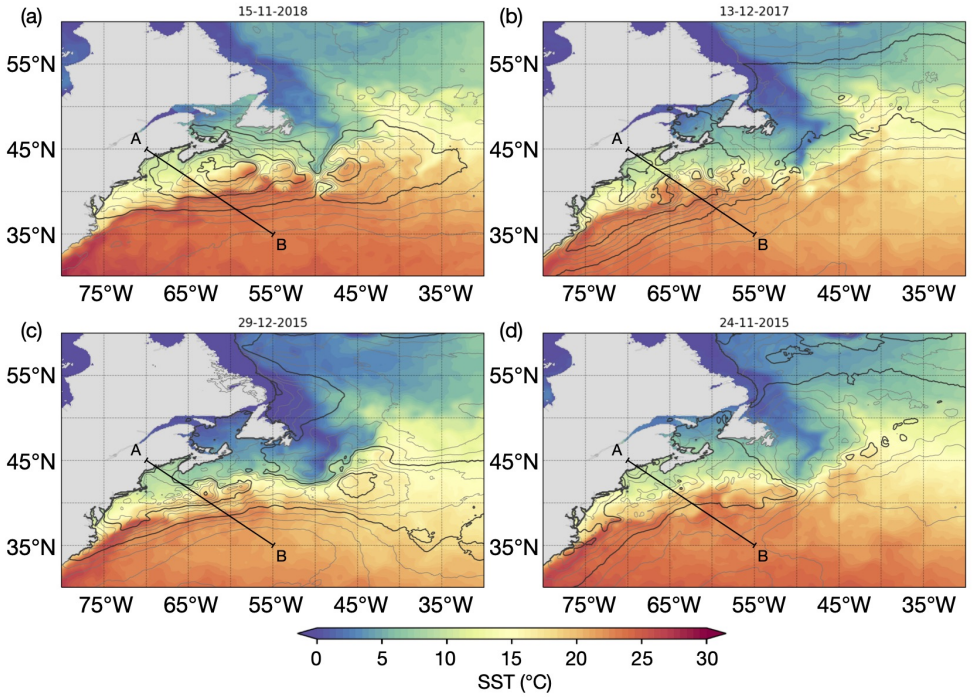

Figure 4.4: Time mean of the product between time–space anomalies in F and T over the spatial domain shown (contours, every 50 Wm^{-2} K, thick contours every 200 Wm^{-2} K) and SST on the day of the peak for the four case studies (a–d respectively). The black line joining A to B indicates the path considered for the cross sections shown in Figs. 4.7, 4.10, 4.13, 4.16.

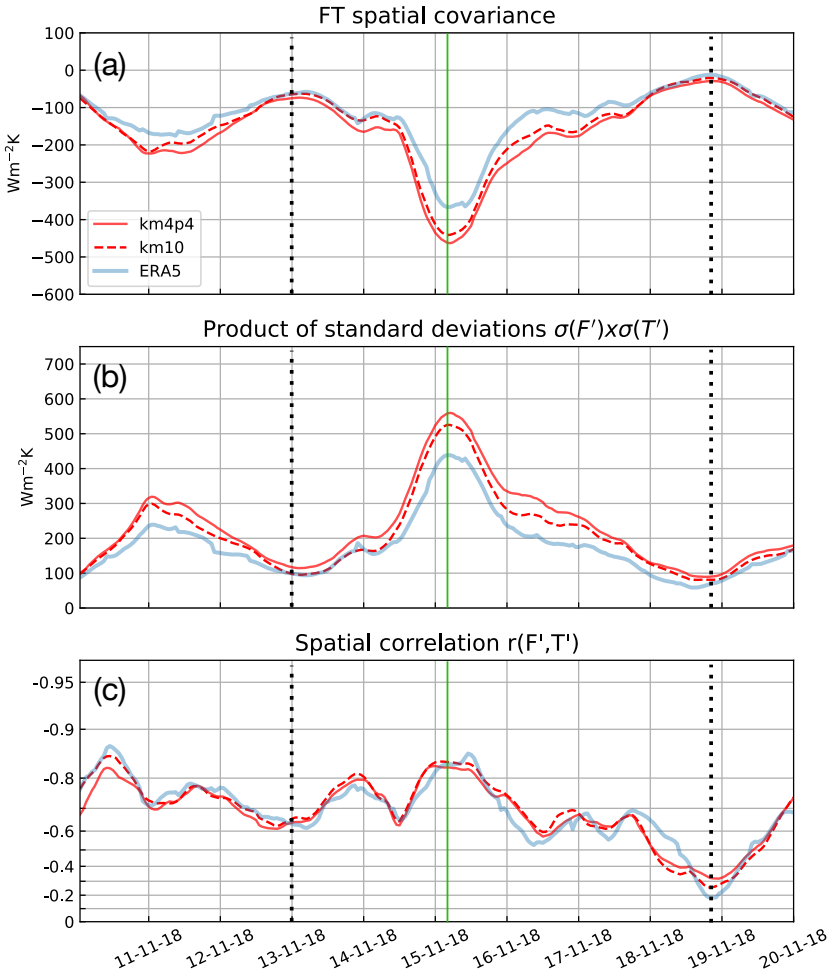

Figure 4.5: Time series of the FT index (a) and of the product of spatial standard deviations (b) and correlation (c) between F' and T' resulting from reanalysis (ERA5, solid light blue lines), lower-resolution (km10, dashed red lines) and higher-resolution (km4p4, solid red lines) simulations for Case Study N.1 (Nov 2018). Solid green vertical lines denote the time of the FT index peak as derived from ERA5, dotted black lines indicate times before and after the peak that are inspected in Figs. 4.6, 4.7.

4.3.1 Case Study N.1

The first case study involves a low pressure system to the east of Newfoundland (see Fig. 4.2, upper left panel) featuring an extensive cold front stretching along the Gulf Stream Extension region and marking the advection of cold continental air over the North Atlantic ocean. The interaction of this cold air mass with the underlying warm ocean surface leads to a peak in the FT index of ≈ -460 Wm^{-2} K, occurring on 15-11-2018 at 4:00 UTC. The numerical simulation extends between 10-11-2018 and 20-11-2018.

Figure 4.5 shows the time evolution of the FT index and its components. It can be seen that the spatial standard deviations play a major role in driving the index, both at the time of the peak and during a secondary peak in the first couple of days of the simulation. Spatial correlation remains relatively high in the first half of the simulation, with a local maximum in correspondence with the peak in the FT index, while it is seen to contribute most to the FT index weakening towards the end of the simulation.

Two days before the peak, on 13-11-2018 at 00:00 UTC (Fig. 4.6a,d), we can see that a low pressure system in the NE sector of the domain is advecting cold air masses southwards over the Gulf Stream. However, despite a relatively high level of correlation between F' and T' (≈ -0.7), the spatial variability associated with F' and T' is visibly lower than that observed at the peak a couple of days later, on 13-11-2018 at 4:00 UTC (Fig. 4.6b,e), when the cold sector of a more intense extra-tropical cyclone (lower minimum 500hPa geopotential – Z500 – at the centre of the cyclone) is advected off the North American continent over a larger fraction of the SST front associated with Gulf Stream, resulting in increased variability in both F' and T'.

The boundary layer within the cold sector deepens and exceeds the 850hPa level over a larger portion of the domain compared to a couple of days before (Fig. 4.6g,h). As the cyclone evolves, it travels downstream along the North Atlantic storm track over the few days after the peak. The atmospheric circulation over the Gulf Stream Extension region weakens and becomes more zonally aligned, as we can see on 18-11-2018 at 21:00 UTC (Fig. 4.6c,f,i), when both the spatial standard deviations and correlation reach their minimum value. While there is still some thermodynamic activity in the eastern sector of the spatial domain (Fig. 4.6f), it occurs on a smaller scale compared to what is observed at the peak (Fig. 4.6e) and does not give a dominant contribution to the total covariance over the whole spatial domain.

The vertical structure of the flow at different stages of the covariance evolution is portrayed in Fig. 4.7, where we show the vertical potential temperature profile, surface sensible heat flux, boundary layer height and SST along the cross sections indicated in Fig. 4.4. It can be seen that, within the entire extent of the boundary layer, potential temperature profiles are almost adiabatic at any time during the evolution of covariance. In fact, this is even more evident than in Fig. 4.3a, where the meridional averaging

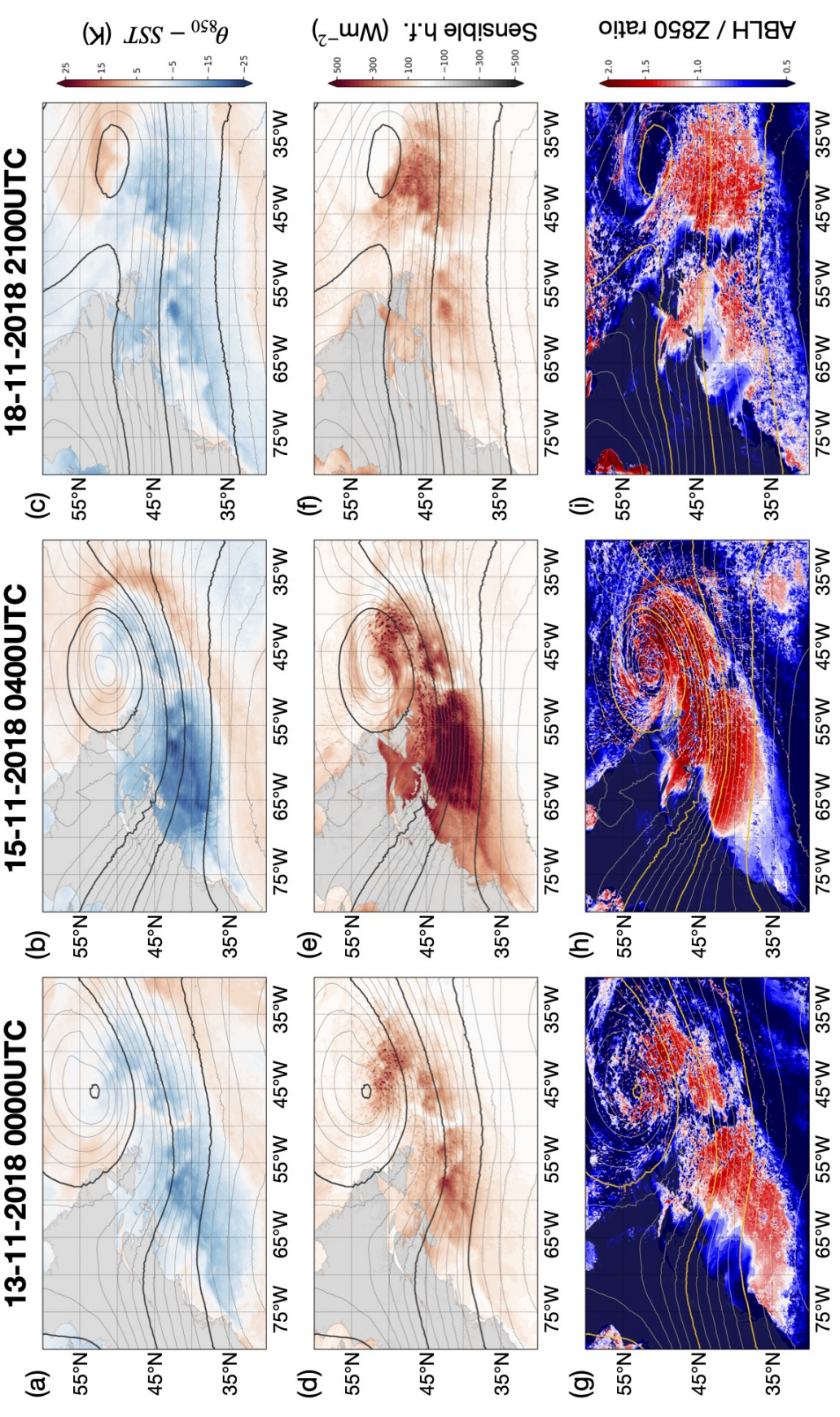

Figure 4.6: Maps of θ_{850} minus SST (shading, a–c), surface sensible heat flux (shading, positive upwards, d–f), boundary layer height to Z850 ratio (shading, g–i) and Z500 (contours every 5dam, thick contours every 25dam, black a–f, yellow g–i) for Case Study N.1 (Nov 2018). Panels on the left (a,d,g), centre (b,e,h) and right (c,f,i) correspond, respectively, to the left dotted black line, central green solid line and right dotted black line in Fig. 4.5. Data from the 4.4km, convection-permitting simulation.

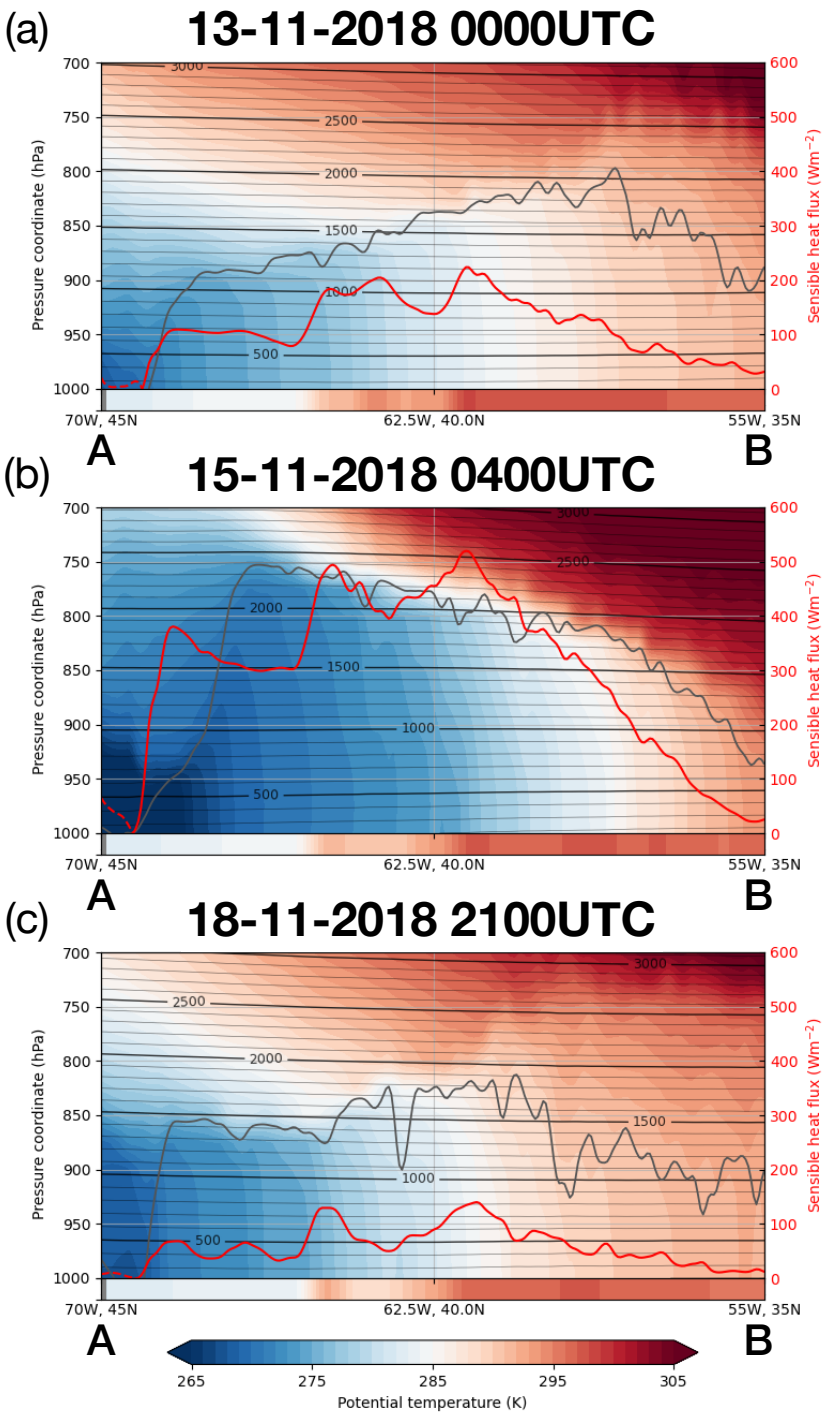

Figure 4.7: Surface sensible heat flux (red line, scale on the right of each panel, negative values dashed), pressure at the top of the boundary layer (grey line), vertical cross sections of lower-tropospheric potential temperature (colour shading) and SST (bar at the bottom of each panel, same colour shading as for potential temperature) along the path A–B indicated in Fig. 4.4 for Case Study N.1 (Nov 2018). Time coordinates of panels at the top (a), middle (b) and bottom (c) correspond, respectively, to the left dotted black line, central green solid line and right dotted black line in Fig. 4.5. Data from the 4.4km, convection-permitting simulation.

may partly hinder the visualisation of the precise vertical structure.

As we approach the peak in covariance, the signature of the cold sector becomes more evident, surface heat fluxes strengthen and the boundary layer consequently deepens, reaching higher into the troposphere and even beyond the 850hPa level. In particular, we can compare the vertical cross sections before and after the peak (Fig. 4.7a,c respectively) to that at the peak (Fig. 4.7b) and observe that, when the covariance is stronger, the temperature field at 850hPa is visibly coupled to the surface, where the difference in temperature between the atmosphere and the ocean (represented by the bar at the bottom of each panel in Fig. 4.7) sets the intensity of the heat exchange (solid red lines), whereas air at the 850hPa level is more stably stratified during weaker covariance and the thermal coupling to the surface is consequently weakened.

4.3.2 Case Study N.2

In the second case study, we follow the evolution of a midlatitude low pressure system which develops over the North American continent and then moves eastwards onto the western North Atlantic ocean (see Fig. 4.2, upper right panel), eventually decaying as it travels northeastwards towards Greenland. The cold front associated with the low-pressure system is observed to stretch across the Gulf Stream at the time of the FT index peak (-500 Wm^{-2} K), which occurs on 13-12-2017 at 17:00 UTC. The numerical simulation lasts 10 days between 08-12-2017 and 18-12-2017.

Figure 4.8 shows the time evolution of the index and its components. Also in this case, the spatial standard deviations are seen to have a primary role in driving the evolution of the FT index. However, compared to what was observed in Case Study N.1, this time the spatial correlation arguably exerts a larger influence on the evolution of the index. In fact, the spatial correlation is seen to increase as the variances intensify and, conversely, is lower when variances are weak, although correlation steadily attains high values throughout the evolution of the FT index peak without showing any noticeable peak value.

The large-scale circulation on 11-12-2017 is characterised by a low pressure to the south of Greenland coupled to a high pressure over the Azores archipelago, which reflects the influence exercised by the eddy-driven jet upon the flow at the surface, which is broadly aligned with the SST front associated with the Gulf Stream. The spatial domain is characterised by

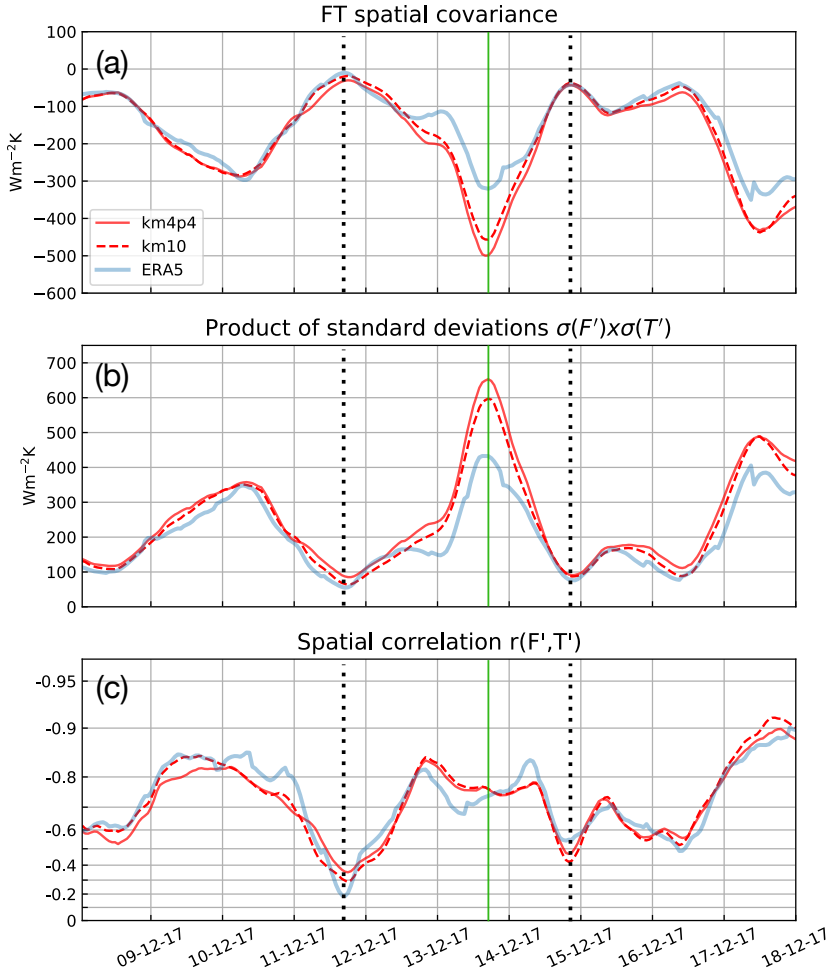

Figure 4.8: As in Fig. 4.5 for Case Study N.2 (Dec 2017). Solid green vertical lines denote the time of the FT index peak as derived from ERA5, dotted black lines indicate times before and after the peak that are inspected in Figs. 4.9, 4.10.

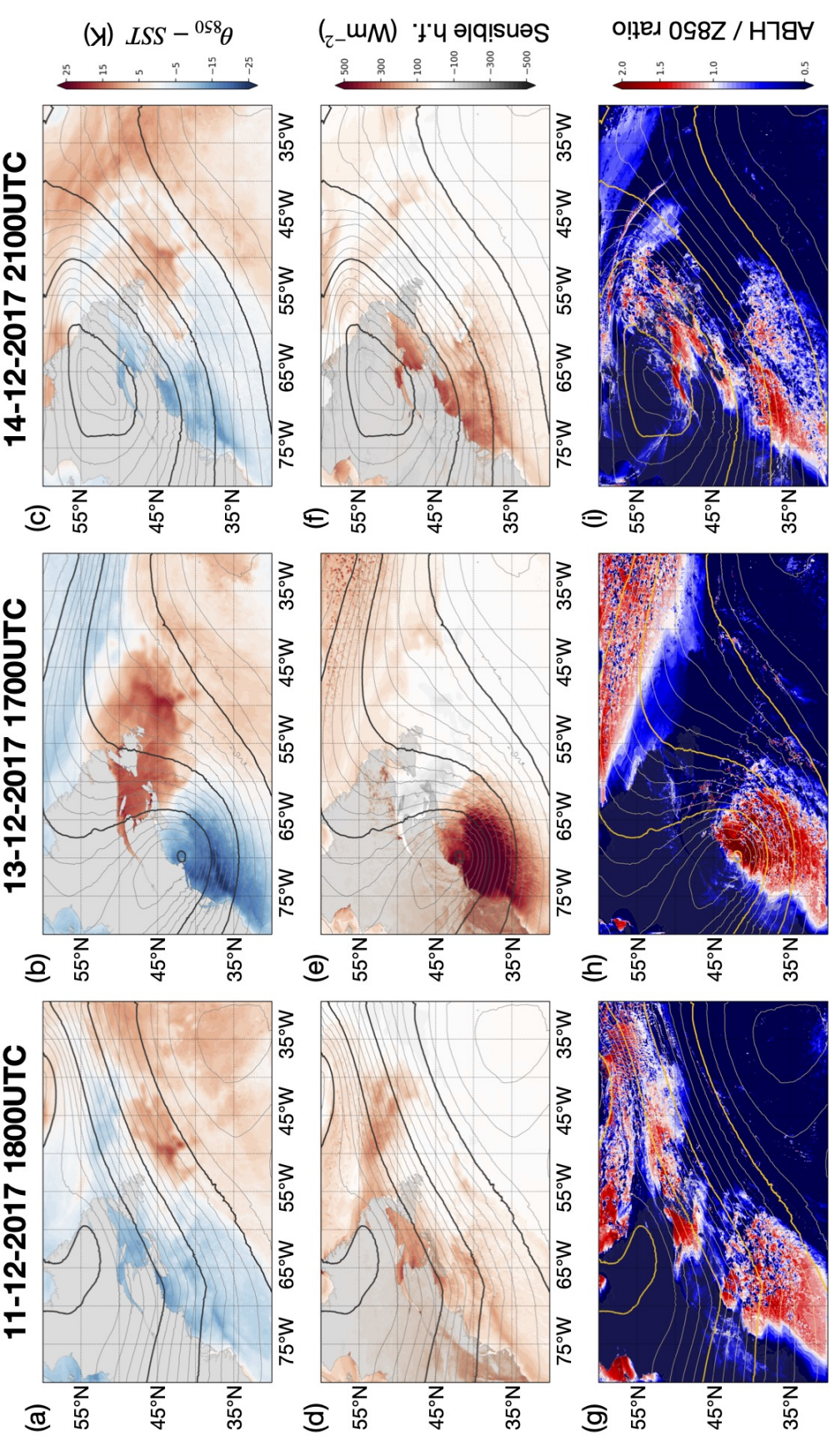

Figure 4.9: As in Fig. 4.6 for Case Study N.2 (Dec 2017). Panels on the left (a,d,g), centre (b,e,h) and right (c,f,i) correspond, respectively, to the left dotted black line, central green solid line and right dotted black line in Fig. 4.8.

a large-scale thermal contrast between warm maritime and cold continental air masses, which occupy the eastern and western sector of the domain (Fig. 4.9a), respectively. Although the advection of the cold air mass coincides with enhanced surface heat exchange locally resulting in a slightly stronger thermal coupling (as Fig. 4.7a suggests), the atmosphere–ocean temperature contrast is relatively weak, as the flow at the surface is parallel to the SST front and the cold air mass is confined over the colder ocean surface north of the SST front. While we can detect some level of heat exchange between the ocean and the cold air mass, the thermal interaction between the warm air mass and the underlying ocean is visibly weaker (Fig. 4.9d). As the contribution from the thermal interaction between the cold air mass and the ocean is minimal while a larger fraction of the domain is occupied by the warm air mass (coinciding with damped surface heat fluxes), the resulting spatial correlation averaged over the whole spatial domain remains low.

Between 11-12-2017 and 13-12-2017, an extra-tropical cyclone develops over NE United States which, as it evolves and travels in the NE direction, advects cold continental air over the western North Atlantic ocean, specifically across the SST front. This causes the amplification of the atmosphere–ocean thermal contrast (Fig. 4.9b), as surface heat fluxes become more vigorous (Fig. 4.9e) and the boundary layer deepens (Fig. 4.9h), eventually leading to the peak in the FT index, which is reached on 13-12-2017 at 17:00 UTC. We notice that the thermal interaction between cold polar air and the Labrador sea (which also results in a deeper boundary layer all over the northern sector, see Fig. 4.9h) also contributes in part to the high level of spatial correlation and covariance between F' and T', while most of the spatial variance derives from the air–sea heat exchange along the SST front in the Gulf Stream region.

Over the couple of days after the FT index peak, the cyclone reaches its mature stage and starts decaying as it moves in the NE direction towards Greenland. The flow is seen to re-align with the SST front and both covariance and correlation reach minimum values on 14-12-2017 at 21:00 UTC (Fig. 4.9c,f,i), visually resembling the configuration that was observed on 11-12-2017.

The evolution of the vertical structure of the flow is shown in Fig. 4.10. Away from the peaks in covariance, most of the 850-hPa level is characterised by a stably stratified lower troposphere which explains the observed

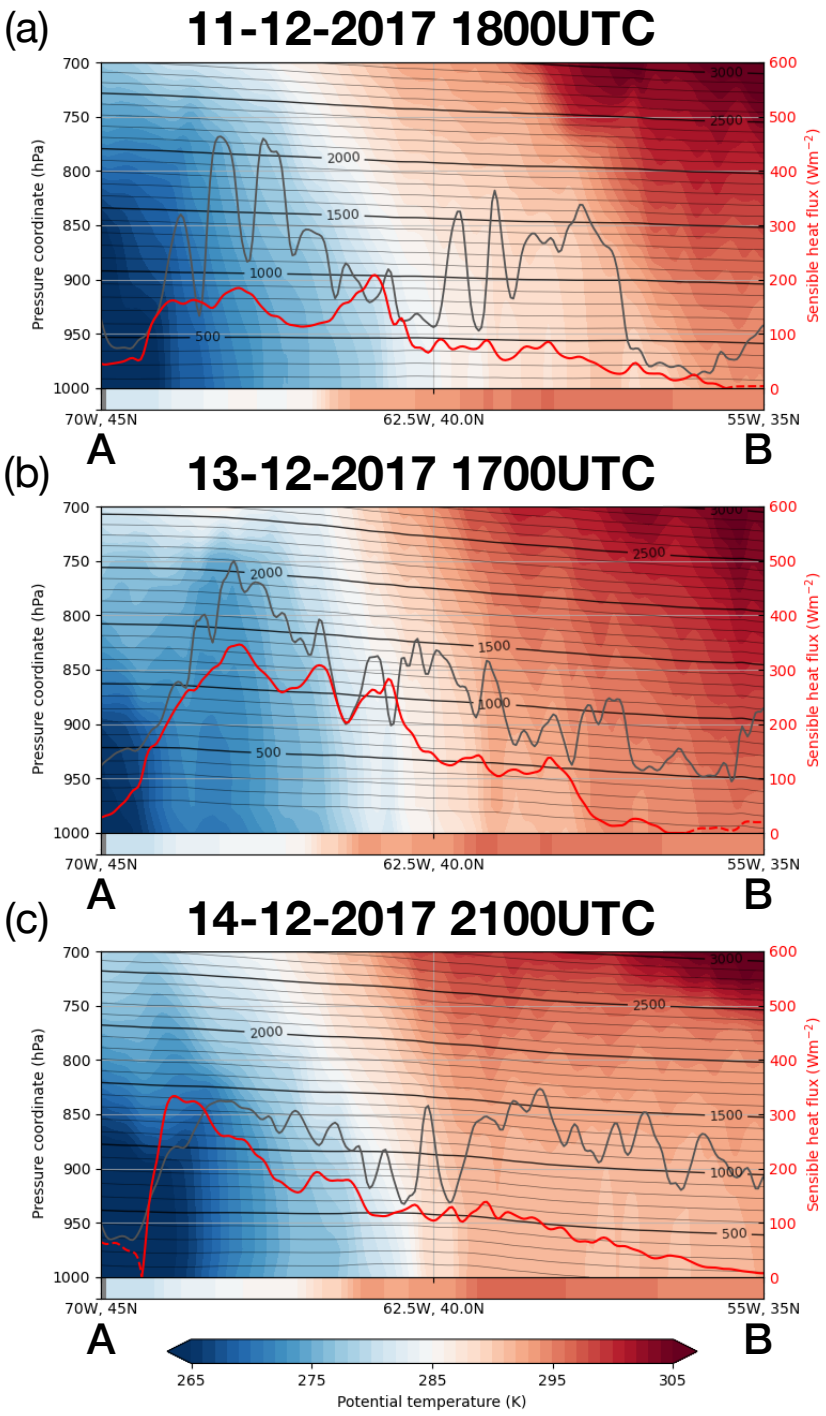

Figure 4.10: As in Fig. 4.7 for Case Study N.2 (Dec 2017). Time coordinates of panels at the top (a), middle (b) and bottom (c) correspond, respectively, to the left dotted black line, central green solid line and right dotted black line in Fig. 4.8.

low values of correlation and covariance. In particular, after the peak in covariance (Fig. 4.10c) the boundary layer depth appears to be fairly uniform along the cross section and mainly below the 850-hPa level, which is also consistent with low correlation.

When we are at peak covariance, as Fig. 4.10b shows, the well-mixed boundary layer exerts a larger influence on the 850-hPa level and the temperature profile correlates more strongly with the SST and sensible heat flux fields, which results in the observed larger covariance. Sensible heat fluxes seem to go along predominantly with the air–sea temperature contrast and are visually well correlated with the depth of the boundary layer, consistent with the idea of higher variance associated with enhanced fluxes corresponding with a deeper boundary layer and stronger surface–troposphere thermal coupling, as outlined in Chapter 3.

4.3.3 Case Study N.3

The third case study is focussed on an FT index peak of about -560 Wm^{-2} K occurring on 29-12-2015 at 2:00 UTC, which is associated with a cold air outbreak over the western North Atlantic that follows the transit of the cold front of a system that is centred further eastward (see Fig. 4.2, lower left panel). The numerical simulation lasts 10 days between 24-12-2015 and 3-1-2016.

From the visual inspection of the index and its components' time evolution (Fig. 4.11), it appears like a canonical case of both correlation and variances jointly increasing in the build up to a peak in covariance. In fact, all the time series in Fig. 4.11 visibly peak at the same time on 29-12-2015, while in the previous case studies that we considered so far the peak in correlation did not stand out as clearly.

In the few days before the peak in the FT index, the flow in the lower troposphere is almost entirely aligned with the zonal direction over the Gulf Stream region. On 28-12-2015 (2:00 UTC, Fig. 4.6a,d,g), the advection of cold continental air results in enhanced surface heat fluxes primarily in the eastern sector of the domain, while the rest of the domain does not show any significant heat exchange, which explains the low levels of both correlation and variances.

During the 24 hours preceding the peak, the meandering of the eddy-driven jet causes the lower tropospheric flow to bend to the south, which eventually results in a cold air outbreak over the North Atlantic SST front.

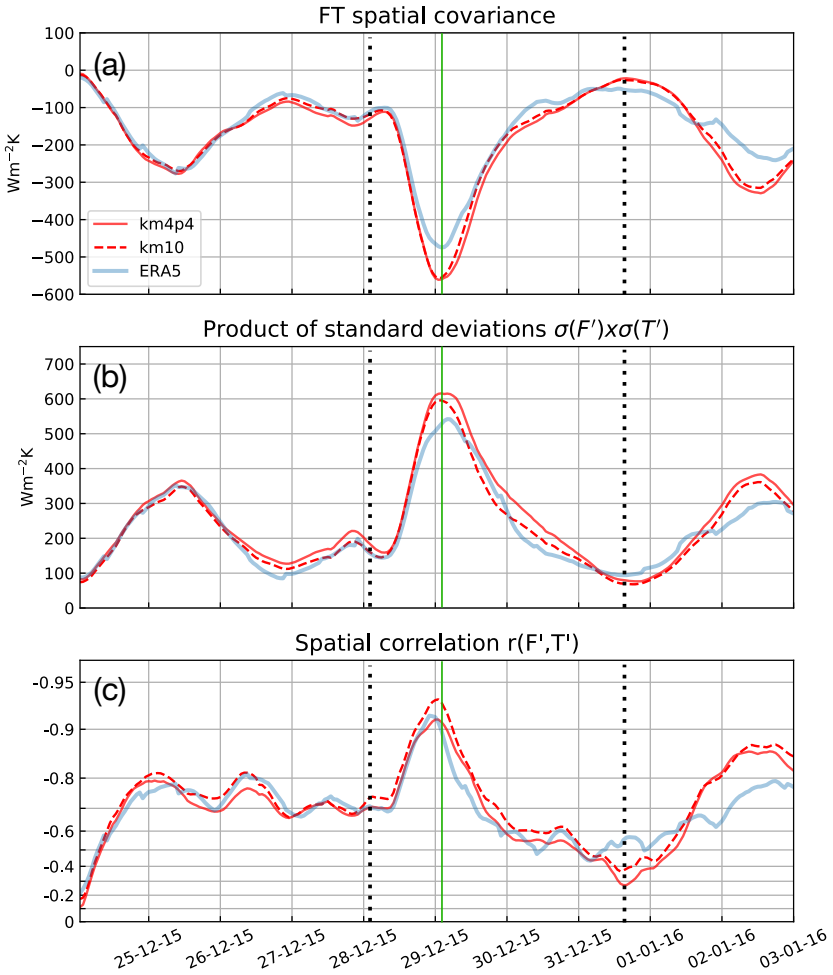

Figure 4.11: As in Fig. 4.5 for Case Study N.3 (Dec 2015/Jan 2016). Solid green vertical lines denote the time of the FT index peak as derived from ERA5, dotted black lines indicate times before and after the peak that are inspected in Figs. 4.12, 4.13.

As the cold air enters in contact with the warmer ocean surface, surface heat fluxes visibly intensify and the top of the boundary layer reaches the 850hPa level over a large fraction of the spatial domain. We should notice that most of the variance increase is due to surface heat fluxes arising in response to the cold air mass being advected over the ocean surface. In fact, the imprint of the SST front associated with the Gulf Stream is evident in the surface heat flux field (Fig. 4.6e, compare with Fig. 4.4c).

In the couple of days following the peak, the flow gradually shifts back to a more zonally-aligned configuration and on 31-12-2015 at 15:00 UTC (Fig. 4.6g,h,i) covariance, variances and correlation reach a local minimum.

The general picture that we get from inspection of the evolution of the

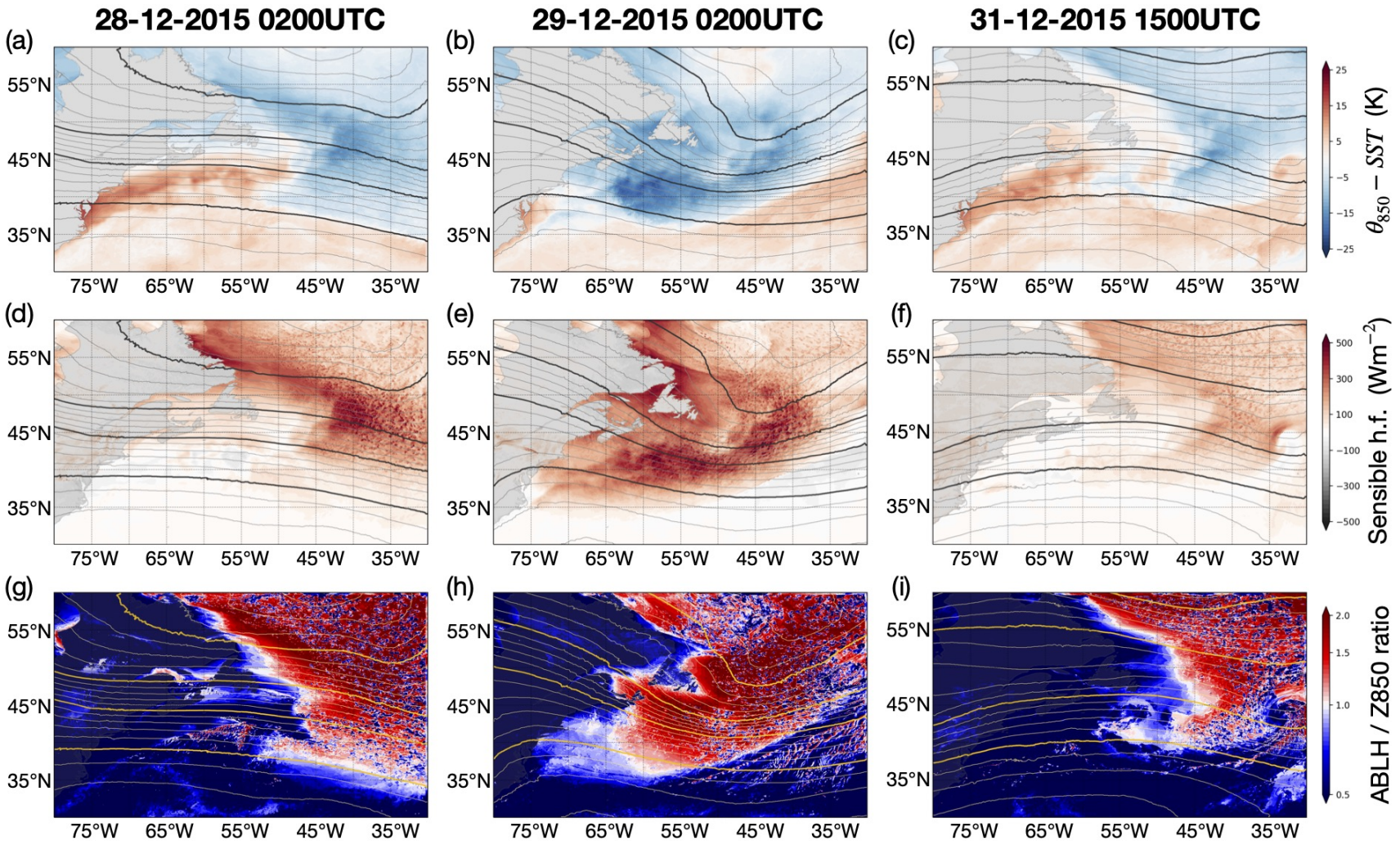

Figure 4.12: As in Fig. 4.6 for Case Study N.3 (Dec 2015/Jan 2016). Panels on the left (a,d,g), centre (b,e,h) and right (c,f,i) correspond, respectively, to the left dotted black line, central green solid line and right dotted black line in Fig. 4.11.

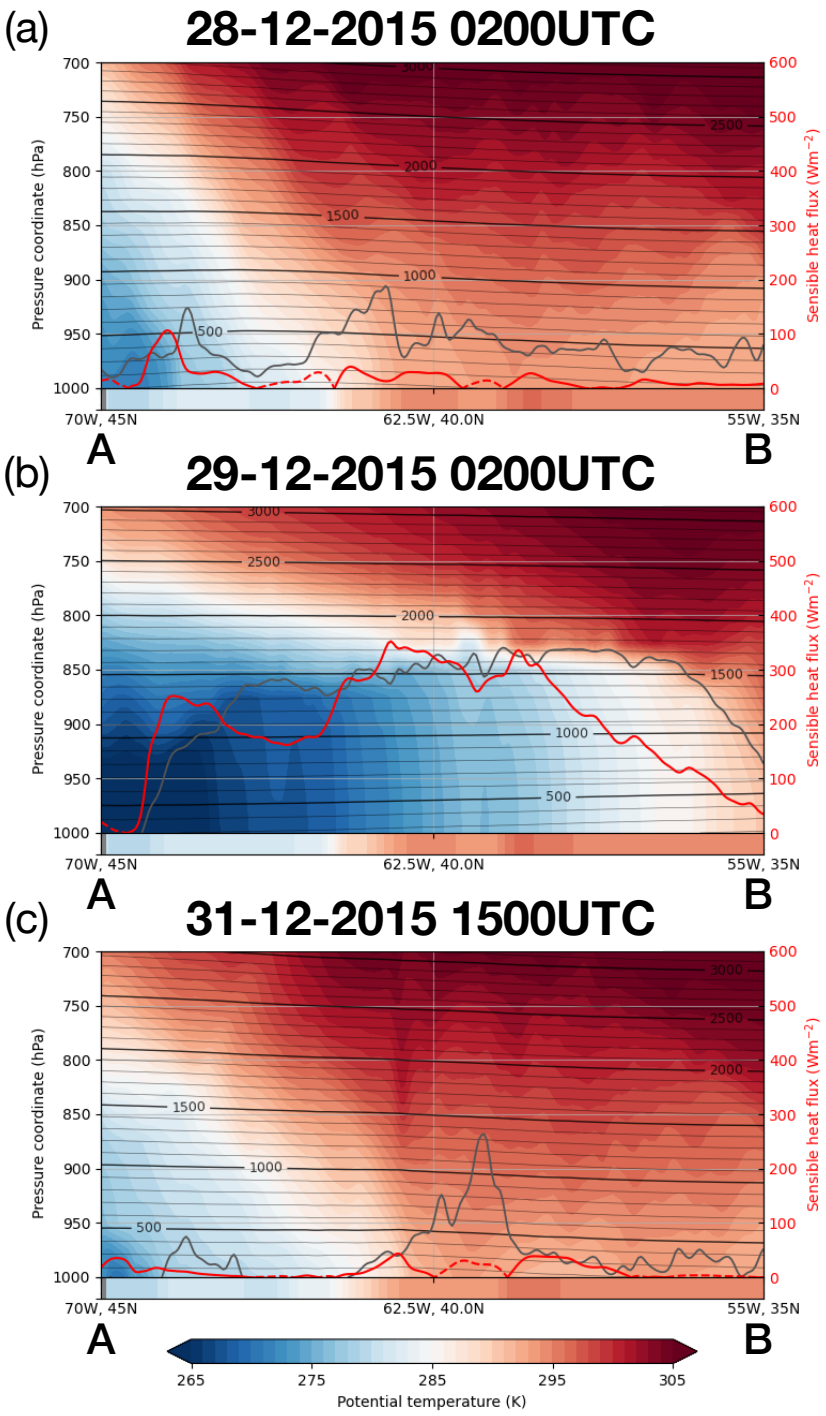

Figure 4.13: As in Fig. 4.7 for Case Study N.3 (Dec 2015/Jan 2016). Time coordinates of panels at the top (a), middle (b) and bottom (c) correspond, respectively, to the left dotted black line, central green solid line and right dotted black line in Fig. 4.11.

flow's vertical structure in Fig. 4.13 is particularly consistent with our model of a well-mixed boundary layer thermal structure driving the coupling of the surface to the 850hPa level. In fact, away from the peak in covariance, a shallow boundary layer occupies a large fraction of the cross section and is well below the 850hPa level, which is characterised by higher stratification and a weaker correlation with low surface heat flux. Fig. 4.13a,c highlight the impact of the stably stratified layer on the surface–troposphere thermal interaction, which is visibly damped. On the other hand, at the time of the peak in covariance (Fig. 4.13b) the advection of colder and denser air over the ocean leads to enhanced surface heat flux and a deeper boundary layer, which reaches very close to the 850hPa level, thus leading to the high level of correlation that results in the peak.

This case study is an eminent example of how the thermal structure of the boundary layer can influence the thermal coupling between the surface and the lower troposphere, as the temperature profiles in the cross sections shown in Fig. 4.13 have a distinct vertical structure across the top of the boundary layer.

4.3.4 Case Study N.4

The fourth and final case study that we are going to consider is centred upon a cold air outbreak induced by the shift and anticlockwise tilt of the eddy-driven jet, which pushes cold continental air over the Gulf Stream (see Fig. 4.2, lower right panel) leading to an FT index peak of about -300 Wm^{-2} K occurring on 24-11-2018 at 9:00 UTC. Figure 4.5 shows the time evolution of the index and its components. Unlike the previous case studies, we can see that the FT index remains close to peak values for about 24 hours as the cold air outbreak persists over the SST front. The FT index subsequently reaches a local minimum two days after the peak, before increasing again due to a second event of jet-induced cold air advection, which is not included in the present case study. Both the spatial standard deviations and correlation between F' and T' can be seen to drive the FT index as they increase concomitantly in approaching the index peak and, similarly, decrease slowly in the wake of the peak.

The conditions before the peak, on 22-11-2015 at 21:00 UTC, are illustrated in Fig. 4.15a,d,g. Warm air masses are stationed over the colder side of the SST front, however, that does not seem to induce a significant air–sea thermal interaction. This is also reflected in the average depth of

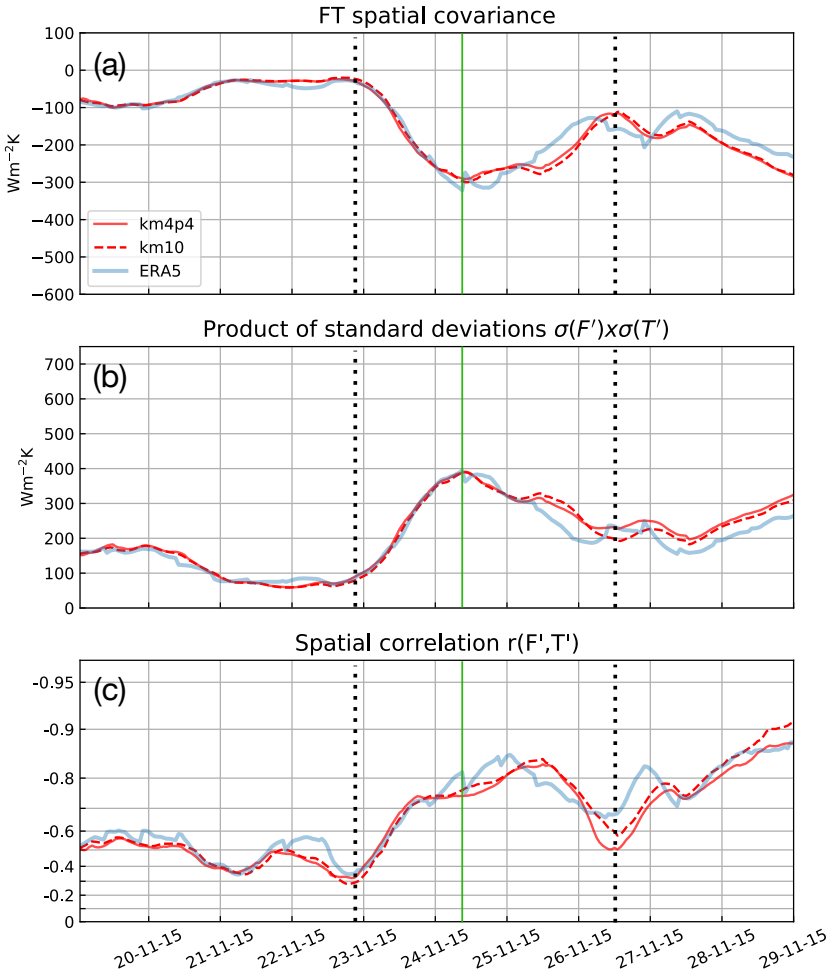

Figure 4.14: As in Fig. 4.5 for Case Study N.4 (Nov 2015). Solid green vertical lines denote the time of the FT index peak as derived from ERA5, dotted black lines indicate times before and after the peak that are inspected in Figs. 4.15, 4.16.

the boundary layer, which lies below the 850hPa almost everywhere in the spatial domain considered. In the following 36 hours, the jet tilts and cold continental air is advected over the ocean and starts interacting with it, as shown in Fig. 4.15b,e. The boundary layer deepens where the presence of the cold air mass induces enhanced surface heat fluxes, although over a limited spatial extent compared to previous cases (Fig. 4.15h), which reflects into the relatively low value of the FT index peak. On 26-11-2015 at 12:00 UTC the FT index is at a local minimum, which is associated with a more zonally-aligned flow over the spatial domain, though the air–sea temperature contrast and the associated surface heat exchange does not vanish, which explains the relatively high value of the index even at the minimum.

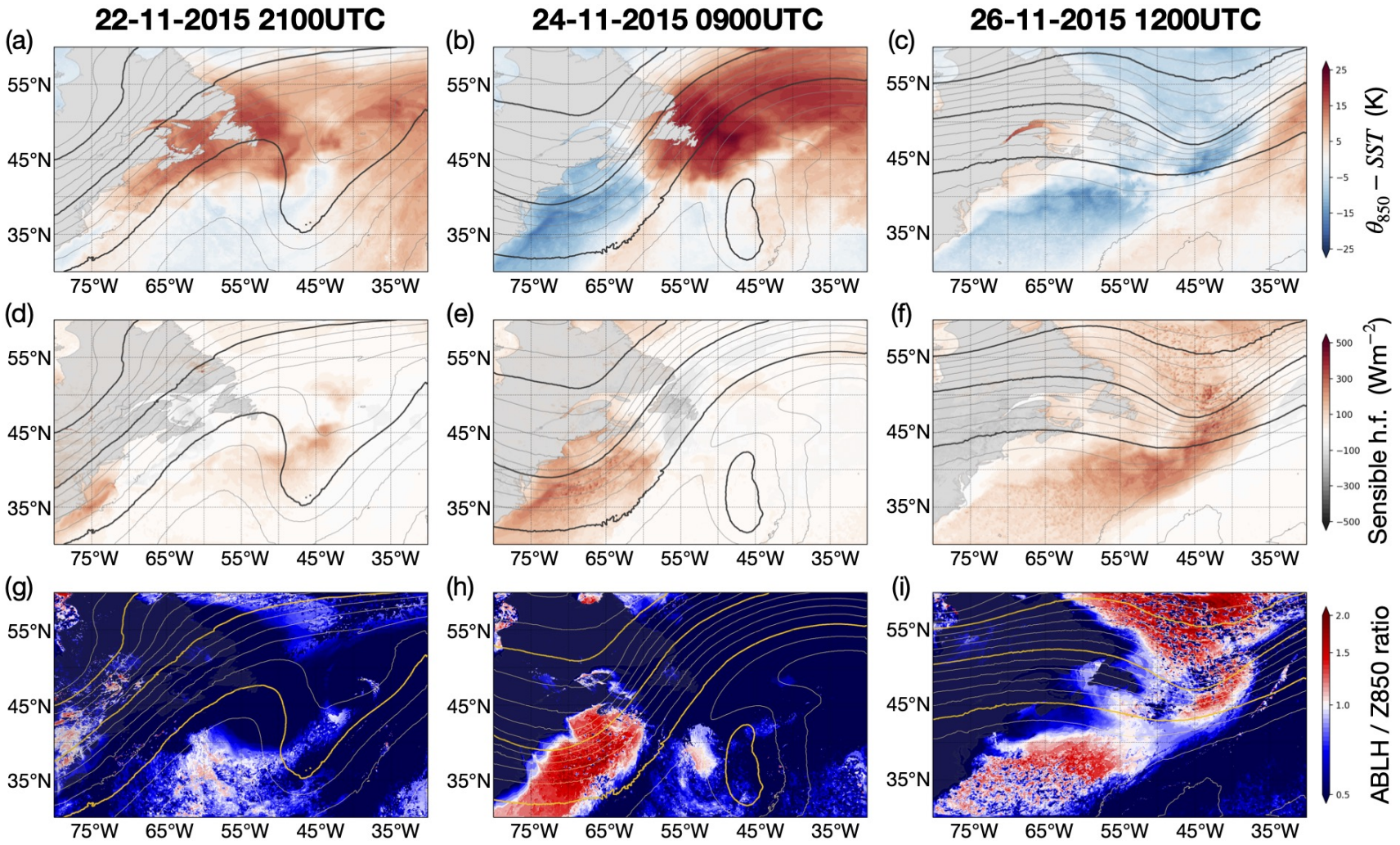

Figure 4.15: As in Fig. 4.6 for Case Study N.4 (Nov 2015). Panels on the left (a,d,g), centre (b,e,h) and right (c,f,i) correspond, respectively, to the left dotted black line, central green solid line and right dotted black line in Fig. 4.14.

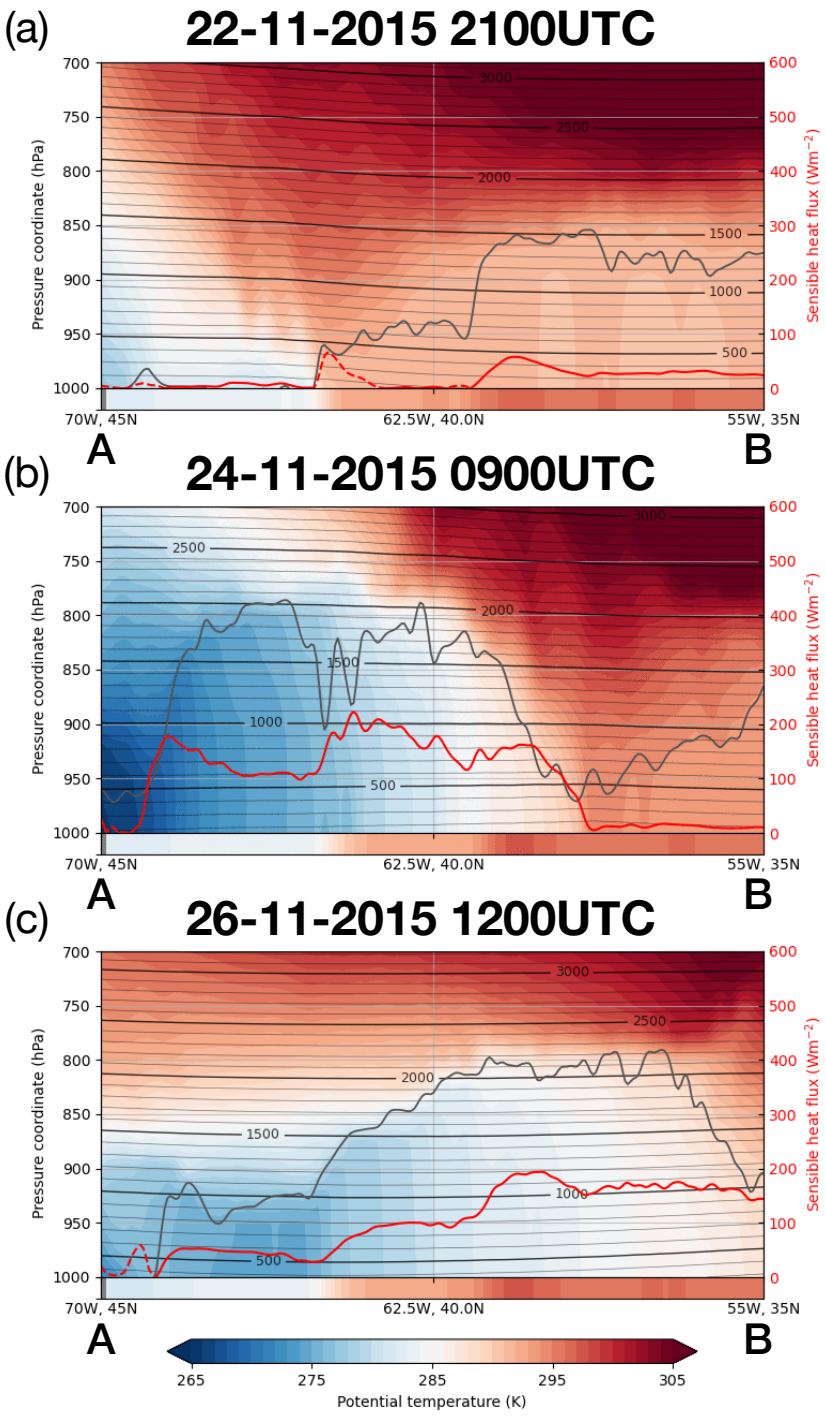

Figure 4.16: As in Fig. 4.7 for Case Study N.4 (Nov 2015). Time coordinates of panels at the top (a), middle (b) and bottom (c) correspond, respectively, to the left dotted black line, central green solid line and right dotted black line in Fig. 4.14.

The impact of the cold air outbreak on the intensity of the surface–troposphere thermal coupling can be easily traced back in the vertical structure of the lower troposphere, shown in Fig. 4.16. There we can see that, before the peak, the weak interaction of warm air with the underlying ocean results in low surface heat fluxes and a shallow boundary layer (Fig. 4.16a), while the advection of cold air corresponds with a visible deepening of the boundary layer (Fig. 4.16b), which induces the stronger thermal coupling of the surface to the 850hPa level that leads to a higher level of correlation. The FT index remains relatively strong also at the time of the minimum on 26-11-2015 as the temperature contrast between the ocean surface and the lower troposphere is still large enough to sustain sensible heat exchange. Surface heat fluxes are strong enough to keep the top of the boundary layer close to the 850hPa level (Fig. 4.16c), which explains the high level of correlation between F' and T' that is retained in the days following the peak.

4.4 The effect of model resolution

The simulations of the four case studies involve a double nesting of high resolution LAMs onto each other in the transition from the lower-resolution global driving model to the final very-high resolution LAM ($\approx$ 4.4km) which we base our analyses upon. As we outline in Appendix B, we first nest a LAM with a horizontal resolution ($\approx$ 10km) closer to that of the global driving model and then consider a smaller, higher-resolution LAM that we nest onto the first LAM. In the process of generating the 4.4km-resolution output, we are also necessarily performing a 10km-resolution simulation using the first nested LAM. Therefore, one can easily compare the results we obtain from the two different resolution runs of the same event and assess the observed differences in the representation of the $F' - T'$ spatial covariance.

As we can see from Figs. 4.5, 4.8, 4.11, 4.14, on average, the higher resolution runs result in a slightly stronger FT index, which can be ascribed to the larger variances associated with higher-resolution runs which are able to capture a larger fraction of the total spatial variability in the region. On the other hand, the impact of resolution on correlation appears to be in the opposite direction, as correlation is seen to be higher in the 10km runs compared to the 4.4km runs. It is possible that the additional variance deriving from finer-scale physical processes (e.g. localised convection and boundary layer instabilities) is not, on average, well correlated with the synoptic evolution of the system, which then results in a lower correlation between surface heat flux and lower-tropospheric temperature.

In Fig. 4.17, we present a preliminary quantitative analysis of the impact of resolution on the representation of the FT index. In particular, we compute the correlation between the time series of the FT index as obtained from the use of reanalysis data (ERA5) and the time series of the FT indices deriving from the higher-resolution simulations. We then plot the correlation values against the variance associated with the index time series across the four case studies, normalised to the variance of the reanalysis FT index. We notice that higher-resolution runs (shown in red) are visibly characterised by a higher degree of variance. While correlation values appear to decrease with increasing resolution, this reduction does not result in lower covariance, as the increase in variance is predominant. The November 2015 case study (plus symbols in Fig. 4.17) is perhaps an exception to this *rule*, although we should notice that in this particular case the differences across

the two different-resolution simulations is minimal, while it is still true that they are both associated with stronger covariance than the lower-resolution reanalysis.

Our study of the impact of changing resolution on the representation of the heat-flux–temperature covariance is perhaps limited in the number of diagnostics taken into account and in the amount of data that was available for analysis. However, the preliminary results seem to indicate that higher resolution results in enhanced heat flux and temperature variances, which leads to a stronger spatial covariance despite a decrease in correlation that is associated with the additional uncorrelated variance.

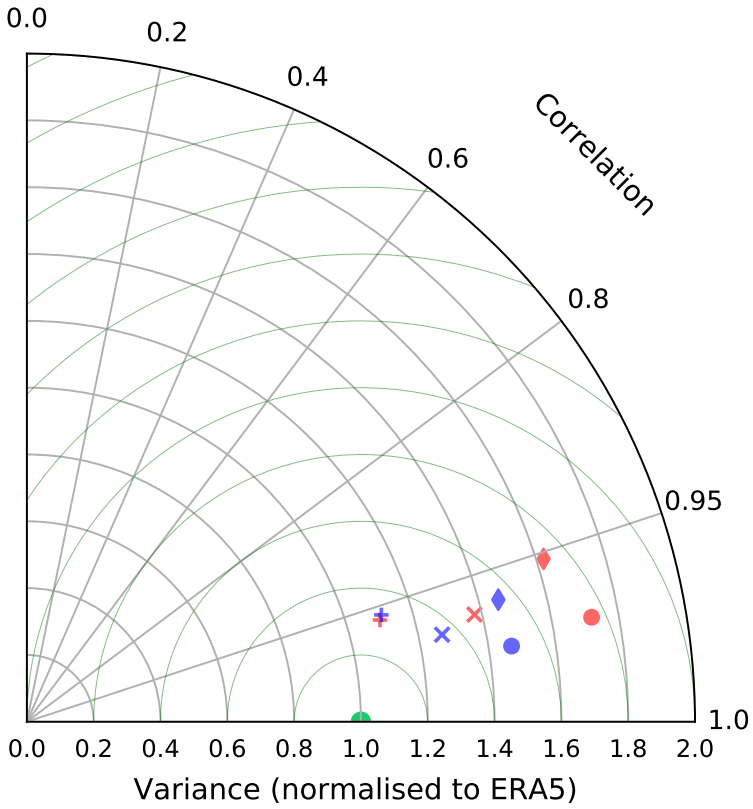

Figure 4.17: Taylor diagram for the correlation and variances of the FT indices deriving from the different resolution simulations of the four case studies. Each case study is represented by a different symbol (circles, diamonds, crosses and pluses for cases 1 to 4 respectively), with blue and red corresponding to lower and higher resolution runs, respectively. Variances for each case study are normalised to the variance associated with the FT index resulting from ERA5 (green circle).

4.5 Effects of model air–sea coupling

The level of spatial resolution in the ocean component of the model can have a significant impact on the atmospheric response to oceanic forcing, as oceanic mesoscale eddies become *visible* to the atmospheric component. In Chapter 2, we argued that the higher level of spatial variability over the Gulf Stream extension explains the observed lead in time of the increase of surface heat flux variance on temperature variance, as the atmosphere reacts to the SST field below.

Much effort has been put into atmosphere–ocean coupling in numerical models, as it would improve the representation of air–sea interactions that can be crucial for an accurate description of the evolution of the atmospheric circulation. However, increasing the spatial resolution of weather or climate coupled models can be computationally expensive. In fact, high-resolution coupled models usually have a limited spatial extent, with boundary conditions retrieved from lower-resolution global models. Therefore, it is useful to understand under what circumstances air–sea coupling is most beneficial for the correct representation of *real-world* phenomena.

The variability in time of the ocean surface properties may be expected to have an influence on the evolution of the heat-flux–temperature spatial covariance. However, the coupling in numerical models between the atmosphere and the ocean does not necessarily give a substantial contribution to the representation of the thermal coupling between the surface and the lower troposphere. In fact, the time scales associated with ocean dynamics are considerably longer than those associated with synoptic development (up to 10 days).Therefore, on synoptic timescales, we could expect the atmosphere to evolve as if the ocean surface were fixed in time, which would imply that minimal changes in the SST field do not substantially affect the atmospheric circulation.

Barsugli and Battisti (1998) explored the effects of air–sea thermal coupling on mid-latitude variability by examining a simple stochastically forced, one-dimensional, linear, coupled energy balance model, where they only consider an atmospheric and an oceanic component. They compared the power spectra associated with ocean temperatures and atmospheric temperatures (i.e., the square of the norm of the Fourier-transformed temperature, $P = |\mathcal{F}(T)|^2$) for an uncoupled configuration to those for a coupled configuration of the model and showed that air–sea model coupling in the midlatitudes enhances their variance and decrease energy flux between the

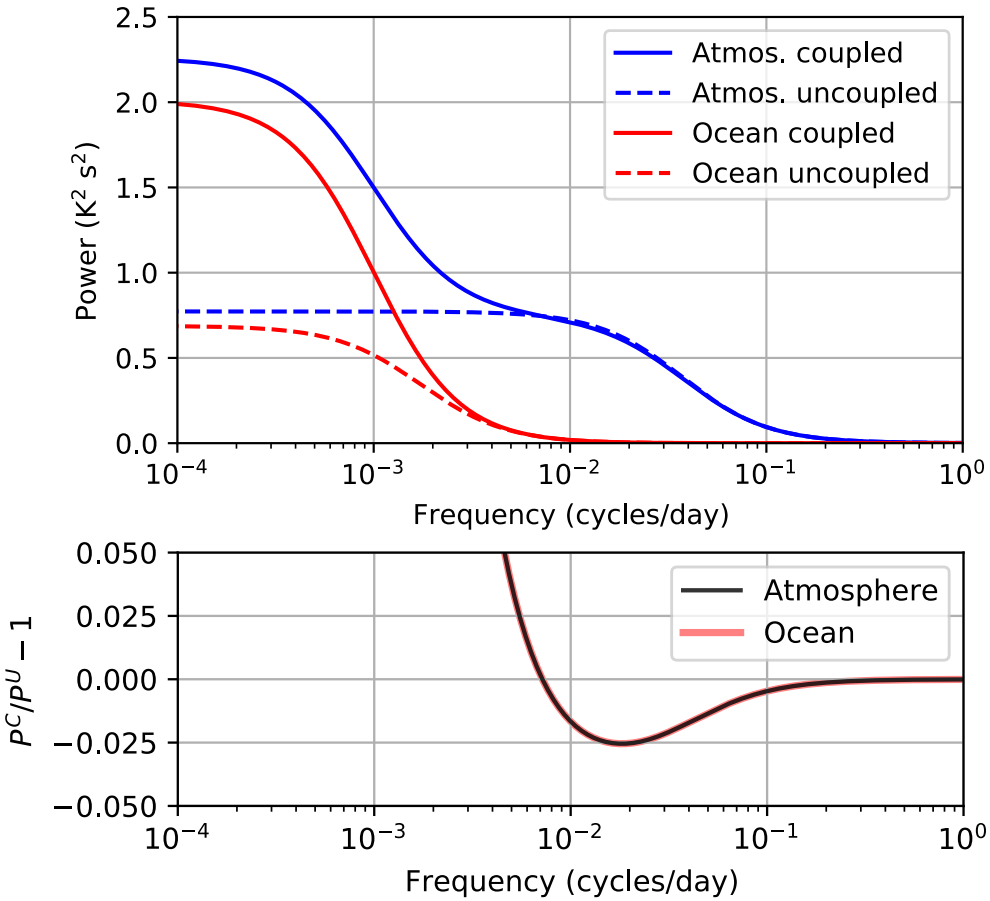

Figure 4.18: (a) Power spectra of atmosphere and ocean temperature for the coupled and uncoupled configurations of the model by Barsugli and Battisti (1998), with standard parameters taken from their Table 1. (b) Ratio of coupled to uncoupled power spectra of atmosphere and ocean temperature, from which we subtract 1.

two components, as illustrated in Fig. 4.18a.

The study by Barsugli and Battisti (1998) is focused on low-frequency variance and links the persistence of storm tracks to active air–sea coupling. The picture is less clear for higher frequencies. Although their results suggest that there is less variability at higher frequencies for coupled with respect to uncoupled configurations of the model, the difference is much more limited than that observed at lower frequencies, as we can see from Fig. 4.18b where we take a closer look at the high-frequency end of the power spectra shown in Fig. 4.18a (and Figure 4 of Barsugli and Battisti, 1998).

The regional coupled research system, developed and evaluated un-

der the UK Environmental Prediction (UKEP) collaboration, incorporates models of the atmosphere (i.e. MetUM), land surface with river routing, shelf-sea ocean and ocean surface waves, coupled together with 10 km horizontal resolution and a 10-minute coupling frequency between the different components. In this framework, it is possible to run very high-resolution regional simulations of the atmosphere–ocean system using different configurations for the coupling. In particular, in order to assess the improvements that coupling brings to the representation of the system, it is insightful to compare model output from an uncoupled atmosphere configuration to configurations with an increasing level of coupling, namely atmosphere–ocean and atmosphere–ocean–waves coupling. Our analyses are based on output from the fourth version of the regional coupling model, termed as UKC4. It is an incremental update of its previous version, UKC3, which is extensively described in Lewis et al. (2019).

Following from the implications on higher frequencies of the study by Barsugli and Battisti (1998), we would not expect the degree of coupling between the different components of the system (i.e. atmosphere, ocean and waves) to have a tangible impact on the representation of the spatial covariance between surface heat flux and temperature. In fact, further indications that this was the case derived from our examination of Eq. 3.6, as we observed that synoptic-scale SST time variability gives an almost imperceptible contribution to the total $F' - T'$ spatial covariance. This allowed us to simplify Eq. 3.6 into Eq. 3.7 by neglecting terms containing SST variance, implying that the temporal evolution of the ocean's surface temperature field is irrelevant to the atmospheric thermodynamics on synoptic timescales.

We now provide an example of the effects of model coupling on the representation of $F'-T'$ covariance. We compare time series of the FT index computed on model output from the UKC4 model with an increasing level of coupling between the different model components. Specifically, we consider four different configurations of the UKC4 model,

- uncoupled atmosphere at low spatial resolution,
- uncoupled atmosphere at high spatial resolution,
- coupled atmosphere–ocean system at high spatial resolution,
- fully coupled atmosphere–ocean–wave system at high spatial resolution.

The UKC4 is defined over a spatial domain centred upon the British Isles, corresponding to the domain used for the UK variable-resolution (UKV) atmosphere model (Bush et al., 2020), currently in operational use at the Met Office.

We consider a UK summer heatwave event (data readily available for analysis as already under study at the Met Office), taking place between 21-07-2018 and 26-07-2018. The time anomalies in the computation of the index are defined as departures from the 5-day time mean rather than 10-day, due to the more limited extend of UKC4 runs. Although the resulting index may be weaker than the one deriving from our standard definition, the meaning of the index is unchanged.

The resulting time series are shown in Fig. 4.19 together with the FT index computed on reanalysis data (i.e. ERA5) for a comparison with the *real* state of the atmosphere. We notice that the differences across the different configurations are small throughout the time period considered, with the most evident spread occurring at local minima and maxima in the FT index, which is consistent with the idea of the marginal impact that model coupling has on the FT index.

We can get a broader and clearer picture of the effects of coupling on the representation of heat-flux–temperature covariance if we examine a larger number of different case studies, involving, in particular, stronger air–sea interactions and located on regions where the ocean plays more a primary role in affecting the atmospheric circulation. To that extent, the implementation of the regional coupling used in UKC4 over the Gulf Stream region, which we considered[1] for our uncoupled LAM simulations, would allow for a more proper assessment of the role played by model coupling.

4.6 Summary and conclusion

The interactions between the atmosphere and the ocean take place over a broad range of time and length scales and in Chapter 2 we highlighted the damping effect that these interactions can have on synoptic development in the atmosphere. In particular, the response of the atmospheric circulation to the spatially variable temperature field of the ocean surface is shown to lead to the observed increase of correlation with variances in the build-up to strong heat-flux–temperature spatial covariance, which is associated on

[1] not carried forward due to lack of time

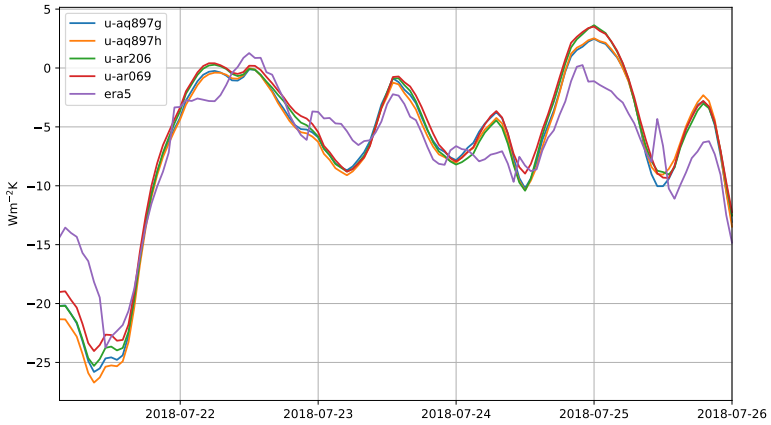

Figure 4.19: Time series of the FT index defined over the UKV spatial domain for the period 21-07-2018 to 26-07-2018. The labels correspond to the model suite identification tag for each of the different configurations considered in running UKC4: atmosphere only at low (u-aq897g, blue) and high (u-aq897h, orange) resolution; atmosphere–ocean coupled at high resolution (u-ar206, green); atmosphere–ocean–wave at high resolution (u-ar069, red). The FT index calculated using ERA5 data is plotted in purple.

average with a reduction of the mean baroclinicity of the flow. In Chapter 3 we proposed a qualitative model for the atmospheric boundary layer that links the joint increase of correlation and variances to the influence exerted by boundary layer dynamics and thermodynamics on the coupling between the surface and the lower troposphere. As surface heat fluxes arise in response to stark air–sea thermal contrasts over the Gulf Stream Extension region, turbulent mixing and enhanced convection result in a deeper extent of the mixed layer, which typically extends over a large fraction of the entire boundary layer. Within the mixed layer, temperatures follow an almost adiabatic vertical profile and, as a consequence, the temperature variance at the surface strongly correlates with the variance at the top of the boundary layer, eventually resulting in enhanced thermal coupling of the surface to the lower layers of the free troposphere, which is reflected in the observed statistical coupling.

In this chapter, we examine a series of individual events characterised by a peak in the FT spatial covariance (or FT index, see Chapter 2) to corroborate the climatological overview that was presented in Chapter 3. The case studies all coincide with the advection of cold air masses over the

stark SST gradients in the western North Atlantic. In half of the cases, the advection of the cold air mass is directly associated with the cold sector of an extra-tropical weather system, while the other half involve a cold air outbreak primarily associated with the meandering of the eddy-driven jet than with a storm's cold sector. The evolution of each case study is unique and deviates at times from the climatological picture that we obtained in Chapter 2 (which was used to formulate the model in Chapter 3), as the link between correlation and variances is not always evident. Nonetheless, in all of the case studies we are able to identify the dynamical mechanisms that explain the observed correlation–variances relationship, specifically the advection of cold air masses over the ocean surface and the enhanced convection and turbulent mixing that simultaneously lead to stronger heat flux and temperature variance and correlation.

In light of the crucial role of boundary layer dynamics and thermodynamics in explaining the relationship between heat-flux–temperature correlation and variances, reanalysis data are potentially not finely resolved enough to capture the full picture behind the influence of the boundary layer on the lower troposphere. In order to validate our analyses of reanalysis data, we therefore performed numerical simulations of the selected case studies using the Met Office Unified Model in a Limited Area Model configuration, which allowed us to reproduce the events we first observed in the ERA5 reanalysis dataset with a much higher horizontal resolution of up to 4.4 km and a vertical resolution of 25hPa up to 700hPa (against 50hPa in ERA5).

Despite the different synoptic situations that each case study represents, the analysis of the thermodynamic structure of the lower troposphere confirmed the climatological picture that we gained in Chapter 3. Specifically, the inspection of cross sections during different stages of the evolution of the FT covariance evidenced the role played by the boundary layer in strengthening the thermal coupling of the surface to the lower layers of the free troposphere, as the boundary layer is seen to be eminently characterised by almost vertical isentropic surfaces, while above the boundary layer the flow is highly stratified and virtually uncoupled with surface variability.

Finally, we briefly looked at the effect of model resolution and model air–sea coupling on the representation of the FT covariance. Based on the analysis of the four case studies considered in this chapter, higher-resolution numerical simulations feature stronger surface heat flux and temperature

spatial variance and the additional variance appears to be partly uncorrelated, as the increase in covariance is somewhat damped by an overall reduction in spatial correlation. On the other hand, from a preliminary analysis of a single case study, the numerical coupling of the atmosphere to the ocean and wave model components does not seem to play a significant role in the representation of the FT covariance, as the longer timescales of the ocean variability with respect to the atmospheric variability means that, on synoptic timescales, the atmosphere sees the ocean as essentially fixed in time and thus any changes in the SST field does not affect the surface–troposphere coupling within the lifespan of a single weather system.

Chapter 5

The life cycle of meridional heat flux peaks

The work presented in this chapter is published in Marcheggiani et al. (2022). Additional material (not included in the published article) is provided in Section 5.6.

Abstract

Covariance between meridional wind and air temperature in the lower troposphere quantifies the poleward flux of dry static energy in the atmosphere; in the mid-latitudes, this is primarily realised by baroclinic weather systems. It is shown that strong covariance between temperature and meridional wind results from both enhanced correlation and enhanced variance, and that the two evolve according to a distinct temporal structure akin to a life-cycle. Starting from a state of low correlation and variance, there is first a gradual build up to modal growth at constant, high correlation, followed by a rapid decay at relatively low correlation values. This life-cycle evolution is observed most markedly over oceanic regions, and cannot be explained on purely statistical grounds. We find that local peaks of meridional heat flux are not exclusively linked to the action of individual weather systems and can affect the atmospheric circulation on larger length scales through wave propagation along waveguides.

5.1 Introduction

Meridional heat fluxes[1] in the mid-latitudes can be viewed as the climate system's response to the thermal imbalance originating from the differential radiative heating between the equator and the poles. Poleward of roughly 30° latitude, the atmosphere accounts for the bulk of this flux. In the seminal work by Lorenz (1955) on the energetics of the atmospheric circulation, the meridional flux (or transport) of heat is associated with a conversion term of zonal available potential energy to eddy available potential energy, which can be thought of as the main energy reservoir for mid-latitude weather systems to feed on. More recent estimates of the sign and magnitude of this conversion term (Peixoto and Oort, 1992) confirm this view, meaning that meridional heat fluxes play a central role in shaping storm track dynamics.

Early work by Swanson and Pierrehumbert (1997) first highlighted the importance played by sporadic, transient events of extreme heat flux activity in setting the climatological-mean heat transport. Specifically, Messori and Czaja (2013) later showed that, every season, only a few days of peak meridional heat transport associated both with baroclinic systems and planetary-scale motions (Messori and Czaja, 2014) can account for more than half of the net seasonal transport. Messori and Czaja (2015) further explored the mechanisms behind the occurrence of these local extreme events, which, in storm track regions, are found to correspond primarily to synoptic structures akin to warm conveyor belts.

The intermittency observed in meridional heat transport extremes was linked to the energy available to weather systems to develop and evolve by Novak et al. (2017), who demonstrated the existence of a predator–prey relationship between meridional heat flux and baroclinicity (taken as a local measure of available potential energy) with the help of a nonlinear oscillator model for storm track variability (Ambaum and Novak, 2014).

More recently, Marcheggiani and Ambaum (2020)[2] explored the use of spatial covariance between surface heat-flux and temperature as a descriptor of local air–sea thermal interactions, which in the Lorenz energetics scheme can be associated with diabatic generation or reduction of transient available potential energy. It was found that these air–sea heat fluxes

[1] we hereafter refer to the eddy transport of dry static energy as meridional heat flux (footnote included in published article)

[2] see Chapter 2

also feature bursts of activity comparable to those in meridional heat fluxes and, in particular, it was observed that strong covariance resulted from a concomitant increase of both correlation and variances in heat flux and temperature. Analogously, we can interpret covariance between meridional wind speed (v) and air temperature (T) as a measure of local meridional heat transport, which in the Northern Hemisphere is climatologically positive, but can locally attain large negative values depending on season and spatio-temporal scale of the relevant disturbances (Lembo et al., 2019).

Mid-latitude storm tracks are typically identified by maxima in either eddy kinetic or available potential energy, which can be measured, respectively, by time variance in meridional wind, $\overline{v'^2}$ (with the bar indicating a time average), and temperature, $\overline{T'^2}$. Their co-variation in time, $\overline{v'T'}$, represents the conversion of background potential energy to transient available potential energy and, as such, is also associated with storm track intensity. These statistics provide a coherent large-scale picture, yet present differences in the exact location and extent of the storm track, suggesting that the latter's structure and life cycle cannot be fully explained by variance alone.

Schemm and Rivière (2019) highlighted the importance of the efficiency of transient eddies in extracting energy from the background baroclinicity. Their definition of eddy efficiency is based upon the dot product between the vector fields of eddy heat flux and background baroclinicity. In particular, an efficiency equal to one corresponds to a flow configuration whereby baroclinic conversion of eddy available potential energy into eddy kinetic energy is maximised. Schemm and Rivière (2019) surmised that the anomalous poleward tilt with height of eddies entering the North Pacific storm track through its northern seeding branch, which makes them less efficient, is partly responsible for the observed midwinter suppression of storm track activity (Nakamura, 1992). In fact, a lower level of correlation is associated with a non-optimal spatial configuration of synoptic eddies whose damping effect on the temperature spatial variance is not as strong as in the case of higher-correlated systems, which can instead have a larger impact on the local available potential energy.

In this chapter[3], we explore the idea that the correlation between v and T and their variances can be used to probe the dynamics of the meridional heat transport, and carry information about the evolution of mid-latitude

[3]'study' in published article

weather systems and storm tracks. The overarching aim of our study is to add detail to the meaning of variance and, by focusing on the evolution of correlation, to isolate the contribution to eddy kinetic energy that is associated with conversion from eddy available potential energy (and measured by covariance between meridional wind and temperature).

In this framework, we observe a concurrent increase of correlation and variances in the build-up to strong $v' - T'$ covariance (our notation for the spatial covariance between v' and T'; analogously, for $v - T$ time covariance), corresponding to sporadic heat flux events, and then dissect the distinct roles of variance and correlation in contributing to these events. The analysis indicates the importance of modal growth in the initial phase and uncorrelated decay in the final phase of an event, according to a well-defined life-cycle evolution.

The chapter[4] is structured as follows: Section 5.2 illustrates the relationship between time correlation and variances over the North Atlantic ocean; Section 5.3 introduces the particular space-time framework in which we study the evolution of the spatial covariance between v and T; in Section 5.4 we then describe the life cycle of $v' - T'$ covariance through the study of the phase space of its components and explore the link to the evolution of weather systems; finally, in Section 5.5 we provide a summary of our results and discuss its implications.

5.2 Properties of time correlation and variance

The climatological average of meridional heat transport was found to be shaped primarily by sporadic extreme events of limited longitudinal and temporal extent (Messori and Czaja, 2013, 2014; Messori et al., 2017). These events can be associated with a stronger spatial correlation between v and moist static energy time anomalies, which typically characterise baroclinic, or 'weather', synoptic systems.

Efficient meridional transport of the dry static energy component relies on a strong correlation between v and T. A positive correlation between v and T is usually expected to occur in the Northern Hemisphere, as northerly and southerly winds contribute to the advection of cold and warm air respectively. Therefore, the covariance between v and T can be interpreted

[4]'study' in published article

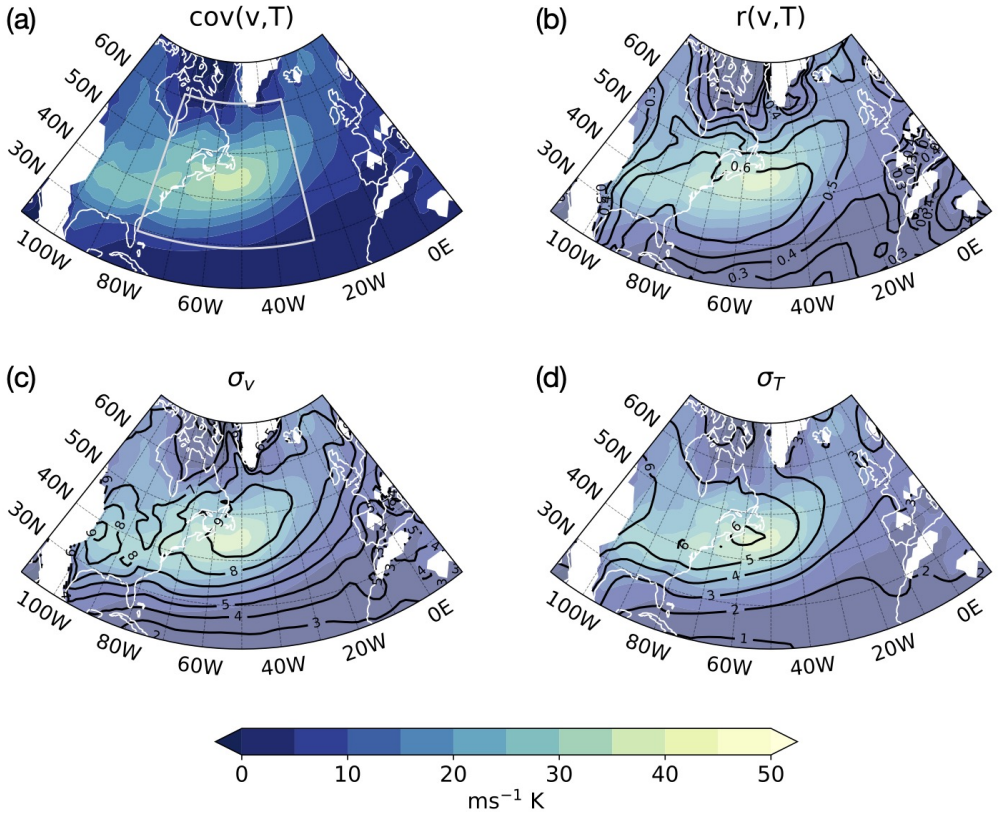

Figure 5.1: Decomposition of synoptic-scale $v-T$ time covariance (Eq. 5.2) into its components. Time covariance (colour shading), correlation and standard deviations of v and T (black contours) evaluated at the 850hPa level are represented in panels (a-d) respectively. Colour shading in all panels represents $v-T$ covariance (shading in panels b–d is faded to highlight solid contours). The area within the light grey contour in panel (a) corresponds with the spatial domain where $v'-T'$ spatial covariance is calculated (see text). Regions where orography is higher than 1000m (white shading) are not included in our analyses.

as a measure of the strength of meridional heat transport, as the larger and more positively correlated v and T anomalies become, the larger the poleward heat transport.

Covariance between v and T (either in time or in space) is defined as the product of correlation r between v and T and their standard deviations σ,

$$\mathrm{cov}(v,T) = r(v,T)\sigma_v\sigma_T. \tag{5.1}$$

A related statistic which we often refer to in this study is the variance of v and T, which is the square of standard deviation.

Our study focuses on the boreal winter season (December, January and

February) and is based upon data from the European Centre for Medium-Range Weather Forecast (ECMWF) Re-Analysis Interim data set (ERA-Interim, Dee et al., 2011), spanning winters from 1979 to 2019 with a time resolution of 6 hours and interpolated onto a $1.5°\times1.5°$ longitude-latitude spatial grid. Meridional wind speed v and air temperature T at the 850 hPa level are considered.

In the computation of time covariance, correlation and standard deviations, time anomalies are defined as departures from a running mean with a time window of 10 days, as opposed to simply removing the climatological mean. The time covariance between v and T, for example, is computed as

$$\mathrm{cov}(v,T) = \tfrac{1}{N}\sum_i (v_i - \hat{v}_i)(T_i - \hat{T}_i) = \tfrac{1}{N}\sum_i v_i' T_i', \tag{5.2}$$

where N is the total number of time steps i and $\hat{v}_i, \hat{T}_i$ indicate the 10-day running means of v and T evaluated at times i. This allows us to filter out any lower-frequency variability not associated with synoptic systems (Athanasiadis and Ambaum, 2009) without excessively manipulating the data, given the simplicity of the time filter implemented. Throughout this study, no further time filtering is applied to the original data.

Figure 5.1 shows the different components of synoptic-scale $v-T$ time covariance over the North Atlantic basin in winter, when storm activity is the most intense. Covariance is observed to peak along the major storm track region, which is consistent with the definition of storm tracks from a Eulerian point of view (Blackmon et al., 1977). What is more, we also notice that the spatial patterns for covariance and its components resemble each other, all reaching the highest values along the North Atlantic storm track, with the maximum in correlation slightly to the south of the maximum in covariance. A simple visual comparison between the spatial patterns of the components of covariance thus seems to suggest that stronger covariance is the result not only of larger variance but also of enhanced correlation.

This geographical correspondence is made even more evident when correlation r is plotted pointwise against the product of standard deviations $\sigma_v\sigma_T$, using values from Fig. 5.1. In order to account for the different weight each point contributes with in building the empirical density distribution, we perform a kernel density estimation (i.e. each point is assigned a Gaussian distribution function and then summed over all points; see Appendix A for technical details) and multiply each contribution by

the areal extent associated with it, which varies depending on its latitude. The resulting picture indicates the total area that contributes to each point in the correlation–variances space. The resulting distribution is shown in Fig. 5.2, where we make a distinction between land and sea points. We notice that increased correlation systematically matches increased variance over sea surfaces (Fig. 5.2b), while over land the relation is not as clear (Fig. 5.2a). The sea points further display a secondary data cluster where high variances correspond to a range of correlation values.

From a statistical point of view, correlation between two variables is not expected to necessarily vary jointly with the standard deviation (or, equally, variance σ^2) of either of the variables. In fact, a simple addition of uncorrelated variance would lead to a reduction in correlation. Furthermore, if we consider a simple diffusive model for the relationship between meridional wind and temperature anomalies (i.e. $T' \approx -\tau v' \partial \hat{T}/\partial y$, where τ is a decorrelation time and $\hat{T}$ is the 10-day running mean), we actually find that the resulting wind–temperature correlation increases significantly and independently of variances (see supplementary material at the end of this chapter[5]). It thus appears that the observed increase in correlation with variances is driven by some physical mechanism.

This hypothesis is also supported by the different behaviour over land and sea areas. The presence of a secondary data cluster in Fig. 5.2b, further suggests that the relationship between correlation and variance may be linked to the distinct dynamical characteristics of the atmosphere over different regions of the oceanic basins. Indeed, grid points contributing to the secondary data cluster of high variance values were found to be located predominantly in the polar regions of the North Atlantic basin, between Canada and Greenland (not shown).

Marcheggiani and Ambaum (2020) observed a similar behaviour in correlation and variances between surface heat flux and air temperature, suggesting that the simultaneous growth of correlation and variance could be a generic property of air–sea thermal interactions. Enhanced convection at the surface in cold sectors of extra-tropical weather systems leads to deeper atmospheric boundary layers, thus strengthening the coupling of the surface to the free troposphere. Nonetheless, it is not obvious how a related mechanism could be responsible for the increase in correlation between v and T and their variances.

[5]not included in published article

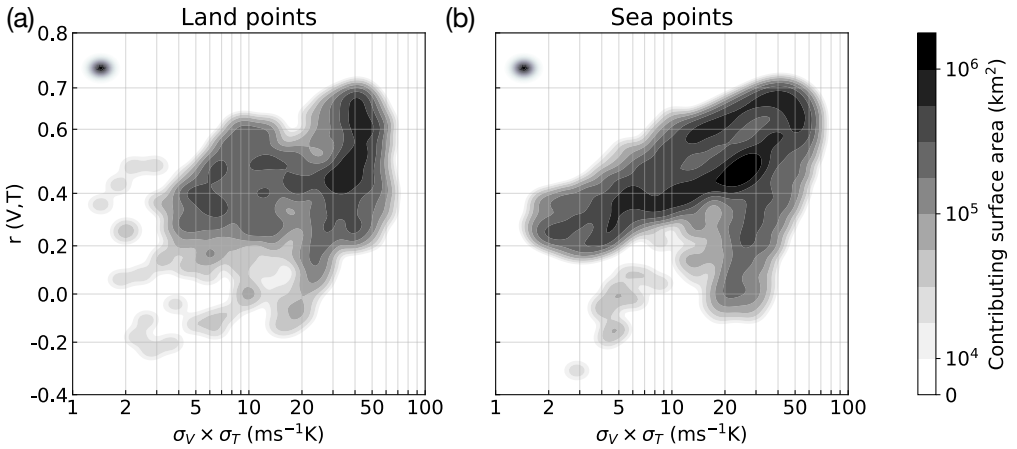

Figure 5.2: Kernel density estimate of the distribution of $v - T$ time correlation against the product of σ_v and σ_T for land-covered (a) and sea-covered (b) grid points. Shading represents surface area extent contributing to each point. The black-shaded dot in the left side of the plots indicates the shape in the correlation–standard deviations space of each contributing point from Fig. 5.1.

5.3 Phase space analysis of spatial correlation and variances

The climatological mean picture considered above hides details of the dynamical evolution of the covariance between v and T on synoptic time scales. Therefore, we next take into consideration spatial variability and its evolution in time, which enables us to investigate the temporal evolution of covariance. Following Marcheggiani and Ambaum (2020), we construct a hybrid space-time framework where we consider the spatial variances and correlation between time-anomalous fields of v and T over a fixed spatial domain. Time anomalies of v and T are again defined as deviations from a 10-day running mean and the spatial domain we selected broadly coincides with the Gulf Stream extension region ($30° - 60°$N, $30° - 79.5°$W) and is shown in Fig. 5.1a. In our analyses, only non-land grid points are taken into account in order to concentrate on the role the ocean plays in the dynamical evolution of correlation and variances, as Fig. 5.2 suggested that the increase of correlation with variance is observed predominantly over sea surfaces.

In this framework, the time-evolving covariance, correlation and variances are related to each other analogously to Eq. 5.1. Specifically, co-

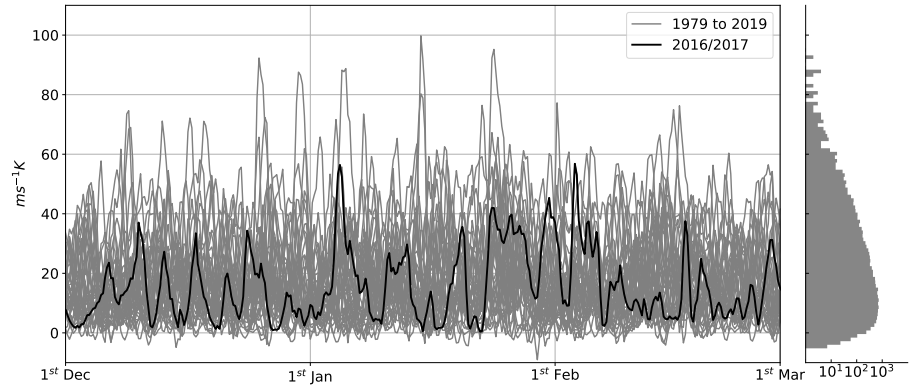

Figure 5.3: Time series of $v' - T'$ spatial covariance computed over the upstream region of the North Atlantic storm track (30–60° N, 30–79.5° W), spanning winters from 1979 to 2019 (grey solid lines), highlighting a sample season (2016/2017, solid black line). To the right, the corresponding empirical distribution of the values of covariance is shown (semi-log scale).

variance is computed as the spatial average of the pointwise product of space-time anomalies in v and T,

$$\begin{aligned} \mathrm{cov}(v', T') = \langle v'^* T'^* \rangle &= \langle (v' - \langle v' \rangle)(T' - \langle T' \rangle) \rangle \\ &= \langle v' T' \rangle - \langle v' \rangle \langle T' \rangle, \end{aligned} \tag{5.3}$$

where primes denote time anomalies, angle brackets indicate the spatial average operator and asterisks deviations from this spatial average. We thus obtain a time series for the spatial covariance between v and T time anomalies for all winters from 1979 to 2019, which is shown in Fig. 5.3. As expected, the temporal evolution of the $v' - T'$ covariance is characterised by intermittent bursts of activity (or peaks) that alternate with periods of weaker-amplitude variability, which is reflected in the corresponding empirical distribution shown on the right in Fig. 5.3 (mode below $10 ms^{-1}K$, extensive tail towards higher values).

To corroborate our interpretation of $v' - T'$ covariance as a measure of meridional heat flux, we construct a phase space where the coordinate axes correspond to $v' - T'$ covariance and local mean baroclinicity. Therein, we plot the time series for covariance against that for the mean lower-tropospheric baroclinicity, measured as the maximum Eady growth rate at 750hPa (Hoskins and Valdes, 1990) and spatially averaged across the region

marked in Figs. 5.7-5.7. We then apply a Gaussian kernel smoother in the phase space and obtain a phase portrait for their average co-evolution. The size of the Gaussian kernel can be adjusted to filter out small-scale features due to the intrinsically chaotic nature of the systems and evince the main circulation in the phase space.

Kernel filtering is employed exclusively in the phase space and no time filtering is applied to the raw data series used to build phase portraits, save the removal of a 10-day running mean in the computation of the time anomalies in v and T. There are several examples in recent literature (e.g. Novak et al., 2017; Marcheggiani and Ambaum, 2020; Yano et al., 2020) for the use of kernel averaging and phase space analysis to examine the dynamical evolution of chaotic non-linear weather and climate systems[6]. Novak et al. (2017) provides a thorough description of kernel averaging in a phase space that we employ in this study (in particular, see their Figure 4; see also Appendix A here).

The picture of the average circulation in the phase space that we obtain, shown in Fig. 5.4, is very similar to the phase portrait of heat-flux–baroclinicity presented by Novak et al. (2017) in their Fig. 5. It is also consistent with the predator–prey relationship highlighted in the same study, whereby meridional heat fluxes *feed* on mean background baroclinicity, which can only recover when heat fluxes are weak.

We thus find a clockwise mean circulation in phase space where in quiescent periods the baroclinicity builds up to exceed a critical value (about $0.5\,\mathrm{day}^{-1}$) after which the $v' - T'$ covariance shoots up and at the same time starts to erode the baroclinicity because of the attendant reduction in temperature gradient due to the downgradient heat fluxes. When the baroclinicity has reduced below criticality, the $v' - T'$ covariance starts to decay and the cycle starts again.

The $v' - T'$ covariance is seen to be positive most of the time, with a small fraction of events associated with negative correlation. This is only partly an artefact of kernel averaging, as the raw data also shows occasional negative correlations for short periods of time.

Similar to what was observed from the time-only perspective presented in Section 5.2, we find that for an increase of $v' - T'$ covariance, the spatial

[6]Similarly, an earlier study by Frame et al. (2013) also made use of a phase space of the two leading principal components for the North Atlantic eddy-driven jet in order to examine the evidence for its systematic flow-dependent predictability (footnote not included in published article).

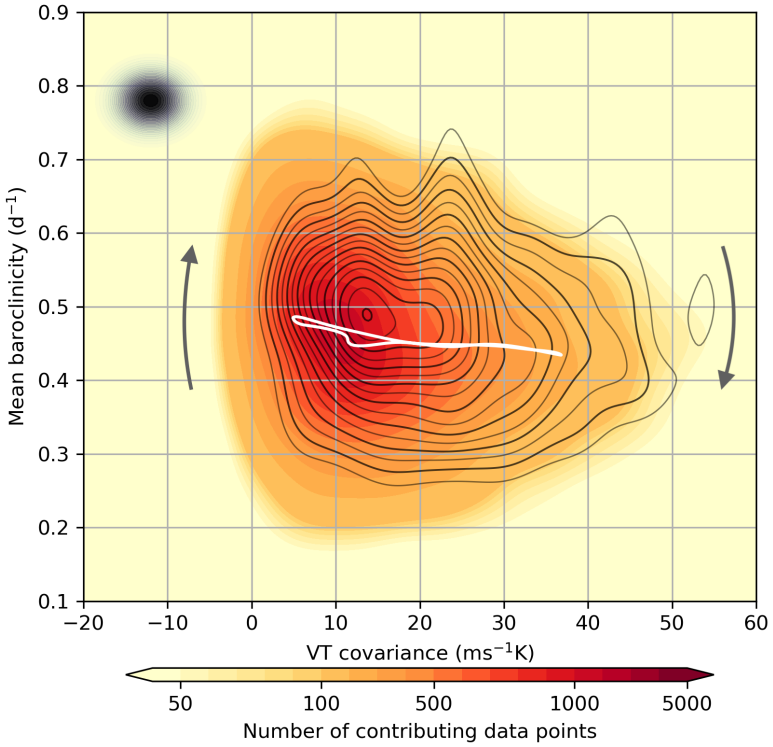

Figure 5.4: Kernel averaged circulation in the $v' - T'$ spatial covariance–baroclinicity phase space. Contours represent lines of constant streamfunction and the arrows the direction of the flow. The size of the averaging Gaussian filter is indicated by the black-shaded dot in the left side of the plot. The white line represents the projection onto this phase space of the kernel-averaged baroclinicity along the closed trajectory marked in Fig. 5.6 (see Section 5.4 for details).

correlation and variances are seen to increase at the same time. In Fig. 5.5, we plot spatial correlation against the product of standard deviations in v' and T'. Despite the large spread in the data distribution, Fig. 5.5 suggests that higher values of spatial correlation occur more frequently at higher variances, while lower variance is typically associated with weaker correlation. This provides further evidence of the existence of a physical process that ties the change in variance to the change in correlation.

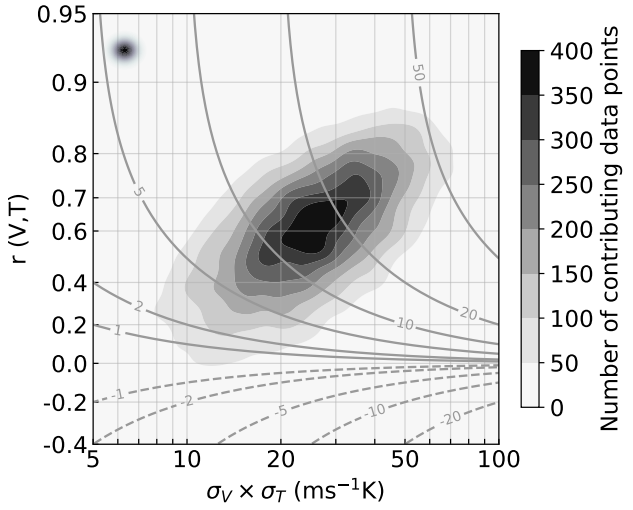

Figure 5.5: Kernel density estimate of the distribution of $v' - T'$ spatial correlation against the product of $\sigma_{v'}$ and $\sigma_{T'}$. Contours represent $v' - T'$ spatial covariance and shading the number of points contributing to the kernel average. The size of the averaging Gaussian filter is indicated by the black-shaded dot in the left side of the plot.

5.4 The life cycle of $v' - T'$ covariance

Further understanding of the dynamical relationship between correlation and variances can be achieved through the construction of a correlation–variances phase space, thus investigating the evolution of covariance in terms of its components.

The calculation of $v' - T'$ spatial covariance follows from Eq. 5.3 and consists essentially of the sum of the products of v and T departures from the area-mean values over all the grid-points within the chosen spatial domain. The sum is weighted according to the area represented by each grid point, which is proportional to the cosine of its latitude. We choose to represent the fields for meridional wind and temperature time anomalies in the form of vectors whose components correspond to every grid point in the longitude-latitude grid and we can thus write the spatial covariance between v' and T' at any time t as the weighted inner product between these two vectors,

$$\mathrm{cov}(v', T')\Big|_t = \sum_i^N v'_i \, T'_i \, \tilde{w}_i = \mathbf{v'} \cdot \mathbf{T'} = \|\mathbf{v'}\| \, \|\mathbf{T'}\| \cos\phi,$$

where N is the total number of grid-points making up the spatial domain considered, $\tilde{w}_i = w_i / \sum_i^N w_i$ are the normalised weights proportional to the

area each grid-point represents and ϕ is the angle between the vectors (characters in bold). The weighted inner product between two vectors is defined as the dot product of the two vectors after a pointwise multiplication with the weights vector $\mathbf{w} = (w_1, w_2, ...)$. The weighted inner product then induces a norm $\|\mathbf{v'}\| = \sqrt{\mathbf{v'} \cdot \mathbf{v'}}$ which we can interpret as the spatial standard deviation of v' ($\sigma_{v'}$) at time t and, analogously, $\|\mathbf{T'}\| = \sigma_{T'}$. The angle ϕ that vectors **v'** and **T'** form between each other is related to the spatial correlation between v' and T',

$$\mathrm{r}(v', T')\Big|_t = \frac{\mathbf{v'} \cdot \mathbf{T'}}{\|\mathbf{v'}\| \, \|\mathbf{T'}\|} = \cos\phi. \tag{5.4}$$

The vectors **v'** and **T'** share the same dimensionality (i.e. number of grid-points considered, in our case) which guarantees that ϕ is an angle.

This representation of covariance then suggests a way to plot the different components of covariance in a 2-dimensional space in polar coordinates, with the radial and azimuthal coordinates corresponding to $|\mathbf{v'}| \, |\mathbf{T'}|$ and $\phi = \cos^{-1}\mathrm{r}$ respectively. In this space, covariance increases linearly in the horizontal (x) direction, being the product of the radial coordinate and the cosine of the azimuthal coordinate. The space itself is isotropic with the x and y directions having the same physical dimension ($|\mathbf{v'}| \, |\mathbf{T'}|$). By the same token, the distance between two points in this space would be given by their Euclidean distance rather than the difference in their $v' - T'$ covariance.

Time series for $\sigma_{v'} \times \sigma_{T'}$ and $r(v', T')$ are plotted against each other and the resulting picture smoothed by taking a Gaussian kernel average to filter out small-scale noise. A streamfunction ψ of the resulting circulation can be defined such that:

$$u_r = \frac{1}{r}\frac{\partial\psi}{\partial\phi}, \quad u_\phi = -\frac{\partial\psi}{\partial r}, \tag{5.5}$$

where u_r, u_ϕ denote the radial and azimuthal phase speeds respectively. The visualisation of the stream function helps evince the correlation–variance dynamical co-evolution, as can be seen in Fig. 5.6, which is the polar-coordinate version of Fig. 5.5. There, contours of ψ are plotted along with the number of data points (in shading) contributing to the kernel average at each point in the phase space (refer to Section 5.6.2[7] for a discussion of the statistical significance of the kernel averaged circulation in Fig. 5.6).

Data is almost entirely distributed in the positive-correlation sector of

[7]Appendix B in the published article

the phase space and the few negative instances are partly an artefact of kernel averaging. Furthermore, the average circulation is in the anticlockwise direction, with increases in $v' - T'$ covariance occurring on average at high correlations (around 0.9), while decreases in covariance occur at lower correlation values (around 0.5). This suggests that a higher level of correlation is crucial to the build-up of variance, and covariance more in general.

To further our understanding of the mechanisms at play in the evolution of $v'-T'$ covariance, we explore the dynamics associated with the circulation in the phase space. To this effect, we identify a closed trajectory in the kernel-averaged circulation by selecting a stream function isoline, ensuring it crosses regions of high data density in order to retain robustness in the analysis' results. We take as reference starting point of the chosen trajectory, namely day 0, the minimum in $v' - T'$ covariance. It takes about five days (4.7d) for a complete revolution along this trajectory, which is outlined in Fig. 5.6, where each day is marked with a black dot. Along this trajectory, one may distinguish four separate stages in the evolution of covariance:

(i) covariance build up with increasing correlation at low variances (days 0–1);

(ii) increasing variance at high correlation (days 1–2);

(iii) peak covariance as variances keep increasing while correlation starts to decay (days 2–3);

(iv) covariance decay with both decreasing variances and correlation (days 3–0).

While demarcation points between different stages are somewhat subjective, the results of our analysis are not susceptible to minor changes in the above partition. We should point out that the time reference we take does not map trivially onto the evolution of a single system as it corresponds to the drift speed in the correlation–variances phase space. It takes on average five days for a complete cycle, however, individual stages might last longer or shorter in actual events.

At each point along the trajectory we calculate the kernel average of geopotential height at 1000hPa (Z1000) and 500hPa (Z500). The choice of Z1000 and Z500 fields is meant to help visualise the structure of the atmospheric flow at multiple levels while also bearing information about temperature advection occurring between the two levels, as temperature

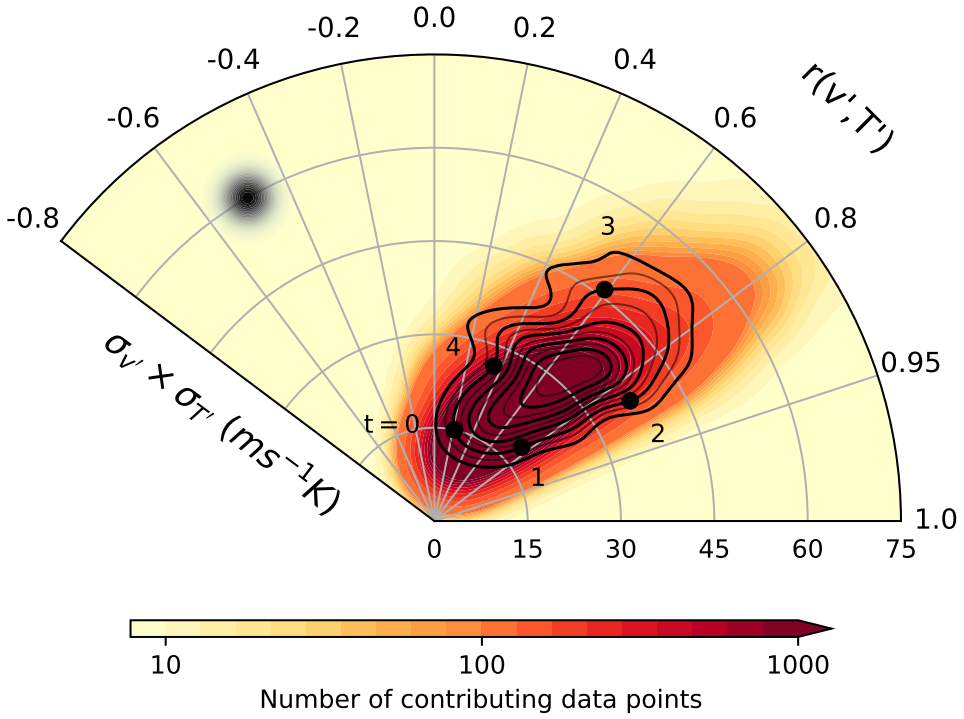

Figure 5.6: Kernel averaged circulation in the spatial variances–correlation phase space (based on the same data series as in Figure 5.5, using a polar coordinate system). The radial coordinate corresponds to the product of $\sigma_{v'}$ and $\sigma_{T'}$, the cosine of the azimuthal coordinate to $r(v', T')$ as per Eq.5.4. Contours represent lines of constant streamfunction, defined by Eq. 5.5. The flow in the phase space is in the anticlockwise direction. See text for labels along one of the contour lines. The size of the averaging Gaussian filter is indicated by the black-shaded dot in the left side of the plot.

advection between Z1000 and Z500 is proportional to the Jacobian of Z1000 and Z500.

The resulting kernel-averaged picture of the circulation in the phase space is shown in Figs. 5.7 (stages 1–2) and 5.8 (stages 3–4)[8]. Although the choice of a specific closed trajectory is somewhat arbitrary, our qualitative results are not sensitive to this choice and the use of different closed trajectories resembling the one in Fig. 5.6 leads to a similar evolution as that portrayed in Figs. 5.7,5.8 (not shown). Each composite in Figs. 5.7,5.8 represents the average of a large number of events, whose contribution is weighted according to the difference between their associated correlation and variances and those of the point where the kernel average is being com-

[8]Published article only includes panels for days 0, 1.5, 2.5 and 3.5; supplementary material at the end of this chapter include analogous composites over the entire Northern Hemisphere (together with an extra panel for day 1.0).

puted. Systems with similar correlation and variances do not necessarily coincide geographically but contribute equally to the average, so that specific, smaller scale features would typically be averaged out and the resulting picture highlights the typical large-scale structure of the flow at each stage in the evolution of a meridional heat flux peak. Therefore, although the composites are ineluctably affected by some degree of noise, it is nonetheless possible to relate the large-scale picture to the life-cycle viewpoint discussed above.

In the first stage of the life cycle, the flow is initially mostly aligned with the zonal direction within the spatial domain considered, while it veers to the north further downstream (Fig. 5.7a,b). We observe that the average vertical structure of systems feature a S-SW tilt (see centres of negative anomalies to the southeast of Greenland). The vertical tilt in geopotential is not conducive to poleward heat flux[9] even in the presence of a westward tilt as it also features a marked southward component. The largest, negative anomalies in geopotential height are located in the northeastern corner of the spatial domain and further downstream in the eastern North Atlantic, which points to the predominance of synoptic variability (associated with the amplitude of a propagating Rossby wave, as we discuss further below) downstream of the storm track during this stage. We also notice a weaker high-pressure anomaly in the southwestern sector of the domain, which will intensify as it propagates northeastward in the transition to the second stage.

In the transition from first to second stage, after correlation has reached larger values (above 0.5), variances slowly increase. The increase of variance at high correlation is indicative of baroclinic growth of synoptic eddies, as synoptic disturbances typically develop and evolve along the region of enhanced low-level baroclinicity that is co-located with the strong SST gradients associated with the Gulf Stream. Given the large spatial extent of the study region, the spatial distribution of the occurrence of synoptic systems is sporadic and the correct representation of their intensity may be hidden by the composition of a kernel-averaged picture. However, the distinctive baroclinic structure is captured in the region in the later part of the first life cycle stage (not shown) and emerges more evidently in the transition to the next stage, as the vertical tilt in geopotential becomes more aligned in

[9]This does not equal saying that baroclinic growth is necessarily hindered, as a tilt in the equatorward direction could still be conducive to growth if the shear vector points poleward (not included in published article).

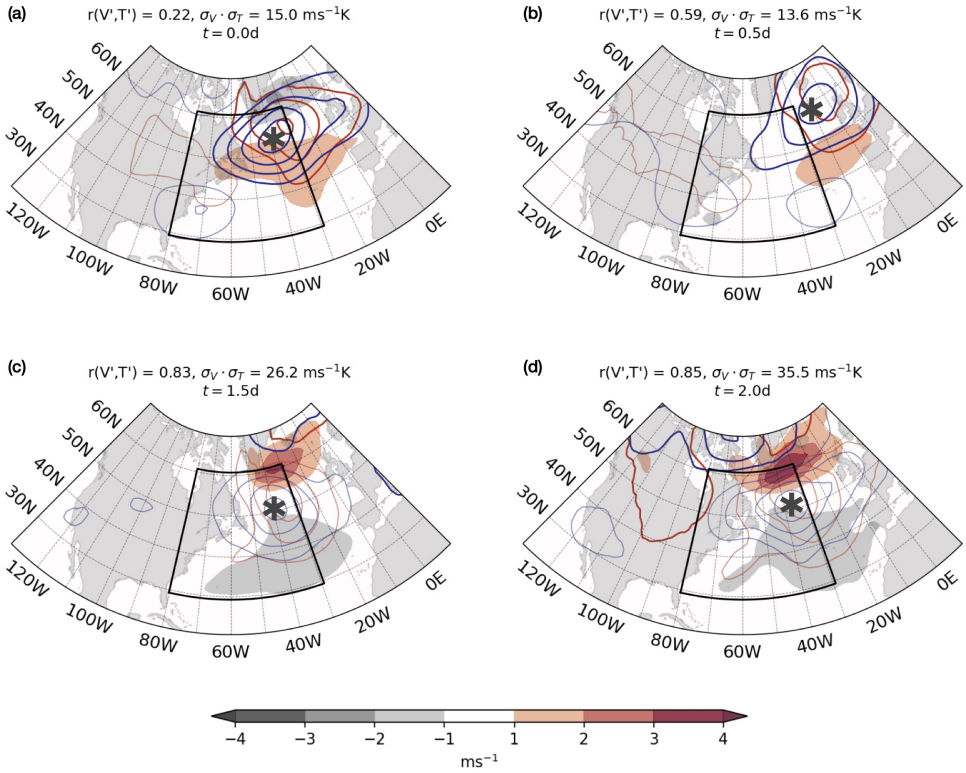

Figure 5.7: Kernel-averaged composites of Z1000, Z500 and zonal wind (vertically averaged between 950hPa and 750hPa) minus climatology for days 0 (a), 0.5 (b), 1.5 (c) and 2.0 (d). Contours for Z1000 (red) and Z500 (blue) are plotted every 1m, omitting 0m contours; negative contours are plotted in bold. Colour shading represents zonal wind anomalies. Stars indicate crests of a propagating Rossby wave (see text for details).

the East-West direction.

In the second life-cycle stage, the rise in the variances' magnitude becomes the predominant mechanism in driving the increase in $v' - T'$ covariance (Fig. 5.6, days 1–2). The low-pressure system that was dominant in the first stage leaves the spatial domain, where anomalous high pressure now dominates (Fig. 5.7c,d[10]), possibly having evolved from the weaker positive anomaly off the eastern coast of the North American continent seen in Fig. 5.7a.

The third stage corresponds with covariance reaching its peak value (43-44ms^{-1}K), while correlation starts decaying after $t = 2.0$d, having attained the highest values between $t = 1.5$–2.0d. Around $t = 2.5$d (Fig. 5.8a), the baroclinic structure of the flow is also evident, as the vertical tilt in geopotential at this stage is aligned mostly West to East. At the same time,

[10]Panel d not shown in published article.

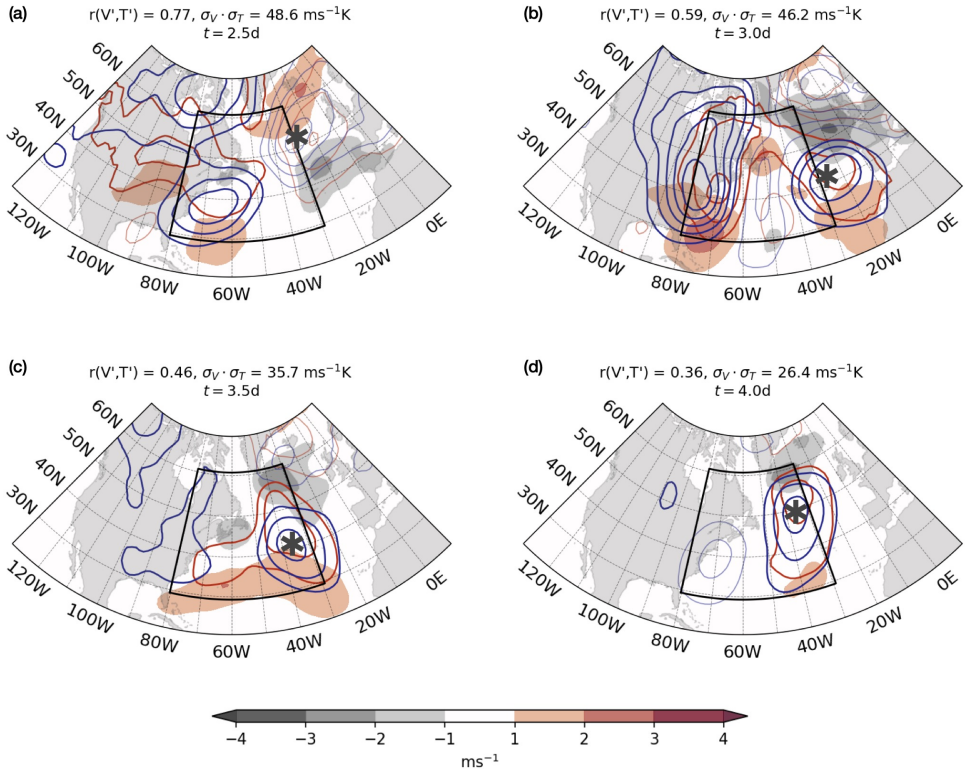

Figure 5.8: As in Fig. 5.7 for days 2.5 (a), 3.0 (b), 3.5 (c) and 4.0 (d).

the strongest temperature advection is seen to occur, which is consistent with observed peak in meridional heat transport as measured by the $v' - T'$ spatial covariance..

In the fourth and final stage, $v' - T'$ covariance decay is primarily associated with the variances decreasing at low correlation. The flow in this stage (Fig. 5.8b–d[11]) is characterised by the decay of the previously noted baroclinic system, as it transitions back to the onset state of minimum correlation and variances (Fig. 5.7a).

The development and subsequent evolution of geopotential anomalies across the four stages of the covariance life cycle can be understood in terms of Rossby wave propagation. Rossby wave propagation dominates in the mid-latitudes and our study suggests that peaks of meridional heat flux are most clearly linked to Rossby wave propagation than to Lagrangian propagation of individual weather systems, which was found to be dominant in the evolution of surface heat-flux–temperature covariance (Marcheggiani and Ambaum, 2020)[12]. In fact, it is difficult to identify and track the

[11]Panels b,d not shown in published article.

[12]See Chapter 2, where we saw that the evolution of surface heat-flux–temperature co-

evolution of specific features in the composites of the atmospheric flow at different points in the life cycle of $v'-T'$ covariance, while the transition from one stage to the other is reminiscent of stationary Rossby waves propagating along the North Atlantic waveguide[13] described in Hoskins and Ambrizzi (1993). In particular, we would not expect large scale Rossby waves to be averaged out across different stages in the phase-space evolution, because these large scale waves are quasi-stationary and make up the planetary wave structure.

An example of Rossby wave propagation can be seen in the transition from the third stage to the fourth (Fig. 5.8a–c[14]): the peak intensity of the Rossby wave packet is seen to propagate downstream due to the eastward group speed while the phase speed appears to be mostly stationary as the corresponding centres between panels do not move much in the longitudinal direction (compare centres of high and low geopotential anomalies between 25–35°W, indicated respectively by stars in panels a and c[15]). The change in sign of the anomalies with largest amplitudes is associated with group propagation rather than phase propagation as crests and troughs of higher wave numbers remain fixed in space and change sign depending on the propagation of the envelope of the wave packet.

Another example of this propagation mechanism can be found in the second stage of the life cycle, where the development of the large positive geopotential height anomaly in Fig. 5.7c can also be interpreted as the result of Rossby wave propagation of the low-amplitude positive anomaly taking shape in the south-western sector of the spatial domain in Fig. 5.7a. From examining composites at various intermediate stages (not shown) we can confirm that the evolution of the composites in the phase space is consistent with this Rossby wave propagation mechanism, rather than advection of a weather system: the individual centres do not move much (stars in panels a,b,c[16]) but the wave activity propagates downstream[17].

---

variance is typically associated with the advection of the cold sector of a weather system, which was easily identifiable both from composites for peak values in the FT index and from kernel composites along the standard-deviations' phase space (not shown).

[13]See Fig. 5.14 in the supplementary material for an overview of the kernel composites over the entire Northern Hemisphere.

[14]Panel b not shown in published article.

[15]Panels c and d of Fig. 7 in published article.

[16]Panel b not shown in published article

[17]The evolution of the life cycle emerging from the phase portrait maps onto time in a non-trivial way, as the time coordinate associated with the closed trajectory in Fig. 5.6 derives from the mean drift in the phase space and does not necessarily represent the typical duration of a peak; in light of this, the evolution of anomalies in the composites does

We also find that in the initial, growing stage the Rossby wave propagation is more along the SW–NE axis, while in the decaying phase the propagation is more along the W–E axis. This appears consistent with a general northward tilting of the waveguide during the heat flux events perhaps following the general northward tilting of the low-level jet stream (Franzke et al., 2011; Novak et al., 2015). Hoskins and Ambrizzi (1993) also show that especially over the North Atlantic region the Rossby wave propagation can be quite dispersed with distinct centres of action both in the NE direction and the SE direction.

The different configurations of the flow following the evolution of $v' - T'$ covariance are reminiscent of the three most persistent regimes of the North Atlantic eddy-driven jet, namely the southern, central and northern jet states as identified by the jet latitudinal position (Woollings et al., 2010). Each regime is associated with distinct stages in the evolution of the storm track and in the dominant type of Rossby wave breaking, mostly cyclonic and anticyclonic in the southern and northern regimes, respectively, while the central regime is influenced by both (Novak et al., 2015). In particular, Franzke et al. (2011) showed that the preferred transitions across the different regimes are from southern to central, from northern to southern and from central to northern, which is suggestive of an average poleward propagation of the eddy-driven jet in the cyclical evolution of the jet.

Novak et al. (2015) linked the transitions across the three jet regimes to the different stages in the life cycle of the North Atlantic storm track by drawing a parallel with the predator–prey cyclical relationship between heat fluxes and baroclinicity, as predicted by the non-linear model proposed in Ambaum and Novak (2014). Messori et al. (2017) in addition[18] linked this non-linear relationship to the temporal variability of the meridional heat transport.

We can draw an analogy between the evolution of the system in the correlation–variances phase space and that of the eddy-driven jet latitudinal variability by concentrating on the structure of the anomalous flow portrayed by the kernel composites in Figs. 5.7, 5.8.

- Initially (Fig. 5.7a), the picture that results from kernel averaging is comparable to that associated with the central regime of the jet's latitudinal position (see Fig.4 in Woollings et al., 2010), which gradually

not simply map onto baroclinic development, which actually involves phase propagation.

[18] 'in turn' in the published article

shifts northwards over the following day in the life cycle.

- As we enter the second stage of the life cycle, we can observe the transition from the central to the northern regime, as high pressure becomes predominant, the flow is deflected northwards and the maximum zonal wind moves northwards to around 60°N (Fig. 5.7c,d[19]).

- During the third stage, $v' - T'$ covariance and meridional temperature advection is largest (Fig. 5.8a,b[20]) and negative anomalies in geopotential height start to build up, chiefly in the south-west quadrant of the North Atlantic, which reflects the abrupt transition from the northern to the southern regime in the jet latitudinal variability, as positive zonal wind anomalies in the southern sector of the domain start to appear and intensify in the later part of the third stage (Fig. 5.8b,c).

- Finally, the jet gradually moves back to the initial central regime during the course of the fourth stage we identified (Fig. 5.8c,d[21] and back to Fig. 5.7a), which is arguably the least well defined, as several different dynamical processes might be simultaneously at play (e.g. the influence of the sub-tropical jet in the southern regime or non-modal system growth).

The evolution of the flow during the life cycle of $v' - T'$ covariance is thus consistent with the preferred regime transitions (i.e. southern → central → northern → southern) observed for the eddy-driven jet (Novak et al., 2015).

In Fig. 5.10a we show the average evolution of the area-mean baroclinicity (over the same spatial domain where we compute the covariance) across the correlation–variances phase space, while in Fig. 5.10b we show that of the jet's latitudinal variability index. The jet latitude index is computed in a similar way to Novak et al. (2015), that is as the latitudinal position of the maximum in lower-tropospheric (950hPa to 750hPa) zonal wind, zonally averaged between 60°W–0°E excluding regions covered by land. Baroclinicity is observed to decay on average during the build-up of $v' - T'$ covariance, particularly as variances amplify, reaching a minimum at peak values in $v' - T'$ covariance. At the same time, the eddy-driven jet is seen to gradually shift northwards in the first and second stages of the covariance life

[19]Panel d not shown in published article.
[20]Panel b not shown in published article.
[21]Panel d not shown in published article.

cycle, while it is located at lower latitudes in the decaying stage[22], consistent with the average evolution of the flow shown in Figs. 5.7, 5.8.

The observed variability in baroclinicity is limited compared to its full range of variability within the North Atlantic storm track seen in Fig. 5.4, where in white we plotted covariance against the kernel averaged baroclinicity along the closed trajectory that we selected in the correlation–variances phase space (Fig.5.6). This might be indicative of the higher degree of complexity in the relationship between $v' - T'$ covariance and the storm track life cycle compared to what correlation–variances phase portraits convey, as the covariance life cycle does not map entirely on a baroclinic life cycle, especially in the final decay stage where different driving mechanisms might be at play. Furthermore, the level of noise associated with the kernel average is not negligible compared to the magnitude of the emerging signal in baroclinicity. However, we notice that baroclinicity values for the region considered are normally distributed around their mean (Fig. 5.9[23].), with a sample standard deviation (≈ 0.1 day^{-1}) of comparable size with the amplitude of the variability observed in Fig. 5.10a (0.43–0.48 day^{-1}). Thus, the resulting signal can be interpreted at least qualitatively as the average response of baroclinicity to $v' - T'$ covariance amplitude variability.

On a similar note, notwithstanding the fact that the full range of latitudinal variability spanned by the eddy-driven jet is clearly larger than that associated with the $v' - T'$ covariance life cycle shown in Fig. 5.10b, the clear signal of the jet's northward progression supports a physical link between jet latitude and the evolution of $v' - T'$ covariance over the Gulf Stream extension region. Finally, it should be noted that the difference in the time scales of amplitude variability in $v' - T'$ covariance (associated with high-frequency eddy activity) and the downstream jet meandering can also be contributing to the limited magnitude of the average signal.

[22]Results from the kernel-averaged evolution of the eddy-driven jet (in particular, the split and shift from its northern state to the southern, most persistent state) are reminiscent of the findings by Frame et al. (2013), who also looked at the evolution of the jet in a phase space of its two leading principal components (footnote not included in published article).

[23]Figure not included in published article

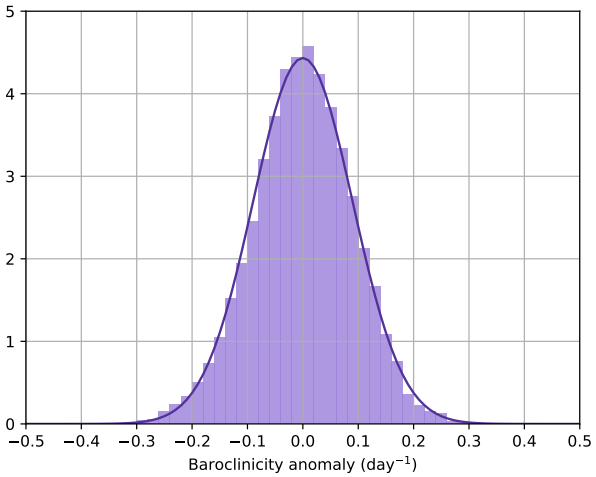

Figure 5.9: Empirical distribution of the area-mean baroclinicity anomalies over the spatial domain considered, defined as departures from the 10-day running mean. The thick line corresponds to a Gaussian distribution with the same mean and variance as the empirical distribution.

5.5 Conclusions

In this chapter[24] we examined the temporal evolution in of the spatial covariance between meridional wind speed and air temperature as a tool to understand the dynamics underlying local heat transport variability. Specifically, we took an approach similar to that introduced by Marcheggiani and Ambaum (2020) and considered the spatial covariance between synoptic-scale (2–10 days) time anomalies in meridional wind speed and air temperature over the western sector of the North Atlantic ocean. We found that $v' - T'$ spatial covariance (i.e. the spatial covariance between meridional wind and air temperature time anomalies) features frequent bursts of activity, reminiscent of the sporadic nature of meridional energy transport described in Messori and Czaja (2013), and its dynamical relationship with mean baroclinicity is consistent with recent studies on storm track variability (Novak et al., 2015, 2017).

We further noticed that $v' - T'$ correlation and variances increase jointly in the build up to strong covariance. This was also observed for covariance in time, especially over oceanic regions. Correlation between two variables is defined as the ratio of their covariance to the product of their standard deviations, and would not be expected to change with variances on purely

[24]'study' in published article

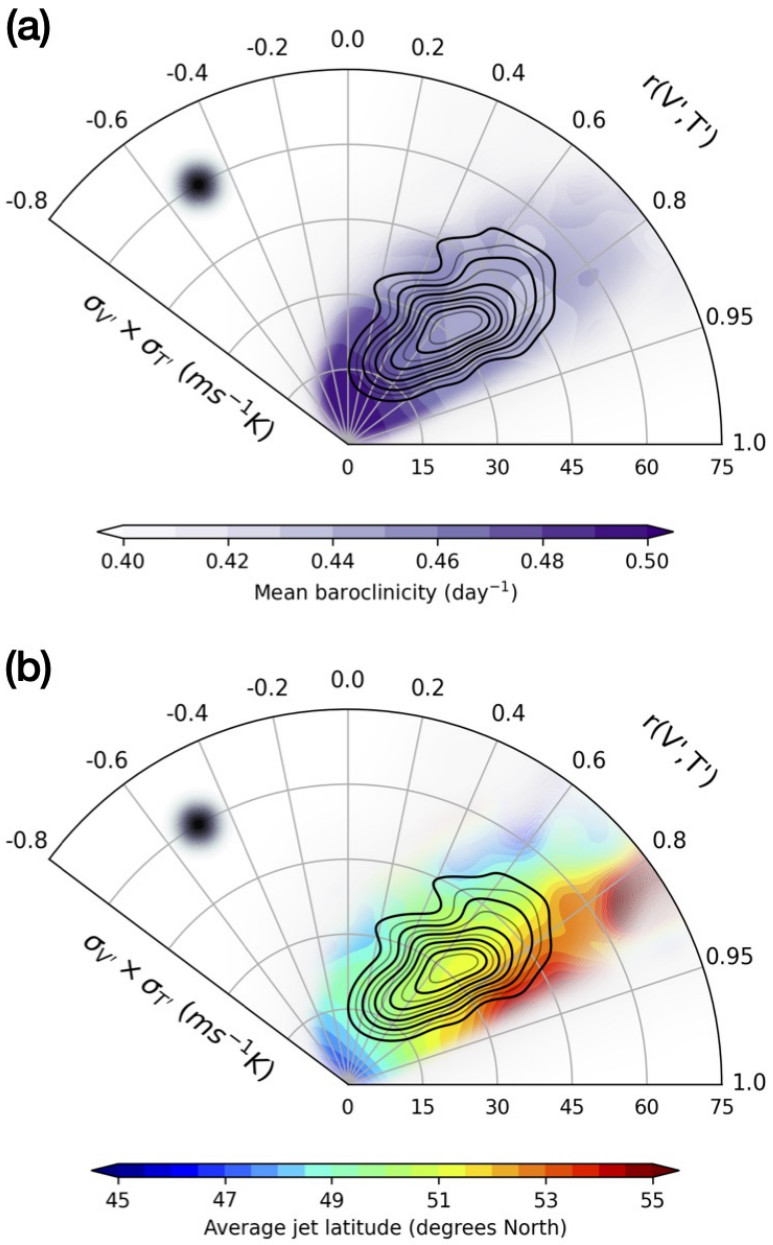

Figure 5.10: Kernel average (colour shading) of the area-mean baroclinicity (a) and eddy-driven jet latitudinal position (b). Contours as in Fig. 5.6. The size of the averaging Gaussian filter is indicated by the black-shaded dot in the upper-left corner of both panels.

statistical grounds. This points to the idea that some physical processes are driving this behaviour. Our analyses suggest that these can be partly ascribed to the dynamics of baroclinic development and eddy modal growth, which is characterised by a fixed correlation between anomalies in meridional wind and temperature and corresponds with phase-locked Rossby waves. The roles played by baroclinic development and modal growth appear to

be particularly relevant in the build up stages of the covariance's cyclical evolution, while different mechanisms are likely to be at play in the decay stage.

An initial small increase in covariance occurs at low variance due to correlation increasing from low values up to around 0.9. Subsequently, variances start to grow at high correlation. These two growing stages are associated with baroclinic development further downstream of the mid-latitude eddy-driven jet and eddy modal growth at constant, high correlation that leads to the peak in covariance. After the peak in covariance, correlation rapidly decays, while variances remain high and eventually also decay at low correlation. This brings the local velocity and temperature back to their initial low covariance state, which we took as the returning point of this intermittent life-cycle as it coincides with the area of largest data density.

We uncovered a link between the evolution of $v' - T'$ covariance and Rossby wave propagation in the analysis of the average evolution of the flow, which suggests that localised peaks of meridional heat flux precede Rossby wave propagation along the Atlantic waveguide[25](Hoskins and Ambrizzi, 1993). The examination of refractive indices for Rossby waves in the phase space could shed more light into the role of $v' - T'$ covariance in storm track dynamics.

Furthermore, we evinced[26] a correspondence between the life-cycle–like evolution of covariance and the different regimes of the eddy-driven jet's latitudinal variability as described in Woollings et al. (2010). Moreover, the jet's regime transitions observed in our analyses match with the preferred transitions described in Franzke et al. (2011) and Novak et al. (2015). This correspondence points to the fact that spatial covariance and its components can be seen as dynamical variables carrying information about the evolution

[25]that is, localised peaks are, on average, associated with anomalies downstream of the North Atlantic storm track whose spatial pattern is reminiscent of a propagating Rossby wave

[26]Each of the composites shown in Figs. 5.7, 5.8 are the result of the contribution of a large number of different events, which implies that specific features traceable back to actually observed configurations of the atmospheric flow are not straight-forward to identify and potentially hidden by the high variability of the flow itself. However, it is useful to interpret each composite as the average signal that we get from different events with similar levels of correlation and variance and it is in this regard that we highlighted the link between the life cycle of meridional heat flux peaks and the northward propagation of the eddy-driven jet. In particular, our results suggest that, on average, in the run-up to peak of meridional heat flux the jet stream shifts northwards, while the occurrence of the transition from a northern-like to a southern-like regime coincides with the decay stage following the peak.

of weather systems.

Further insights into the importance of baroclinic development in shaping the correlation–variances co-evolution could be gained through the study of simple models of baroclinic instability and their skill in reproducing the different stages in the $v' - T'$ covariance life cycle as observed in our phase space analysis.

5.6 Supplementary material

In this section we present additional material which was not discussed in the published article.

5.6.1 Correlation–variances relationship in a simple diffusive model

If we assume temperature anomalies to be linearly dependent on the wind speed anomalies and the background temperature gradient, we have that

$$\frac{1}{\tau}T' \approx \frac{\partial}{\partial t}T' = -v'\frac{\partial \hat{T}}{\partial y} \tag{5.6}$$

where τ is a decorrelation timescale and $\hat{T}$ is the 10-day rolling average of T. The resulting covariance between v and T is driven essentially by the variance in v and weighted by the magnitude of the meridional temperature gradient,

$$\overline{v'T'} = -\tau\,\overline{v'^2\frac{\partial \hat{T}}{\partial y}}$$

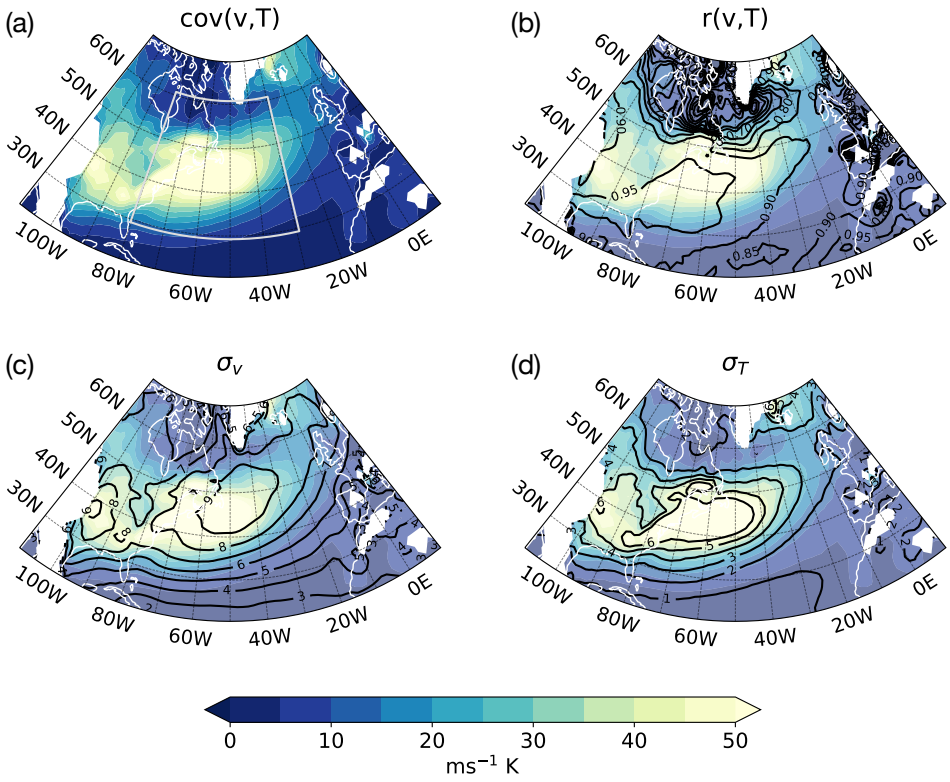

Figure 5.11: As in Fig. 5.1, using temperature anomalies from Eq. 5.6.

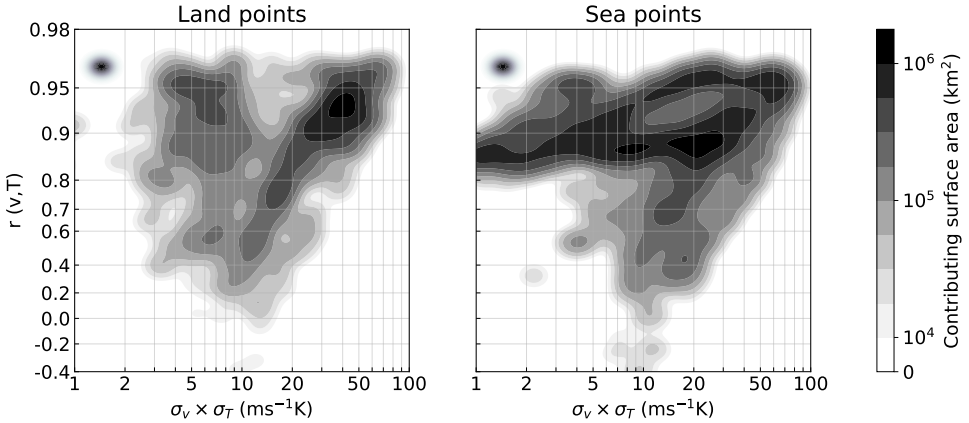

Figure 5.12: As in Fig. 5.2 (note the different scale of the correlation axis, going up to 0.98), using temperature anomalies from Eq. 5.6.

with $\tau = 18h$. This is what we observe in Fig. 5.11, which is constructed in the same way as Fig. 5.1, in this case using temperature anomalies deriving from the definition in Eq. 5.6.

The resulting correlation coefficients (Fig. 5.11b) are considerably higher than what we found using real data, which is indicative of the stronger coupling between wind and temperature anomalies we implicitly introduced in the diffusive model of Eq. 5.6.

The corresponding correlation–variances distribution, presented in Fig. 5.12, shows how the dependence of correlation on variance is less evident, with high levels of correlation observed across a wide range of variances, with the exception of the region north of Canada which resembles the same secondary cluster observed in Fig. 5.2.

5.6.2 Statistical significance of kernel averaged phase space circulation

This subsection was published in Marcheggiani et al. (2022) as Appendix B.

Yano et al. (2020) provide measures for both the signal-to-noise ratio and the statistical significance of the kernel averaged phase velocities. The signal-to-noise ratio is defined (see Equation 4.1 in Yano et al., 2020) as the ratio between the size of the signal compared to the underlying spread, while the statistical significance is defined (see Equation 2.10 in Yano et al., 2020) as the ratio of number of data contributing to the average (i.e. data density) to the underlying expectations from the noise, in other words describing how many standard deviations the signal rises above the noise.

In Fig. 5.13 we show the signal-to-noise ratio and statistical significance for the kernel averaged circulation in the correlation–standard deviations phase space. The signal-to-noise ratio is well below one across the regions with highest data density, which implies that fluctuations of individual trajectories around the kernel averaged circulation are quite large. This, however, does not affect the statistical significance of the averaged circulation, as panel b indicates.

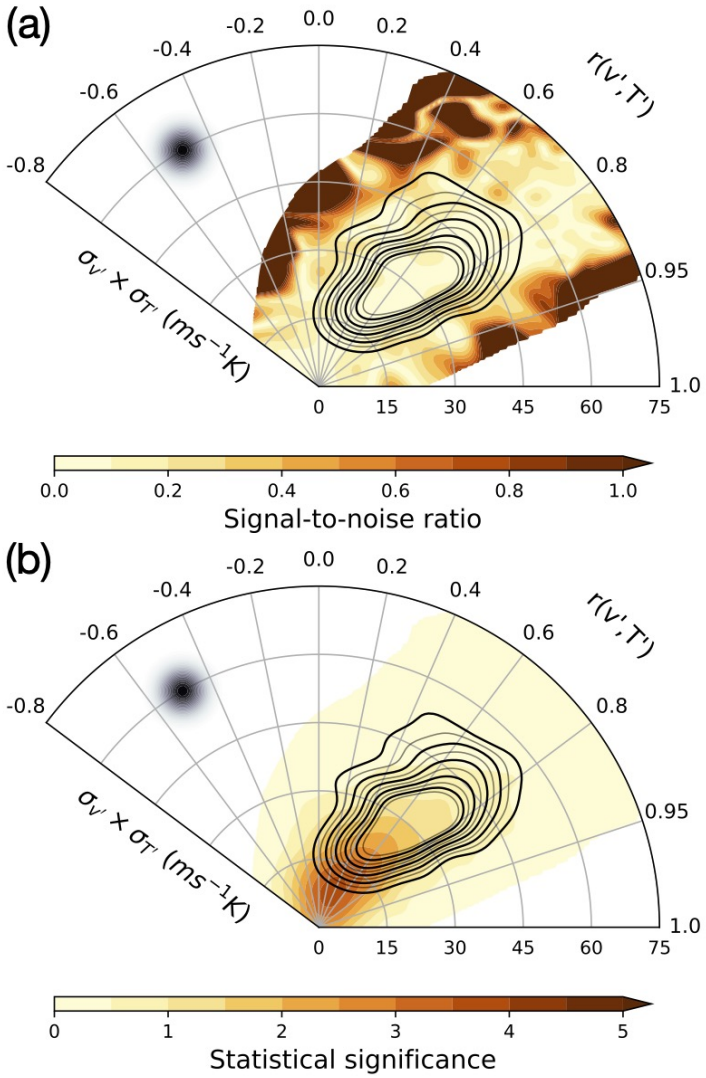

Figure 5.13: Signal-to-noise ratio (a) and statistical significance (b) computed, respectively, as in Equations 4.1 and 2.10 from Yano et al. (2020) for the phase velocities in the correlation–variances phase space, shown where the effective number of data points contributing to the average is greater than 1. Contours represent streamfunction associated with kernel averaged circulation.

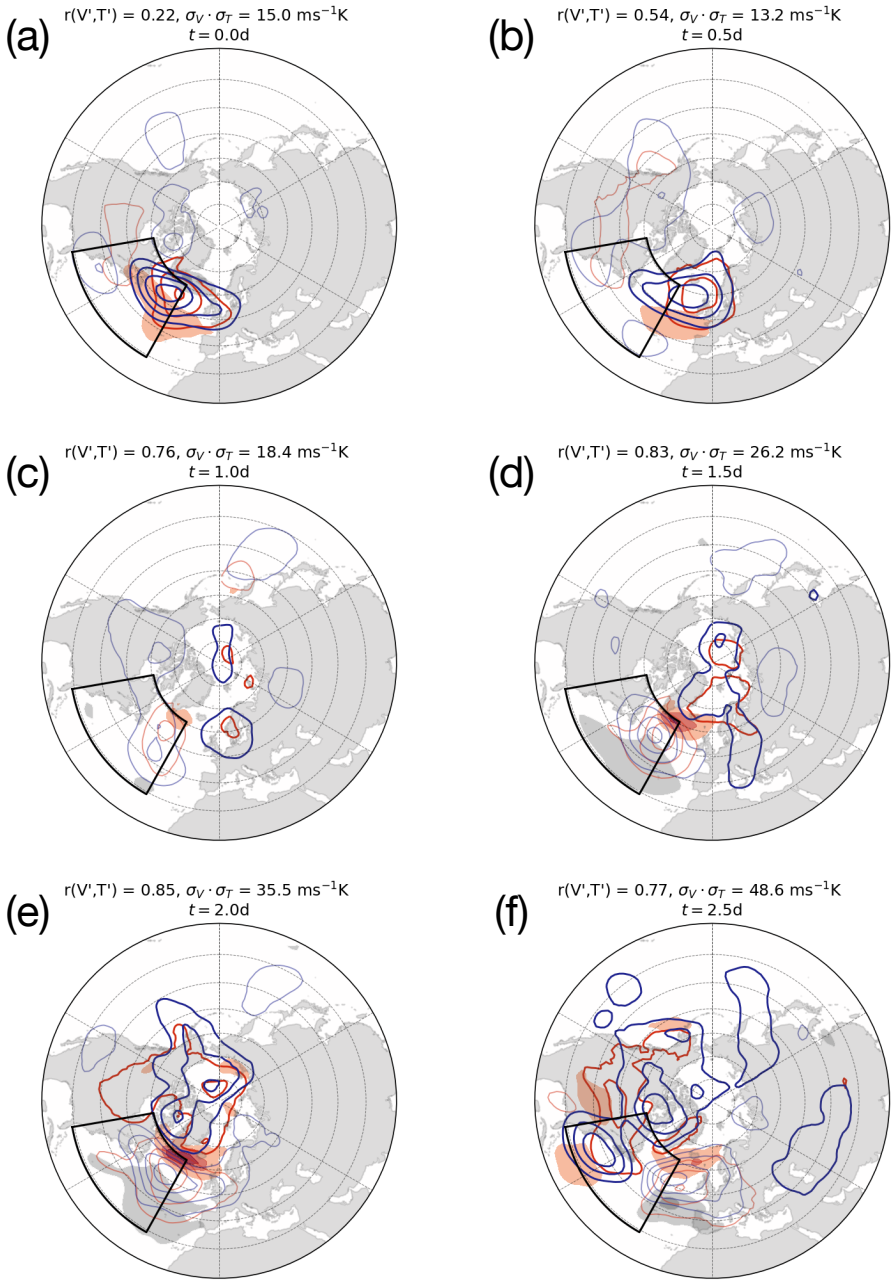
(a)
r(V',T') = 0.22, $\sigma_V \cdot \sigma_T$ = 15.0 ms^{-1}K
t = 0.0d
(b)
r(V',T') = 0.54, $\sigma_V \cdot \sigma_T$ = 13.2 ms^{-1}K
t = 0.5d
(c)
r(V',T') = 0.76, $\sigma_V \cdot \sigma_T$ = 18.4 ms^{-1}K
t = 1.0d
(d)
r(V',T') = 0.83, $\sigma_V \cdot \sigma_T$ = 26.2 ms^{-1}K
t = 1.5d
(e)
r(V',T') = 0.85, $\sigma_V \cdot \sigma_T$ = 35.5 ms^{-1}K
t = 2.0d
(f)
r(V',T') = 0.77, $\sigma_V \cdot \sigma_T$ = 48.6 ms^{-1}K
t = 2.5d

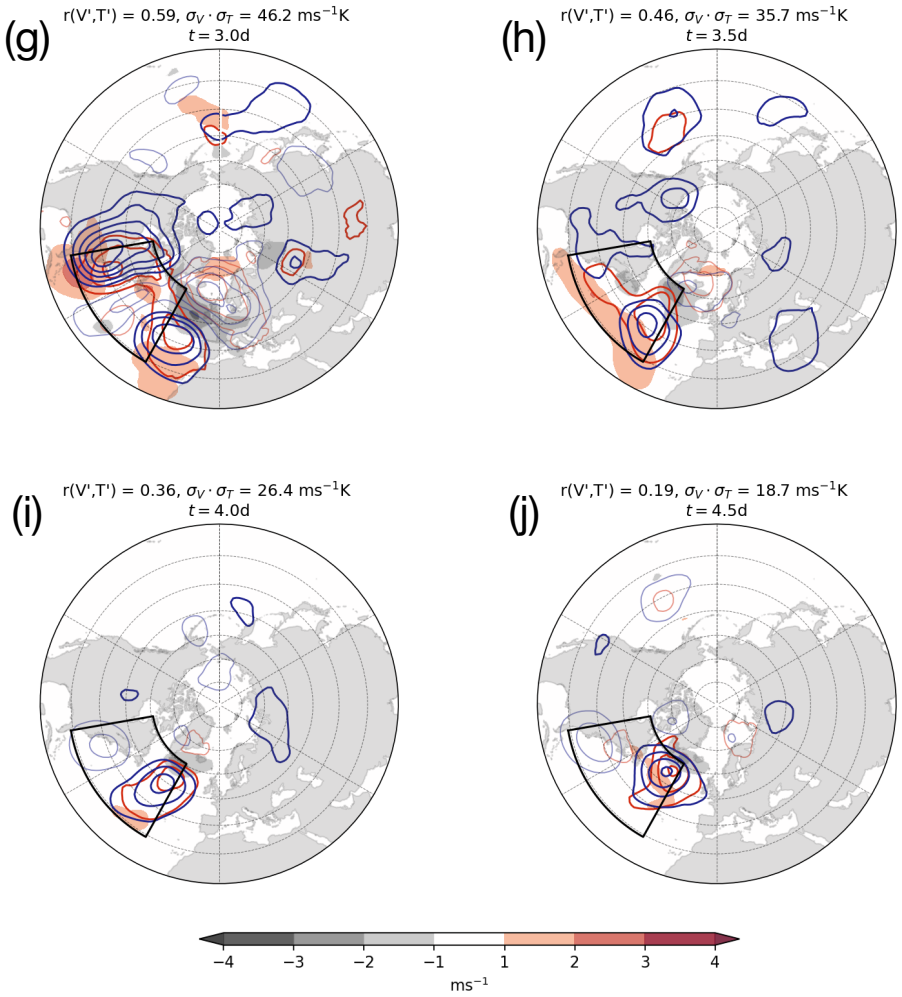

Figure 5.14: As in Fig. 5.7, displaying the entire Northern Hemisphere.

5.6.3 Kernel composites over the Northern Hemisphere

Figure 5.14 shows the same composites presented in Figs. 5.7,5.8 of geopotential height (Z1000 and Z500) and zonal wind speed but over the entire Northern Hemisphere. It can be seen that at the peak of $v' - T'$ spatial covariance (between day 2 and 3, panels e–g) the anomalies in geopotential observed in the North Atlantic are part of Rossby wave that propagates along the North Atlantic waveguide and beyond towards North-Eastern Asia. An extra panel for day 1 is included (Fig. 5.14c) which adds to the gradual build-up of the high pressure anomaly that is dominant in Fig. 5.7c.

5.6.4 Evolution of correlation in a simple baroclinic instability model

As we might expect different growth mechanisms to contribute to different part of the kernel averaged circulation in the correlation–standard-deviations' phase space, in this section we examine the relationship between correlation and variances in the classical Eady model, to which we add Ekman friction at the lower boundary to account for the effects that the planetary boundary layer may have on the dynamical evolution of baroclinic instabilities.

Davies and Bishop (1994) examined the importance of coupling between surface and tropopause level disturbances in the development of baroclinic instabilities from a quasi-geostrophic potential vorticity viewpoint. They considered a classical Eady problem for a quasi-geostrophic flow of an incompressible fluid and then add small amplitude perturbations to the background state in the form of Eady edge waves at the surface (lower boundary) and at the tropopause (upper boundary) of the spatial domain. Following from the perturbation potential vorticity and thermodynamic linearised equations, the dynamics of the system are determined by the thermal distributions on the two bounding surfaces. They showed that only intermediate and long wave couplets are able to go in a phase-locked state. In particular, long and intermediate waves are optimal for an upper disturbance to trigger a response at the bottom boundary that grows exponentially in time, while shortwaves couplets do not sustain it (i.e., the ratio of the lower *triggered* eddy wave amplitude to that of the initial upper edge wave remains below 0.5 for time periods up to three days).

In a wave packet, counter dispersion and amplitude growth are argued to be a potential mechanism for localised rapid growth, especially in the case of long and intermediate-scale waves, whose associated vertical structure evolution resembles real-world observed developments. In this context, the evolution of correlation between meridional wind and temperature might reflect the interaction of the large scale circulation with surface disturbances, which can grow depending on the relative disposition and length scale (as counter-propagating Rossby wave theory would suggest Heifetz et al., 2004a,b). There are examples in the literature of how the evolution of baroclinic waves can be described in terms of the strength of interactions between different components of counter-propagating Rossby waves (e.g., De Vries et al., 2010) that include moist processes. In this section, we con-

sider a much simpler framework and examine the evolution of meridional heat flux peaks in the context of the classical Eady model.

Following Davies and Bishop (1994), we consider a classical Eady problem for a quasi-geostrophic flow of an incompressible fluid in a channel of depth d, where the basic state is assumed to be a steady background flow U with constant vertical shear Λ, no shear in the horizontal direction and uniform stratification N^2. We then consider small amplitude perturbations to the background state in the form of Eady edge waves at the lower upper boundary of our spatial domain. The dynamics of the system are determined by the thermal distributions on the two bounding surfaces, as it follows from the perturbation potential vorticity and thermodynamic linearised equations. By definition of the Eady edge wave, each wave is associated exclusively with the thermal perturbation on the respective bounding surface,

$$\theta'_T = T \sin(kx + \varepsilon_T) \sin ly \, \frac{\sinh \mu z}{\sinh \mu d}, \tag{5.7a}$$

$$\theta'_B = B \sin(kx + \varepsilon_B) \sin ly \, \frac{\sinh \mu (d-z)}{\sinh \mu d}, \tag{5.7b}$$

where k, l are the zonal and meridional wave numbers, $\mu = N/f_0\sqrt{k^2 + l^2}$ and B, T are the temperature amplitudes of the bottom and top edge wave respectively. Through the thermal wind balance relation, we can relate the temperature perturbation field to the perturbation streamfunction,

$$\frac{d\psi'}{dz} = \frac{g}{f_0 \theta_0} (\theta'_T + \theta'_B). \tag{5.8}$$

From Eq. 5.8 we can derive an expression for the perturbation streamfunction, ψ',

$$\psi' = \frac{g}{f_0 \theta_0} \frac{\sin ly}{\mu \sinh \mu d} \Big[T \cosh \mu z \sin(kx + \varepsilon_T) - B \cosh(\mu(d-z)) \, \sin(kx + \varepsilon_B) \Big],$$

from which we can obtain the perturbation meridional wind, v',

$$v' = \frac{\partial \psi'}{\partial x} = \frac{g}{f_0 \theta_0} \frac{k \sin ly}{\mu \sinh \mu d} \Big[T \cosh \mu z \cos(kx + \varepsilon_T) - B \cosh(\mu(d-z)) \, \cos(kx + \varepsilon_B) \Big],$$

and then calculate the meridional heat flux,

$$\overline{v'\theta'} = -\frac{1}{2} \frac{gk}{f_0 \theta_0 \mu} \frac{\sin^2 ly}{\sinh \mu d} \, TB \sin(\varepsilon_T - \varepsilon_B),$$

where θ_0 is a reference temperature. Notice that the meridional heat flux does not vary with height, therefore any change in correlation between meridional wind and temperature anomalies derives from variations in their variances. In fact, the correlation r is defined as

$$r(v',\theta') = \frac{\mathrm{cov}v'\theta'}{\sigma(v')\,\sigma(\theta')} = \frac{\overline{v'\theta'}}{\sqrt{\overline{v'^2}}\sqrt{\overline{\theta'^2}}}.$$

The sign of correlation can be shown to be given by the phase difference between the edge waves at the top and at the bottom (specifically by $-\sin(\varepsilon_T - \varepsilon_B)$). We provide an example for the correlation at the bottom of the channel ($z = 0$),

$$r(v',\theta')|_{z=0} = \frac{T\sin\varepsilon}{\sqrt{T^2 + B^2\cosh^2\mu d - 2BT\cosh\mu d\cos\varepsilon}},$$

which we can rearrange in the following way,

$$r(v',\theta')|_{z=0} = \left[1 + \left(\tfrac{B}{T}\right)^2\cosh^2\mu d - 2\tfrac{B}{T}\cosh\mu d\cos\epsilon\right]^{-1/2}\sin\epsilon,$$

to highlight the dependence of correlation on a set of variables that will be introduced later (namely the ratio B/T and the phase difference $\varepsilon = \varepsilon_T - \varepsilon_B$). The temporal evolution of correlation is therefore driven by the evolution of the edge waves amplitudes and phases.

While the classical Eady model is based on the flow between flat upper and lower boundaries, in our model we consider symmetrical sloping boundaries which create an effect similar to the beta-effect (Mason, 1975), thus accounting for differential rotation. Furthermore, we introduce Ekman friction on the lower boundary in order to simulate the impact of the boundary layer on the dynamical evolution of the system. This corresponds to the following boundary conditions,

$$f_0\Big(\frac{\partial}{\partial t} + \Lambda d\frac{\partial}{\partial x}\Big)\frac{\partial\psi'}{\partial z} - \Big(f_0\Lambda + N^2\Delta_\eta\Big)\frac{\partial\psi'}{\partial x} = 0 \quad \text{at} \quad z = d, \tag{5.9}$$

$$f_0\frac{\partial}{\partial t}\frac{\partial\psi'}{\partial z} - \Big(f_0\Lambda - N^2\Delta_\eta\Big)\frac{\partial\psi'}{\partial x} + N^2 r\nabla^2\psi' = 0 \quad \text{at} \quad z = 0, \tag{5.10}$$

where Δ_η is the slope of both the lower and upper boundaries and r is the Ekman parameter that is proportional to the depth of the Ekman layer.

Table 5.1

Parameter	Expression	Meaning
α_1	$k\Lambda/\mu\sinh(\mu d)$	time scale set by basic state
α_2	$\Delta_\eta N^2/\Lambda f_0$	effect of sloping boundaries
α_3	$r\mu^2 f_0/k\Lambda$	effect of Ekman friction
α_4	$\cosh(\mu d) - \frac{1}{2}\mu d\sinh(\mu d)$	geometric factor
α_5	$\mu d\sinh(\mu d) - 2\alpha_2\cosh(\mu d)$	geometric factor

The substitution of the expression for ψ' that we get from Eq. 5.8 into Eqs. 5.9 yields the following set of evolution equations,

$$\frac{\partial T}{\partial t} = -\alpha_1(1+\alpha_2)B\sin\varepsilon, \tag{5.11a}$$

$$\frac{\partial B}{\partial t} = -\alpha_1(1-\alpha_2)T\sin\varepsilon - \alpha_1\alpha_3(B\cosh\mu d - T\cos\varepsilon), \tag{5.11b}$$

$$\frac{\partial \varepsilon}{\partial t} = 2\alpha_1\Big[\alpha_4 - \tfrac{1}{2}\Big(\Big(\tfrac{B}{T}+\tfrac{T}{B}\Big) + \alpha_2\Big(\tfrac{B}{T}-\tfrac{T}{B}\Big)\Big)\cos\varepsilon - \frac{1}{2}\alpha_3\tfrac{T}{B}\sin\varepsilon\Big], \tag{5.11c}$$

$$\frac{\partial \hat{\varepsilon}}{\partial t} = -\tfrac{1}{2}\alpha_1\Big[\alpha_5 + \Big(\Big(\tfrac{B}{T}-\tfrac{T}{B}\Big) + \alpha_2\Big(\tfrac{B}{T}+\tfrac{T}{B}\Big)\Big)\cos\varepsilon - \alpha_3\tfrac{T}{B}\sin\varepsilon\Big], \tag{5.11d}$$

where $\hat{\varepsilon} = \frac{1}{2}(\varepsilon_T + \varepsilon_B)$ is the absolute phase of the coupled wave system, $\varepsilon = \varepsilon_T - \varepsilon_B$ is the phase difference between the top and bottom edge waves and the parameters α_i are defined in Table 5.1.

In Davies and Bishop (1994), no beta-effect or Ekman friction is included in their model, which can be derived by setting α_2 and α_3 in Eqs. 5.11 to zero. This would make the study of the system of equations in Eqs. 5.11 much simpler: in the case of initial equal amplitudes ($B = T$), these would remain equal at any subsequent time (modal growth) and any changes in correlation would be due to the phase differences between the two waves. Specifically, in the case of phase locking ($\dot{\varepsilon}$=0), correlation would reach a fixed saturation value while variances would keep on growing (which is reminiscent of the first two stages in the life cycle of meridional heat flux peaks).

The inclusion of Ekman friction and sloping boundaries emulating the beta-effect significantly complicates the identification of stationary analytical solutions to the model in Eqs. 5.11 and we would need to rely on its numerical integration. However, this proves to be a convincing, starting point for further investigation into the theoretical basis for the observed correlation–variances co-evolution. In fact, preliminary results seem to indicate that there are some preferred ways correlation and variances evolve,

though our analyses have not yet led to definitive results.

Chapter 6

Conclusion

6.1 Summary

The overall aim of this thesis is to shed some light on the way heat enters the North Atlantic storm track region and evaluate its thermodynamic consequences, building upon recent studies on the role of meridional heat fluxes in the life cycle of storm tracks (Ambaum and Novak, 2014; Novak et al., 2015). The contribution from heat fluxes to the synoptic evolution of weather systems is unclear as they play different roles in the storm track life cycle. In fact, diabatic processes can act both to replenish the background baroclinicity of the flow and to damp the temperature contrasts on which extra-tropical weather systems derive their energy.

Transient eddies in the storm track develop with the aim of flattening the isentropic surfaces, which are climatologically steepest in the midlatitudes and in correspondence with strong large-scale SST fronts. The latent heat release associated with the transient eddies then acts to restore the baroclinicity in the wake of eddies through the deformation of isentropic surfaces (thus generating slope, Papritz and Spengler, 2015). Sensible heating at the surface also contributes to tilting the isentropic surfaces closer to the surface (Hotta and Nakamura, 2011).

In the first part of this thesis, we considered a mixed space-time framework where we examined the spatial variability of synoptic-scale time anomalies (i.e. 2–10 day variability band) over the Gulf Stream Extension region. We defined a measure of the local heat exchange between the ocean and the atmosphere based on the covariance of surface heat flux and lower tropospheric temperature. The heat-flux–temperature covariance is found to be always negative, which is suggestive of the damping effect that surface

sensible heating exerts on the available potential energy of the flow as the atmosphere is heated where it is cold and cooled where it is warm.

In this framework, we are able to relate the temporal evolution of the air–sea sensible heat exchange to mean quantities that describe the state of the flow by studying the kernel averaged phase portraits traced by these quantities. Specifically, we observe an average decrease of the area-mean baroclinicity when the heat-flux–temperature covariance reaches a peak, which occurs in correspondence with the advection of the cold sector of weather systems. Baroclinicity is then seen to recover once covariance weakens and the presence of the cold sector in the spatial domain considered is no longer dominant. Therefore, we find that the local covariation of sensible heat flux and temperature in the lower troposphere, which is a measure of the intensity of the surface–troposphere thermal coupling, is associated, on average, with a reduction of the mean baroclinicity. This answers the first of the research questions presented in the introduction, as we found that the local heat exchange in the atmosphere does not always enhance the evolution of extra-tropical storms.

In our study of the evolution of heat-flux–temperature spatial covariance, we showed that the damping effect of surface heat fluxes on the temperature variance (and mean baroclinicity) occurs primarily in the cold sectors of extra-tropical cyclones. We find that both stronger correlation between heat flux and temperature and their respective variances are equally contributing to peaks of covariance. The second part of this thesis thus focused on the identification of the physical mechanisms that drive the evolution of covariance through changes in correlation and variances in the build-up to a peak of covariance.

Over the Gulf Stream, where the SST spatial variability is largest with respect to the whole North Atlantic ocean, an increase in heat-flux variance leads in time on a similar increase of air temperature variance, as the cold air masses advected by the storms' cold sectors start to thermally interact with the ocean surface. The enhanced convection and turbulent mixing over warm ocean waters locally induces a deeper atmospheric boundary layer, where vertical temperature profiles are almost adiabatic. Temperatures in the proximity of the top of the boundary layer are not expected to deviate substantially from the almost adiabatic profile. Therefore, as the boundary layer deepens, a larger fraction of the lower troposphere becomes more tightly thermally coupled with the surface, which is reflected in the

higher level of correlation between the two levels that contributes to the covariance peak.

In Chapter 3, we linked the influence of the atmospheric boundary layer on the lower troposphere to the turbulent nature of its mixed layer, as potential temperature within the boundary layer does not deviate significantly from that at the surface. The analyses of the evolution of surface heat flux and temperature spatial covariance in the first part of the thesis were based exclusively on reanalysis data, which arguably provide only a limited overview of boundary layer dynamics. We can gain further insights into the role of boundary layer dynamics through very-high-resolution numerical simulations of selected case studies of intense heat exchange. These were run using the Met Office Unified Model in a regional configuration of limited spatial extent, centred over the Gulf Stream region. Cross-sections across the Gulf Stream track confirmed the validity of our model for the boundary layer effect on correlation, as cold air masses progressing over the SST front are characterised by adiabatic vertical profiles throughout the boundary layer, which reaches well into the lower troposphere during peaks of surface heat flux variance.

Meridional heat fluxes, defined as the product of meridional wind and temperature zonal anomalies, are also characterised by sporadic bursts of activity, which have been shown to contribute substantially to shaping their climatology (e.g., see Swanson and Pierrehumbert, 1997; Messori and Czaja, 2013). In the final part of the thesis, we studied the evolution of meridional heat flux peaks in the same mixed space-time framework introduced in the first part of the thesis, thus concentrating on the synoptic-scale variability. In this framework, the spatial correlation between lower tropospheric meridional wind and air temperature time anomalies and their spatial variances are seen to carry information about the growth of baroclinic instabilities.

The picture that we gathered from the average phase portrait traced in the correlation–variances phase space is that the correlation needs to reach a threshold value before the variances are seen to increase, which would correspond to a weather system's growth. Conversely, the decreasing correlation after a peak is followed by decaying variances and weather activity propagating downstream of the North Atlantic storm track, to the northeast of the spatial domain where the covariance, correlation and variances are computed.

The covariance of surface heat fluxes with air temperature captured the

local thermal interaction of the cold sector of weather systems with the ocean, consistent with a Lagrangian propagation mechanism. On the other hand, the evolution of the covariance between meridional wind and temperature is found to be entangled with the large-scale dynamical evolution of the atmospheric circulation. In particular, we found that the life cycle of meridional heat flux peaks can be understood in terms of a propagating Rossby wave packet that is centred over the Gulf Stream Extension region and that, in the wake of a peak, propagates along the North Atlantic waveguide downstream towards Europe. The covariance of meridional wind and temperature, therefore, captures the importance of wave propagation mechanisms over Lagrangian propagation in the evolution of meridional heat flux peaks. In light of this, we can interpret the spatial correlation between heat flux and temperature as an independent dynamical variable carrying information about the evolution of midlatitude storm tracks.

6.2 Future work

Our understanding of the way sensible heating affects the mean baroclinicity of the flow is not yet complete. In Chapter 2, despite global estimates indicating that sensible heating be regarded as a source of baroclinicity (e.g., Li et al., 2007), we showed that locally sensible heat fluxes appear to be linked with the erosion of baroclinicity (see Fig. 2.6 in Section 2.4). In the context of isentropic surfaces dynamics, this would imply the coexistence of a steepening and a flattening action by sensible heat fluxes on sloping isentropic surfaces. We might be able to explain this apparent contradiction by considering that the observed reduction in baroclinicity during events of strong heat-flux–temperature covariance is essentially driven by the meridional temperature-mixing action of the transient, synoptic eddies. In their evolution, eddies attempt to reduce the slope of isentropic surfaces and sensible heating may effectively act to damp the flattening effect of eddies. In fact, the inspection of kernel composites of mean baroclinicity in the evolution of surface heat flux-temperature covariance reveals a weak signal of higher baroclinicity (about 0.05 day^{-1} above climatology, not shown) in the build-up to a covariance peak. This suggests that the link between sensible heating and baroclinicity is still needing of further investigation, with a specific focus on the contribution from different timescales (shorter and longer timescales having primary roles, respectively, in the temperature mixing

and gradient restoration).

Preliminary research into the flux–temperature covariance in regions downstream of midlatitude storm tracks suggest that different mechanisms are driving the evolution of covariance (see Section 2.6.3). The lower SST spatial variability that characterises the eastern North Atlantic or eastern North Pacific oceans potentially weakens the restoring action of the ocean on surface baroclinicity, which is of primary importance in the Gulf Stream region (Nakamura et al., 2008). Future interesting avenues of research may include a broader exploration of the role of heat-flux temperature covariance in these dynamically distinct regions. There we would expect, on average, more mature weather systems and their interaction with the ocean could have a different impact on their further development. Bui and Spengler (2021) recently looked into the influence exerted by different distributions of the SSTs in idealised numerical simulations and suggested that sensible heat fluxes associated with a strong SST gradient have a detrimental effect on a cyclone's development, although their role was shown to be of secondary importance with respect to latent heating. In a scenario of weak SST gradients, therefore, sensible heating at the surface might play a different, minor role in the evolution of weather systems.

Furthermore, it would be insightful to study the specific role of surface latent heat fluxes on storm evolution, disentangling the local contribution from remote effects due to large-scale precipitation and building upon recent work by Haualand and Spengler (2020), who investigated the direct and indirect effects of surface heat fluxes on moist baroclinic development through idealised numerical simulations and highlighted the importance of respective locations of weather systems' features (e.g. the warm conveyor belt) and surface heating. The distribution of latent heat release within an individual cyclone exerts a primary influence on its evolution and, most importantly, to the subsequent development of following cyclones, ultimately underpinning the self-maintenance of the storm track.

The spatial correlation in numerical models between the surface and higher levels in the free troposphere depends on the degree of spatial and temporal resolution of both the atmospheric and ocean components of the models. We found that a strong heat-flux–temperature covariance is associated, on average, with the damping of the temperature contrasts within the atmosphere. The weakening of temperature gradients thus affects the evolution of synoptic eddies that developed in the first place in response to

these temperature gradients.

We would expect a model run with finer horizontal resolution to be able to capture a larger fraction of the effects of sensible heat fluxes on the evolution of extra-tropical storms and, more generally, on the structure of storm tracks. It is not clear, however, if and how the picture changes substantially with resolution and when it proves to be most beneficial.

Our work concentrated on a selection of individual events (Section 4.2) with the aim to provide evidence for the validity of the qualitative model we proposed for the role of the boundary layer in the evolution of heat-flux–temperature covariance (Section 3.4). The inclusion in our analyses of a larger number of events (perhaps through the identification and Lagrangian tracking of extra-tropical systems), simulated at different horizontal resolutions, could help assess the importance of a correct representation of surface heat fluxes and their influence on the large-scale circulation. In the same context, we would also be able to quantify the contribution that model air–sea coupling brings to a correct representation of air–sea interactions on the synoptic scale, thus allowing us to understand when and how model coupling is crucial for downstream storm prediction.

Finally, in our investigation of the physical mechanisms that drive the life cycle of meridional heat flux peaks we hinted at the role of modal and non-modal growth mechanisms in different stages of a peak life cycle (Section 5.4). Specifically, a preliminary examination of theoretical expectations from a simple baroclinic instability model (Davies and Bishop, 1994) appears to suggest that the increase of variances at a fixed, high correlation value might derive from the phase locking between interacting edge waves at the surface and at the tropopause. The inclusion of Ekman friction at the surface and of a tilt of the boundary surfaces (emulating the meridional gradient in planetary vorticity, i.e. the beta-effect) makes an analytical interpretation of the model predictions more difficult to obtain, although exploratory numerical integrations feature oscillations that resemble the observed correlation–variances behaviour. If we also consider wave mean flow interaction and linear damping consistent with radiative relaxation in the numerical integration of the model, then we are able to reproduce the cyclical occurrence of peaks of meridional heat flux, although the associated time scales are longer. Further exploration of the theoretical prediction of such idealised models could help us disentangle the contribution from different growth mechanisms with different time and length scales.

Appendix A

Phase space analysis and kernel estimation

A.1 Phase space analysis

A powerful tool to study properties of a dynamical system consists in the construction of a *phase space* where coordinate axes correspond to variables whose relationship is being examined.

In the simple case of an harmonic oscillator like a pendulum, we take into consideration a position–momentum phase space. By plotting the position against momentum of the suspended weight we obtain a phase *portrait* of the oscillator dynamical evolution, which in this particular case consists of circular closed trajectories with different radii according to the initial state of the pendulum.

If we then take into account the effects of friction onto the pendulum motion, this would slowly lose momentum, resulting in narrower oscillations until it comes to a halt. This translates in the a phase portrait characterised by trajectories spiralling around the origin of the axes, where they ultimately converge. Therefore, the dynamical evolution of the pendulum is easily reconstructed just by visually inspecting the phase portrait traced by the pendulum in the position–momentum phase space, where we see momentum and position oscillate in counter-phase.

The dynamical evolution of the atmospheric flow, clearly, is more complex and chaotic than the simple harmonic oscillator case we considered above. In fact, in the atmosphere a multitude of different dynamical variables can simultaneously affect the evolution of the system under study. These variables can have a finite temporal extension (e.g., precipitation

events and the corresponding latent heat release) or be cyclically repeating themselves (e.g., diurnal or seasonal cycles), acting either as sources or sinks in the energetic balance of the system. Consequently, interpreting a phase portrait to reconstruct the driving mechanisms behind the chaotic evolution is not always a trivial task, especially if the dynamical relationship between the variables under examination is not explicitly evident. Nonetheless, when we consider a set of variables that are deemed to have a distinctive relationship, the resulting phase portrait can shed some light on the characteristics of their dynamical coupling, thus helping us understand the driving mechanisms at the base of their relationship.

The technical details of constructing and analysing a phase space are described in Novak et al. (2017), where a two-dimensional phase space was considered to identify a predator-prey relationship between meridional heat fluxes and mean baroclinicity, which were used as coordinates in the phase space.

Throughout this thesis, we make an extensive use of phase space analysis. In Chapter 2, we construct a phase space where the horizontal and vertical coordinate axes correspond, respectively, to the spatial standard deviation in surface heat flux and in air temperature. In order to explore the dynamics behind the evolution of heat flux–temperature spatial covariance, we plot in this phase space the time series for the spatial standard deviations (spanning all winters from 1979 to 2019) one against the other. In Chapter 5, we construct a phase space using a polar coordinate system where the radial and polar axes correspond, respectively, to the product of standard deviations of wind and temperature anomalies and the inverse cosine of the correlation between them.

A.2 Kernel estimation

Trajectories in phase portraits of real chaotic systems rarely follow the same path twice and often cluster around selected points or succession of points. On that account and given the large amount of data we are simultaneously visualising (6-hourly winter data from 1979 to 2019 amounts to more than $10,000$ data entries), it becomes necessary to apply some level of filtering to the resulting phase portrait in order to evince the average circulation in the phase space.

We can filter out part of the noise due to the chaotic nature of the

system by applying a kernel averaging operator (or smoother) to the raw data. The kernel averaging operator that we use is based essentially on a kernel density estimator (for a detailed description see Wand and Jones, 1994) and computes the sum of the contributions from every data entry weighted according to their distance from the point where the operator is applied. Mathematically, the kernel density estimator returns the average number of contributing data entries to the average value at any specific point in the phase space. In one dimension, the number of contributing data points N at a point x_0 along the x-axis can be expressed as

$$N(x_0; h) = \sum_{i=1}^{n} K_h(x_0 - X_i), \tag{A.1}$$

where n is the number of discrete points that form the time series X_i, K_h is the kernel (which we choose to be a unimodal function, symmetric about zero) and h is a positive number controlling the window width (or bandwidth) of the kernel. The choice of the kernel in Eq. A.1 is most naturally chosen to be a Gaussian kernel, which in one dimension takes the following form,

$$K_h(x) = \exp\left\{-\frac{1}{2}\left(\frac{x}{h}\right)^2\right\}, \tag{A.2}$$

where x is the Eulerian distance between two points. While the particular choice of kernel is somewhat arbitrary, for the sake of the validity and significance of the results of our analyses these should not be too much sensitive to the specific kernel implemented nor to its window width. Furthermore, Eq. A.2 is not normalised in the usual way of a Gaussian probability density function. Instead, the kernel has a peak value of 1, which allows for the sum of all the weights to be interpreted as the total number of contributing data points.

For reference, in Fig. A.1 we compare the unfiltered phase portrait in the baroclinicity–FT index phase space (a) and the kernel smoothed portrait (b, corresponding to Fig. 2.6), noticing how its interpretation is made much easier and clearer in the latter case.

We can adjust the width of the Gaussian distribution function (that is, the size of the kernel K_h) by tuning the bandwidth parameter h. In particular, in our analyses we take h to be a fraction $f = h/\sigma$ of the standard deviation of the time series associated with the coordinate axes in the phase space. Large-sized kernels are useful to get a general overview of the system's dynamical evolution, while small-sized kernels allow for finer

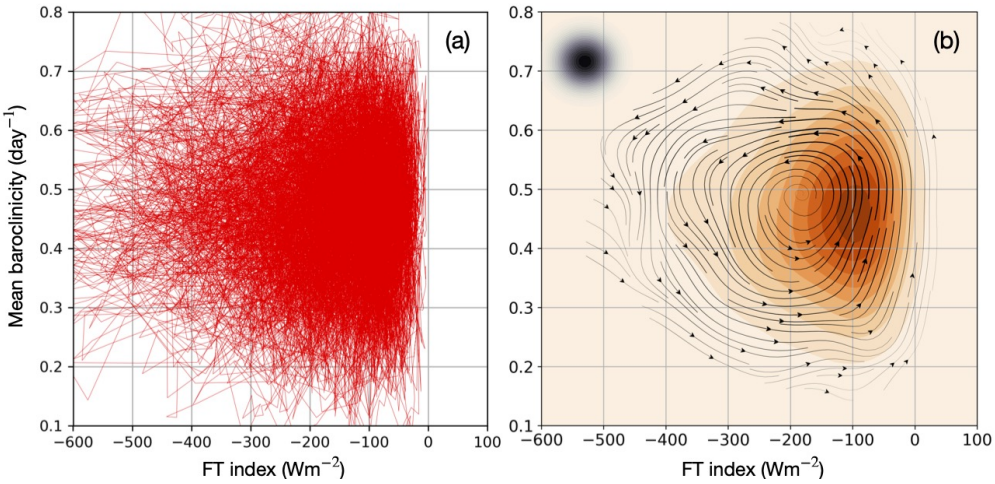

Figure A.1: Unfiltered circulation in the FT index-mean baroclinicity phase space (a) and the associated kernel average (b), as in Fig. 2.6.

details in the circulation to emerge. However, it must be noticed that smaller kernels are inevitably associated with a non-negligible amount of noise, as smoothing of raw data would be minimal and potentially making the averaging process pointless.

An example is presented in Fig. A.2, where we show phase portraits that result from applying the same Gaussian kernel smoother but with different kernel size, the panels corresponding with smaller kernels featuring finer and finer details until the circulation gets chaotic again. Therefore, a compromise must be reached in the selection of an appropriate kernel size so that a sensible interpretation of the phase portrait can be achieved.

We can also calculate the average value of a variable q across the phase space by computing its kernel average. To do this, we multiply the variable of interest by the weights following from the kernel averaging process and then divide by the estimated density to obtain the kernel averaged value of the variable at a precise point in the phase space,

$$\overline{q}_0^k = \frac{1}{N(x_0; h)} \sum_i K_h(x_i - x_0, y_i - y_0) q_i. \tag{A.3}$$

Here, $\overline{q}_0^k$ represents the kernel average at the point (x_0, y_0) in the phase space of the variable q and the sum is over all points (x_i, y_i) where the variable has the value q_i. The kernel $K_h(x, y)$ is the extension in two dimensions

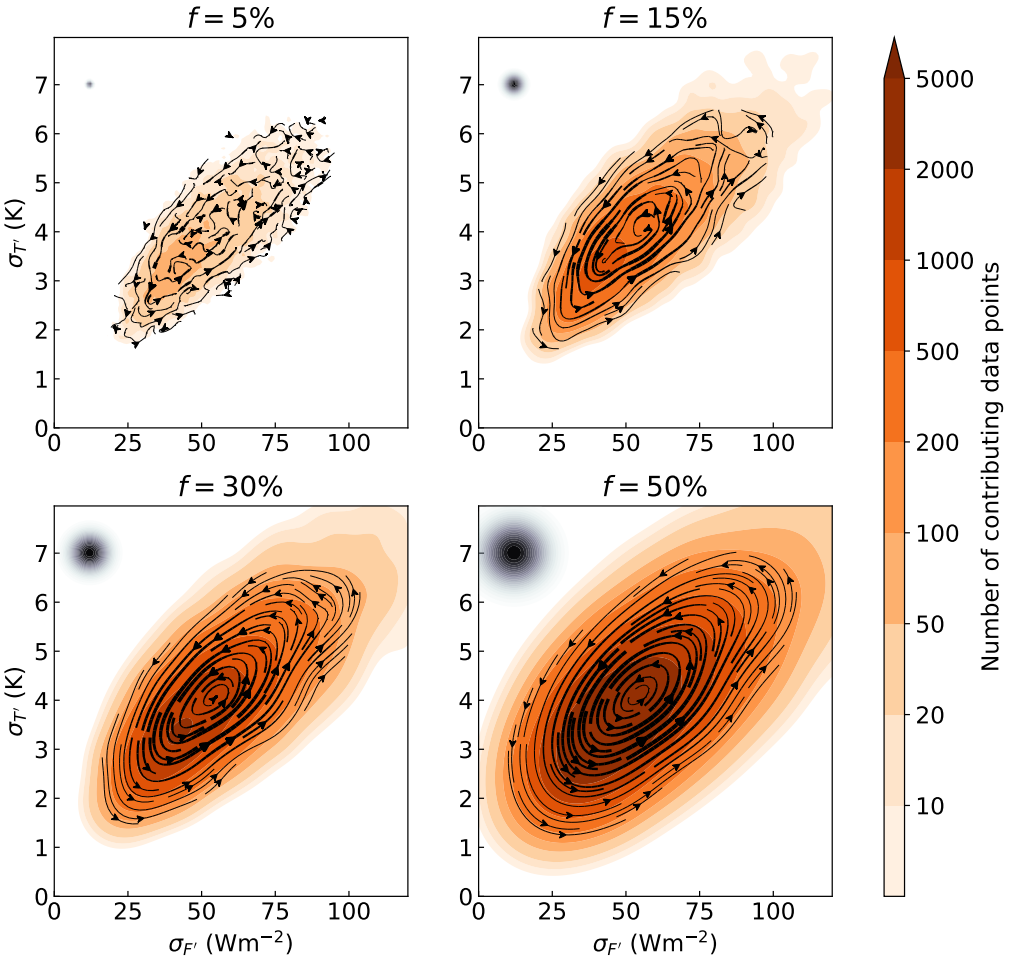

Figure A.2: Kernel density estimation of the distribution of data in the $\sigma_{F'}-$ $-\sigma_{T'}$ phase space using a Gaussian kernel with bandwidth equal to a fraction f of the standard deviations of the $\sigma_{F',T'}$ time series. The shape and size of the Gaussian kernel is represented by the black dot in the top right corner of each panel for comparison. Shading indicates the number of data entries contributing to the average in each point in the phase space. Streamlines represent the average circulation resulting from the kernel averaged phase tendencies of $\sigma_{F'}$ and$\sigma_{T'}$.

of the one-dimensional Gaussian kernel in Eq. A.2,

$$K_{\mathbf{h}}(x,y) = \exp\left(-\frac{1}{2}\left(\left(\frac{x}{h_x}\right)^2 + \left(\frac{y}{h_y}\right)^2\right)\right)$$

The parameter $\mathbf{h} = (h_x, h_y)$ is equal to the product of $\sigma_{x,y}$ (standard deviations of the X, Y time series) and $f_{x,y}$, which tunes the bandwidth and effectively determines the shape of the Gaussian distribution corresponding to the kernel $K(x,y)$. In our analyses we assume $f_x = f_y = f$ for the sake

of simplicity, which means the parameter $\mathbf{h}$ becomes $\mathbf{h} = (f\sigma_x, f\sigma_y)$.

In Chapter 2 we focus on the kernel averages across the standard deviations phase space of area-mean values like mean air temperature or sensible heat flux (see Fig. 2.9) to get a general understanding of the evolution of the spatial covariance and its driving mechanisms. In addition, we can also extend our attention to the evolution of the flow over a larger domain if we compute the kernel average of the variable under consideration at each longitude–latitude grid point and observe its evolution across the phase space, as we do for the 500hPa and 1000hPa geopotential height fields in Chapter 5 (see Figs. 5.7, 5.8).

Appendix B

Regional configuration of the Unified Model

Chapter 4 involves very-high-resolution, storm-resolving (0–10km) model simulations of four case studies of strong spatial covariance between surface heat flux and air temperature over the Gulf Stream Extension region. A storm-resolving (or convection-permitting) resolution allows for a more accurate and realistic representation of finer-scale features like convection and local air–sea thermal interactions that are central to our study of the role of surface heat flux in the life cycle of the North Atlantic storm track and which are underrepresented in global-resolution models (10–100km) that are used to produce reanalysis data sets (e.g., ERA-Interim, ERA5, etc).

In order to be able to computationally afford a high level of model horizontal resolution we need to define our model over a spatial domain of reduced size compared to that of a global circulation model. To that extent, we consider a limited-area model (LAM) with convection-permitting horizontal resolution and nest it on a global driving model of lower resolution which provides the LAM with appropriate lateral boundary conditions. Specifically, in our experiments data from the ECMWF ERA5 dataset (Hersbach et al., 2020) acts as the driving model to the LAM. Data from ERA5 is provided with a horizontal resolution of 31km ($\approx 0.25°$) and is based on cycle Cy41r2 (operational in 2016) of the ECMWF's Integrated Forecasting System (IFS) spectral model. IFS has been assimilating sea surface boundary conditions from the Operational Sea-surface Temperature and Sea Ice Analysis (OSTIA, Donlon et al., 2012) since 2007.

Given the considerable jump in horizontal resolution from ERA5 (31km) to convection-permitting (4.4km), it becomes necessary to introduce an in-

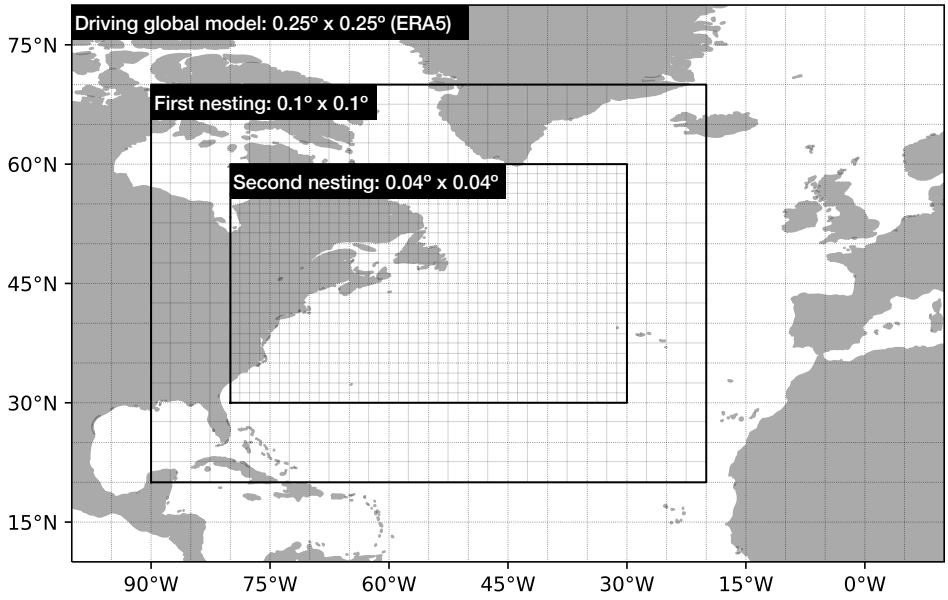

Figure B.1: The different domains used in the nesting suite approach. The grids are not to scale and are provided just for a qualitative overview.

termediate step so that the interpolation of the wind field's lateral boundary conditions across the different resolutions is more consistent. Therefore, we define a convection-parametrised LAM with a horizontal resolution of about 10km which will be driven by ERA5 and then used to nest the convection permitting LAM. Lateral boundary conditions (LBCs) for each nested LAM are generated from an interpolation of the driving model, which includes balance calculations described in Davies (2014).

The two convection-parametrised and convection-permitting LAMs are run with specific configurations of the Met Office Unified Model (MetUM). The MetUM is a finite-difference model that solves the non-hydrostatic, deep-atmosphere dynamical equations with a semi-implicit, semi-Lagrangian integration scheme (Davies et al., 2005). The model uses Arakawa C staggering in the horizontal (Arakawa and Lamb, 1977) and is terrain following in the vertical with a hybrid-height coordinate and Charney-Phillips staggering (Charney and Phillips, 1953).

The single-nested, convection-parametrised LAM is run with the Global Atmosphere 6.0 (GA6, Walters et al., 2017) configuration of the MetUM, which uses extensively modified microphysics based on Wilson and Ballard (1999), a revised version of the convection scheme of Gregory and Rowntree (1990) and the radiation scheme of Edwards and Slingo (1996) with

a configuration based on Cusack et al. (1998) with a number of significant updates. The LAM extends over the western North Atlantic sector (20°N–70°N, 90°W–20°W) and is based on an unrotated horizontal grid (i.e., it maintains the same coordinate system of the global model) with a horizontal resolution of 0.1° in both longitude and latitude (corresponding to a typical spacing between grid points of 10km, depending on latitude) and 70 vertical levels with a lid at a height of 40km. The integration time step used with the GA6 configuration is 300 seconds.

The double-nested, convection-permitting LAM is then nested onto the first LAM. The double-nested LAM is run with the second Regional Atmosphere and Land science configuration (RAL2) of the MetUM optimised for the mid-latitudes. RAL2 builds upon an older configuration (RAL1), described in Bush et al. (2020), and the main differences relate to land processes and boundary layer dynamics (Mike Bush 2021, personal communication), specifically implementing a parametrisation of part of the vertical turbulent flux as a function of local horizontal gradients following from the study by Moeng et al. (2010). Further details are reported in an internal assessment document accessible to registered users at

`https://code.metoffice.gov.uk/trac/rmed/attachment/wiki/ra2/RA2_Assessment_210319.pdf` (last access July 2021).

The spatial domain over which the double-nested LAM is defined corresponds to the Gulf Stream Extension region (30°N–60°N, 80°W–30°W), which was the focus of our previous work (Marcheggiani and Ambaum, 2020). It is based on an unrotated horizontal grid with a horizontal grid resolution of 0.04° (typical grid spacing of 4.4km, depending on latitude) and 90 vertical levels with a lid at 40km. The integration time step used with RAL2 configuration is 120 seconds. Figure B.1 illustrates the geographical disposition of the various spatial domains adopted.

In both high and low resolution LAMs, sea surface boundary conditions are passed daily (at UTC0000) from OSTIA, after a reconfiguration from the native 0.05° degree resolution (≈ 5.5km). Given the high resolution of the ocean component, the spatial variability associated with mesoscale oceanic eddies is expected to be fully visible by the atmospheric component (especially by the higher-resolution LAM).

The lateral boundary conditions are passed to the nested models from the driving model every 3 hours. Given that we use ERA5 reanalysis, the driving model is always on *analysis time* (in case the Global UM were used as

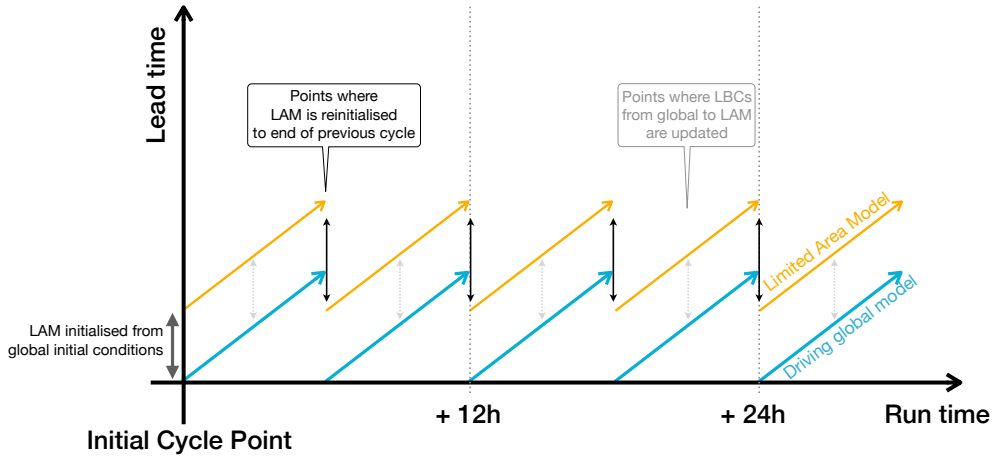

Figure B.2: Diagram of the nesting approach in the UM.

driving model, it would be reinitialised on a 6-hourly basis). The two nested LAMs are reinitialised at the end of every 6-hour cycle to the endpoint of the previous cycle and are said to be *free-running*, that is they are essentially kept running seamlessly throughout the entire duration of the simulation. An illustrative diagram is shown in Fig. B.2 in the case of a single nesting of a LAM onto a global driving model.

Bibliography

Ambaum, M. H. P. and Novak, L.: A nonlinear oscillator describing storm track variability, Quarterly Journal of the Royal Meteorological Society, 140, 2680–2684, 2014.

Arakawa, A. and Lamb, V. R.: Computational design of the basic dynamical processes of the UCLA general circulation model, General Circulation Models of the Atmosphere, 17, 173–265, 1977.

Athanasiadis, P. J. and Ambaum, M. H. P.: Linear Contributions of Different Time Scales to Teleconnectivity, Journal of Climate, 22, 3720–3728, https://doi.org/https://doi.org/10.1175/2009JCLI2707.1, 2009.

Barsugli, J. J. and Battisti, D. S.: The basic effects of atmosphere–ocean thermal coupling on midlatitude variability, Journal of the Atmospheric Sciences, 55, 477–493, 1998.

Blackmon, M. L., Wallace, J. M., Lau, N.-C., and Mullen, S. L.: An observational study of the Northern Hemisphere wintertime circulation, Journal of the Atmospheric Sciences, 34, 1040–1053, 1977.

Bowen, I. S.: The Ratio of Heat Losses by Conduction and by Evaporation from any Water Surface, Physical Review, 27, 779–787, https://doi.org/10.1103/PhysRev.27.779, 1926.

Brayshaw, D. J., Hoskins, B., and Blackburn, M.: The basic ingredients of the North Atlantic storm track. Part I: Land–sea contrast and orography, Journal of the Atmospheric Sciences, 66, 2539–2558, 2009.

Brayshaw, D. J., Hoskins, B., and Blackburn, M.: The basic ingredients of the North Atlantic storm track. Part II: Sea surface temperatures, Journal of the Atmospheric Sciences, 68, 1784–1805, 2011.

Bui, H. and Spengler, T.: On the influence of sea surface temperature distributions on the development of extratropical cyclones, Journal of the Atmospheric Sciences, 78, 1173–1188, 2021.

Bush, M., Allen, T., Bain, C., Boutle, I., Edwards, J., Finnenkoetter, A., Franklin, C., Hanley, K., Lean, H., Lock, A., Manners, J., Mittermaier, M., Morcrette, C., North, R., Petch, J., Short, C., Vosper, S., Walters, D., Webster, S., Weeks, M., Wilkinson, J., Wood, N., and Zerroukat, M.: The first Met Office unified model–JULES regional atmosphere and land configuration, RAL1, Geoscientific Model Development, 13, 1999–2029, 2020.

Chang, E. K. M. and Zurita-Gotor, P.: Simulating the seasonal cycle of the Northern Hemisphere storm tracks using idealized nonlinear storm-track models, Journal of the Atmospheric Sciences, 64, 2309–2331, 2007.

Chang, E. K. M., Lee, S., and Swanson, K. L.: Storm track dynamics, Journal of Climate, 15, 2163–2183, 2002.

Charney, J. G. and Phillips, N. A.: Numerical integration of the quasi-geostrophic equations for barotropic and simple baroclinic flows, Journal of Atmospheric Sciences, 10, 71–99, 1953.

Chelton, D. B., Schlax, M. G., Freilich, M. H., and Milliff, R. F.: Satellite measurements reveal persistent small-scale features in ocean winds, Science, 303, 978–983, 2004.

Ciasto, L. M. and Thompson, D. W. J.: North Atlantic atmosphere–ocean interaction on intraseasonal time scales, Journal of Climate, 17, 1617–1621, 2004.

Cusack, S., Slingo, A., Edwards, J. M., and Wild, M.: The radiative impact of a simple aerosol climatology on the Hadley Centre atmospheric GCM, Quarterly Journal of the Royal Meteorological Society, 124, 2517–2526, 1998.

Czaja, A. and Frankignoul, C.: Influence of the North Atlantic SST on the atmospheric circulation, Geophysical Research Letters, 26, 2969–2972, 1999.

Czaja, A. and Frankignoul, C.: Observed Impact of Atlantic SST Anomalies on the North Atlantic Oscillation, Journal of Climate, 15, 606

– 623, https://doi.org/10.1175/1520-0442(2002)015<0606:OIOASA>2.0.CO;2, 2002.

Czaja, A., Frankignoul, C., Minobe, S., and Vannière, B.: Simulating the Midlatitude Atmospheric Circulation: What Might We Gain From High-Resolution Modeling of Air-Sea Interactions?, Current Climate Change Reports, pp. 1–17, 2019.

Davies, H. C. and Bishop, C. H.: Eady edge waves and rapid development, Journal of Atmospheric Sciences, 51, 1930–1946, 1994.

Davies, T.: Lateral boundary conditions for limited area models, Quarterly Journal of the Royal Meteorological Society, 140, 185–196, 2014.

Davies, T., Cullen, M. J. P., Malcolm, A. J., Mawson, M. H., Staniforth, A., White, A. A., and Wood, N.: A new dynamical core for the Met Office's global and regional modelling of the atmosphere, Quarterly Journal of the Royal Meteorological Society, 131, 1759–1782, 2005.

Davis, R. E.: Predictability of Sea Surface Temperature and Sea Level Pressure Anomalies over the North Pacific Ocean, Journal of Physical Oceanography, 6, 249–266, 1976.

De Vries, H., Methven, J., Frame, T. H., and Hoskins, B. J.: Baroclinic waves with parameterized effects of moisture interpreted using Rossby wave components, Journal of the atmospheric sciences, 67, 2766–2784, 2010.

De Vries, H., Scher, S., Haarsma, R., Drijfhout, S., and van Delden, A.: How Gulf-Stream SST-fronts influence Atlantic winter storms, Climate Dynamics, pp. 1–11, 2018.

Dee, D. P., Uppala, S. M., Simmons, A. J., Berrisford, P., Poli, P., Kobayashi, S., Andrae, U., Balmaseda, M. A., Balsamo, G., Bauer, d. P., and Bechtold, P.: The ERA-Interim reanalysis: Configuration and performance of the data assimilation system, Quarterly Journal of the Royal Meteorological Society, 137, 553–597, 2011.

Deser, C. and Timlin, M. S.: Atmosphere–Ocean Interaction on Weekly Timescales in the North Atlantic and Pacific, Journal of Climate, 10, 393–408, 1997.

Deser, C., Alexander, M. A., and Timlin, M. S.: Understanding the persistence of sea surface temperature anomalies in midlatitudes, Journal of Climate, 16, 57–72, 2003.

Deser, C., Alexander, M. A., Xie, S.-P., and Phillips, A. S.: Sea surface temperature variability: Patterns and mechanisms, Annual review of marine science, 2, 115–143, 2010.

Donlon, C. J., Martin, M., Stark, J., Roberts-Jones, J., Fiedler, E., and Wimmer, W.: The operational sea surface temperature and sea ice analysis (OSTIA) system, Remote Sensing of Environment, 116, 140–158, 2012.

Eady, E. T.: Long Waves and Cyclone Waves, Tellus, 1, 33–52, https://doi.org/10.3402/tellusa.v1i3.8507, 1949.

ECMWF: IFS Documentation CY36R1 - Part IV: Physical Processes, chap. 3, pp. 33–55, no. 4 in IFS Documentation, ECMWF, https://doi.org/10.21957/2loi3bxcz, 2010.

Edwards, J. M. and Slingo, A.: Studies with a flexible new radiation code. I: Choosing a configuration for a large-scale model, Quarterly Journal of the Royal Meteorological Society, 122, 689–719, 1996.

Ferranti, L., Molteni, F., and Palmer, T. N.: Impact of localized tropical and extratropical SST anomalies in ensembles of seasonal GCM integrations, Quarterly Journal of the Royal Meteorological Society, 120, 1613–1645, 1994.

Foussard, A., Lapeyre, G., and Plougonven, R.: Storm track response to oceanic eddies in idealized atmospheric simulations, Journal of Climate, 32, 445–463, 2019.

Frame, T., Methven, J., Gray, S., and Ambaum, M.: Flow-dependent predictability of the North Atlantic jet, Geophysical Research Letters, 40, 2411–2416, 2013.

Frankignoul, C. and Hasselmann, K.: Stochastic climate models, Part II Application to sea-surface temperature anomalies and thermocline variability, Tellus, 29, 289–305, 1977.

Franzke, C., Woollings, T., and Martius, O.: Persistent circulation regimes and preferred regime transitions in the North Atlantic, Journal of the Atmospheric Sciences, 68, 2809–2825, 2011.

Frenger, I., Gruber, N., Knutti, R., and Münnich, M.: Imprint of Southern Ocean eddies on winds, clouds and rainfall, Nature Geoscience, 6, 608–612, 2013.

Frolov, S., Reynolds, C. A., Alexander, M., Flatau, M., Barton, N. P., Hogan, P., and Rowley, C.: Coupled Ocean–Atmosphere Covariances in Global Ensemble Simulations: Impact of an Eddy-Resolving Ocean, Monthly Weather Review, 149, 1193–1209, 2021.

Gill, A. E.: International Geophysics, 30: Atmosphere-ocean Dynamics, Elsevier, 1982.

Gregory, D. and Rowntree, P. R.: A mass flux convection scheme with representation of cloud ensemble characteristics and stability-dependent closure, Monthly Weather Review, 118, 1483–1506, 1990.

Hanley, J. and Caballero, R.: Objective identification and tracking of multicentre cyclones in the ERA-Interim reanalysis dataset, Quarterly Journal of the Royal Meteorological Society, 138, 612–625, 2012.

Haualand, K. F. and Spengler, T.: Direct and indirect effects of surface fluxes on moist baroclinic development in an idealized framework, Journal of the Atmospheric Sciences, 77, 3211–3225, 2020.

Hausmann, U., Czaja, A., and Marshall, J.: Mechanisms controlling the SST air-sea heat flux feedback and its dependence on spatial scale, Climate Dynamics, 48, 1297–1307, 2017.

Heifetz, E., Bishop, C., Hoskins, B., and Methven, J.: The counter-propagating Rossby-wave perspective on baroclinic instability. I: Mathematical basis, Quarterly Journal of the Royal Meteorological Society, 130, 211–231, 2004a.

Heifetz, E., Methven, J., Hoskins, B., and Bishop, C.: The counter-propagating Rossby-wave perspective on baroclinic instability. II: Application to the Charney model, Quarterly Journal of the Royal Meteorological Society, 130, 233–258, 2004b.

Held, I. M. and Phillipps, P. J.: Sensitivity of the eddy momentum flux to meridional resolution in atmospheric GCMs, Journal of Climate, 6, 499–507, 1993.

Hersbach, H., Bell, B., Berrisford, P., Hirahara, S., Horányi, A., Muñoz-Sabater, J., Nicolas, J., Peubey, C., Radu, R., Schepers, D., Dimmons, A., Soci, C., Abdalla, S., Abellan, X., Balsamo, G., Bechtold, P., Biavati, G., Bidlot, J., Bonavita, M., De Chiara, G., Dahlgren, P., Dee, D. P., Diamantakis, M., Dragani, R., Flemming, J., Forbes, R., Fuentes, M., Geer, A., Haimberger, L., Healy, S., Hogan, R. J., Hólm, E., Janisková, M., Keeley, S., Laloyaux, P., Lopez, P., Lupu, C., Radnoti, G., de Rosnay, P., Rozum, I., Vamborg, F., Villaume, S., and Thépaut, J.: The ERA5 global reanalysis, Quarterly Journal of the Royal Meteorological Society, 146, 1999–2049, 2020.

Hoskins, B., Pedder, M., and Jones, D. W.: The omega equation and potential vorticity, Quarterly Journal of the Royal Meteorological Society: A journal of the atmospheric sciences, applied meteorology and physical oceanography, 129, 3277–3303, 2003.

Hoskins, B. J. and Ambrizzi, T.: Rossby wave propagation on a realistic longitudinally varying flow, Journal of the Atmospheric Sciences, 50, 1661–1671, 1993.

Hoskins, B. J. and Heckley, W. A. J.: Cold and warm fronts in baroclinic waves, Quarterly Journal of the Royal Meteorological Society, 107, 79–90, 1981.

Hoskins, B. J. and Hodges, K.: New perspectives on the Northern Hemisphere winter storm tracks, Journal of the Atmospheric Sciences, 59, 1041–1061, 2002.

Hoskins, B. J. and Valdes, P. J.: On the existence of storm-tracks, Journal of the Atmospheric Sciences, 47, 1854–1864, 1990.

Hoskins, B. J., James, I. N., and White, G. H.: The shape, propagation and mean-flow interaction of large-scale weather systems, Journal of the Atmospheric Sciences, 40, 1595–1612, 1983.

Hotta, D. and Nakamura, H.: On the significance of the sensible heat supply from the ocean in the maintenance of the mean baroclinicity along storm tracks, Journal of Climate, 24, 3377–3401, 2011.

Iwasaki, T. and Mochizuki, Y.: Mass-weighted isentropic zonal mean equatorward flow in the Northern Hemispheric winter, Sola, 8, 115–118, 2012.

Iwasaki, T., Shoji, T., Kanno, Y., Sawada, M., Ujiie, M., and Takaya, K.: Isentropic analysis of polar cold airmass streams in the Northern Hemispheric winter, Journal of the Atmospheric Sciences, 71, 2230–2243, 2014.

James, I. N.: Introduction to Circulating Atmospheres, Cambridge University Press, 1995.

Kalnay, E., Kanamitsu, M., Kistler, R., Collins, W., Deaven, D., Gandin, L., Iredell, M., Saha, S., White, G., Woollen, J., et al.: The NCEP/NCAR 40-year reanalysis project, Bulletin of the American meteorological Society, 77, 437–472, 1996.

Kilpatrick, T., Schneider, N., and Qiu, B.: Atmospheric response to a midlatitude SST front: Alongfront winds, Journal of the Atmospheric Sciences, 73, 3489–3509, 2016.

Klaver, R., Haarsma, R., Vidale, P. L., and Hazeleger, W.: Effective resolution in high resolution global atmospheric models for climate studies, Atmospheric Science Letters, 21, e952, 2020.

Kushnir, Y., Robinson, W. A., Bladé, I., Hall, N. M. J., Peng, S., and Sutton, R.: Atmospheric GCM response to extratropical SST anomalies: Synthesis and evaluation, Journal of Climate, 15, 2233–2256, 2002.

Lembo, V., Messori, G., Graversen, R., and Lucarini, V.: Spectral decomposition and extremes of atmospheric meridional energy transport in the Northern Hemisphere midlatitudes, Geophysical Research Letters, 46, 7602–7613, 2019.

Lewis, H. W., Castillo Sanchez, J. M., Arnold, A., Fallmann, J., Saulter, A., Graham, J., Bush, M., Siddorn, J., Palmer, T., Lock, A., et al.: The UKC3 regional coupled environmental prediction system, Geoscientific Model Development, 12, 2357–2400, 2019.

Li, L., Ingersoll, A. P., Jiang, X., Feldman, D., and Yung, Y. L.: Lorenz energy cycle of the global atmosphere based on reanalysis datasets, Geophysical Research Letters, 34, L16 813, https://doi.org/10.1029/2007GL029985, 2007.

Lim, G. H. and Wallace, J. M.: Structure and evolution of baroclinic waves as inferred from regression analysis, Journal of the Atmospheric Sciences, 48, 1718–1732, 1991.

Lorenz, E. N.: Available potential energy and the maintenance of the general circulation, Tellus, 7, 157–167, 1955.

Ma, X., Chang, P., Saravanan, R., Montuoro, R., Nakamura, H., Wu, D., Lin, X., and Wu, L.: Importance of resolving Kuroshio front and eddy influence in simulating the North Pacific storm track, Journal of Climate, 30, 1861–1880, 2017.

Mailier, P. J., Stephenson, D. B., Ferro, C. A., and Hodges, K. I.: Serial clustering of extratropical cyclones, Monthly weather review, 134, 2224–2240, 2006.

Marcheggiani, A. and Ambaum, M. H. P.: The role of heat-flux–temperature covariance in the evolution of weather systems, Weather and Climate Dynamics, 1, 701–713, 2020.

Marcheggiani, A., Ambaum, M. H. P., and Messori, G.: The Life Cycle of Meridional Heat Flux Peaks, Quarterly Journal of the Royal Meteorological Society, https://doi.org/doi:10.1002/qj.4249, 2022.

Margules, M.: Über die Energie der Stürme, Jahrb. Zentralanst. Meteor., pp. 1–26, 1903.

Marques, C. A., Rocha, A., Corte-Real, J., Castanheira, J. M., Ferreira, J., and Melo-Gonçalves, P.: Global atmospheric energetics from NCEP–Reanalysis 2 and ECMWF–ERA40 Reanalysis, International Journal of Climatology, 29, 159–174, 2009.

Marshall, J., Johnson, H., and Goodman, J.: A study of the interaction of the North Atlantic Oscillation with ocean circulation, Journal of Climate, 14, 1399–1421, 2001a.

Marshall, J., Kushnir, Y., Battisti, D., Chang, P., Czaja, A., Dickson, R., Hurrell, J., McCartney, M., Saravanan, R., and Visbeck, M.: North Atlantic climate variability: phenomena, impacts and mechanisms, International Journal of Climatology: A Journal of the Royal Meteorological Society, 21, 1863–1898, 2001b.

Mason, P. J.: Baroclinic waves in a container with sloping end walls, Philosophical Transactions of the Royal Society of London. Series A, Mathematical and Physical Sciences, 278, 397–445, 1975.

Messori, G. and Czaja, A.: On the sporadic nature of meridional heat transport by transient eddies, Quarterly Journal of the Royal Meteorological Society, 139, 999–1008, 2013.

Messori, G. and Czaja, A.: Some considerations on the spectral features of meridional heat transport by transient eddies, Quarterly Journal of the Royal Meteorological Society, 140, 1377–1386, 2014.

Messori, G. and Czaja, A.: On local and zonal pulses of atmospheric heat transport in reanalysis data, Quarterly Journal of the Royal Meteorological Society, 141, 2376–2389, 2015.

Messori, G., Geen, R., and Czaja, A.: On the spatial and temporal variability of atmospheric heat transport in a hierarchy of models, Journal of the Atmospheric Sciences, 74, 2163–2189, 2017.

Minobe, S., Kuwano-Yoshida, A., Komori, N., Xie, S.-P., and Small, R. J.: Influence of the Gulf Stream on the troposphere, Nature, 452, 206–209, 2008.

Moeng, C. H., Sullivan, P. P., Khairoutdinov, M. F., and Randall, D. A.: A mixed scheme for subgrid-scale fluxes in cloud-resolving models, Journal of the Atmospheric Sciences, 67, 3692–3705, 2010.

Moreton, S. M., Ferreira, D., Roberts, M. J., and Hewitt, H. T.: Evaluating surface eddy properties in coupled climate simulations with 'eddy-present'and 'eddy-rich'ocean resolution, Ocean Modelling, 147, 101 567, 2020.

Moreton, S. M., Ferreira, D., Roberts, M. J., and Hewitt, H. T.: Air-Sea Turbulent Heat Flux Feedback Over Mesoscale Eddies, Geophysical Research Letters, 48, https://doi.org/https://doi.org/10.1029/2021GL095407, 2021.

Nakamura, H.: Midwinter suppression of baroclinic wave activity in the Pacific, Journal of Atmospheric Sciences, 49, 1629–1642, 1992.

Nakamura, H., Sampe, T., Goto, A., Ohfuchi, W., and Xie, S.-P.: On the importance of midlatitude oceanic frontal zones for the mean state and dominant variability in the tropospheric circulation, Geophysical Research Letters, 35, L15 709, 2008.

Novak, L. and Tailleux, R.: On the local view of atmospheric available potential energy, Journal of the Atmospheric Sciences, 75, 1891–1907, 2018.

Novak, L., Ambaum, M. H. P., and Tailleux, R.: The life cycle of the North Atlantic storm track, Journal of the Atmospheric Sciences, 72, 821–833, 2015.

Novak, L., Ambaum, M. H. P., and Tailleux, R.: Marginal stability and predator–prey behaviour within storm tracks, Quarterly Journal of the Royal Meteorological Society, 143, 1421–1433, 2017.

Oort, A. H.: On estimates of the atmospheric energy cycle, Monthly Weather Review, 92, 483–493, 1964.

Oort, A. H. and Peixóto, J. P.: The annual cycle of the energetics of the atmosphere on a planetary scale, Journal of Geophysical Research, 79, 2705–2719, 1974.

Orlanski, I.: Bifurcation in eddy life cycles: Implications for storm track variability, Journal of the Atmospheric Sciences, 60, 993–1023, 2003.

Papritz, L. and Spengler, T.: Analysis of the slope of isentropic surfaces and its tendencies over the North Atlantic, Quarterly Journal of the Royal Meteorological Society, 141, 3226–3238, 2015.

Peixoto, J. P. and Oort, A. H.: Physics of Climate, New York, NY (United States); American Institute of Physics, 1992.

Peng, S. and Robinson, W. A.: Relationships between atmospheric internal variability and the responses to an extratropical SST anomaly, Journal of climate, 14, 2943–2959, 2001.

Peng, S., Robinson, W. A., and Li, S.: Mechanisms for the NAO responses to the North Atlantic SST tripole, Journal of Climate, 16, 1987–2004, 2003.

Pinto, J. G., Spangehl, T., Ulbrich, U., and Speth, P.: Sensitivities of a cyclone detection and tracking algorithm: individual tracks and climatology, Meteorologische Zeitschrift, 14, 823–838, 2005.

Priestley, M. D. K., Pinto, J. G., Dacre, H. F., and Shaffrey, L. C.: Rossby wave breaking, the upper level jet, and serial clustering of extratropical cyclones in western Europe, Geophysical Research Letters, 44, 514–521, 2017.

Rivière, G.: Effect of latitudinal variations in low-level baroclinicity on eddy life cycles and upper-tropospheric wave-breaking processes, Journal of the Atmospheric Sciences, 66, 1569–1592, 2009.

Scaife, A. A. and Smith, D.: A signal-to-noise paradox in climate science, npj Climate and Atmospheric Science, 1, 1–8, 2018.

Schemm, S. and Rivière, G.: On the efficiency of baroclinic eddy growth and how it reduces the North Pacific storm-track intensity in midwinter, Journal of Climate, 32, 8373–8398, 2019.

Shaw, T. A., Baldwin, M., Barnes, E. A., Caballero, R., Garfinkel, C. I., Hwang, Y.-T., Li, C., O'gorman, P. A., Rivière, G., Simpson, I. R., et al.: Storm track processes and the opposing influences of climate change, Nature Geoscience, 9, 656–664, 2016.

Smith, D. M., Scaife, A. A., Eade, R., Athanasiadis, P., Bellucci, A., Bethke, I., Bilbao, R., Borchert, L. F., Caron, L.-P., Counillon, F., et al.: North Atlantic climate far more predictable than models imply, Nature, 583, 796–800, 2020.

Stull, R. B.: Mean boundary layer characteristics, in: An Introduction to Boundary Layer Meteorology, pp. 1–27, Springer, 1988.

Swanson, K. L. and Pierrehumbert, R. T.: Lower-tropospheric heat transport in the Pacific storm track, Journal of the Atmospheric Sciences, 54, 1533–1543, 1997.

Tailleux, R.: Available potential energy and exergy in stratified fluids, Annual review of fluid mechanics, 45, 35–58, 2013.

Ulbrich, U. and Speth, P.: The global energy cycle of stationary and transient atmospheric waves: results from ECMWF analyses, Meteorology and Atmospheric Physics, 45, 125–138, 1991.

Ulbrich, U., Leckebusch, G. C., and Pinto, J. G.: Extra-tropical cyclones in the present and future climate: a review, Theoretical and Applied Climatology, 96, 117–131, 2009.

Vannière, B., Czaja, A., Dacre, H., Woollings, T., and Parfitt, R.: A potential vorticity signature for the cold sector of winter extratropical cyclones, Quarterly Journal of the Royal Meteorological Society, 142, 432–442, 2016.

Vannière, B., Czaja, A., Dacre, H., and Woollings, T.: A "cold path" for the Gulf Stream–troposphere connection, Journal of Climate, 30, 1363–1379, 2017a.

Vannière, B., Czaja, A., and Dacre, H. F.: Contribution of the cold sector of extratropical cyclones to mean state features over the Gulf Stream in winter, Quarterly Journal of the Royal Meteorological Society, 143, 1990–2000, 2017b.

Wai, M. M.-K. and Stage, S. A.: Dynamical analyses of marine atmospheric boundary layer structure near the Gulf Stream oceanic front, Quarterly Journal of the Royal Meteorological Society, 115, 29–44, 1989.

Wallace, J. M., Smith, C., and Jiang, Q.: Spatial Patterns of Atmosphere-Ocean Interaction in the Northern Winter, Journal of Climate, 3, 990–998, 1990.

Walters, D., Boutle, I., Brooks, M., Melvin, T., Stratton, R., Vosper, S., Wells, H., Williams, K., Wood, N., Allen, T., et al.: The Met Office unified model global atmosphere 6.0/6.1 and JULES global land 6.0/6.1 configurations, Geoscientific Model Development, 10, 1487–1520, 2017.

Wand, M. P. and Jones, M. C.: Kernel smoothing, CRC press, 1994.

Wilks, D. S.: Statistical Methods in the Atmospheric Sciences, vol. 100, Academic Press, 2011.

Willison, J., Robinson, W. A., and Lackmann, G. M.: The importance of resolving mesoscale latent heating in the North Atlantic storm track, Journal of the Atmospheric Sciences, 70, 2234–2250, 2013.

Wills, S. M., Thompson, D. W. J., and Ciasto, L. M.: On the observed relationships between variability in Gulf Stream sea surface temperatures and

the atmospheric circulation over the North Atlantic, Journal of Climate, 29, 3719–3730, 2016.

Wilson, D. R. and Ballard, S. P.: A microphysically based precipitation scheme for the UK Meteorological Office Unified Model, Quarterly Journal of the Royal Meteorological Society, 125, 1607–1636, 1999.

Woollings, T., Hannachi, A., and Hoskins, B.: Variability of the North Atlantic eddy-driven jet stream, Quarterly Journal of the Royal Meteorological Society, 136, 856–868, 2010.

Yano, J.-I., Ambaum, M. H. P., Dacre, H. F., and Manzato, A.: A dynamical–system description of precipitation over the tropics and the midlatitudes, Tellus A: Dynamic Meteorology and Oceanography, 72, 1–17, 2020.

Zhang, X., Ma, X., and Wu, L.: Effect of Mesoscale Oceanic Eddies on Extratropical Cyclogenesis: a Tracking Approach, Journal of Geophysical Research: Atmospheres, 124, 6411–6422, 2019.